Experimental characterization of airfoil boundary layers for improvement of aeroacoustic and aerodynamic modeling

Fischer, Andreas

Publication date:
2011

Document Version
Publisher's PDF, also known as Version of record

Experimental characterization of airfoil boundary layers for improvement of aeroacoustic and aerodynamic modeling

Andreas Fischer

PhD Thesis
Roskilde, November 2011

Technical University of Denmark
National Laboratory for Sustainable Energy, Wind Energy Department
Frederiksborgvej 399, DK-4000 Roskilde, Denmark
Phone +45 46774677
risoe@risoe.dtu.dk
www.risoe.dk

Summary

The present work aims at the characterization of aerodynamic noise from wind turbines. There is a consensus among scientists that the dominant aerodynamic noise mechanism is turbulent boundary trailing edge noise. In almost all operational conditions the boundary layer flow over the wind turbine blades makes a transition from laminar to turbulent. In the turbulent boundary layer eddies are created which are a potential noise sources. They are ineffective as noise source on the airfoil surface or in free flow, but when convecting past the trailing edge of the airfoil their efficiency is much increased and audible sound is radiated.
We performed measurements of the boundary layer velocity fluctuations and the fluctuating surface pressure field in two different wind tunnels and on three different airfoils. The first wind tunnel is the one of LM Wind Power A/S following the classic concept for aerodynamic wind tunnels with a hard wall test section. Acoustic far field sound measurements are not possible in this tunnel due to the high background noise. The second wind tunnel is owned by Virginia Tech University. The test section has Kevlar walls which are acoustically transparent and it is surrounded by an anechoic chamber. In this experiment the far field sound was measured with a microphone array placed in the anechoic chamber.
The measurements were compared to predictions with an analytical model for trailing edge noise. The analytical model is divided into two steps. First the fluctuating velocity field is related to the fluctuating surface pressure field, then the far field trailing edge noise is related to the surface pressure field close to the trailing edge of the airfoil. The data base of measurements was used to evaluate the different parts of the original analytical trailing edge noise model and to improve it, because the predictions gave in general too low far field noise levels.
Our main finding is that the acoustic formulations to relate the fluctuating surface pressure field close to the trailing edge of airfoil to the radiated far field sound give excellent results when compared to far field sound measurements

with a microphone array and measured surface pressure statistics as input up to a frequency of about 2000-3000Hz. The fluctuating surface pressure field can be measured in a wind tunnel with high background noise due to the high level of the fluctuating surface pressure field. Hence, trailing edge noise can be evaluated by means of measured surface pressure field, even in cases where a direct measurement of trailing edge noise is not possible. This opens up great new vistas, i.e. by testing new airfoils in a standard industrial wind tunnel or by testing new wind turbine rotors in the field.
The main difficulty for trailing edge noise modeling is to predict the fluctuating surface pressure field correctly and one uncertainty of the original model was the assumption of isotropic turbulence. This was investigated in the present work and a new model to relate the boundary layer velocity field to the surface pressure field accounting for an anisotropic turbulence spectrum was proposed. The results were very similar compared to the original model and underestimated the measured one point surface pressure spectrum, even though the prediction of the one point velocity spectra was improved.

Resumé

Dette arbejde har fokus på modelleringen af vindmøllestøj. Forskere er enige om at den dominerende støjkilde er turbulent grænselags-bagkantstøj. I næsten alle driftssituationer sker der et omslag fra laminar til turbulent strømning i grænselaget på vingens overflade. Hvirvler generes i det turbulente grænselag. Disse hvirvler er en potentiel støjkilde. Hvirvlerne er ineffektive på profilets overflade og i fri strømning, men deres effektivitet bliver øget i nærheden af profilets bagkant og lyd udstråles som konsekvens deraf.
Vi gennemførte hastighedsmålinger i profilets grænselag og målinger af det fluktuerende overfladetryk på profilet i to forskellige vindtunneler og på tre forskellige profiler. Den første vindtunnel tilhørende LM Wind Power A/S er opbygget på den traditionelle måde for aerodynamiske vindtunneler med hårde vægge i testsektionen. Akustiske fjernfelt støjmålinger kan ikke gennemføres i denne type vindtunnel på grund af det høje baggrundsstøjniveau. Den anden vindtunnel er ejet af Virginia Tech University. Testsektionen har Kevlar-vægge som er gennemtrængelige for lyd, og den er omgivet af et lyddødt rum. Fjernfeltstøjmålinger blev udført med et mikrofonarray placeret i det lyddøde rum i dette eksperiment.
Målingerne blev sammenlignet med en analytisk model for bagkantstøj. Den analytiske model er delt i to beregningskridt. Det fluktuerende strømningsfelt relateres til det fluktuerende overfladetrykfelt i det første beregningsskridt. I det andet beregningsskridt bliver bagkantstøjen beregnet for overfladetrykfeltet. Målingerne blev brugt til at vurdere de forskellige led i den analytiske bagkantstøjmodel og til at forbedre den, da modellen generelt giver for lave støjniveauer.
Vores vigtigste resultat er at den akustiske formulering som relaterer fjernfeltstøjen med overfladetrykfeltet giver fortræffelige resultater op til 2000-3000Hz, når vi bruger målingerne for at beskrive overfladetrykfeltet og sammenligger med

fjernfeltstøjmålingerne. Det fluktuerende overfladetryk kan måles i en vindtunnel med høj baggrundstøjniveau på grund af det fluktuerende overfladetryks endnu højere niveau. Det betyder at bagkantstøjen kan blive estimeret ved målingen af overfladetrykfeltet i de tilfælde, hvor det ikke er muligt at måle bagkantstøjen i fjernfeltet. Dette åbner store perspektiver for fremtidig eksperimentel karakterisering af aerodynamisk støj, eksempelvis ved test af nye profiler i en standard industriel vindtunnel og ved test af nye vindmøllerotorer i fri vind. Hovedproblemet ved modellering af bagkantstøj er den korrekte beregning af det fluktuerende overfladetrykfelt, og én af usikkerhederne i den originale model er antagelsen af isotrop turbulens. Dette er undersøgt i PhD arbejdet, hvor en ny model til at relatere det fluktuerende hastighedsfelt til det fluktuerende overfladetrykfelt, som tager hensyn til anisotropien af hastighedsspektrummet, er blevet udviklet. Resultaterne var meget lig resultaterne fra den originale model og undervurderer overfladetrykmålingerne, selv om forudsigelsen af hastighedsspektrummet var bedre.

Preface and Acknowledgments

This Ph.D. thesis has been prepared at Risø DTU National Laboratory for Sustainable Energy, Wind Energy Department (VEA) - Technical University of Denmark (DTU), during the period from October 2008 to November 2011 as a partial fulfillment of the requirements for acquiring the Ph.D. degree in engineering. The work has been supervised by Research Specialist Helge Aagaard Madsen (Risø DTU) and co-supervised by Senior Scientist Franck Bertagnolio (Risø DTU) and Associate Professor Wen Zhong Shen (DTU-MEK).
The project was funded by the Danish Energy Agency (Energistyrelsen) through the EUDP project 'Low Noise Airfoil', Journalnr.: 64009-0272 and partly founded through the project 'DAN-AERO MW' within the Danish Energy Research program EFP-2007, Journalnr.: 33033-0074.

I would like to thank my supervisors for teaching me with patience the very complicated field of aeroacoustic. Their doors were always open to me and the working atmosphere they created at Risø-DTU was very inspiring and motivating. I also want to thank the colleagues in my working group who helped me. We did a lot of experimental work and many, many people worked hard to make the outcome of those experiments successful. I am very grateful to all of them. There are simply too many people involved to name all of them, but I do not forget anyone who had helped me.
I received a lot of help from the technician group at Risø and foremost I want to mention Per Hansen who was involved in every single experiment setting up the equipment. He did not only solve all the problems we encountered, but became also a good friend. I also have to mention the mechanics at Risø workshop who

produced very nice equipment for the wind tunnel, no matter how confusing my drawings were.
We had two industrial partners in the project: LM Wind Power A/S and Brüel & Kjær Sound and Vibration A/S. During the project I met a lot of good people working in those two companies who contributed a lot to this work. It was great to work with you guys.
A special thanks goes to William Devenport, Professor at Virginia Tech University and director of the Stability Wind Tunnel. He was a great mentor during my three month stay at Virginia Tech and it was very nice to meet him and his working group at the university as well as in private. My stay was a great experience thanks to the people I met there.
Finally I want to thank my family and friends for their support. The most important person during all this time was my beloved girlfriend Sandrine who was always cheering me up and motivating me.

Roskilde, November 2011

Andreas Fischer

Contents

Chapter 1

Introduction

1.1 Motivation

The market for renewable energy technology is increasing rapidly all over the world. Most governments of the industrialized and newly industrializing countries promote research and industry involved in this technology. The reason for this promotion is twofold. The most important reason is to reduce the emission of CO_2 and to soothe its negative effects on the environment and climate. But there is also the endeavor of each country to be able to cover its energy consumption and become independent of other countries with natural resources like gas or oil. Wind energy plays a very important role among the renewable energy technologies.
For example in Denmark the government decided that the contribution of wind power in the national energy supply should be drastically increased in the coming decades. To achieve this goal, a large amount of wind turbines will have to be installed onshore close to urban areas (to reduce transport costs). Noise regulations are very restrictive on these sites and often limit the installation of new wind turbines. On top of that it is also reported by wind turbine site operators that wind turbines had to be derated to meet the noise regulations and potential energy production was lost.
There are various noise sources on a wind turbine of both mechanic and aerodynamic origin. Mechanic noise radiates from vibrating surfaces of the structure

and can be reduced efficiently by well-known engineering methods. Aerodynamic noise originates from the wind turbine blades and is mainly linked to the interaction of turbulence with the blade surface. The reduction of aerodynamic noise is still a problem to the present day. Already in the 1990s manufactures had been able to reduce mechanic noise to level below aerodynamic noise. Aerodynamic noise will become even more dominant in the future, because wind turbines will increase in size and aerodynamic noise increases faster with the dimension of the turbine than mechanic noise.
Hence, better understanding of aerodynamic noise sources is required to reduce the overall noise emission from wind turbines. It gives the possibility to install more of them and/or to operate the existing ones more efficiently. The present work wants to contribute to this effort.

1.2 Previous Work

The first step in reducing the noise from wind turbines is the identification of the noise sources. A very good overview of the noise sources is given in the book [1] which was published in 1996. At this time it was already clear that mechanic noise is dominated by aerodynamic noise. But it was not known which aerodynamic noise mechanism was the most important.
From January 2003 to February 2007 the SIRROCO (silent rotors by acoustic optimization) project [2, 3] was conducted. In this project acoustic measurements on two different wind turbines were conducted: a three bladed Gamesa 850kW turbine and a GE 2.3MW wind turbine with a rotor diameter of 94m and a tower height of 100m. Those measurements were conducted with a phased microphone array system to be able to separate the noise sources [4, 5]. In both cases it was found that turbulent boundary layer trailing edge (TE) noise from the blade outboard section was the dominant noise source. Because of convective amplification and directivity, practically all of this noise is produced during the downward movement of the blade.
The physical principle of TE noise is illustrated in figure 1.1. Transition from laminar to turbulent flow will occur at a certain chordwise position in the airfoil boundary layer. In the turbulent boundary layer eddies are created. Those eddies are the sources of noise. They are ineffective on the airfoil surface and in free space. In the close vicinity of the edge the efficiency of the eddies as noise sources is largely amplified due to scattering.
The theoretical description of aerodynamically generated sound started in the 1950s with Lighthill's pioneering work [6, 7]. He combined the continuity equation and the momentum equation (Navier-Stokes eq.) by taking the time derivative of the continuity eq. and the divergence of the Navier-Stokes eq. and transformed so those flow defining equations into the mathematical form of a wave

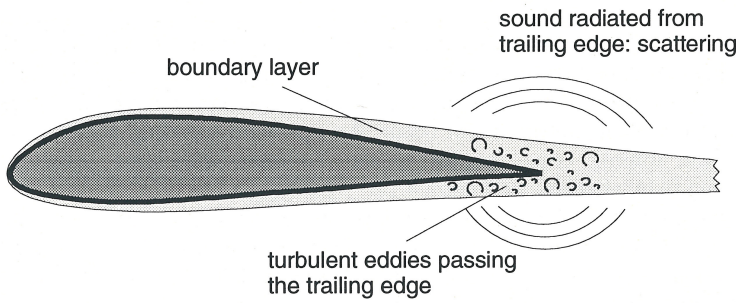

Figure 1.1: Physical Principle of TE Noise from [1]

equation. The propagation of sound is described by the wave equation. On the right hand side of Lighthill's wave equation (well-known as Lighthill's acoustic analogy) appear the sources of sound. These sources are called Lighthill tensor. Lighthill could even determine which of the sources was the leading one: the Reynolds stress tensor. In other words, he found that turbulence is the source of noise in every technical relevant flow configuration. Hence, the description of aerodynamically generated sound is inseparably linked to the modeling of turbulence.
Lighthill developed his theory for the investigation of jet noise. The next big step in applying Lighthill's acoustic analogy to TE noise was performed by Ffowcs Williams and Hall [8]. They solved Lighthill's equation for a flow situation with the mean flow parallel to an infinite half-plane and found so the theoretical explanation why the turbulent sound sources are much more efficient in the vicinity of an edge. They also found the classical result that TE noise scales with the 5th power of the flow speed.
Chase [9] related the sound radiated from a half plane in turbulent flow to the surface pressure on the half plane in the vicinity of the edge. His approach was revised by Chandiramani [10] and finally generalized by Howe [11]. The relation of the surface pressure and the far field sound pressure of Howe is directly derived from Lighthills acoustic analogy. The main difference between Howe's and Chase's formulation is that Chase's approach assumes a zero mean flow while Howe's formulation takes into account the effects of a mean velocity. The diffraction integral was solved by the Wiener-Hopf technique. The simultaneous measurements of surface pressure fluctuations and far field sound on a NACA0012 airfoil by Brooks and Hodgson [12] revealed that Howe's formulation of the far field sound with input from measured surface pressure statistics gives excellent results. However, the number of test cases was very restricted.
Independently, Amiet [13] developed a theory which also relates the far field noise to the surface pressure similar to Chase. The difference is the airfoil response function. Amiet takes into account the presence of a mean flow. Recently,

Amiet's formulation was extend to three dimensions and to account for a finite chord length by Roger [14]. Moreau [15] measured the surface pressure fluctuations on a flat plate and a cambered airfoil for use in cooling fans simultaneously with the far field sound. He found that both Amiet's formulation with Roger's extensions as well as Howe's formulation give very good results. The main difference between the two formulations is that the directivity pattern of TE noise is described in more detail by Amiet's formulation with Roger's extensions.
The disadvantage of the acoustic formulations above is that a model for the surface pressure frequency wave number spectral density is necessary. This is a very challenging task. To avoid this problem, Brooks, Pope and Marcollini [16] developed an empirical model for TE noise based on a series of far field noise and boundary layer flow measurements on a NACA0012 airfoil. The model is called BPM model and it is widely used in wind turbine noise codes. The main input parameter from the airfoil flow to the BPM model is the displacement thickness. For TE noise optimization of airfoils a more detailed model is necessary and the issue of surface pressure modeling has to be addressed.
The first contribution to this subject is from Kraichnan [17] in 1956. He considers boundary layer on an infinite straight surface with the mean flow parallel to the surface and seeks a solution of the Poisson equation. He assumed that the flow was homogeneous in the streamwise and horizontal direction and inhomogeneous in the vertical direction due to the blockage of the surface. Hence, the Fourier transform may be introduced in the two directions of homogeneity. He neglects the source terms involving non-linear turbulence-turbulence interaction and finds that the dominant contribution to the surface pressure fluctuations should only depend on the mean velocity profile and the two-point quadratic correlation of the fluctuating velocity component perpendicular to the surface. Blake [18] introduces some simplifications of the fluctuating velocity correlation and develops a basis for the modeling of this quantity.
In 1998 Parchen [19] developed a model for TE noise based on the work of Blake and the acoustic formulation of Howe [11] (simplified for one specific observer position). This model was implemented by Lutz [20] and Kamruzzaman [21] from the University of Stuttgart, Germany and also by Bertagnolio [22] from Risø-DTU National Laboratory, Denmark. The TNO model was tested intensively by the comparison of the predictions with far field sound measurements on different airfoils. Lutz/Kamruzzaman and Bertagnolio found independently that the model is in good qualitative agreement with the measurements, but the level is underestimated by up to 10dB in the worst case. One of the shortcomings of the TNO model is that the spectrum of the vertical velocity fluctuations is modeled by the isotropic von Karman spectrum, even though the velocity spectrum in the boundary layer is anisotropic in reality. Kamruzzaman [23] did some empirical anisotropy modeling and was able to match the level of the predicted and measured far field sound in a few cases. Bertagnolio [24] showed recently that the TNO model can be improved for a number of different flow situations by adding an empirical anisotropy factor which depends on the pressure

gradient on the airfoil surface.

1.3 Framework and Objective

The present work aims first on the creation of a measurement data base which can be used for the improvement of TE noise modeling and on the development of measurement techniques necessary for this task. Secondly, the acquired data base shall be used for a detailed comparison with results of the TE noise model and lead to an improvement of it.
This work was mainly funded through and part of the EUDP-project 'Low Noise Airfoil'. EUDP projects aim on the development and demonstration of technology. At the end of the project there has to stand an industrial product which in our case is a noise optimized airfoil. The project involves two partners from the industry: LM Wind Power A/S (the largest wind turbine blades manufacturer in the world) and Brüel & Kjær Sound and Vibration A/S (a world wide leader in pressure transducer technology).
LM Wind Power owns a wind tunnel which is optimized for aerodynamic testing, but not suitable for acoustic measurements because of the high background noise level in the test section. The first part of the project was to develop a measurement technique to evaluate TE noise in the wind tunnel of LM Wind Power A/S (LSWT). The following step was the improvement of the existing TE noise model [22] based on the data obtained from the measurements in the LSWT. Then an airfoil used for wind turbine blades should be optimized acoustically while keeping its aerodynamic properties by using the improved TE noise model. Finally, the noise reduction should be verified by the noise measurement technology in the LSWT.
Unfortunately, all attempts to measure far field sound in the LSWT failed. The project was changed therefore. Instead of measuring TE noise directly, it should be evaluated by measurements of the surface pressure. The results of [12] and [15] indicated that this was possible, but to prove the concept a series of far field sound measurements combined with fluctuating surface pressure measurements on a wind turbine airfoil were necessary. Consequently, a measurement campaign in the acoustic wind tunnel of Virginia Tech was conducted.
The revised objectives of the present work are:

- An improvement of the measurement method for the fluctuating surface pressure developed in the DAN-AERO project [25] to enhance accuracy in the high frequency range and to make the method suitable for measurements very close to the TE. And based on that the development of a surface pressure microphone setup close to the TE which allows the evaluation of TE noise according to the expressions by [11] or [14].

- The measurement of the fluctuating velocity in the boundary layer and the surface pressure fluctuations of a NACA0015 airfoil in the LSWT to obtain a data base for the improvement of the analytical model of the fluctuating surface pressure (the first part of the TE noise model). This task included the development of a probe traversing system with very high accuracy for the velocity measurements in the boundary layer.

- The measurement of far field sound in conjunction with the fluctuating surface pressure on a NACA64-618 airfoil and a noise optimized airfoil in the acoustic wind tunnel of Virginia Tech to validate the relation between surface pressure fluctuations and far field sound by [11] and [14] for wind turbine airfoils. Additionally measurements of the fluctuating velocity in the boundary layer to extend the data base for the improvement of the analytical model of the fluctuating surface pressure.

- The improvement of the TNO model for TE noise.

The goals of the EUDP-project 'Low Noise Airfoil' require the comparison of the far field sound emitted from the NACA64-618 airfoil and the optimized one. This is not part of the present work, but it influenced the choice of the airfoil types used in the Virginia Tech experiment. Those airfoils are not a good choice for model validation, because the NACA64-618 was designed for laminar flow and transition occurs far downstream of the leading edge. Effects like laminar separation or relaminarisation occur and make the modeling of the airfoil flow very difficult. The optimized airfoil is similar.

1.4 Structure

At first we introduce the relevant theory for the understanding of TE noise modeling in chapter 2. It contains the acoustic formulations of [11] and [14] for the evaluation of the far field sound pressure with known surface pressure statistics. The surface pressure theory by [17] is repeated and the development by [18] as well as some development by the author to this theory is presented. Then the issue of turbulence modeling is addressed for the simple isotropic case and for the more complicated anisotropic turbulence model of [26]. To conclude chapter 2 the TNO model for TE noise is repeated and then the new TE noise model is formulated.
In chapter 3 the experimental technique is outlined. The wind tunnel of LM Wind Power A/S (LSWT) and the wind tunnel of Virginia Tech (VTST) with their equipment are described. Hot wire anemometry and the fluctuating surface pressure measurement technique are paramount for the present work. They

are dedicated a full section of chapter 3 each.
In chapter 4 the in-house flow solver EllipSys2D for the Reynolds-averaged Navier-Stokes equations (RANS) is presented. It provides the input for the TE noise models. The computational domain and grid to simulate the conditions in the LSWT and VTST is shown and explained. In the other section a large eddy simulation (LES) performed at DTU is presented. The data will be used for further validation of the TE noise models. It provides data for the two-point quadratic correlation of the fluctuating velocity component perpendicular to the surface which could not be obtained by measurements.
The results are collected in chapter 5. The first section deals with wind tunnel correction applied to the data obtained in the VTST to convert the data from the conditions in the VTST to free space. Two different correction methods proposed by William Devenport were investigated. The resulting airfoil polar was compared to published measurements and the pressure distribution was compared to the one obtained from Ellipsys2D RANS computations. Those corrections are considerable, contrary to the situation in the LSWT where wind tunnel corrections have a negligible impact. In the next section the focus is on the flow in the boundary layer. Measured velocity profiles are compared to the ones computed with EllipSys2D for validation. Then a method to relate the input parameter of the new TE noise model to the output of the $k-\omega$ turbulence model of EllipSys2D is developed by comparison with the measured one point velocity spectra for the data from the NACA0015 airfoil. Results from the LES computation for the NACA0015 airfoil are used for comparison of the cross correlation of the velocity fluctuations. The new model is then applied to model the one point velocity spectra for the airfoils tested in the VTST. In the following section surface pressure predictions are compared to the original TNO model and to measurements.
The next section of chapter 5 deals with surface pressure statistics. The one point surface pressure spectra from the experiment in the LSWT and the experiment in the VTST are analyzed for scaling laws. The streamwise and spanwise surface pressure statistics from the experiment in the VTST are investigated, because those give the input for the noise prediction in the last section. In the final section we compare far field sound predictions with input from measured surface pressure statistics to measurements with the microphone array in the far field.
The work is rounded up by some concluding remarks and suggestions for future work.

Chapter 2

Theory

In this chapter the relevant theory for the understanding of TE noise modeling is collected. It contains the acoustic formulations of [11] and [14]. Both give a relation for the far field sound pressure in dependence of the frequency wave number spectral density of the pressure on the airfoil surface. To be able to fully predict the far field sound without any measurement involved, one needs to model the surface pressure. The surface pressure theory by [17] is repeated and the development by [18] as well as some development by the author to this theory is presented. It will turn out that the most crucial part of the expression for the fluctuating surface pressure is describing the fluctuations of the vertical velocity component. This leads immediately to the issue of turbulence modeling. We summarize the equations valid the simple isotropic case and investigate the more complicated anisotropic turbulence model of [26]. This model has the capability to describe the two-point quadratic correlation of the fluctuating velocity component perpendicular to the surface. Using this formulation leads to a completely new way of modeling the surface pressure fluctuations. To conclude chapter 2 the TNO model for TE noise is repeated and then the new TE noise model is formulated.

2.1 Trailing Edge Noise Modeling

The first attempt to model trailing edge (TE) noise analytically was done by Ffwocs Williams and Hall [8] in 1970. They applied Lighthill's acoustic analogy to flow on a semi-infinite half plane and determined the radiation in terms of the assumed velocity field. Chase [9] developed a theory to relate the sound field to the surface pressure fluctuations on the surface close to the TE of the airfoil. His approach was refined by Chandiramani [10] and some years later Howe [11] unified the TE noise theory and generalized Chase's [9] and Chandiramani's [10] theory. He showed that the model can be directly derived from Lighthill's acoustic analogy.
Amiet [13] developed a theory based one a similar approach as Chase [9], but with a different response function from the airfoil. His theory was recently revised by Roger [14]. In the present work Howe's formulation and Amiet's model with Roger's extension are applied. The derivation of these models is repeated below.

2.1.1 Howe's [11] relation between far field sound pressure and surface pressure spectrum

The airfoil is modeled as semi-infinite half plane ($x_2 = 0$, $x_1 < 0$, see figure 2.1). Following Howe [11], for fluids in motion it is more convenient to define the

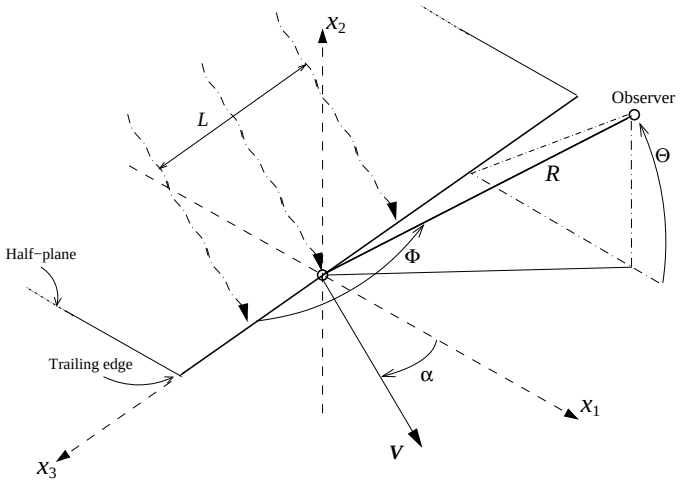

Figure 2.1: Half plane configuration (from [22])

stagnation enthalpy rather than the pressure as fundamental acoustic variable.

$$B = \int \frac{dp}{\rho} + \frac{1}{2}v^2 \tag{2.1}$$

Lighthill's acoustic analogy can be written in the enthalpy form

$$\left\{ \frac{D}{Dt}\left(\frac{1}{c_0^2}\frac{D}{Dt}\right) + \frac{1}{c_0^2}\frac{D\vec{v}}{Dt}\cdot\nabla - \nabla^2 \right\} B = \nabla\cdot(\vec{\omega}\times\vec{v}) - \frac{1}{c_0^2}\frac{D\vec{v}}{Dt}\cdot(\vec{\omega}\times\vec{v}) \tag{2.2}$$

with

$$\vec{\omega} = \nabla\times\vec{v} \tag{2.3}$$

the curl of the eddy convection velocity.
Eq. 2.2 can be simplified by introducing the following approximations:

1. A boundary layer eddy is frozen during the time it convects past the TE.
2. The eddy convection velocity $\vec{v}$ is approximated by the local boundary layer mean velocity $\vec{V} \rightarrow \nabla\cdot(\vec{\omega}\times\vec{v}) \cong \nabla\cdot(\vec{\omega}\times\vec{V})$.
3. There is no significant correlation between eddies which translate with different convection velocities.
4. The fluid compressibility is unimportant near the TE. Terms in the wave operator which involve the speed of sound c are significant only in the propagation region where fluctuations in B can be linearized about a mean value B_0 and the velocity is equal to the free stream velocity $\vec{v} = U_\infty$.
5. The Kutta condition results in a vortex shedding of strength $\vec{\omega}_s$. The shed vorticity is frozen and convects with the velocity $\vec{W}$.
6. The Mach numbers are small, $M_v^2, M_W^2 << 1$

With these approximations eq. 2.2 yields

$$\left\{ \frac{1}{c_0^2}\left(\frac{\partial}{\partial t} + U_\infty\frac{\partial}{\partial x_1}\right)^2 - \nabla^2 \right\} B = \nabla\cdot(\vec{\omega}\times\vec{V}) + \nabla\cdot(\vec{\omega}_s\times\vec{W}). \tag{2.4}$$

The terms on the right represent acoustic dipole sources associated with the incident and shed vorticity. Howe introduces the strength of the dipole sources

$$\vec{\omega}(x_1 - V_1 t, x_2, x_3 - V_3 t)\times\vec{V}(x_2) = \vec{Q}(x_1 - V_1 t, x_3 - V_3 t, x_2) \tag{2.5}$$

$$\vec{\omega}_s\times\vec{W} = \delta(x_2)\int_0^\infty \vec{q}(x_1 - V_1 t, x_3 - V_3 t, z)dz \tag{2.6}$$

and eq. 2.4 becomes

$$\left\{\frac{1}{c_0^2}\left(\frac{\partial}{\partial t}+U_\infty\frac{\partial}{\partial x_1}\right)^2-\nabla^2\right\}b=\nabla\cdot(\vec{Q}\delta(x_2-z))+\nabla\cdot(\vec{q}\delta(x_2)) \tag{2.7}$$

where

$$B=\int_0^\infty b\,dz. \tag{2.8}$$

Howe solves this diffraction problem with the component b fulfilling the normal velocity condition $\frac{\partial b}{\partial x_2}=0$ on $(x_2=0, x_1<0)$ and the radiation condition of outgoing acoustic waves at large distances from the TE. The result is valid for small free flow Mach numbers, i.e. $M_0 << 1$. The component b is split up according to

$$b=b_Q+b_q \tag{2.9}$$

where b_Q corresponds to the incident dipole source and b_q to the wake dipole source. The solution is then given by

$$\begin{aligned}b_Q=&-\frac{1}{2}\int\int_{-\infty}^{\infty}dK_1dK_3\frac{\vec{K}\cdot\vec{\hat{Q}}}{\gamma(K_1)}e^{i(K_1x_1+\gamma(K_1)(z-x_2)+K_3x_3-\omega_z t)}\\&-\frac{i\,\mathrm{sgn}(x_2)}{4\pi}\int_{-\infty+i\epsilon}^{\infty+i\epsilon}dk\int\int_{-\infty}^{\infty}dK_1dK_3\\&\cdot\frac{\vec{K}\cdot\vec{\hat{Q}}\;e^{i((k-M_0\omega_z/c_0)x_1+\Upsilon(k)|x_2|+\gamma(K_1)z+K_3x_3-\omega_z t)}}{\sqrt{\lambda+k}\sqrt{\lambda-(K_1+M_0\omega_z/c_0)}(k-(K_1+M_0\omega_z/c_0))}\end{aligned} \tag{2.10}$$

$$\begin{aligned}b_q=&-\frac{1}{2}\int\int_{-\infty}^{\infty}dK_1dK_3\frac{\vec{N}\cdot\vec{\hat{q}}}{\gamma(\nu_1)}e^{i(\nu_1x_1+\gamma(\nu_1)x_2+K_3x_3-\omega_z t)}\\&-\frac{i\,\mathrm{sgn}(x_2)}{4\pi}\int_{-\infty+i\epsilon}^{\infty+i\epsilon}dk\int\int_{-\infty}^{\infty}dK_1dK_3\\&\cdot\frac{\vec{N}\cdot\vec{\hat{q}}\;e^{i((k-M_0\omega_z/c_0)x_1+\Upsilon(k)|x_2|+K_3x_3-\omega_z t)}}{\sqrt{\lambda+k}\sqrt{\lambda-(\nu_1+M_0\omega_z/c_0)}(k-(\nu_1+M_0\omega_z/c_0))}\end{aligned} \tag{2.11}$$

where $\epsilon\to+0$.
The Fourier transforms $\vec{\hat{Q}}$ and $\vec{\hat{q}}$ are defined by

$$\vec{\hat{Q}}(K_1,K_3,z)=\frac{1}{(2\pi)^2}\int\int_{-\infty}^{\infty}dx_1dx_3\vec{Q}(x1,x3,z)\;e^{-i(K_1x_1+K_3x_3)}. \tag{2.12}$$

The convective frequency ω_z is given by

$$\omega_z(z)=K_1V_1(z)+K_3V_3(z), \tag{2.13}$$

the sub-functions are given by

$$\lambda=\begin{cases}sgn(\omega_z) & \left|\frac{\omega_z^2}{c_0^2}-K_3^2\right|^{1/2}\\ +i\end{cases} \tag{2.14}$$

and

$$\gamma(\xi) = \begin{cases} sgn(\omega_z) \\ +i \end{cases} \left| \lambda^2 - \left(\xi + \frac{M_0 \omega_z}{c_0} \right)^2 \right|^{1/2} \tag{2.15}$$

$$\Upsilon(k) = \begin{cases} sgn(\omega_z) \\ +i \end{cases} \left| \lambda^2 - k^2 \right|^{1/2}. \tag{2.16}$$

They are chosen according to if the argument under the square root in eq. 2.14 to 2.16 is whether positive or negative. The three-dimensional vectors $\vec{k}$ and $\vec{N}$ are defined as

$$\vec{K} = (K_1, -\gamma(K_1), K_3) \tag{2.17}$$

$$\vec{N} = (\nu_1, -\gamma(\nu_1), K_3) \tag{2.18}$$

where

$$\nu_1 = (1/W_1)(K_1 V_1 + K_3(V_3 - W_3)). \tag{2.19}$$

From the expressions with square root in eq. 2.10 and 2.11 always the positive branch is chosen.
The first integral on the right hand side of eq. 2.10 and 2.11 represents the evanescent sound wave field generated by the dipoles $\vec{Q}$, $\vec{q}$ in the absence of the half plane. It is only valid for $x_2 \leq 0$. The second integral accounts for the diffraction of the plate and is valid for the whole space.
The strength of the wake dipole $\vec{q}$ is unknown and depends on the flow at the TE of the half plane. Howe considers two scenarios. The first one is that the Kutta condition has to be applied over the whole frequency range. In this case the flow must leave the edge tangentially and Howe finds the strength of the wake dipole as

$$\vec{N} \cdot \vec{\hat{q}} = -\vec{K} \cdot \vec{\hat{Q}}\, e^{i\gamma(K_1)z} \sqrt{\frac{\lambda - (\nu_1 + M_0\omega_z/c_0)}{\lambda - (K_1 + M_0\omega_z/c_0)}}. \tag{2.20}$$

However, there is some experimental evidence that the Kutta condition is not fulfilled for unsteady flow. Therefore also the other extreme is considered, i.e. there is no counteracting vortex shedding in the wake $\vec{q} = 0$. In reality probably a mixture between the two extrema is the case.
However, the total enthalpy is not a quantity which is easily seizable. Therefore it is convenient to give a solution in terms of the acoustic pressure perturbation p rather than the total enthalpy. Howe advances in the following steps to find a solution which relates the surface pressure frequency wave number spectrum to the acoustic far field sound pressure spectrum:

1. Find the relation between the total enthalpy and the far field sound pressure and the relation between total enthalpy and the fluctuating pressure on the rigid half plane.

2. Find an expression of the far field sound pressure and the pressure on the half plane.
3. Define the spectrum of the acoustic far field sound pressure and the spectrum of the acoustic pressure on the half plane.
4. Introduce a vorticity spectrum which contains the dipole source terms.
5. Eliminate the vorticity spectrum from the expression of the far field sound pressure by comparison with the expression for the surface pressure spectrum.

If the mean flow Mach number M_0 is small, the acoustic pressure perturbation in the far field is

$$p_f = \frac{\rho_0 b}{1 + M_{0R}} \tag{2.21}$$

where $M_{0R} = M_0(x_1/R)$ is the component of the free stream Mach number in observer direction. The pressure on the surface of the rigid half plane is accordingly

$$p_s = (\rho_0/\omega)(\omega + i\vec{W} \cdot \nabla)b. \tag{2.22}$$

The integrals in k and K_3 in eqs. 2.10 and 2.11 are solved by the method of steepest descents with the saddle point in the (k,K_3)-plane located at $k = (\omega_z/c_0)\sin\Phi\cos\Theta$ and $K_3 = (\omega_z/c_0)\cos\Phi$ and the integral with respect to K_1 is replaced by an integral over all values of the convective frequency ω_z according to eq. 2.13. The subscript z is therefore dropped in the following. This yields

$$p_{fK} = \frac{-i\rho_0 \sin(\Theta/2)\sqrt{\sin\alpha}}{R\sqrt{2}(1+M_{0R})(1-M_{WR})} \int_{-\infty}^{\infty} \frac{d\omega}{\omega} \int_0^{\infty} dz \cdot \frac{\sqrt{M_{v1}}(1-\sigma(z))[\vec{K}\cdot\vec{\vec{Q}}]e^{-(|\omega|z/V_1)(1-M_{v3}\cos\Phi)+(i\omega/c_0)(R-M_0x_1-c_0t)}}{(1-M_{vR})(1-M_{v1}\sin\Phi-M_{v3}\cos\Phi)^{(1/2)}} \tag{2.23}$$

for the far field sound pressure and

$$p_{sK} = -\frac{\rho_0}{2} \int\int_{-\infty}^{\infty} dK_1 dK_3 \int_0^{\infty} dz \left\{1 + \mathrm{sgn}(x_2)\mathrm{Erf}\left(\sqrt{ix_1(\lambda + K_1 + \frac{M_0\omega}{c_0})}\right)\right\} \cdot \frac{\vec{K}\cdot(\vec{V}-\vec{W})(\vec{K}\cdot\vec{\vec{Q}})}{\omega\gamma(K_1)} e^{i(K_1x_1+K_3x_3+z\gamma(K_1)-\omega t)} \tag{2.24}$$

for the fluctuating pressure on the surface of the rigid half plane. The function σ is defined as $\sigma(z) = \vec{W}/\vec{V}(z)$. The notation $[\vec{K}\cdot\vec{\vec{Q}}]$ means that $\vec{K}\cdot\vec{\vec{Q}}(K_1, K_3, z)$ has to be evaluated at $K_1 = (\omega/V_1)(1 - M_{v3}\cos\Phi)$ and $K_3 = (\omega/c_0)\cos\Phi$. Note that both solutions are given for the case when the full Kutta condition is applied, i.e. the wake dipole strength in eq. 2.11 is evaluated with eq. 2.20.

When the Kutta condition is not applied, the pressure perturbations at the TE become singular and it is difficult to find an expression for them. This case is hence not considered in the following and the subscript K is discarded.
The introduction of a pressure spectrum was outlined by Howe for the surface pressure. He first neglected the contribution of the error function in eq. 2.24. Because of this, the formula is only correct for points x_1 located in the wake or on the plane within a characteristic hydrodynamic wave length of the TE. In this region the pressure fluctuations induced by frozen vorticity are a stationary random function and a spectrum function may be introduced:

$$\langle p_s(x_1, x_3, t) p_s(x_1 + \overline{x}_1, x_3 + \overline{x}_3, t + \tau) \rangle = \int_{-\infty}^{\infty} \Pi_s(\vec{\kappa}, \omega) e^{i(K_1 \overline{x}_1 + K_3 \overline{x}_3 - \omega t)} d^2\vec{\kappa} d\omega. \tag{2.25}$$

$\vec{\kappa} = (K_1, K_3)$ is the two-dimensional convective wave number vector in the x_1, x_3-plane. The incident vorticity is contained in the dipole term $\vec{K} \cdot \vec{\hat{Q}}$. Howe defines a vorticity spectrum function Φ_i in the following way

$$\left\langle (\vec{K} \cdot \vec{\hat{Q}}(\vec{\kappa}, z))(\vec{\overline{K}} \cdot \vec{\hat{Q}}(\vec{\overline{\kappa}}, \overline{z})) \right\rangle = -\Phi_i(l_1 K_1, l_3 K_3, \frac{\overline{z} - z}{l_2}, \frac{z}{l_0}) \delta(K_1 + \overline{K}_1) \frac{\sin(L/2(K_3 + \overline{K}_3))}{\pi(K_3 + \overline{K}_3)} \tag{2.26}$$

where $\Phi_i \geq 0$. It follows from eq. 2.25 and 2.26 that the frequency wave number spectrum of the surface pressure fluctuations close to the TE is given by

$$\Pi_s(\vec{\kappa}, \omega) = \int_0^{\infty} f(\vec{\kappa}, z) \delta(\omega - \vec{K} \cdot \vec{V}) dz \tag{2.27}$$

where

$$f(\vec{\kappa}, z) = \frac{\rho_0^2 (1 - \sigma(z))^2}{4|\gamma(K_1)|^2} e^{-2z|\gamma(K_1)|} \int_0^{\infty} \Phi(l_1 K_1, l_3 K_3, \frac{\overline{z} - z}{l_2}, \frac{z}{l_0}) d\overline{z}. \tag{2.28}$$

Consider next the acoustic far field. The far field sound pressure spectrum is defined as

$$\langle p_f^2 \rangle = \int_0^{\infty} S_f(\omega) d\omega. \tag{2.29}$$

Using a similar development as for the surface pressure spectrum, the far field sound pressure spectrum becomes

$$S_f(\omega) = \frac{2L\omega}{\pi c_0 R^2} \frac{\sin\Phi \sin^2(\Theta/2)}{(1 + M_{0R})^2 (1 - M_{WR})^2} \int_0^{\infty} \frac{f((\omega/V_1)(1 - M_{v3}\cos\Phi), (\omega/c_0)\cos\Phi, z)}{(1 - M_{vR})^2 (1 - M_{v1}\sin\Phi)} dz. \tag{2.30}$$

Howe eliminates $f(\vec{\kappa}, z)$ between eq. 2.27 and 2.30 by taking advantage of the δ-function in eq. 2.27 and using the transform $K_1 = (\omega/V_1(z))(1 - M_{v3}\cos\Phi)$. This yields the relation between the surface pressure frequency wave number

spectrum and the far field sound pressure spectrum:

$$S_f(\omega) = \frac{2L\omega}{\pi c_0 R^2} \frac{\sin\Phi \sin^2(\Theta/2)\cos\alpha}{(1+M_{0R})^2(1-M_{WR})^2} \int_0^\infty \frac{\Pi_s(K_1, (\omega/c_0)\cos\Phi, \omega)}{|\vec{K}\cdot\vec{n}|(1-M_{vR})^2(1-M_{v1}\sin\Phi)} dk_1 \tag{2.31}$$

where $\vec{K} = (K_1, (\omega/c_0)\cos\Phi)$, $\vec{M}_v = (M_{v1}, M_{v3}) = \frac{\omega}{c_0 \vec{K}\cdot\vec{n}}\vec{n}$ is the eddy convection Mach number. $M_{vR} = \vec{M}_v \cdot \vec{r}$ is the component of the eddy convection Mach number in observer direction. $\vec{n} = (\cos\alpha, \sin\alpha)$ is a unit vector in the direction of the mean boundary layer/eddy convection velocity. $\vec{r} = (\sin\Phi\cos\Theta, \cos\Phi)$ is a unit vector in observer direction. Note that the component in $x_2 (= \sin\Phi\sin\Theta)$ of $\vec{r}$ was omitted, because the corresponding component of $\vec{n}$ is equal to zero. This formula is the general form of the result due to Chase [27].

2.1.2 Discussion of Howe's result

The Kutta condition was applied throughout the whole frequency range to derive eq. 2.31. However, experimental results indicate that the Kutta condition is only partially fulfilled at high frequencies. According to the above findings the radiation of sound will be increased if the Kutta condition is not fulfilled and one would expect eq. 2.31 to underestimate the emitted sound pressure. Howe[11] gives also a relation between the frequency wave number pressure spectrum and the far field sound pressure spectrum for the case with no Kutta condition, i.e. $\vec{q} = 0$. But in this case the frequency wave number pressure spectrum has to be evaluated in the wake of the airfoil (because of the singularity at the TE) and therefore this relation is of little practical use.
For the experimental conditions of the present work as well as for most wind tunnel experiments, eq. 2.31 can be simplified significantly. We will assume that the mean flow is in the direction of x_1 ($\alpha = 0$) and the observer is located in the middle of the wetted span with an elevation of 90 ° ($\Phi = 90\,°$, $\Theta = 90\,°$). Inserting this into eq. 2.31 yields

$$S_f(\omega) = \frac{L\omega}{\pi c_0 R^2} \int_0^\infty \frac{\Pi_s(K_1, 0, \omega)}{|K_1|(1-\frac{\omega}{c_0 K_1})} dK_1. \tag{2.32}$$

With the assumption that eddies convect with the mean boundary layer velocity $\vec{V}$ the factor $(1-\frac{\omega}{c_0 K_1})$ is the same as $(1-M_{v1})$ and can be neglected for $M_{v1} << 1$, which is in general the case in the present investigation. Eq. 2.32 then reads

$$S_f(\omega) = \frac{L\omega}{\pi c_0 R^2} \int_0^\infty \frac{\Pi_s(K_1, 0, \omega)}{|k_1|} dK_1 \tag{2.33}$$

which is equivalent to the result of Chase[27].
We should also have a look on what consequences the neglect of the Error

function in eq. 2.24 has on the surface pressure modeling, if the analytical surface pressure model assumes an infinitely extended plane ($x_2 = 0$). This corresponds to the limit $x_1 \to -\infty$ in Howe's half plane configuration. On the upper surface of the half plane, the pressure is doubled compared to the one at the TE. Consequently the relation between the spectra is $\Pi_{s,x_1=0} = \frac{1}{4}\Pi_{s,x_1\to-\infty}$. Inserting this into eq. 2.33 we obtain eq. 2.155 which is used in the TNO model. The near field scatter represented by the Error function in eq. 2.24 becomes important when evaluating the surface pressure close to the TE. If it is not neglected, eq. 2.27 has to be refined and reads

$$\Pi_{s,x_1}(x_1,\vec{\kappa},\omega) = \int_0^\infty \left(1+\mathrm{sgn}(x_2)\mathrm{Erf}\sqrt{ix_1(\lambda(z)+K_1+\frac{M_0\omega_z(z)}{c_0}}\right)^* \left(1+\mathrm{sgn}(x_2)\mathrm{Erf}\sqrt{ix_1(\lambda(z)+K_1+\frac{M_0\omega_z(z)}{c_0}}\right) f(\vec{\kappa},z)\delta(\omega-\vec{K}\cdot\vec{V})dz. \quad (2.34)$$

A simple relation between Π_s and $\Pi_{s,x1}$ can only exist if the convection velocity is approximated as constant over the boundary layer. In this case the convective frequency ω_z becomes independent of z and the factors including the Error function can be taken out of the integral:

$$\Pi_{s,x_1}(x_1,\vec{\kappa},\omega) = \left(1+\mathrm{sgn}(x_2)\mathrm{Erf}\sqrt{ix_1(\overline{\lambda}+K_1+\frac{M_0\overline{\omega}_z}{c_0}}\right)^* \left(1+\mathrm{sgn}(x_2)\mathrm{Erf}\sqrt{ix_1(\overline{\lambda}+K_1+\frac{M_0\overline{\omega}_z}{c_0}}\right) \Pi_s(\vec{\kappa},\omega). \quad (2.35)$$

If we assume that the velocity and pressure field is frozen, we can simplify eq. 2.31 and make it suitable for the use of measured surface pressure statistics. With this assumption eq. 2.31 becomes

$$S_f(\omega) = \frac{2LM_c}{\pi R^2}\frac{\sin\Phi\sin^2(\Theta/2)\cos\alpha}{(1+M_{0R})^2(1-M_{WR})^2}\frac{\Pi_s(\omega/U_c,(\omega/c_0)\cos\Phi)}{(1-M_c\vec{n}\cdot\vec{r})^2(1-M_c\sin\Phi)} \quad (2.36)$$

2.1.3 Amiet's Model with Roger's Extension

Amiet [13] assumes in his model that the turbulent flow convecting over the airfoil produces a convective pressure pattern on the surface of the airfoil. The convective pressure pattern creates a radiating pressure field near the TE of the airfoil. The radiation of sound to the far field is then solved with a Schwartzschild technique.
The approach of Amiet [13] assumes a 2 dimensional setup and an infinite chord

length. Roger [14] extends Amiet's model to be valid for a 3 dimensional flow field and corrects for a finite chord length. We used his 3 dimensional model in the present work and will repeat his derivation here briefly. Roger used a different coordinate system than the one used in the present work. We adopted his solution to the coordinate system shown in figure 2.1. The airfoil extends the plane $x_2 = 0,\ -2b < x_1 < 0$ with $b = c/2$ half a chord length. The free stream velocity U_∞ is assumed to be parallel with the x_1-axis.
The fluctuating pressure for the 3 dimensional case is expressed as

$$\frac{\partial^2 p'}{\partial x_1^2} + \frac{\partial^2 p'}{\partial x_2^2} + \frac{\partial^2 p'}{\partial x_3^2} + \frac{1}{c_0^2}\left(\frac{\partial}{\partial t} + U_\infty \frac{\partial}{\partial x_1}\right)^2 p' = 0 \tag{2.37}$$

The general solution is of the form

$$p'(\vec{x}, t) = P(\vec{x}) e^{i\omega t} \tag{2.38}$$

$$P(\vec{x}) = p(x_1, x_2) e^{i(k_0 M_0/\beta^2)} e^{-ik_3 x_3} \tag{2.39}$$

where $k_0 = \frac{\omega}{c_0}$ denotes the acoustic wave number and $\beta^2 = 1 - M_0^2$. $M_0 = U_\infty / c_0$ is the free stream Mach number. The incident wall pressure gust is generalized according to the boundary conditions as

$$P_0 = e^{-ia_v \overline{K} X_1} e^{-i\overline{K}_3 X_3} \tag{2.40}$$

Introducing eqs. 2.38-2.40 in eq. 2.37 yields the wave equation

$$\frac{\partial^2 p}{\partial X_1^2} + \frac{\partial^2 p}{\partial X_2^2} + \overline{\kappa}^2 p = 0 \tag{2.41}$$

where

$$\overline{\kappa}^2 = \overline{\mu}^2 - \frac{\overline{K}_3^2}{\beta^2} \tag{2.42}$$

The canonical problem which can be solved by the Schwarzschild solution as described in [14] is recovered, if $\overline{\kappa}^2 > 0$. This implies the condition

$$\left|\overline{K}_3\right| < \frac{\overline{K} M_0}{\beta} \tag{2.43}$$

The normalized coordinates

$$X_1 = \frac{x_1}{b},\ X_2 = \frac{\beta x_2}{b},\ X_3 = \frac{x_3}{b} \tag{2.44}$$

were introduced. $K = \frac{\omega}{U_\infty}$ is the convective free stream wave number. $K_1 = a_v K$ is the streamwise wave number of the pressure field. The factor $a_v = \frac{U_\infty}{U_c}$ is the ratio between the free stream speed and the eddy convection speed of the surface pressure field. The convection speed U_c is lower than the free flow speed

U_∞. The overline of the wave number means the normalization with the half chord length b, i.e. $\overline{K} = Kb$. $\overline{\mu} = \frac{\overline{K}M_0}{\beta^2}$ is the normalized wave number of the 2 dimensional canonical problem.
First, it is assumed that the inequality 2.43 is fulfilled and the solution for the supercritical gust can be obtained. The airfoil is artificially extended to negative infinity, covering $X_1 < 0$, to obtain a system of equations which can be solved by Schwartzschild's solution. The Kutta condition implies that P_0 must be cancelled in the wake. Hence, Roger adds a disturbance pressure P_1 so that $P = P_0 + P_1 = 0$ for $X_1 \geq 0$. Since the airfoil is assumed to be perfectly rigid it must be $\frac{\partial P_1}{\partial X_2} = 0$ for $X < 0$. The system of equations

$$\frac{\partial^2 p_1}{\partial X_1^2} + \frac{\partial^2 p_1}{\partial X_2^2} + \overline{\kappa}^2 p_1 = 0 \tag{2.45}$$

$$\frac{\partial p_1}{\partial X_2}(X_1, 0) = 0 \qquad X_1 < 0 \tag{2.46}$$

$$p_1 = -e^{-i\overline{K}X_1(a_v + M_0^2/\beta^2)} \qquad X_1 \geq 0 \tag{2.47}$$

is obtained. The solution for the main scattering term derived by [14] is

$$P_1(X_1, 0) = e^{-ia_v\overline{K}X_1}\left((1+i)\,E^*\left(-\left[a_v\overline{K} + \overline{\kappa} + M_0\overline{\mu}\right]X_1\right) - 1\right) \tag{2.48}$$

with the complex function

$$E^*(x) = \int_0^x \frac{e^{-it}}{\sqrt{2\pi t}}dt = C_2(x) - iS_2(x) \tag{2.49}$$

$C_2(x)$ and $S_2(x)$ are Fresnel integrals [28].
To correct for the back-scattering from the leading edge, Roger relates the disturbance pressure to the disturbance potential. Then he applies the condition that the potential must vanish for $X_1 < -2$ and finds a back-scattering disturbance pressure P_2. It yields the full solution by linear superposition with the main scattering term P_1. The back-scattering disturbance pressure P_2 does not fulfill the Kutta condition and should be corrected in principle. But Roger [14] shows that those corrections are negligible. The back-scattering disturbance pressure P_2 reads

$$\begin{aligned} P_2(X_1, 0) \simeq \frac{(1+i)e^{-i4\overline{\kappa}}}{2\sqrt{\pi}(a_v - 1)\overline{K}} \frac{1 - \Theta^2}{\sqrt{a_v\overline{K} + M_0\overline{\mu} + \overline{\kappa}}} e^{i(M_0\overline{\mu} - \overline{\kappa})X_1} \\ \left(i(\overline{K} + M_0\overline{\mu} - \overline{\kappa})\,\{-\}^c + \left(\frac{\partial}{\partial X_1}\,\{-\}\right)^c\right) \end{aligned} \tag{2.50}$$

where

$$\Theta = \sqrt{\frac{\overline{K}_1 + M_0\overline{\mu} + \overline{\kappa}}{\overline{K} + M_0\overline{\mu} + \overline{\kappa}}} \tag{2.51}$$

The place holder $\{-\}^c$ stands for $\left\{e^{i2\overline{\mu}(X_1+2)}[1-(1+i)E^*(2\overline{\mu}(X_1+2))]\right\}^c$. The superscript c indicates that the imaginary part of the expression in the brackets has to be corrected due to some simplifications introduced in the derivation of eq. 2.50 by [14]. The correction of the imaginary part is $Im(\{Z\}^c) = \varepsilon Im(Z)$ with $\varepsilon = \left(1+\frac{1}{4\overline{\mu}}\right)^{-1/2}$.
As discussed above, this solution is only valid for the super critical gust where the condition 2.43 is fulfilled. Roger [14] treats also the case of the sub-critical gust ($\left|\overline{K}_3\right| > \frac{\overline{K}M_0}{\beta}$) and the critical gust ($\left|\overline{K}_3\right| = 0$). These cases are of limited relevance for the present work and the reader is referred to [14] for details.
The acoustic far field sound pressure is given by the radiation integral

$$p_a(\vec{y},\omega) = \frac{-i\omega y_2}{4\pi c_0 S_0^2}\int_{-2b}^{0}\int_{-L/2}^{L/2}\Delta P e^{-i\omega R_t/c_0}dx_3dx_1 \tag{2.52}$$

where $\vec{y} = (y_1, y_2, y_3)$ stands for the observer coordinates in figure 2.1 (y replaces x). Roger sets $\Delta P = 2(P_1 + P_2)$ for the induced source distribution. The factor 2 accounts for the opposite disturbance pressures induced on both sides of the airfoil when the incident pressure is scattered by the TE. Strictly speaking, this is only valid for symmetric flow on the airfoil. In the more general case, pressure and suction side have to be treated separately. In the present work we divide the result of Roger by 2 and add the contribution from pressure and suction side, but we keep his formulation in the following. The modified coordinates

$$R_t = \frac{1}{\beta^2}(R_s - M_0(y_1 - x_1)) \tag{2.53}$$

$$R_s = S_0\left(1 - \frac{y_1x_1 + \beta^2 y_3x_3}{S_0^2}\right) \tag{2.54}$$

$$S_0 = y_1^2 + \beta^2(y_2^2 + y_3^2) \tag{2.55}$$

account for the convection of the acoustic waves by the mean flow. The induced source distribution $\Delta P/2$ can be expressed by $\Delta P/2 = (f_1+f_2)e^{-i(\overline{K}_1X_1+\overline{K}_3X_3)}$. f_1 and f_2 is the complex amplitude of the source distribution according to the main scattering term P_1 and the backscattering correction P_2. The far field sound pressure becomes then

$$\begin{aligned} p_a(\vec{y},\omega) = {} & \frac{-i\omega y_2 Lb}{2\pi c_0 S_0^2} sinc\left\{\frac{L}{2b}\left(\overline{K}_3 - \overline{k_0}\frac{y_3}{S_0}\right)\right\} \\ & e^{-i(k/\beta^2)(S_0 - M_0y_1)}\int_{-2}^{0}\left(f_1(X_1) + f_2(X_1)\right)e^{-iCX_1}dX_1 \end{aligned} \tag{2.56}$$

with

$$C = \overline{K}_1 - \overline{\mu}\left(\frac{y_1}{S_0} - M_0\right) \tag{2.57}$$

The complex amplitude of the main scattering term is $f_1(X_1) = (1+i)E^*(-BX_1) - 1$ with $B = \overline{K}_1 + M_0\overline{\mu} + \overline{\kappa}$ and the solution to the radiation integral for the main scattering term is

$$\int_{-2}^{0} f_1(X_1)e^{-iCX_1}dX_1 = -\frac{e^{i2C}}{iC}\left((1+i)e^{-i2C}\sqrt{2B}\frac{E^*(2(B-C))}{\sqrt{2(B-C)}} - (1+i)E^*(2B) + 1 - e^{-i2C}\right) \tag{2.58}$$

The term e^{-i2C} is considered to balance the contribution of the incident pressure field P_0 to the sound radiation. It must be discarded [13].
The complex amplitude for the back scattering correction P_2 is

$$f_2(X_1) = He^{i(\overline{K}_1+M_0\overline{\mu}+\overline{\kappa})X_1}\left(i(\overline{K}+M_0\overline{\mu}+\overline{\kappa})\{-\}^c + \left(\frac{\partial}{\partial X_1}\{-\}\right)^c\right) \tag{2.59}$$

with

$$H = \frac{(1+i)e^{-i4\overline{\kappa}}(1-\Theta^2)}{2\sqrt{\pi}(a_v-1)\overline{K}\sqrt{B}} \tag{2.60}$$

The radiation integral of the back scattering term is then

$$\frac{1}{H}\int_{-2}^{0} f_2(X_1)e^{-iCX_1}dX_1 = \left\{e^{i4\overline{\kappa}}(1-(1+i)E^*(4\overline{\kappa}))\right\}^c - e^{i2D} + i(D+\overline{K}+M_0\overline{\mu}-\overline{\kappa})G \tag{2.61}$$

with $D = \overline{\kappa} - \overline{\mu}y_1/S_0$ and

$$\begin{aligned} G = {} & (1+\varepsilon)e^{i(2\overline{\kappa}+D)}\frac{\sin(D-2\overline{\kappa})}{D-2\overline{\kappa}} + (1-\varepsilon)e^{i(-2\overline{\kappa}+D)}\frac{\sin(D+2\overline{\kappa})}{D+2\overline{\kappa}} \\ & + \frac{(1+\varepsilon)(1-i)}{2(D-2\overline{\kappa})}e^{i4\overline{\kappa}}E^*(4\overline{\kappa}) - \frac{(1-\varepsilon)(1+i)}{2(D+2\overline{\kappa})}e^{-i4\overline{\kappa}}E(4\overline{\kappa}) \\ & \frac{e^{i2D}}{\sqrt{2}}\sqrt{2\overline{\kappa}}\frac{E^*(2D)}{\sqrt{2D}}\left(\frac{(1-\varepsilon)(1+i)}{D+2\overline{\kappa}} - \frac{(1+\varepsilon)(1-i)}{D-2\overline{\kappa}}\right) \end{aligned} \tag{2.62}$$

Roger also derives the corresponding radiation integrals for the sub-critical gust. We will not repeat this derivation.
The far field sound pressure spectral density is

$$\begin{aligned} S_f(\vec{y},\omega) = {} & \left(\frac{\omega y_2 Lb}{2\pi c_0 S_0^2}\right)^2 \frac{1}{b}\int_{-\infty}^{\infty}\Pi_0\left(\frac{\omega}{U_c},\overline{K}_3\right) \\ & sinc^2\left\{\frac{L}{2b}\left(\overline{K}_3 - \overline{k_0}\frac{y_3}{S_0}\right)\right\}\left|I\left(\frac{\overline{\omega}}{U_c},\overline{K}_3\right)\right|^2 d\overline{K}_3 \end{aligned} \tag{2.63}$$

with the radiation integral $I(\overline{K}_1, \overline{K}_3) = \int_{-2}^{0}(f_1(X_1) + f_2(X_1))e^{-iCX_1}dX_1$. The integration over the wave number $\overline{K}_1$ is already performed in eq. 2.63. It was assumed that the pressure field is frozen. In this case the integration over $\overline{K}_1$ picks out the value $\overline{K}_1 = \frac{\overline{\omega}}{U_c}$. This process will be explained in detail in section 2.2. Π_0 is the incident surface pressure frequency wave number spectral density integrated over $\overline{K}_1$.
If the aspect ratio L/b is large enough, the $sinc^2$ function in eq. 2.63 can be approximated by a dirac delta function

$$sinc^2\left\{\frac{L}{2b}\left(\overline{K}_3 - \overline{k_0}\frac{y_3}{S_0}\right)\right\} \simeq \frac{2\pi b}{L}\delta\left(\overline{K}_3 - \overline{k_0}\frac{y_3}{S_0}\right) \tag{2.64}$$

This leads to a considerable simplification of eq. 2.63

$$S_f(\vec{y},\omega) = \left(\frac{\omega y_2 b}{2\pi c_0 S_0^2}\right)^2 2\pi L\left|I\left(\frac{\overline{\omega}}{U_c}, \overline{K}_3\right)\right|^2 \Pi_0\left(\frac{\omega}{U_c}, k_0\frac{y_3}{S_0}\right). \tag{2.65}$$

Next Roger transforms the surface pressure frequency wave number spectral density to a form which is more suitable for measurements without making any approximation. It can be written as

$$\Pi_0\left(\frac{\omega}{U_c}, k_0\frac{y_3}{S_0}\right) = \frac{1}{\pi}\Phi_{pp}(\omega) l_3(k_0\frac{y_3}{S_0}, \omega) \tag{2.66}$$

where $\Phi_{pp}(\omega)$ is the one point PSD of the surface pressure. l_3 is the spanwise correlation length scale. It is given by

$$l_3(\overline{K}_3, \omega) = \int_0^\infty \sqrt{\gamma^2(0, \eta_3, \omega)}\cos(K_3\eta_3)d\eta_3. \tag{2.67}$$

γ^2 is the correlation function in homogeneous flow given by

$$\gamma^2(\eta_1, \eta_3, \omega) = \frac{|\Phi_{pp}(\eta_1, \eta_3, \omega)|^2}{\Phi_{pp}^2(\omega)} \tag{2.68}$$

where η_1 is the streamwise separation distance and η_3 is the spanwise separation distance.

2.2 Modeling of the Surface Pressure

To find an approximate solution of the NS equations for the surface pressure of an airfoil with turbulent boundary layer we consider a simplified situation where the boundary layer flow is bounded by a plane ($x_2 = 0$), figure 2.2. The

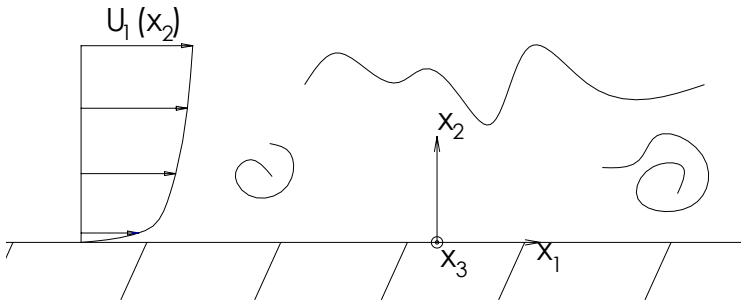

Figure 2.2: The configuration of the analytical surface pressure models

surface pressure fluctuations are mainly induced by the velocity fluctuations in the boundary layer. The first one to treat this problem analytically was Kraichnan[17] in 1956. He neglected the effect of compressibility. Blake[18] solved the same problem for the compressible NS equations, but dropped the terms involving compressibility effects in his final solution. In the following derivation we follow Kraichnan's[17] solution, because it is easier to comprehend. Then we will compare the solution to the solution for compressible flow by Blake[18].

2.2.1 Derivation of the Poisson Equation for the Fluctuating Pressure

The starting point is the NS equations for incompressible flow[29]:

$$\frac{\partial u_i}{\partial t} + u_j \frac{\partial u_i}{\partial x_j} = -\frac{1}{\rho}\frac{\partial p}{\partial x_i} + \nu \frac{\partial^2 u_i}{\partial x_j \partial x_j}. \tag{2.69}$$

Taking the divergence of eq. 2.69 and regrouping the partial derivatives gives

$$\frac{\partial}{\partial t}\left(\frac{\partial u_i}{\partial x_i}\right) + \frac{\partial}{\partial x_i}\left(u_j \frac{\partial u_i}{\partial x_j}\right) = -\frac{1}{\rho}\frac{\partial^2 p}{\partial x_i^2} + \nu \frac{\partial^2}{\partial x_j \partial x_j}\left(\frac{\partial u_i}{\partial x_i}\right) \tag{2.70}$$

with the continuity equation for incompressible flow

$$\frac{\partial u_i}{\partial x_i} = 0 \tag{2.71}$$

it yields

$$\frac{\partial^2 p}{\partial x_i \partial x_i} = -\rho \frac{\partial u_i}{\partial x_j}\frac{\partial u_j}{\partial x_i} \tag{2.72}$$

which is the Poisson equation. Note that the right hand side was simplified by applying the continuity eq. 2.71 again. As we are interested in the fluctuating pressures we will apply the Reynolds decomposition

$$\begin{aligned} p &= P + p' \\ u_i &= U_i + u_i' \end{aligned}$$

to eq. 2.72. The mean quantities are denoted by capital and the fluctuating quantities by primes. We obtain

$$\frac{\partial^2 P}{\partial x_i \partial x_i} + \frac{\partial^2 p'}{\partial x_i \partial x_i} = -\rho \left(\frac{\partial U_i}{\partial x_j} \frac{\partial U_j}{\partial x_i} + 2 \frac{\partial U_i}{\partial x_j} \frac{\partial u_j'}{\partial x_i} + \frac{\partial u_i'}{\partial x_j} \frac{\partial u_j'}{\partial x_i} \right). \tag{2.73}$$

The Reynolds decomposed quantities have the following properties when the averaging operator is applied:

$$\begin{aligned} \langle u_i' \rangle &= 0 \\ \langle U_j u_i' \rangle &= U_j \langle u_i' \rangle = 0 \\ \left\langle \frac{\partial u_i'}{\partial x_j} \right\rangle &= \frac{\partial \langle u_i' \rangle}{\partial x_j}. \end{aligned}$$

Taking the average of eq. 2.73 yields:

$$\frac{\partial^2 P}{\partial x_i \partial x_i} = -\rho \left(\frac{\partial U_i}{\partial x_j} \frac{\partial U_j}{\partial x_i} + \left\langle \frac{\partial u_i'}{\partial x_j} \frac{\partial u_j'}{\partial x_i} \right\rangle \right). \tag{2.74}$$

Subtracting eq. 2.74 from eq. 2.73 finally yields the Poisson equation for the fluctuating pressure:

$$\frac{\partial^2 p'}{\partial x_i \partial x_i} = -\rho \left(2 \frac{\partial U_i}{\partial x_j} \frac{\partial u_j'}{\partial x_i} + \frac{\partial u_i'}{\partial x_j} \frac{\partial u_j'}{\partial x_i} - \left\langle \frac{\partial u_i'}{\partial x_j} \frac{\partial u_j'}{\partial x_i} \right\rangle \right). \tag{2.75}$$

The source terms on the right hand side can be divided according to the physical meaning. The first source term describes the mean shear-turbulence interaction (MS). This term is linear. The second and the third source term describe the turbulence-turbulence interaction and it is non-linear. To formally make a distinction between the two source terms we introduce

$$\mathscr{S} = \mathscr{S}^{MS} + \mathscr{S}^{TT} \tag{2.76}$$

where

$$\mathscr{S}^{MS} = 2\rho \frac{\partial U_i}{\partial x_j} \frac{\partial u_j'}{\partial x_i} \tag{2.77}$$

$$\mathscr{S}^{TT} = \rho \frac{\partial u_i'}{\partial x_j} \frac{\partial u_j'}{\partial x_i} - \rho \left\langle \frac{\partial u_i'}{\partial x_j} \frac{\partial u_j'}{\partial x_i} \right\rangle. \tag{2.78}$$

For high Reynolds number flows the turbulence-turbulence interaction term $\mathscr{S}^{TT}$ can be neglected, see the discussion in Blake[18]. This is a very important result, because it is possible to express the spectrum of the mean shear source term analytically, but not the one of the turbulence-turbulence source term. The expression of the MS source term becomes very simple, if we assume the mean flow vector is parallel with the x_1-axis and the flow is homogeneous in the x_1 and x_3-direction. Then there is only a mean flow gradient in the boundary layer in the x_2-direction. With these assumptions the MS source term simplifies to

$$\mathscr{S}^{MS} = 2\rho \frac{dU_1}{dx_2} \frac{\partial u_2'}{\partial x_1}. \tag{2.79}$$

2.2.2 Kraichnan's[17] Solution for Bounded Flow

Now we reproduce Kraichnan's[17] solution of the Poisson equation of the fluctuating pressure for the flow situation displayed in figure 2.2. For convenience the primes are dropped in the following. We introduce the two dimensional Fourier transform of the fluctuating pressure and the source term

$$P(x_2, \vec{\kappa}, \omega) = \frac{1}{(2\pi)^3} \int_{-\infty}^{\infty} p(\vec{x}, t) e^{-i(k_1 x_1 + k_3 x_3)} e^{i\omega t} \, dx_1 dx_3 dt \tag{2.80}$$

$$\mathscr{C}(x_2, \vec{\kappa}, \omega) = \frac{1}{(2\pi)^3} \int_{-\infty}^{\infty} \mathscr{S}(\vec{x}, t) e^{-i(k_1 x_1 + k_3 x_3)} e^{i\omega t} \, dx_1 dx_3 dt. \tag{2.81}$$

$\vec{\kappa} = (k_1, k_3)$ is a two dimensional wave vector. By introducing this Fourier transform, one makes the assumption that the flow is homogeneous and of large extend in the x_1 and x_3-direction. This is approximately the case for a slowly growing turbulent boundary layer. The flow situation on an airfoil is generally different and care has to be taken when applying this theory to airfoil flow. The flow is inhomogeneous in the direction of x_2.
From eq. 2.75 we get with eqs. 2.80 and 2.81

$$\frac{\partial^2 P(x_2, \vec{\kappa}, \omega)}{\partial x_2^2} - \vec{\kappa}^2 P(x_2, \vec{\kappa}, \omega) = -\mathscr{C}(x_2, \vec{\kappa}, \omega). \tag{2.82}$$

The general solution of this linear inhomogeneous ordinary differential equation with constant coefficients is

$$P(x_2, \vec{\kappa}, \omega) = A e^{\kappa x_2} + B e^{-\kappa x_2} + \frac{1}{2} \kappa^{-1} \int_{-\infty}^{\infty} e^{-\kappa |y_2 - x_2|} \mathscr{C}(y_2, \vec{\kappa}, \omega) dy_2 \tag{2.83}$$

where y_2 is an axis aligned with the x_2-axis. A and B are constants of integration which are chosen to satisfy the boundary conditions. Considering the flow occupying the half space $x_2 > 0$ and assuming the wall $x_2 = 0$ is rigid, the lower

bound of the integration in eq. 2.83 can be set to 0, because all source terms are 0 for $x_2 < 0$. Very far from the surface the flow should be approximately laminar and the pressure fluctuations should vanish. Therefore it must be $A = 0$. The boundary condition on the rigid surface reads

$$\left(\frac{\partial P(x_2, \vec{\kappa}, \omega)}{\partial x_2}\right)_{x_2=0} = 0. \tag{2.84}$$

The integration constant B is evaluated with eq. 2.84 and the solution for the flow situation outlined above is

$$\begin{aligned} P(x_2, \vec{\kappa}, \omega) = \frac{1}{2}\kappa^{-1} e^{-\kappa x_2} \int_0^\infty e^{-\kappa y_2} \mathscr{C}(y_2, \vec{\kappa}, \omega) dy_2 \\ + \frac{1}{2}\kappa^{-1} \int_0^\infty e^{-\kappa |y_2 - x_2|} \mathscr{C}(y_2, \vec{\kappa}, \omega) dy_2. \end{aligned} \tag{2.85}$$

The surface pressure fluctuations ($x_2 = 0$) are given by

$$P(0, \vec{\kappa}, \omega) = \kappa^{-1} \int_0^\infty e^{-\kappa y_2} \mathscr{C}(y_2, \vec{\kappa}, \omega) dy_2. \tag{2.86}$$

The frequency wave number spectrum of the surface pressure fluctuations can be introduced as

$$\Pi_{pp} \delta(\vec{\kappa} - \vec{\overline{\kappa}}) \delta(\omega - \overline{\omega}) = \langle P^*(0, \overline{y}_2, \vec{\kappa}, \omega) P(0, y_2, \vec{\kappa}, \omega) \rangle \tag{2.87}$$

if $\langle P^*(0, \overline{y}_2, \vec{\kappa}', \omega') P(0, y_2, \vec{\kappa}, \omega) \rangle = 0$ for $\vec{\kappa} \neq \vec{\kappa}'$ and $\omega \neq \omega'$. This is true for homogeneous turbulence and hence applicable in our case. Combining eq. 2.86 and eq. 2.87 then yields

$$\Pi_{pp} = \kappa^{-2} \int \int_0^\infty e^{-\kappa(y_2 + \overline{y}_2)} \langle \mathscr{C}^*(\overline{y}_2, \vec{\kappa}, \omega) \mathscr{C}(y_2, \vec{\kappa}, \omega) \rangle \, dy_2 d\overline{y}_2. \tag{2.88}$$

The turbulence-turbulence interaction is now neglected and the Fourier transform of the MS source term (eq. 2.79) is

$$\mathscr{C}^{MS} = 2\rho \frac{dU_1}{dx_2} i k_1 \hat{u}_2(x_2, \vec{\kappa}, \omega) \tag{2.89}$$

where

$$\hat{u}_2(x_2, \vec{\kappa}, \omega) = \frac{1}{(2\pi)^3} \int_{-\infty}^\infty u_2(\vec{x}, t) e^{-i(k_1 x_1 + k_3 x_3)} e^{i\omega t} \, dx_1 dx_3 dt. \tag{2.90}$$

From eq. 2.88 and 2.89 we get

$$\begin{aligned} \Pi_{ppMS} = 4\rho^2 (k_1/\kappa)^2 \int \int_0^\infty e^{-\kappa(y_2 + \overline{y}_2)} \\ \frac{dU_1}{dx_2}(\overline{y}_2) \frac{dU_1}{dx_2}(y_2) \langle \hat{u}_2^*(\overline{y}_2, \vec{\kappa}, \omega) \hat{u}_2(y_2, \vec{\kappa}, \omega) \rangle \, dy_2 d\overline{y}_2. \end{aligned} \tag{2.91}$$

The expression

$$\langle \hat{u}_2^*(\overline{y}_2, \vec{\kappa}, \omega)\hat{u}_2(y_2, \vec{\kappa}, \omega)\rangle = \Phi_{22}(\overline{y}_2, y_2, \vec{\kappa}, \omega) \tag{2.92}$$

is the cross-correlation function of the vertical velocity fluctuation between two strata y_2 and $\overline{y}_2$.
Eq. 2.91 is equivalent to eq. 8-39 of [18]. According to Blake[18], eq. 8-39 is valid in the high wave number range $\delta^{-1} < \kappa < \infty$ with the boundary layer thickness δ. He dropped all terms involving compressibility by assuming $\kappa >> k_0 = \frac{\omega}{c}$ to derive eq. 8-39. Restricting the wavenumber range with a lower boundary of δ^{-1} does not affect generality of the result, because no eddy with a larger extend than the boundary layer thickness can develop in the boundary layer. The second inequality gives the upper limit of frequency for the validity of Blake's equation and eq. 2.91. However, it is difficult to quantify an upper limit, because we don't know exactly in which wave number range most of the energy is contained.

2.2.3 Simplifications of the Spectrum of the Fluctuating Velocity

From a modeling point of view the spectrum of the vertical velocity fluctuation Φ_{22} in eq. 2.91 is the most difficult part. Blake[18] introduced the separable form of the cross spectral density of the vertical velocity fluctuations

$$\Phi_{22}(\overline{y}_2, y_2, \vec{\kappa}, \omega) = \mathscr{R}_{22}(\overline{y}_2 - y_2)\Phi_{22}(y_2, \vec{\kappa}, \omega) \tag{2.93}$$

where the velocity field is assumed to be divided into thin layers in x_2-direction and $\mathscr{R}_{22}(\overline{y}_2 - y_2)$ specifies the cross correlation coefficient function between the layers, figure 2.3. Note that the flow is NOT homogeneous in the x_2-direction and the correlation coefficient function therefore depends not only on the separation $\overline{y}_2 - y_2$, but also on the position y_2. This stratification of the boundary layer is admissible in the wave number range $\kappa > \delta^{-1}$. As shown in figure 2.3, the correlation coefficient function $\mathscr{R}_{22}$ is not symmetric about y_2 because of the blockage by the rigid surface. Blake approximates this function by

$$R_{22}(\overline{y}_2 - y_2) = L_2^{22}\delta(\overline{y}_2 - y_2) \text{ for } \delta >> \overline{y}_2 - y_2 > L_2^{22}. \tag{2.94}$$

This means that the correlation is assumed to vanish for separation greater than L_2^{22}. L_2^{22} is the integral correlation length of the velocity fluctuations in x_2-direction with respect to a separation in x_2-direction. Due to the definition of the length scale, eq. A.9, the proposed approximation of the correlation coefficient function covers only the half $\overline{y}_2 > y_2$ of each strata, because the

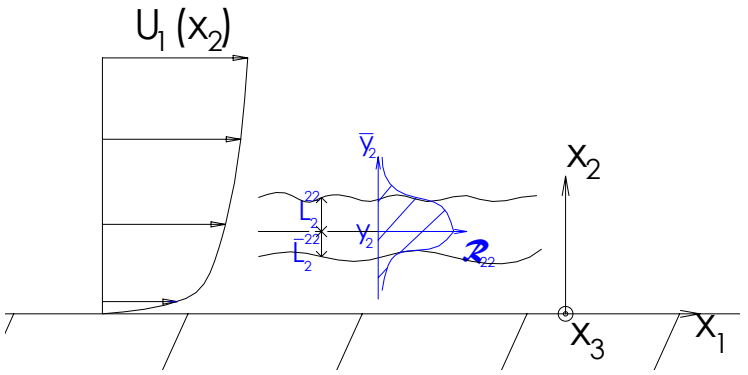

Figure 2.3: The configuration of the analytical surface pressure models

lower boundary of the integration is 0. Therefore we propose to modify eq. 2.94 as

$$\mathscr{R}_{22}(\overline{y}_2 - y_2) = (L_2^{22} + \overline{L}_2^{22})\delta(\overline{y}_2 - y_2) \tag{2.95}$$

where

$$\overline{L}_2^{22} = \int_{-\infty}^{0} \mathscr{R}_{22}((0, \overline{y}_2 - y_2, 0), 0) d\vec{r}. \tag{2.96}$$

For the unbounded flow both correlation length scales are the same, $L_2^{22} = \overline{L}_2^{22}$. As next step Blake[18] separates the frequency and wave number dependence according to

$$\Phi_{22}(y_2, \vec{\kappa}, \omega) = \Phi_{22}(y_2, \vec{\kappa})\Phi_m(k_1, \omega). \tag{2.97}$$

Φ_m is the so-called moving axis spectrum. It describes how the eddies are distorted during their passage. If the Taylor hypothesis of frozen turbulence is valid, the moving axis spectrum equals a delta function

$$\Phi_m(k_1, \omega) = \delta(\omega - U_c k_1) \tag{2.98}$$

with the eddy convection velocity U_c. If the distortion of the eddies during their passage is of importance, we may introduce a moving axis spectrum of exponential form as suggested by Parchen[19]

$$\Phi_m(k_1, \omega) = \frac{1}{\alpha_G \sqrt{\pi}} e^{-\left(\frac{\omega - U_c k_1}{\alpha_G}\right)^2} \tag{2.99}$$

where α_G is a constant with the dimension of a frequency. It determines how sharply peaked the moving axis spectrum is about the maximum. The position of the maximum is defined by the eddy convection velocity U_c. The exponential form of the moving axis spectrum can be directly derived from the diffusion

term of the NS equations.
Using eqs. 2.93, 2.95 and 2.97 to simplify eq. 2.91 we get

$$\Pi_{ppMS} = 4\rho^2(k_1/\kappa)^2 \int_0^\infty e^{-2\kappa y_2} \left(\frac{dU_1}{dx_2}(y_2)\right)^2 L_2^{22}(1+\sigma(y_2))\Phi_{22}(y_2,\vec{\kappa})\Phi_m(k_1,\omega)dy_2 \tag{2.100}$$

where

$$\overline{L}_2^{22} = \sigma(y_2)L_2^{22}. \tag{2.101}$$

Eq. 2.100 is a slightly modified version of Blake's[18] eq. 8-40. Blake's[18] eq. 8-40 is the basis of the original TNO model.

2.3 Modeling of Turbulence

In this section we will first treat the case of homogeneous isotropic turbulence (HIT). It is the simplest case of turbulence, but never occurs in real flows. On the other hand, it makes an analytical treatment possible. Many qualitative observations for isotropic turbulence apply also for the case of anisotropic turbulence. In the next section we outline the Mann [26] model for anisotropic turbulence. It describes the influence of linear shear and blockage of the surface on an initially isotropic spectrum by rapid distortion theory (RDT).

2.3.1 Homogeneous Isotropic Turbulence

Homogeneous turbulence means that the statistical properties are independent of the location in the flow. Strict homogeneity in any direction implies that the flow is infinite or periodic in that direction [30]. Mathematically, the Fourier transform can only be applied in this flow condition. If we deal with a flow of large extent, the inhomogeneity is very weak and assuming homogeneity gives good results. A flow in the middle of a wind tunnel can be approximated as homogeneous in all directions. The boundary layer flow over a flat plate (figure 2.2) is approximately homogeneous in x_3-direction (assuming the spanwise extent is large). If the boundary layer grows slowly, the flow can also be assumed homogeneous in the x_1-direction. However, it is inhomogeneous in the x_2-direction.
In isotropic turbulence, the statical properties are independent with respect to a rotation of the coordinate system[31]. For HIT a 1-dimensional energy spectrum can be defined which describes the complete spectral tensor $\Phi_{ij}(\vec{k},\omega)$. Let us

first introduce the turbulent kinetic energy e_t as

$$e_t = \frac{1}{2}\left(\left\langle u_1^2\right\rangle + \left\langle u_2^2\right\rangle + \left\langle u_3^2\right\rangle\right). \tag{2.102}$$

This definition applies for general turbulence, not only HIT. The derivation of the energy spectrum for HIT starts with reformulating the definition of the turbulent kinetic energy e_t

$$e_t = \frac{1}{2}R_{ii}(\vec{0}) = \frac{1}{2}\int_{-\infty}^{\infty}\Phi_{ii}(\vec{k})\,d^3\vec{k}. \tag{2.103}$$

The time dependence is omitted, because we assume stationary turbulence. Using the spherical symmetry of isotropic turbulence the integration over all $\vec{k}$-space becomes

$$\int_{-\infty}^{\infty}\Phi_{ii}(\vec{k})\,d^3\vec{k} = \int_0^{\infty}4\pi k^2\Phi_{ii}(k)\,dk \tag{2.104}$$

with $k = \sqrt{k_1^2 + k_2^2 + k_3^2}$. The energy spectrum is then defined as

$$E(k) = 2\pi k^2\Phi_{ii}(k) \tag{2.105}$$

with the property

$$e_t = \int_0^{\infty}E(k)\,dk. \tag{2.106}$$

The components of the spectral tensor Φ_{ij} are related to the energy spectrum E by[30]

$$\Phi_{ij} = \frac{E(k)}{4\pi k^2}\left(\delta_{ij} - \frac{k_i k_j}{k^2}\right). \tag{2.107}$$

Von Karman gave an analytical expression of the energy spectrum which is referred to as the von Karman spectrum

$$E(k) = \alpha\bar{\epsilon}^{2/3}L^{5/3}\frac{(Lk)^4}{(1+(Lk)^2)^{17/6}} \tag{2.108}$$

where α is a non-dimensional constant, L is a typical length scale discussed later and $\bar{\epsilon}$ is the mean energy dissipation. The mean energy dissipation can be defined directly from the NS equations

$$\bar{\epsilon} = \frac{1}{2}\nu\left\langle\left(\frac{\partial u_i}{\partial x_j} + \frac{\partial u_j}{\partial x_i}\right)\left(\frac{\partial u_i}{\partial x_j} + \frac{\partial u_j}{\partial x_i}\right)\right\rangle \tag{2.109}$$

which is generally valid (not only for HIT). For HIT it can be reduced to

$$\bar{\epsilon} = 15\nu\left\langle\left(\frac{\partial u_1}{\partial x_1}\right)^2\right\rangle. \tag{2.110}$$

The dissipation can be approximated as

$$\overline{\epsilon} \propto \frac{((2/3)e_t)^{3/2}}{L} \tag{2.111}$$

if the energy containing eddies break up at a time scale equal to their turn over time[32]. Inserting eq. 2.111 into eq. 2.108 yields

$$E(k) = \overline{\alpha} e_t L \frac{(Lk)^4}{(1+(Lk)^2)^{17/6}} \tag{2.112}$$

where $\overline{\alpha}$ is another non-dimensional constant. If the energy spectrum defined in eq. 2.112 shall fulfill eq. 2.106, we find

$$\overline{\alpha} = \frac{110}{27\sqrt{\pi}} \frac{\Gamma(5/6)}{\Gamma(1/3)}. \tag{2.113}$$

Due to the spherical symmetry of HIT there are only two different length scales from auto correlations instead of 9. The length scale is independent of direction, so we may introduce the unit vector $\vec{r}$ in random direction. The velocity component u_p is aligned with $\vec{r}$ and the velocity component u_n is normal to $\vec{r}$. The two constituting length scales for isotropic turbulence are then

$$L_{\vec{r}}^{pp} \equiv L_p = \int_0^\infty \mathscr{R}_{pp}(r) dr \tag{2.114}$$

$$L_{\vec{r}}^{nn} \equiv L_n = \int_0^\infty \mathscr{R}_{nn}(r) dr. \tag{2.115}$$

The relation between L_p and L_n is $L_p = 2L_n$[30].For the von Karman spectrum defined in eq. 2.112 and 2.113 one can find the relation between the length scale L and the integral length scale L_p[30]

$$L_p = \frac{\sqrt{\pi}\Gamma(5/6)}{\Gamma(1/3)} L. \tag{2.116}$$

2.3.2 The Mann Model for Anisotropic Turbulence

Most anisotropic turbulence models introduce so called 'stretching coefficients' in the spectral tensor to model different extensions in different directions. It usually leads to a set of 6 tuning constants. The Mann[26] Model introduces only one additional parameter compared to an isotropic turbulence model. This makes the Mann Model more general than all other anisotropic models known to the author.

2.3.2.1 Formulation of the Mann Model

The Mann Model is based on rapid distortion theory (RDT)[33]. RDT gives an equation for the deformation of the spectral tensor with time. The spectral tensor at the starting time ($t = 0$) is described by the isotropic von Karman tensor 2.107. Mann[26] makes the simplifying assumption that the mean flow is parallel with the x_1-axis and there is a uniform mean shear $\frac{\partial U_1}{\partial x_2}$, figure 2.4. He

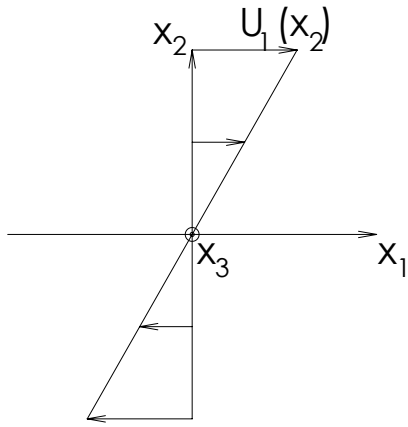

Figure 2.4: The flow conditions of the Mann[26] Model

proposes a simple model which describes the deformation of the spectral tensor due to uniform shear (US model) and a more complex model which describes additionally the effect of blockage due to a rigid surface $x_2 = 0$ (US+B model). The US+B model builds up on the US model. Hence, we will first summarize the derivation of the US model and then introduce the equations constituting the US+B model.
RDT is based on the linearized Poisson equation for the fluctuating pressure and a linearized equation for the fluctuating velocity [34]. The linearized Poisson equation for the pressure is given by eq. 2.75 when considering only the linear source term eq. 2.77. The RDT equation for the fluctuating velocity can be derived by applying the Reynolds decomposition to the Navier-Stokes equation and subtracting the equation for the mean flow. Then all non-linear terms are dropped and it reads

$$\frac{\partial u_j'}{\partial t} + U_i \frac{\partial u_j'}{\partial x_i} = -u_i' \frac{\partial U_j}{\partial x_i} - \frac{1}{\rho} \frac{\partial p'}{\partial x_j}. \tag{2.117}$$

These are the same simplification as used for modeling the surface pressure with the linearized source term. Hence, RDT does not introduce further simplifications to the surface pressure modeling.
Pope[34] shows that the solution of eq. 2.117 using Fourier transform reads

$$\vec{u}(\vec{x},t) = \hat{\vec{u}}(t)e^{i\vec{k}(t)\vec{x}} \tag{2.118}$$

where $\hat{\vec{u}}$ and $\vec{k}$ have to satisfy

$$\frac{dk_i}{dt} = -k_j \frac{\partial U_j}{\partial x_i} \tag{2.119}$$

$$\frac{D\hat{u}_j}{Dt} = -\hat{u}_i \frac{\partial U_l}{\partial x_i}\left(\delta_{jl} - 2\frac{k_j k_l}{k^2}\right). \tag{2.120}$$

Mann[26] uses the Fourier-Stieltjes integral instead of the Fourier transform of the velocity. The equivalent of eq. 2.120 then reads

$$\frac{DdZ_j}{Dt} = -dZ_i \frac{\partial U_l}{\partial x_i}\left(\delta_{jl} - 2\frac{k_j k_l}{k^2}\right). \tag{2.121}$$

For a flow situation where the mean flow is parallel with the x_1-axis and the mean shear $\frac{\partial U_1}{\partial x_2}$ is uniform, figure 2.4, and the wave number vector at the initial time $t = 0$

$$\vec{k}_0 \equiv \vec{k}(t=0) = (k_1, k_{20}, k_3) \tag{2.122}$$

the solution of eq. 2.119 is

$$\vec{k} \equiv \vec{k}(t) = (k_1, k_2, k_3) \tag{2.123}$$

with

$$k_2 = k_{20} - \beta k_1 \tag{2.124}$$

The non-dimensional time β was introduced as

$$\beta = \frac{\partial U_1}{\partial x_2} t \tag{2.125}$$

Mann[26] finds the solution to eq. 2.121

$$d\vec{Z}(\vec{k},\beta) = \begin{pmatrix} 1 & \xi_1 & 0 \\ 0 & \frac{k_0^2}{k^2} & 0 \\ 0 & \xi_2 & 1 \end{pmatrix} d\vec{Z}(\vec{k}_0, 0) \tag{2.126}$$

with the subfunctions

$$\xi_1 = C_1 - \frac{k_3}{k_1} C_2 \tag{2.127}$$

$$\xi_2 = \frac{k_3}{k_1} C_1 + C_2 \tag{2.128}$$

where

$$C_1 = \frac{\beta k_1^2 (k_0^2 - 2k_{20}^2 + \beta k_1 k_{20})}{k^2 (k_1^2 + k_3^2)} \tag{2.129}$$

$$C_2 = \frac{k_3 k_0^2}{(k_1^2 + k_3^2)(3/2)} \arctan \left[\frac{\beta k_1 \sqrt{k_1^2 + k_3^2}}{k_0^2 - k_{20} k_1 \beta} \right]. \tag{2.130}$$

Eq. 2.123 and eq. 2.126 give the temporal evolution of the Fourier modes. If the spectral tensor at the initial time $t = 0$ is known, an explicit expression for the spectral tensor $\Phi_{ij}(\vec{k}, \beta)$ at time t can be derived by using eq. A.7. By assuming that the initial spectral tensor $\Phi_{ij}(\vec{k}_0, 0) = \Phi_{ij}^{iso}(\vec{k}_0)$ is given by the isotropic von Karman tensor, eq. 2.107 with the energy spectrum of eq. 2.108, Mann[26] finds the expression

$$\Phi_{11}(\vec{k}, \beta) = \frac{E(k_0)}{4\pi k_0^4} (k_0^2 - k_1^2 - 2k_1 k_{20} \xi_1 + (k_1^2 + k_3^2) \xi_1^2) \tag{2.131}$$

$$\Phi_{22}(\vec{k}, \beta) = \frac{E(k_0)}{4\pi k^4} (k_1^2 + k_3^2) \tag{2.132}$$

$$\Phi_{33}(\vec{k}, \beta) = \frac{E(k_0)}{4\pi k_0^4} (k_0^2 - k_3^2 - 2k_3 k_{20} \xi_1 + (k_1^2 + k_3^2) \xi_2^2) \tag{2.133}$$

$$\Phi_{12}(\vec{k}, \beta) = \frac{E(k_0)}{4\pi k_0^2 k^2} (-k_1 k_{20} + (k_1^2 + k_3^2) \xi_1) \tag{2.134}$$

$$\Phi_{13}(\vec{k}, \beta) = \frac{E(k_0)}{4\pi k_0^4} (-k_1 k_3 - k_1 k_{20} \xi_2 - k_3 k_{20} \xi_1 + (k_1^2 + k_3^2) \xi_1 \xi_2) \tag{2.135}$$

$$\Phi_{23}(\vec{k}, \beta) = \frac{E(k_0)}{4\pi k_0^2 k^2} (-k_3 k_{20} + (k_1^2 + k_3^2) \xi_2) \tag{2.136}$$

for the spectral tensor at time t.
The linear deformation of the spectral tensor with time is, however, unrealistic, because the eddies will break up at one point. Mann[26] makes some considerations about the eddy life time and replaces the time t in the relations given by RDT with the eddy life time τ_e to get a stationary spectral tensor.
In his life time model the eddy life time is a function of the eddy size k^{-1}. He assumes further that the destruction of an eddy is mainly due to eddies with the same or a smaller size than its own. The characteristic velocity of those eddies is $\approx \left(\int_k^\infty E(p) dp \right)^{\frac{1}{2}}$ and the life time is assumed to be the eddy size k^{-1} divided by this velocity:

$$\tau_e(k) \propto k^{-1} \left(\int_k^\infty E(p) dp \right)^{-\frac{1}{2}}. \tag{2.137}$$

If one uses the von Karman spectrum, eq. 2.108, for the energy spectrum E in eq. 2.137 we get

$$\tau_e(k) \propto k^{-\frac{2}{3}} \left({}_2F_1 \left[\frac{1}{3}, \frac{17}{6}; \frac{4}{3}; -(kL)^{-2} \right] \right)^{-\frac{1}{2}} \tag{2.138}$$

which can be rewritten as:

$$\tau_e(k) = \Gamma \left(\frac{\partial U_1}{\partial x_2} \right)^{-1} (kL)^{-\frac{2}{3}} \left({}_2F_1 \left[\frac{1}{3}, \frac{17}{6}; \frac{4}{3}; -(kL)^{-2} \right] \right)^{-\frac{1}{2}} \tag{2.139}$$

where Γ is a non-dimensional constant. As the model assumes a constant shear, $\left(\frac{\partial U_1}{\partial x_2} \right)^{-1}$ is a constant with the dimension of time. Finally, the Mann[26] US model is complete by replacing time t with τ_e in eqs. 2.131-2.136.
To formulate the US+B model it is assumed that a rigid surface $x_2 = 0$ is inserted at time $t = 0$. Viscous effects are not taken into account by the model, so the only effect of the rigid surface is to suppress vertical velocity fluctuations. Due to the blockage of the surface the flow is no longer homogeneous in the x_2-direction. The Fourier transform in this direction should therefore be avoided. The spectral tensor is described as a function of the plane wave number vector k_1 and k_3 and the cross correlation between the altitude x_2 and y_2. y_2 is parallel to x_2. The spectral tensor of the US+B model at time $t = \tau_e$ is found following the recipe in [26] as

$$\begin{aligned}
\Phi_{11}^B(\vec{\kappa}, x_2, y_2) = &\int_{-\infty}^{\infty} \Phi_{11} e^{-ik_2(x_2-y_2)} dk_2 + \frac{k_1^2}{\kappa^2} e^{-\kappa(x_2+y_2)} (1+P_1(x_2))^* (1+P_1(y_2)) \Phi_{22} dk_2 \\
&+ i\frac{k_1}{\kappa} \left((1+P_1(y_2)) e^{-ik_2x_2-\kappa y_2} - (1+P_1(x_2))^* e^{ik_2y_2-\kappa x_2} \right) \Phi_{12} dk_2 \qquad (2.140) \\
\Phi_{22}^B(\vec{\kappa}, x_2, y_2) = &\int_{-\infty}^{\infty} \left(e^{-ik_2(x_2-y_2)} - e^{-ik_2x_2-\kappa y_2} - e^{ik_2x_2-\kappa y_2} + e^{-\kappa(x_2+y_2)} \right) \Phi_{22} dk_2 \qquad (2.141) \\
\Phi_{33}^B(\vec{\kappa}, x_2, y_2) = &\int_{-\infty}^{\infty} \Phi_{33} e^{-ik_2(x_2-y_2)} dk_2 + \frac{k_3^2}{\kappa^2} e^{-\kappa(x_2+y_2)} (1+P_2(x_2))^* (1+P_2(y_2)) \Phi_{22} dk_2 \\
&+ i\frac{k_3}{\kappa} (((1+P_2(y_2)) e^{-ik_2x_2-\kappa y_2} - (1+P_2(x_2))^* e^{ik_2y_2-\kappa x_2}) \Phi_{23} dk_2 \qquad (2.142) \\
\Phi_{12}^B(\vec{\kappa}, x_2, y_2) = &\int_{-\infty}^{\infty} \left(e^{ik_2y_2} - e^{-\kappa y_2} \right) \left(\Phi_{12} e^{-ik_2x_2} - \Phi_{22} i\frac{k_1}{\kappa} e^{-\kappa x_2} (1+P_1(x_2))^* \right) dk_2 \qquad (2.143) \\
\Phi_{13}^B(\vec{\kappa}, x_2, y_2) = &\int_{-\infty}^{\infty} \Phi_{13} e^{-ik_2(x_2-y_2)} dk_2 + i\frac{k_3}{\kappa} ((1+P_2(y_2)) e^{-ik_2x_2-\kappa y_2} \Phi_{12} dk_2 \\
&- i\frac{k_1}{\kappa} ((1+P_1(x_2))^* e^{ik_2y_2-\kappa x_2} \Phi_{23} dk_2 \qquad (2.144) \\
\Phi_{23}^B(\vec{\kappa}, x_2, y_2) = &\int_{-\infty}^{\infty} \left(e^{ik_2y_2} - e^{-\kappa y_2} \right) \left(\Phi_{23} e^{-ik_2x_2} - \Phi_{22} i\frac{k_2}{\kappa} e^{-\kappa x_2} (1+P_2(x_2))^* \right) dk_2 \\
&+ \frac{k_1k_3}{\kappa^2} e^{-\kappa(x_2+y_2)} (1+P_1(x_2))^* (1+P_2(y_2)) \Phi_{22} dk_2. \qquad (2.145)
\end{aligned}$$

Note that the coordinate system in Mann[26] is different. To compare the results, the subscripts 2 and 3 have to be swapped.

2.3.2.2 Discussion of the Model

The Mann[26] does NOT conserve the energy inherent in the initial isotropic von Karman spectrum, because RDT describes the energy transfer from the mean shear flow to the turbulence as a function of time. In the model formulation as above, the development in time is described by the non-dimensional time β. β is steered by the coefficient Γ. Hence, an increase of Γ results in an increase of the turbulent kinetic energy e_k as seen in figure 2.5(a). The increase in turbulent

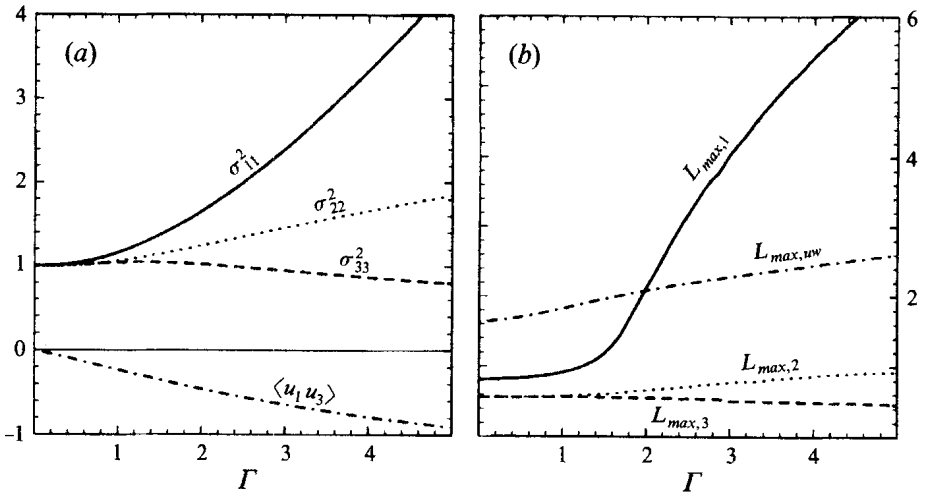

Figure 2.5: Properties of the US model as function of the parameter Γ from [26]: (a) (co-)variances normalized by the variance of the isotropic von Karman model (eq. 2.108); (b) length scales defined in eq. 2.146 normalized by L. Note that the subscripts 2 and 3 have to be swapped to be consistent with the text.

kinetic energy is mainly due to the increase in the variance of the streamwise component. The variance of the horizontal component only increases slightly while the one of the vertical velocity component weakly decreases. The same trend can be observed for the length scale (figure 2.5(b)). The length scale $L_{max,i}$ is defined as

$$L_{max,i} \equiv \frac{1}{k_{1,max,i}} \tag{2.146}$$

where $k_{1,max,i}$ is the wave number at which the pre-multiplied one-dimensional spectrum $k_1 F_1^{ii}(k_1)$ has its maximum.
The effect of blockage decreases the turbulent kinetic energy (figure 2.6(a)) and length scale (figure 2.6(b)) when the distance to the wall is reduced. Considering the distance close to the wall ($\approx z/L < 0.2$), the variance of the streamwise and

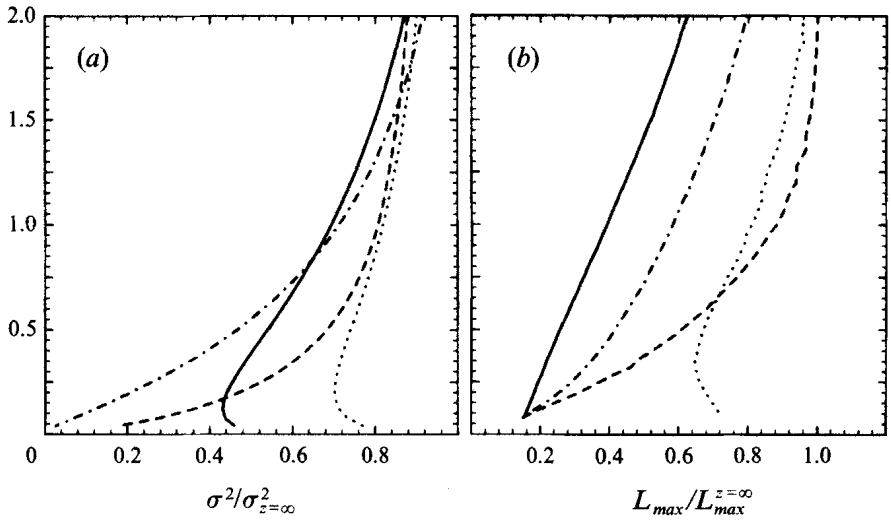

Figure 2.6: The effect of blockage on the (co-)variances (a) and length scales (b) normalized by values infinitely far away from the surface from [26]. Note that the subscripts 2 and 3 have to be swapped to be consistent with the text.

horizontal component increases when approaching the wall. This behavior of the model is unphysical. The model can not take into account the effects of friction, because the terms involving viscosity were neglected in the derivation. Hence, the author does not recommend to use the Mann[26] US+B model to describe the spectrum of the streamwise and horizontal velocity component very close to the wall. The vertical velocity component exhibits a physically correct behavior and it can be attempted to model this component throughout the whole boundary layer.

2.4 Model Formulations

2.4.1 The TNO Model

The TNO model was originally proposed by Parchen[19] of the TNO Institute of Applied Physics in the Netherlands. He gathered the results of Blake[18] and modeled the source terms of the surface pressure. The velocity profile and length scales were related to empirical expressions for a flat plate. Lutz[20] refined the model and related those quantities to output of a RANS computation. We will

follow his approach.
Parchen[19] based his model on eq. 2.100 which neglects non-linear source terms of the surface pressure. In his original formulation the length scale factor σ is omitted. Recently, Bertagnolio[24] objected this and corrected the model by adding a factor of 2. This is the correct formulation if the flow is unbounded. With this correction the basic equation of the TNO model reads

$$\Pi_{ppTNO} = 4\rho^2(k_1/\kappa)^2 \int_0^\infty e^{-2\kappa y_2} \left(\frac{dU_1}{dx_2}(y_2)\right)^2 2L_2^{22}\Phi_{22}(y_2,\vec{\kappa})\Phi_m(k_1,\omega)dy_2 \tag{2.147}$$

The spectral density of the vertical velocity fluctuations $\Phi_{22}(y_2,\vec{\kappa})$ is expressed using the classical von Karman model. Combining eq. 2.112 and eq. 2.107 and integrating over the vertical wave number k_2 yields

$$\Phi_{22} = \frac{4}{9\pi}\frac{2}{3}e_t L^2 \frac{(Lk_1)^2 + (Lk_3)^2}{[1 + (Lk_1)^2 + (Lk_3)^2]^{7/3}} \tag{2.148}$$

The factor $\frac{2}{3}e_t$ equals the variance of the vertical velocity fluctuations $\langle u_2^2 \rangle$ in the isotropic case. Because of the blockage due to the airfoil surface the variance of the vertical velocity fluctuations is reduced. Hence, Parchen reformulates the spectral density as

$$\Phi_{22} = \frac{4}{9\pi}\langle u_2^2 \rangle L^2 \frac{(Lk_1)^2 + (Lk_3)^2}{[1 + (Lk_1)^2 + (Lk_3)^2]^{7/3}} \tag{2.149}$$

and applies $\langle u_2^2 \rangle = 0.45e_t$ on the suction side and $\langle u_2^2 \rangle = 0.3e_t$ on the pressure side of the airfoil. These empirical relation were found by measurements [19].
By the comparison with measurements with a microphone array aligned in streamwise direction on the airfoil surface, Parchen[19] found that a moving axis spectrum of Gaussian form, eq. 2.99, gives the best results. The inclination of the convective ridge of the measured spectrum in the frequency wave number space $f - k_1/(2\pi)$ suggested a convection speed related to the local flow speed by

$$U_c = 0.7U_1(x_2) \tag{2.150}$$

which Parchen uses in the TNO model. A similar distribution of the energy away from the convective ridge as in the measurement was achieved by defining the Gaussian coefficient as

$$\alpha_G = 0.05\frac{U_c}{L_2^{22}} \tag{2.151}$$

Several comments have to be made about Parchen's way of defining the moving axis spectrum:

- Measurements were only performed for one specific airfoil at a single Reynolds number and the lift coefficient equal to zero. There is no proof of generality of the moving axis spectrum.

- The boundary layer close to the trailing edge of an airfoil is inhomogeneous in streamwise direction. The Fourier transform of data of microphones distributed in streamwise direction might be inappropriate.
- The measurements of Brooks and Hodgson[12] showed that the convection speed is a function of the separation of the measurement position. The moving axis spectrum measured by a microphone array distributed in the streamwise direction should therefore be a function of the extend of the microphone array.
- The moving axis spectrum changes with the streamwise traveling distance. For the prediction of TE noise it should be defined according to the streamwise distance of the surface pressure evaluation from the TE. In the limit of an infinitely small distance between surface pressure evaluation and TE, the moving axis spectrum should tend to a dirac delta function, because Taylors hypothesis is exact in this asymptotic case.
- The assumption of the convection velocity being less than the local flow speed is inconsistent with the acoustic formulation of Howe[11] used later in the TNO model.

The velocity profile $U_1(x_2)$ is directly obtained from the RANS computation and the velocity gradient can be calculated. The turbulent kinetic energy e_t is obtained from the $k-\omega$ turbulence model of the RANS solver and the variance of the vertical velocity fluctuation is evaluated with the empirical expressions given above.
The length scale L of eq. 2.149 can be related to the output of the $k-\omega$ turbulence model by comparing the asymptotic behavior of the von Karman spectrum with the Kolmogorov spectrum

$$E_K(k) = C_K \frac{\overline{\epsilon}^{2/3}}{k^{5/3}} \tag{2.152}$$

where the Kolmogorov constant was found as $C_K = 1.5$ in experiments [20]. This comparison yields

$$L = \left(\frac{110\Gamma(5/6)}{C_K 27\sqrt{\pi}\Gamma(1/3)} \right)^{3/2} \frac{e_t^{3/2}}{\overline{\epsilon}} \tag{2.153}$$

The length scale of the vertical velocity fluctuations L_2^{22} is then found by assuming isotropy and applying eq. 2.116 which yields

$$L_2^{22} = \frac{\sqrt{\pi}\Gamma(5/6)}{\Gamma(1/3)} L \tag{2.154}$$

Parchen evaluates the far field sound with eq. 2.33. Note that this equation is only valid for one specific observer position ($\Phi = 90\,°$, $\Theta = 90\,°$). To make the

model more general eq. 2.31 should be used in the model. The correct value of the surface pressure spectrum Φ_s in eq. 2.33 is $\Phi_s = \frac{1}{4}\Pi_{ppTNO}$ according to the discussion of subsection 2.1.2. The expression for the far field sound at the specified observer position is

$$S_f(\omega) = \frac{L_s \omega}{4\pi c_0 R^2} \int_0^\infty \frac{\Pi_{ppTNO}(k_1, 0, \omega)}{|k_1|} dk_1 \tag{2.155}$$

2.4.2 Surface Pressure Model based on Kraichnan's equation and the Mann Turbulence Model (SPKM)

The new model is based on Kraichnan's equation with simplified source term 2.91. The frequency wave number spectral density is modeled with the Mann Model and reads

$$\Phi_{22}(x_2, y_2, \vec{\kappa}, \omega) = \Phi_{22}^B(x_2, y_2, \vec{\kappa}) \Phi_m(k_1, \omega) \tag{2.156}$$

Note that the variable name $\overline{y}_2$ was changed to x_2.
The moving axis spectrum is modeled with the dirac delta function eq. 2.98. There are several reasons for doing so. First, the Gaussian factor α_G of the moving axis spectrum function used in the TNO model eq. 2.151 is tuned in a way that the spectrum has a very sharp peak and gives hardly a different result than if the dirac delta function is used. Second, it is not very probable that the tuning of the constants of the moving axis spectrum by Parchen[19] is general. As there were no measurements to determine the moving axis spectrum for our case available to the author, it was chosen to use a simpler form. Moreover, using the dirac delta function reduces the computational time significantly.
It is more important to model the peak location correctly. The peak location is determined by the convection velocity U_c. In our model we assume that the convection velocity U_c is equal to the local flow velocity U_1. It ensures the conformity with the acoustic formulation for the far field sound pressure of Howe (eq. 2.31) and Amiet (eq. 2.63). Both make the same assumption during the derivation of the respective far field sound pressure equation. But it will also be tested to use the same ratio of convection speed to local flow speed as in [19], eq. 2.150.
The Mann Turbulence Model is based on the von Karman energy spectrum, eq. 2.108, and an eddy life time approximation, eq. 2.139. The von Karman energy spectrum is defined by the mean dissipation times a constant $\alpha\overline{\epsilon}^{2/3}$ and the length scale L. These two parameters can be in principle derived from the $k-\omega$ turbulence model of a RANS solver. A relation will be established in the course of this work by a fit to hot wire boundary layer velocity measurements. The eddy life time approximation includes a proportionality factor Γ. This proportionality describes the degree of anisotropy. It cannot be derived from

the $k-\omega$ turbulence model. Instead an empirical relation will be established. It is most likely that the 3 parameters $\alpha\bar{\epsilon}^{2/3}$, L and Γ will be described as functions of the vertical wall distance x_2, y_2. To model the cross correlation between two positions x_2 and y_2, one has to find one characteristic set of $\alpha\bar{\epsilon}^{2/3}$, L and Γ, because the assumptions under which the Mann Model was developed do not allow that those parameters depend on the wall distance. The same assumption has to be made for the local convection speed U_c.
The first model simply uses arithmetic mean values and is denoted as SPKMa model. A more complicated model using integral mean values, defined as

$$L(x_2, y_2) = \frac{\int_{x_2}^{y_2} L(\overline{x}_2) d\overline{x}_2}{y_2 - x_2} \; y_2 > x_2 \tag{2.157}$$

for the example of L is denoted by SPKMi.
The disadvantage of the cross spectral model supposed above is that the cross spectrum inequality

$$|\Phi(\omega, x_2, y_2)|^2 \leq \Phi(\omega, x_2, x_2)\Phi(\omega, y_2, y_2) \tag{2.158}$$

is not enforced. To enforce ineq. 2.158 we developed a third model and defined the cross spectral density of eq. 2.141 by using the geometric mean value for the Mann US model spectrum

$$\Phi_{22}(x_2, y_2) = \sqrt{\Phi_{22}(\alpha\bar{\epsilon}^{2/3}(x_2), L(x_2), \Gamma(x_2))\Phi_{22}(\alpha\bar{\epsilon}^{2/3}(y_2), L(y_2), \Gamma(y_2))} \tag{2.159}$$

This new model is called SPKMag or SPKMig, depending on which way of evaluation is used for the mean value of the convection velocity.
The full expression for the surface pressure frequency wave number spectrum is then

$$\begin{aligned} \Pi_{ppKM} = 4\rho^2(k_1/\kappa)^2 \int\int_0^\infty \frac{dU_1}{d\overline{x}_2}(x_2)\frac{dU_1}{d\overline{x}_2}(y_2)e^{-\kappa(x_2+y_2)} \\ \Phi_{22}^B(\alpha\bar{\epsilon}^{2/3}(x_2, y_2), L(x_2, y_2), \Gamma(x_2, y_2), x_2, y_2, \vec{\kappa})\delta(\omega - U_c k_1)dx_2 dy_2 \end{aligned} \tag{2.160}$$

The far field sound pressure pressure can be evaluated using Howe's equation 2.31. As explained in subsection 2.4.1, the surface pressure frequency wave number PSD applied in Howe's equation 2.31 is 1/4 of the surface pressure frequency wave number PSD from eq. 2.160. By taking advantage of the delta function and assuming that the mean flow is parallel with the x_1-axis the expression for the far field sound using Howe's result becomes

$$\begin{aligned} S_{KMH} = \frac{2L_s\rho_0^2}{\pi R^2}\frac{\sin(\Phi)\sin^2(\Theta/2)}{(1+M_0\sin(\Phi)\cos(\Theta))^2(1-M_W\sin(\Phi)\cos(\Theta))^2} \\ \int\int_0^\infty \frac{U_c}{c_0}\frac{\frac{dU_1}{d\overline{x}_2}(x_2)\frac{dU_1}{d\overline{x}_2}(y_2)\Phi_{22}^B(\frac{\omega}{U_c}, \frac{\omega}{c_0}\cos(\Phi), x_2, y_2)}{(1-\frac{U_c}{c_0}\sin(\Phi)\cos(\Theta))^2(1-\frac{U_c}{c_0}\sin(\Phi))(1+(\frac{U_c}{c_0}\cos(\Phi))^2)} \\ e^{-\omega\sqrt{(1/U_c)^2+(\cos(\Phi)/c_0)^2}(x_2+y_2)}dx_2 dy_2 \end{aligned} \tag{2.161}$$

Alternatively, we can use Amiet's model with Roger's extensions eq. 2.63 or eq. 2.65 to express the far field sound.

Chapter 3

Experiments

All the experimental data presented in this work were obtained in experiments in two different wind tunnels, the wind tunnel of LM Wind Power A/S (LSWT) and the wind tunnel of Virginia Tech University (VTST). The LSWT is a classical aerodynamic wind tunnel with a hard wall test section optimized for airfoil testing. The boundary layer fluctuating velocity and the surface pressure fluctuations on a NACA0015 were measured. The setup is described in detail.
The VTST is an acoustic wind tunnel with a special test section configuration. Two airfoils were tested in this tunnel and the far field sound was measured with a microphone array. Additionally also the surface pressure fluctuations and the boundary layer fluctuating velocity were measured. The wind tunnel concept and the microphone array measurement technique are outlined in the second section.
The most important measurement techniques for the present work are hot wire anemometry for the fluctuating boundary layer velocity and the fluctuating surface pressure measurement technique. They are discussed in a separate section each.

3.1 The LM Wind Power Experiment

3.1.1 The Wind Tunnel of LM Wind Power A/S (LSWT)

The LSWT is a closed circuit wind tunnel with a closed test section, figure 3.1. The flow is driven by a 1MW fan. A flow speed of up 105m/s can be reached. The tunnel is equipped with a heat exchanger which can cool down the fluid to keep the temperature at a constant level. A good flow quality is achieved with aerodynamically treated corner vanes, a honeycomb structure, 3 screens and a nozzle with a contraction ratio of 10 to 1. The test section is 7m long and has

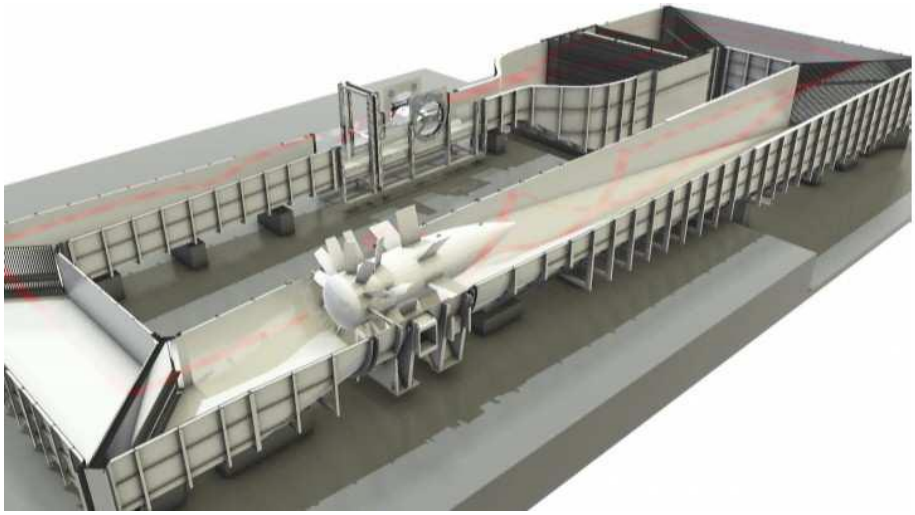

Figure 3.1: The wind tunnel of LM Wind Power A/S (LSWT) (from [35])

a cross section of 1.35m of width and 2.7m of height. The airfoils tested in the wind tunnel span the width and are mounted between two turn tables with the trailing edge 5.2 m downstream of the end of the contraction.
The turbulence intensity in the test section is reported to be $\approx 0.1\%$ for flow speeds of up to 100m/s [35].

3.1.2 NACA0015 Airfoil Model and Instrumentation

The NACA0015 airfoil model has a chord length 0.9m and a span width 1.35m. It is made in aluminum. To install microphones and pressure tabs it was made

in two parts and is divided along the chord line. It is instrumented with a microphone array consisting of 46 Sennheiser microphones type KE 4-211-2. The static pressure distribution is measured separately at 90 pressure holes (0.5mm pinhole diameter). The locations of the microphones and pressure tabs are found in Appendix D. All microphones closer to the trailing edge than x/c=0.9 were installed with a special adapter system. The details of the microphone installation are addressed in section 3.4.
The NACA0015 airfoil mounted in the wind tunnel is shown in figure 3.2. The airfoil is mounted flush with the turn tables to minimize effect from the junction wind tunnel wall/airfoil on the flow. The velocity in the boundary layer is

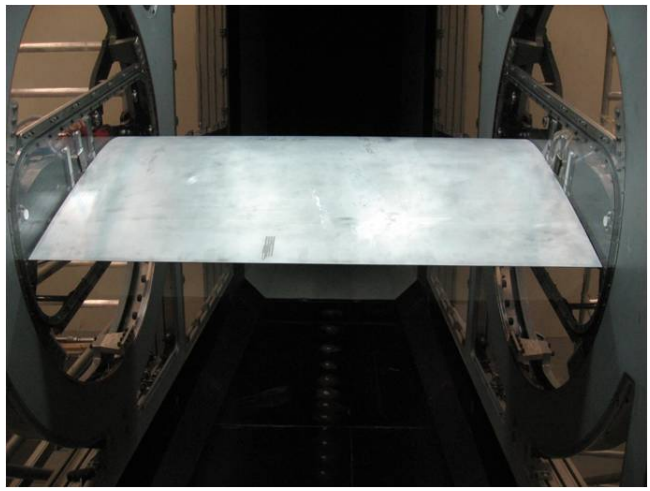

Figure 3.2: The NACA0015 airfoil installed in the test section of the LSWT (view from downstream of the TE)

measured with a hot wire anemometer. Those measurements were performed by Bertagnolio [32]. A traversing system was developed by the author for this experiment, figure 3.3. The traversing system is attached to the turn table and rotates with the airfoil. The traversing direction is normal to the airfoil chord line. The probe movement is controlled by a pinion system driven by a stepper motor type ST5709 from NANOTEC with an angular resolution of 0.45°. The relative positioning accuracy is $\pm 0.1mm$. However, the distance of the first measurement position from the surface of the airfoil has to be measured manually and limits the overall accuracy.

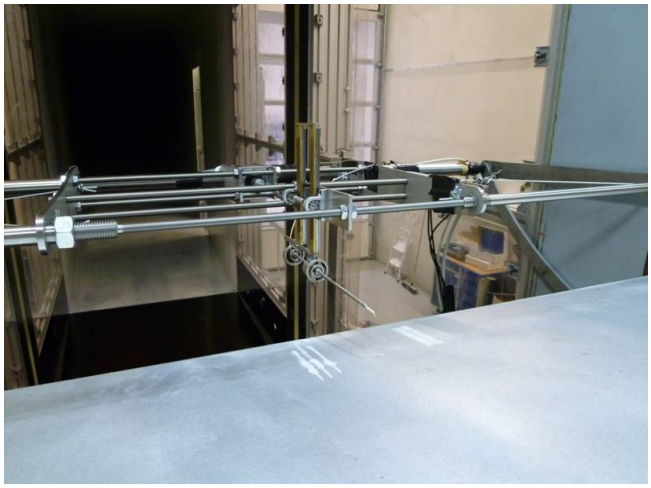

Figure 3.3: The hot wire traverse system in the LSWT

3.1.3 Measurement Conditions for Hot wire Measurements

Bertagnolio [32] investigated 3 different flow speeds: $U_\infty = 30$, 40 and $50 m/s$, as well as four angles of attack: $\alpha = 0°$, 4°, 8° and 12°. The flow temperature was oscillating between approximately $20°C$ and $26°C$ during the experiment. In the present work we investigated his measurements at the chordwise position x/c=0.91 on the suction side of the airfoil. The velocity time series of the hot wire measurement as well as surface pressure microphone recordings were provided. However, there were no recording of the test section static pressure and temperature available to the author. In [32] a mean temperature of $23°C$ is assumed for comparison with calculations. The kinematic viscosity is then equal to $1.58 \cdot 10^{-5} m^2/s$ and the chord based Reynolds correspond to the flow speeds investigated in this experiment are $Re = 1.71M$, $2.28M$ and $2.85M$. Note that there is another data set of surface pressure microphone measurements for Reynolds number $Re = 1.8M$, $3M$ and $3.6M$ from a previous experiment[36] which are also presented in the present work. The test section static pressure and temperature as well as flow speed were recorded and available to the author.

3.2 The Virginia Tech Experiment

3.2.1 The Virginia Tech Stability Wind Tunnel

The Virginia Tech Stability Wind Tunnel is a closed loop subsonic wind tunnel with a 1.83m x 1.83m rectangular removable test section, figure 3.4. The

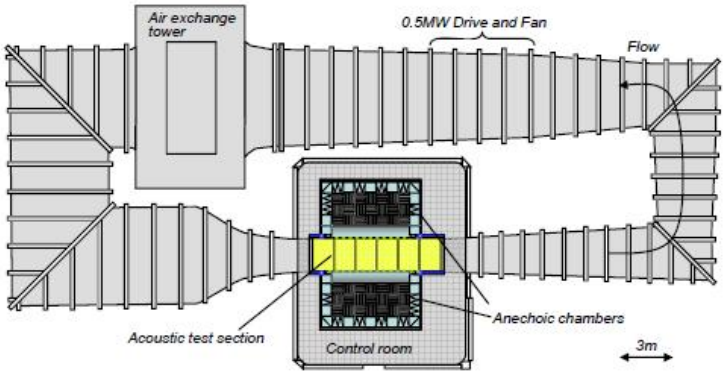

Figure 3.4: Schematic of the Virginia Tech Stability Wind Tunnel in acoustic configuration from [37]

length of the test section is 7.3m. The tunnel is driven by a 0.45MW fan of 5.3m diameter. A flow speed of 75m/s can be reached with empty test section. Downstream of the fan an air exchange tower open to the atmosphere is located. From there the flow is directed into a 5.5m x 5.5m settling chamber. The settling chamber contains 7 screens with an open area ratio of 0.6 and a separation of 0.15m. The flow enters the test section through a nozzle with contraction ratio 9:1 and leaves it through a 3 degree diffuser. All corners of the tunnel are equipped with an array of shaped turning vanes. Turbulence intensities of less than 0.05% were reported from measurements in the aerodynamic test section. Two different test sections are available for the tunnel: a hard wall aerodynamic test section and a acoustic test section with Kevlar walls. In the present experiment the acoustic test section was used. The acoustic test section is surrounded by anechoic chambers, figure 3.5. The Kevlar walls were designed to contain the flow and keep the same aerodynamic performance as with a closed test section while sound waves are transmitted through the walls and can be measured in the anechoic chamber. The details of the acoustic characteristics of the test section can be found in [38].

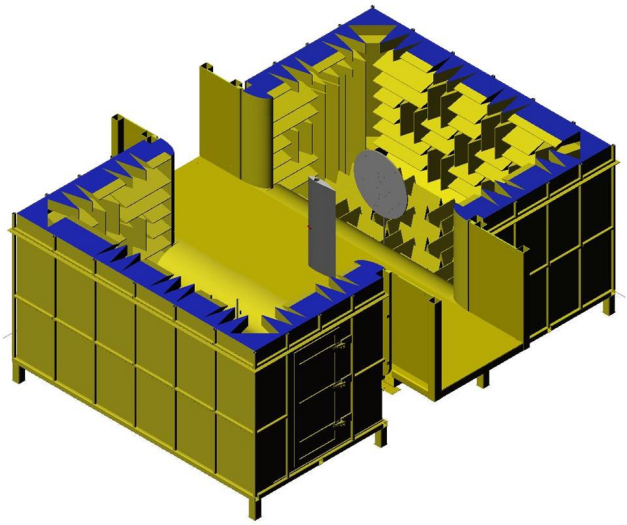

Figure 3.5: The acoustic test section of the VTST

3.2.2 Airfoil Models and Installation

Two airfoil models were tested in the VTST: a NACA64-618 and a modified version called NACA64-618t. The NACA64-618 airfoil is relevant for wind turbine blades in the outer sections, i.e. where most of the noise is generated. The airfoil models had a chord length of 0.6m and a span of 1.82m. They were made from a full aluminum block by RIVAL A/S in Denmark. The machining accuracy of the surface is ±0.1mm measured spanwise from end to end. Each airfoil was equipped with 62 pressure ports (0.5mm pinhole diameter) and 29 surface pressure microphones. The location of the pressure ports and microphones is given in Appendix D. The airfoil models had a lid on the pressure side to install the instrumentation, figure 3.6. Microphones connected to a pinhole close to the trailing edge were installed with an tube adapter (marked red in figure 3.6). The diameter of the pinhole on the surface was 1mm. The other microphones were installed in a cavity on the airfoil surface. The pinhole diameter was 1.3mm. Details of the microphone installation and calibration are given in section 3.4. Figure 3.7 shows the NACA64-618t airfoil mounted in the acoustic test section of the wind tunnel. The airfoil is flush mounted with the wind tunnel walls. The gap between the airfoil and the tunnel wall was bridged with a transition piece made of three layers: aluminum, foam and Teflon. The Teflon layer minimizes friction when sliding over the tunnel walls while changing the angle of attack. To ensure a smooth surface at the junction, a Mylar strip was wrapped around the airfoil and the transition piece and fixed with aluminum tape. At

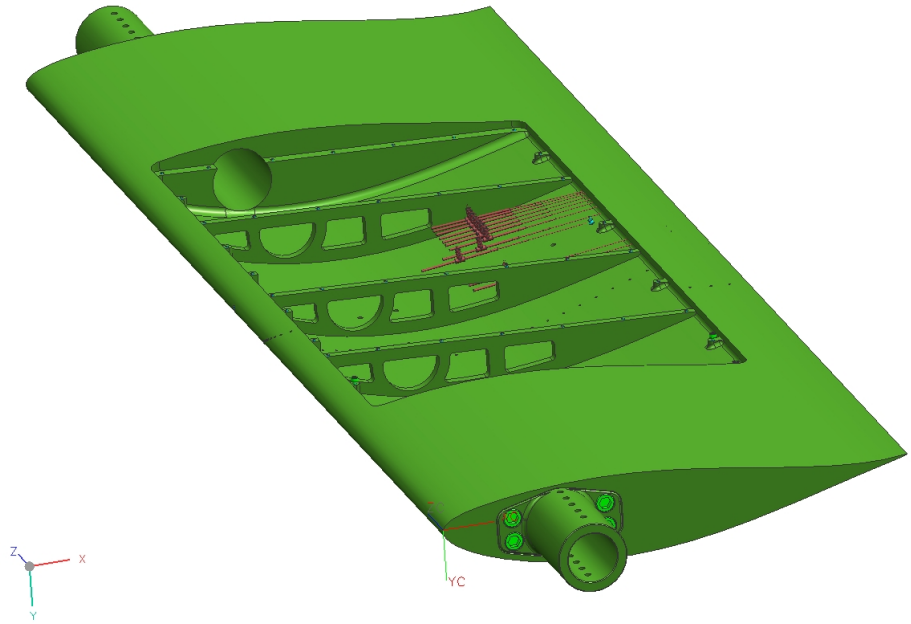

Figure 3.6: CAD rendering of NACA64-618 airfoil with open lid and view on the instrumentation (red: microphone tube adapters)

the junction of airfoil and tunnel walls an approx. 15mm wide Mylar brush was attached to the trailing edge of the airfoil, figure 3.8. These measures reduce spurious noise from the junction.

3.2.3 Instrumentation of the wind tunnel

The static pressure and the flow temperature in the test section are monitored during the experiment. The flow speed in the test section is determined by a measurement of the pressure in the settling chamber and after the contraction. The pressure in the settling chamber is related to the total pressure by calibration and the pressure after the contraction is related to the static pressure by calibration. The contraction and settling chamber pressure are measured with an Esterline 9816/98RK pressure scanner with a range of $\pm 2.5 psi$. The system has a rated accuracy of $\pm 0.05\%$ full scale. The mean pressure distribution on the airfoil was also recorded with the Esterline pressure scanner.
A microphone array consisting of 117 microphones was located in the star-

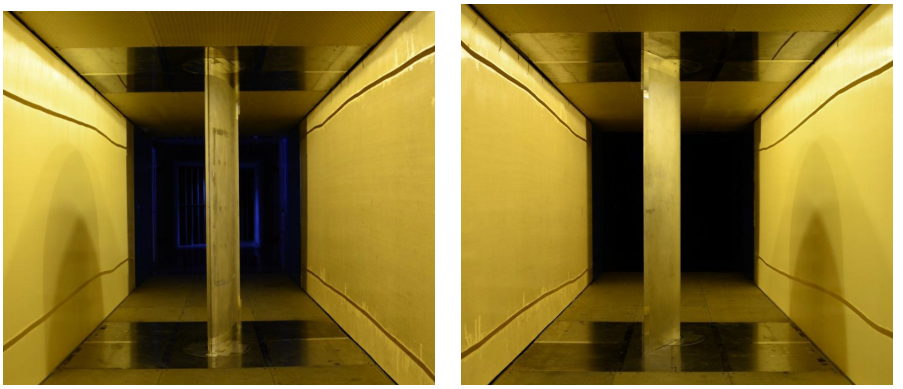

(a) view from upstream (b) view from downstream

Figure 3.7: The NACA64-618t airfoil installed in the acoustic test section

board anechoic chamber, figure 3.9(a). The microphones were arranged in a 9-armed spiral of 13 microphones, figure 3.9(b). The diameter of the array disc is 1.1m. Its exact location relative to the airfoil is given in Appendix B. The microphones used in this array are Panasonic model WM-64PNT Electret microphones. These microphones have a flat frequency response from 20-16000 Hz and a sensitivity of $-44 \pm 3dB$ Re 1V/Pa at 1 kHz. All microphones used in the array were calibrated before being installed in the array and selected to be within $\pm 5°$ phase and $\pm 0.4dB$ amplitude from 500 Hz to 16000 Hz.
In separate measurement runs, a 3 degree of freedom hot wire probe traversing system was inserted in the tunnel, figure 3.10(a). The hot wire probe was traversed in the boundary layer of the airfoils at the chordwise position x/c=0.975, figure 3.10(b). The traversing direction was normal to the surface of the airfoil. The movement of the axes was put into practice by a spindle mechanic driven with a step motor. In the streamwise direction 4 spindle systems were synchronized and 2 in the spanwise direction. There was only a single spindle system for the vertical movement to assure the highest accuracy. The accuracy of the traversing system was very high, but the distance of the first measurement point to the surface had to be measured manually. It introduced some uncertainty in the determination of the absolute position.

3.2.4 Processing of the microphone array data

The microphone array measurements were performed by AVEC, Inc. and the postprocessed data was provided for the author. The postprocessing method

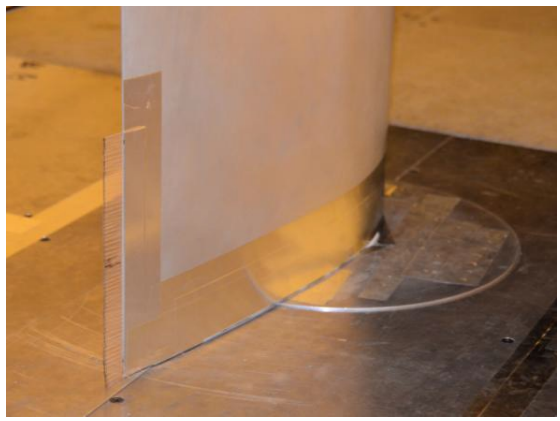

Figure 3.8: Treatment of junction airfoil/tunnel wall

according to the description provided by AVEC, Inc. is outlined in the following.
The raw data obtained from the microphone measurement was processed with frequency domain beamforming to extract the sound pressure level of the TE source from the background noise. The time series were measured with a sampling frequency of 51200Hz during a period of 32 seconds. It was divided into 200 blocks of 8192 samples to compute the averaged cross spectral density matrix. The beamforming algorithm proposed by [39] was used, which is different compared to classical beamforming in two points:

1. The diagonal of the cross spectral density matrix is removed

2. Refraction affects due to the flow in the wind tunnel test section are accounted for by a ray tracing method

To improve the beamforming maps the microphone array was carefully calibrated after installation.
The beamforming maps are integrated to obtain the far field sound pressure spectrum. The integration area was chosen to allow a separation of the TE source from spurious noise caused by the airfoil/wind tunnel junction. It extends 0.6m of the airfoil span and is centered in the center of the test section. A detailed map is found in Appendix B. The integral is normalized in a way that the spectrum represents the sound pressure level which a monopole point source at the center of the integration volume causes at the center of the microphone array. A method proposed by [39] is used to achieve this. The integral level is

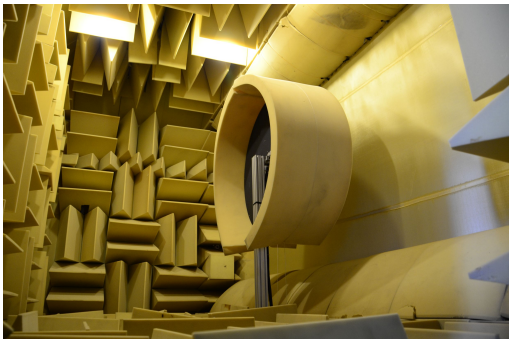

(a) Microphone Array in Starboard Anechoic Chamber

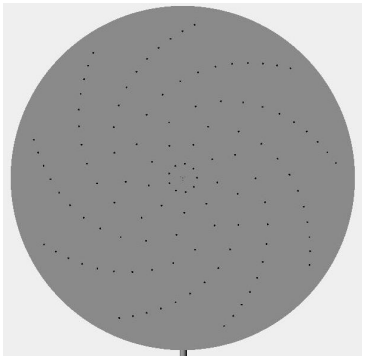

(b) CAD Rendering of the Microphone Array

Figure 3.9: Microphone Array of AVEC, Inc.

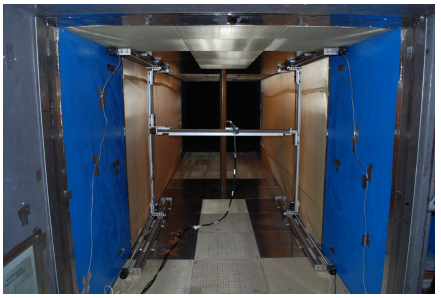

(a) View from Downstream

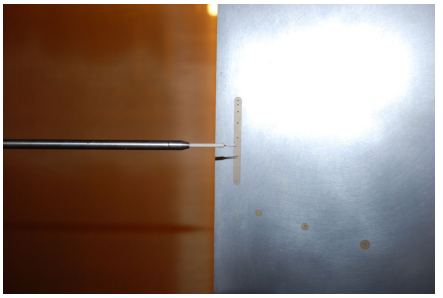

(b) Detailed View on Probe

Figure 3.10: 3 Degree of Freedom Hot Wire Traversing System

obtained as

$$I_{norm}\left(V,f\right)=\frac{\sum_n b_n\left(\vec{x}_n,f\right)}{\xi\left(f\right)},\qquad b_n > b_{max}-\delta \tag{3.1}$$

$b_n(\vec{x}_n, f)$ is the beamforming output at a discrete point $\vec{x}_n$, b_{max} is the maximum value in the beamforming map. δ is a threshold. The function of this threshold is to reject the contributions of the sidelobes of the array to the integral by ignoring sound pressure level which are below the threshold. The value of the threshold depends on the relative level between the mainlobe and the strongest sidelobe. Here a threshold of 5dB was used.
$\xi(f)$ is a normalization factor. It relates the integration output to the one obtained from beamforming a single monopole point source at the center of the

scanning. The normalization factor is given by

$$\xi(f) = \int_V p_0(\vec{x}, \vec{x}_0)\, d\vec{x}, \qquad p_0 > p_{max} - \delta \tag{3.2}$$

where $\vec{x}_0$ is the coordinates of the center of the integration volume. $p_0(\vec{x}, \vec{x}_0)$ is the point spread function, defined as

$$p_0(\vec{x}, \vec{x}_0) = \left| \vec{w}^{\dagger}(\vec{x}) \frac{\vec{C}(\vec{x}_0)}{\left\| \vec{C}(\vec{x}_0) \right\|} \right|^2 . \tag{3.3}$$

$\vec{w}(\vec{x})$ is the microphone weight vector, also referred to as steering vector and $\vec{C}(\vec{x_0})$ is the array propagation vector. The components of the array propagation vector are chosen as

$$C_n(\vec{x}_0) = \frac{e^{-i\omega\sigma(\vec{x}_n, \vec{x}_0)}}{D(\vec{x}_n, \vec{x}_0)} \tag{3.4}$$

where $\sigma(\vec{x}_n, \vec{x}_0)$ is the acoustic travel time from the source position $\vec{x}_0$ to the position of the microphone n $\vec{x}_n$ and D is a magnitude factor. With the choice $D(\vec{x}_n, \vec{x}_0) = 4\pi c_0 \sigma(\vec{x}_n, \vec{x}_0)$ eq. 3.4 describes a monopole radiation pattern and the integral I_{norm} defined in eq. 3.1 is equivalent to the sound pressure level of a monopole point source at the center of the integration volume measured at the center of the microphone array.
In practice it is better to chose $D(\vec{x}_n, \vec{x}_0) = 1$, because with the first definition more weight is put on microphones further away from the source where the signal to noise ratio is worse. When choosing $D(\vec{x}_n, \vec{x}_0) = 1$, the integral I_{norm} represents the average of sound pressure level of a monopole point source at the center of the integration volume measured at the position of the 117 microphones.
The integrated sound pressure spectrum is corrected for losses due to the transmission of sound through the Kevlar windows and the boundary layer built up on the Kevlar wall. The correction for both effects is a frequency dependent factor given in [38]. Note that the beamforming maps are not corrected for the transmission losses.

3.2.5 Measurement Matrix

In the VTST the flow temperature is not controlled and it was subjected to significant changes during the duration of the experiment. Because of this temperature changes it is not always possible to keep the same flow speed and Reynolds number for two different runs. For an acoustic comparison of two airfoils at a low Mach number it is more important to keep the flow speed constant

than the Reynolds number. Therefore the runs are characterized by the flow speed which was held constant. We decided to test at three different flow speeds: $U_\infty = 30$, 45 and $60m/s$. The chord based Reynolds numbers corresponding to these velocities are $Re = 1.0M \pm 4\%$, $Re = 1.5M \pm 4\%$ and $Re = 1.9M \pm 4\%$. The deviation of $\pm 4\%$ is due to temperature changes. The lowest flow temperature measured during the test was $31°C$ and the highest 44°. During a run the temperature was rather constant, but in some runs at the highest flow speed $U_\infty = 60m/s$ a temperature drift of $+5°C$ was monitored.
Four different types of measurements were conducted: the mean pressure distribution on the airfoil (AMP), the surface pressure fluctuations with the microphones (SPM), acoustic far field sound pressure measurements with the microphone array (FFA) and velocity measurements in the boundary layer with a hot wire anemometer (HBL). The AMP, SPM and FFA measurements were conducted in a AoA range of $-10° < \alpha_T < 16°$. α_T denotes the turn table AoA and it has to be corrected for wind tunnel effects. The correction is in the range of $0° < |\Delta\alpha| < 1.5°$ and it is positive for positive lift coefficients and vice versa. Hence the range of effective AoAs is reduced. AMP and SPM measurements were conducted in steps of $\Delta\alpha_T = 1°$, FFA measurements in steps of $\Delta\alpha_T = 2°$. The traversing of the boundary layer with the hot wire probe was more time consuming and the number of AoAs had to be limited. We tested four different turn table AoAs: $\alpha_T = 0°$, 4°, 6° and 8°. The SPM and FFA or the SPM and HBL measurements were synchronized.
Besides the clean airfoil configuration we tested also both airfoils with serated trip tape at a flow speed of $U_\infty = 45m/s$. The trip tape (type: Glasfaser-Flugzeug-Service GmbH 3D Turbulator Tape) was 0.31mm thick, 12mm wide and had an angle of 60°. It was fixed to the airfoil at the cordwise position x/c=0.05 on the suction side and x/c=0.1 on the pressure side.
All measurements conducted during the test are summarized in table 3.1.

run	airfoil type	U_∞ [m/s]	trip ss/ps	AoA seq. [°]	measurement type
3	NACA64-618	60	n/n	-10:1:16	AMP, SPM, FFA
4	NACA64-618	45	n/n	-10:1:16	AMP, SPM, FFA
5	NACA64-618	30	n/n	-10:1:16	AMP, SPM, FFA
6	NACA64-618	45	0.05/0.1	-10:1:16	AMP, SPM, FFA
7	NACA64-618	45	0.05/0.1	0, 4, 6 , 8	AMP, SPM, HBL
8	NACA64-618	45	0.05/0.1	6, 8	AMP, SPM, HBL
9	NACA64-618	45	n/n	0, 4, 6, 8	AMP, SPM, HBL
11	NACA64-618	60	n/n	0, 4, 6, 8	AMP, SPM, HBL
12	NACA64-618	30	n/n	0, 4, 8	AMP, SPM, HBL
13	NACA64-618t	45	n/n	0, 4, 6, 8	AMP, SPM, HBL
14	NACA64-618t	60	n/n	0, 4, 6, 8	AMP, SPM, HBL
15	NACA64-618t	30	n/n	8	AMP, SPM, HBL
16	NACA64-618t	45	0.05/n	0, 4, 6, 8	AMP, SPM, HBL
17	NACA64-618t	45	0.05/0.1	-10:1:16:-2:-10	AMP, SPM, FFA
18	NACA64-618t	45	0.05/n	0:2:10	AMP, SPM, FFA
19	NACA64-618t	45	n/n	-10:1:16:-2:-10	AMP, SPM, FFA
20	NACA64-618t	60	n/n	-10:1:16	AMP, SPM, FFA
21	NACA64-618t	30	n/n	-10:1:16	AMP, SPM, FFA
22	NACA64-618t	45	n/n	0:2:8, 14	AMP, SPM, FFA

Table 3.1: Measurement Matrix of the VT Experiment. The AoA sequence is valid for the AMP, SPM and HBL measurements. For the FFA measurements the AoA sequence was always $-10° : 2° : 16°$.

3.3 Hot Wire Anemometry

The aim of the hot wire measurements is to provide a database of one point velocity spectral density with high frequency resolution in the boundary layer of the airfoil under investigation. For an experimental tuning of the Mann model all 3 directional components of the velocity are desired as well as the cross spectral density of the longitudinal and vertical velocity component. For surface pressure modeling only the vertical velocity component is of importance.
The hot wire measurements in the LM experiment were carried out by Bertagnolio [32] and the details about the data conversion are found there. The author was provided by the velocity time series of this experiment. The equipment used was the same as in the VT experiment and is described below.

3.3.1 Hot Wire Equipment and Data Acquistion

We used a Dantec 55P61 x-wire sensor for the measurements. This sensor measures two perpendicular velocity components at a time. It was preferred over the triple wire sensor Dantec 55P91, because the geometric extend of the 55P61 is much smaller than the one of the 55P91. In a boundary layer the flow conditions change rapidly with position and a small sensor geometry is important to avoid spatial averaging.
The probe is balanced and operated using the Dantec StreamWare Software and a Dantec StreamLine Main Frame 90N10 with a Dantec StreamWare Bridge Module 90C10. Data acquisition is controlled by the StreamWare Software and a A/D card from National Instruments type NI PCI6143. It has 8 differential analog inputs with a resolution of 16bit and allows a maximum sample rate of 250000 samples per second. In the Virginia Tech experiment the sampling rate was set to 100kHz and a low pass filter with a cut-off frequency of 30kHz was applied to avoid aliasing. During each measurement a total of $2^{20} = 1048576$ samples were collected.
In the LM experiment Bertagnolio[32] used a sampling frequency of 25kHz and a low pass filter with a cut-off frequency of 10kHz.

3.3.2 Data Processing

The raw data of the measurement was exported from the StreamWare Software and an in-house MATLAB code was developed for the data processing. The details of the code are outlined below. The data reduction process is taken from [40] and consists of the following steps:

1. Temperature correction of the raw voltage.
2. Conversion of voltage into velocity.
3. Transformation of the calibration velocity into velocity in probe coordinate system.

Temperature Correction

A reference temperature T_{ref} and the overheat ratio a have to be determined when the bridge resistances are set. They control the wire operation temperature T_W. The reference temperature T_{ref} should correspond to the temperature during the measurement T. If the temperature during measurement T changes, the voltage output of the hot wire probe has to be corrected by the relation

$$E_c = E \cdot \left(\frac{T_W - T_{ref}}{T_W - T} \right)^M \tag{3.5}$$

with the exponent M defined as

$$M = \begin{cases} \frac{1+m}{2} \; if \; T > T_{ref} \\ \frac{1-m}{2} \; if \; T < T_{ref}. \end{cases} \tag{3.6}$$

m is the temperature loading factor. A temperature loading factor $m \neq 0$ represents an empirical refinement of eq. 3.5. The StreamWare manual [40] proposes a value of $m = 0.2$ for air flow. This value is used in the present work. The temperature correction, eq. 3.5 is only valid if the difference between the reference temperature T_{ref} and the temperature during measurement T is small. As a rule of thumb it should be less than $\pm 5°C$.

Conversion of Voltage to Velocity

The relation of the calibration velocity and the voltage in the wire is given by King's law [41]

$$E_c^2 = A + BU_{cal}^n \tag{3.7}$$

where A, B and n are calibration constants. King's law is exact in the limiting of an infinite wire length. The coefficient n takes the value of 0.5 in this case. For a real hot wire probe, the coefficients should be obtained by velocity calibration. The coefficient n should be close to 0.5, say $n = 0.5 \pm 0.2$.

Alternatively, a polynomial of order N can be used for the conversion of the voltage into velocity

$$U_{cal} = \sum_{n=0}^{N} C_n E_c^n \tag{3.8}$$

where the polynomial coefficients C_n are obtained by velocity calibration. The polynomial conversion law, eq. 3.8 is purely empirical and has no physical relevance. It should only be used in the range of the maximum and minimum velocity measured during calibration. King's law can be used for a wider range. The polynomial should only be used if it gives significantly better results compared to the calibration velocity than King's law.

Rotation of the Velocity into Probe Coordinate System

This step depends on the probe geometry. For the Dantec 55P61 x-wire probe the relation between the calibration velocity $U_{cal1,2}$ and the velocity in wire coordinate system $U_{w1,2}$ is [42]

$$\begin{aligned} k_1^2 U_{w1}^2 + U_{w2}^2 &= \frac{1}{2}\left(1 + k_1^2\right) U_{cal1}^2 \\ U_{w1}^2 + k_2^2 U_{w2}^2 &= \frac{1}{2}\left(1 + k_2^2\right) U_{cal2}^2 \end{aligned} \tag{3.9}$$

where $k_{1,2}$ are the yaw coefficients of wire 1 and 2. The yaw coefficient appear in eq. 3.9, because the wire voltage is sensitive to flow perpendicular to the wire and to flow parallel to the wire. The sensitivity of the wire voltage towards flow which is parallel to the wire is only a small fraction of the sensitivity towards perpendicular flow. The ratio is expressed by the yaw coefficients. For very accurate measurements the yaw coefficients can be determined by directional calibration. In the present work we used a value of $k_1^2 = k_2^2 = 0.04$ as proposed by the manufacturer.
The solution to eq. 3.9 is

$$\begin{aligned} U_{w1} &= \frac{\sqrt{2}}{2}\sqrt{\frac{1}{k_1^2 k_2^2 - 1}\left[(1 + k_1^2) k_2^2 U_{cal1}^2 - (1 + k_2^2) U_{cal2}^2\right]} \\ U_{w2} &= \frac{\sqrt{2}}{2}\sqrt{\frac{1}{k_1^2 k_2^2 - 1}\left[-(1 + k_1^2) U_{cal1}^2 + (1 + k_2^2) k_1^2 U_{cal2}^2\right]} \end{aligned} \tag{3.10}$$

Finally, the velocity in wire coordinate system $U_{w1,2}$ have to be transformed into velocity in probe coordinate system $U_{p1,2}$. The rotation is described by

$$\begin{aligned} U_{p1} &= \frac{\sqrt{2}}{2}U_{w1} + \frac{\sqrt{2}}{2}U_{w2} \\ U_{p2} &= \frac{\sqrt{2}}{2}U_{w1} - \frac{\sqrt{2}}{2}U_{w2} \end{aligned} \tag{3.11}$$

The component U_{p1} is parallel to the probe stem and points downstream. The component U_{p2} is perpendicular to the probe stem.

3.3.3 Calibration

The hot wire probe was calibrated in the wind tunnel while the airfoil was installed. We searched for a position where the velocity is as close as possible in magnitude and direction to the free stream velocity U_∞. William Devenport simulated the whole wind tunnel setup for an airfoil which has similar characteristics as the NACA64-618 and NACA64-618t airfoil with a panel method. The method takes the deflection and porosity of the Kevlar walls into account. Details of the airfoil for which the simulation was performed are not available due to proprietary reasons. It was found that the airfoil influences the flow the least when it is rotated to its zero lift angle. The velocity distribution and direction in the TE plane for the airfoil at zero lift angle is displayed in figure 3.11.
Based on this velocity distribution, we chose the position $x_2 = -0.5m$ (on the pressure side of the airfoil) in the TE plane for the calibration and adjusted the airfoil to its zero lift angle during the calibration. The velocity is almost equal to the free stream velocity and the yaw angle is less than $0.75°$. A systematic error in the order of $\approx 1\%$ of the velocity magnitude and $\approx 1°$ in flow angle is introduced by this calibration method. There is an uncertainty in the computation, because it was performed for a different airfoil. Consequently, we didn't correct for the systematic error according to the result of the panel method.
The temperature changes of the flow in the VTST during experiment were in the order of $14°C$. As mentioned above, the temperature correction method, eq. 3.5, can only be used in the range $T_{ref} \pm 5°C$. When this range was exceeded we had to reset the reference temperature T_{ref} and recalibrate the probe. This led to a total of 6 different calibration sets used during the experiment. During a calibration run, the free stream velocity U_∞ was linearly increased in steps of $5m/s$. The lowest calibration velocity was $U_\infty = 20m/s$ and the highest $U_\infty = 60m/s$. The velocity was monitored by the VTST tunnel measurement system (via contraction and settling chamber pressure) and the flow temperature by the temperature probe of the streamline system. The calibration curve

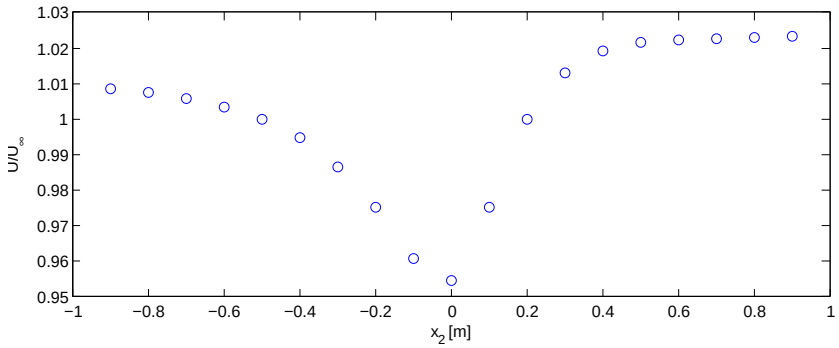

(a) Velocity U/U_∞

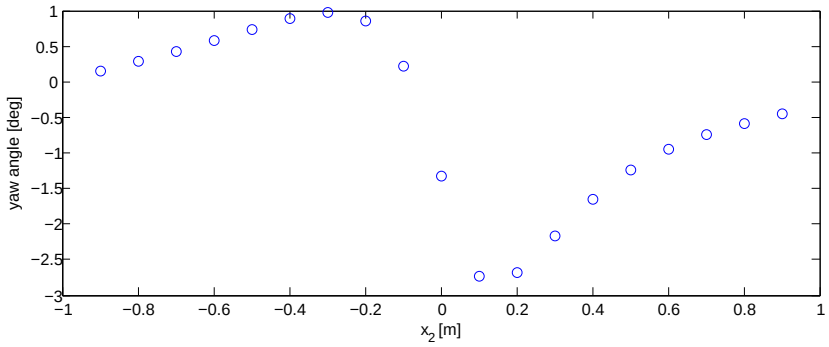

(b) yaw angle

Figure 3.11: The velocity distribution in the VTST tunnel with a thin and cambered airfoil at zero lift angle in the TE plane by panel method (origin of x_2: tunnel center line)

and the relative error are depicted in appendix C.
We chose to use the King's law calibration curve, because the velocity range of the calibration could be exceeded by the fluctuating velocities in the boundary layer. The polynomial is only valid in this range. The uncertainty introduced by using King's law is not much bigger than the one introduced by the polynomial.

3.3.4 Frequency Limitation

We had to use a BNC cable with 12m length to connect the StreamLine bridge module with the probe instead of the recommended 4m length. This introduced an electrical resonance in the circuit and influenced the data for frequen-

cies higher than $\approx 5800Hz$. The spectral plots presented in this work will be marked at this limiting frequency and data at higher frequencies should not be considered.

3.4 Surface Pressure Measurements

3.4.1 Pinhole Microphones

The fluctuating pressure on an airfoil surface is very sensitive to small changes of the surface. Microphones have to be mounted in way which creates the smallest possible disturbance of the surface. This was realized by mounting microphones inside the airfoil and connecting them via a pinhole with the surface. This configuration has the additional advantage that the sensitive area of the sensor on the surface is minimized and its spacial extend is smaller than a typical eddy size at the highest frequency of interest. If the typical eddy size becomes smaller than the sensitive area of the sensor, the signal is attenuated. Corcos [43] is the earliest work trying to resolve this problem and gives a semi-empirical correction for the attenuation of the signal. However, if the surface pressure fluctuations should be determined with low uncertainty, it should not be necessary to apply this correction.
The microphones used in the present experiments were back-electret condenser microphones of Sennheiser type KE4-211-2. A microphone housing which can be integrated in the airfoil surface was developed by [25]. The geometry of this housing and the Sennheiser microphone is given figure 3.12. The design goal

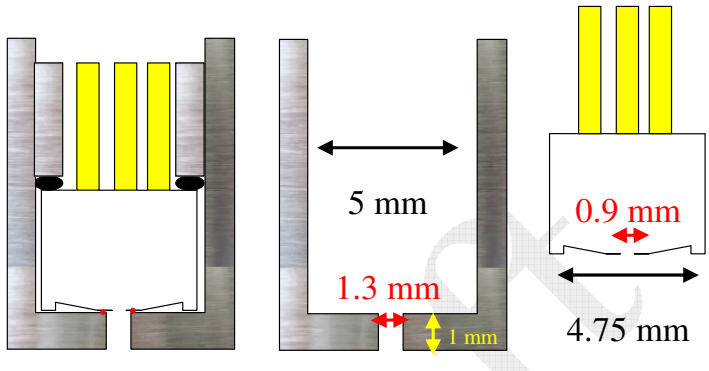

Figure 3.12: The Sennheiser KE4-211-2 condenser microphone and its housing (from [44])

for the housing was to have the Helmholtz eigen frequency of the air in the cavity between pinhole opening and microphone above 10kHz. However, the Helmholtz eigen frequency shifted strongly with small changes in the housing geometry and/or the mounting torque. For accurate measurements the pinhole microphone have to be calibrated when mounted, as outlined below. In the Virginia tech experiment the microphones were directly mounted in the airfoil model without using the housing, if the space inside the airfoil allowed. They were calibrated individually when mounted.
The mounting space close to the trailing edge of the airfoil models was very small. To access this locations the microphones had to be connected to the pinhole via a tubing system. The first generation of the microphone adapter with tubing system is illustrated in figure 3.13. It was used in the NACA0015 airfoil

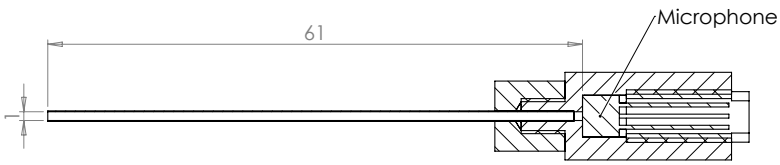

Figure 3.13: The first generation of the microphone adapter with tubing system

model. The reflection in the tubing system created an interference pattern in the transfer function between the pressure at the pinhole and the pressure at the microphone.
A second generation of the tubing system which did not suffer from the flaws was developed. It was copied from the design of [45]. A CAD design is found in Appendix E. This microphone adapter is used in the NACA64-618 and the NACA64-618t model. The main change of the second design compared to the first is the continuation of the tubing system with a 2 meter long plastic tube with internal radius of 3mm downstream of the microphone position. Interference patterns are less strong, because the reflected sound wave is attenuated.

3.4.2 Analytical modeling of the pinhole microphones

An analytic model to describe the transfer function between the pressure at the pinhole and at the microphone location was developed.
The analytical model corresponding to the microphones mounted directly in the airfoil and mounted in the housing of figure 3.12 is the one of a Helmholtz resonator. The transfer function between microphone and source pressure of the

Helmholtz resonator model is given by [46]

$$\frac{\hat{p}_M}{\hat{p}_S} = \frac{1}{1 - (\omega/\omega_0)^2 + i2\xi\omega/\omega_0} \tag{3.12}$$

where ω_0 is the resonance angular frequency and ξ is the damping coefficient. Both have to be determined experimentally. Figure 3.14 shows the analytical transfer function with $f_0 = 12.4$kHz and $\xi = 0.345$ in comparison with the measurements made by Brüel & Kjær Sound and Vibration A/S in laboratory conditions [44]. The curves coalesce up to a frequency well above 10kHz.

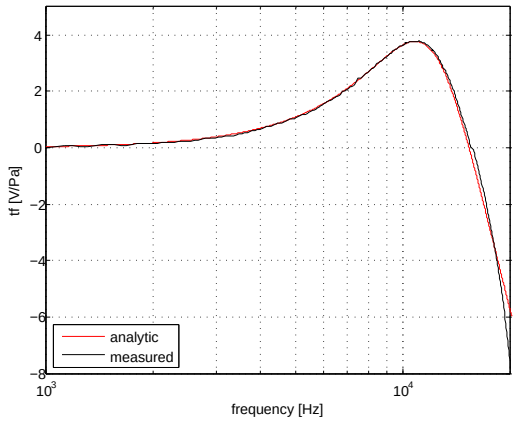

Figure 3.14: Measured and Computed transfer Function for Microphone in Housing

For the tube adapters analytic modeling is more complicated. We used the analytic model for sound transmission in coupled pipes of [47]. This model assumes that frequencies are sufficiently low that sound waves propagating in the tube system are plain. The tube system is then divided into subsystems which represent a tube of constant radius. The analytical model for such a subsystem is given by eq. 4.1 and 4.2a-d of [47] and are repeated here. The transmission of the subsystem is given by the four-pole matrix

$$\begin{pmatrix} \hat{p}_i \\ \hat{q}_i \end{pmatrix} = \begin{pmatrix} A & B \\ C & D \end{pmatrix} \begin{pmatrix} \hat{p}_o \\ \hat{q}_o \end{pmatrix} \tag{3.13}$$

where $\hat{p}_i$, $\hat{p}_o$, $\hat{q}_i$ and $\hat{q}_o$ are the sound pressures and volume velocities at the input and at the output. The components of the transmission matrix are found

by

$$A = \left.\frac{\hat{p}_i}{\hat{p}_o}\right|_{\hat{q}_o=0} \tag{3.14}$$

$$B = \left.\frac{\hat{p}_i}{\hat{q}_o}\right|_{\hat{p}_o=0} \tag{3.15}$$

$$C = \left.\frac{\hat{q}_i}{\hat{p}_o}\right|_{\hat{q}_o=0} \tag{3.16}$$

$$D = \left.\frac{\hat{q}_i}{\hat{q}_o}\right|_{\hat{p}_o=0}. \tag{3.17}$$

However, the original formulation of [47] does not include viscosity effects in the tube system and a new model was formulated which accounts for viscosity effects. A sketch of a subsection is displayed in figure 3.15. The perturbation

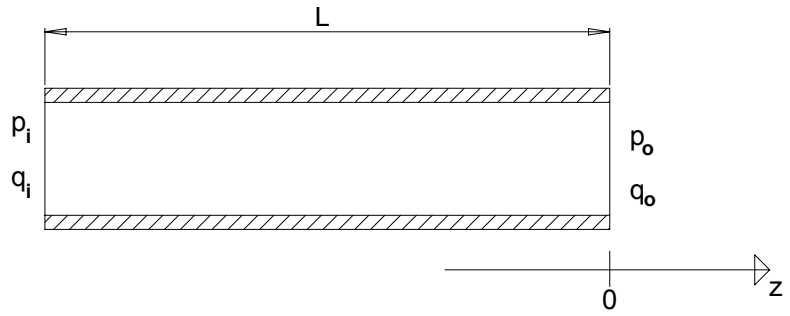

Figure 3.15: Schematic of a subsystem of the remote microphone tubing

pressure in the tube can then be written as

$$p' = \hat{p}\exp(i\omega t) \tag{3.18}$$

$$\hat{p} = p_+ \exp(-ikz) + p_- \exp(ikz) \tag{3.19}$$

where

$$k = k_0 + \alpha(1+i) \tag{3.20}$$

with $k_0 = \omega/c_0$ is a complex wave number [48] which accounts for damping and phase shift due to viscosity effects in the tube. The damping coefficient α is defined as [48]

$$\alpha = \frac{1}{\sqrt{2}}\left(\frac{k_0\mu}{\rho_0 c_0}\right)^{\frac{1}{2}}\left(1+\frac{\gamma-1}{Pr^{\frac{1}{2}}}\right)\frac{1}{r} \tag{3.21}$$

where r is the inner radius of the tube. The volume velocity becomes

$$\hat{q}(z) = \frac{S}{\rho_0 c_0}\frac{k}{k_0}\left(p_+ \exp(-ikz) - p_- \exp(ikz)\right) \tag{3.22}$$

with S the cross sectional area of the tube (in the 1-dimensional case the volume velocity is simply the product of the velocity in z-direction and the cross sectional area). The transmission matrix of the subsystem is then found as

$$\mathbf{T}_{sub} = \begin{pmatrix} \frac{1}{2}\left(e^{-ikL} + e^{ikL}\right) & \frac{\rho_0 c_0}{2S}\frac{k}{k_0}\left(e^{-ikL} - e^{ikL}\right) \\ \frac{S}{2\rho_0 c_0}\frac{k}{k_0}\left(e^{-ikL} - e^{ikL}\right) & \frac{1}{2}\left(e^{-ikL} + e^{ikL}\right) \end{pmatrix} \tag{3.23}$$

With this result the transfer function between microphone and source pressure of the tube adapters can be found by following the methodology of [47]. We will first address the more complex tube adapter of the second generation. It is schematically displayed in figure 3.16. Note that the installation cavity of the

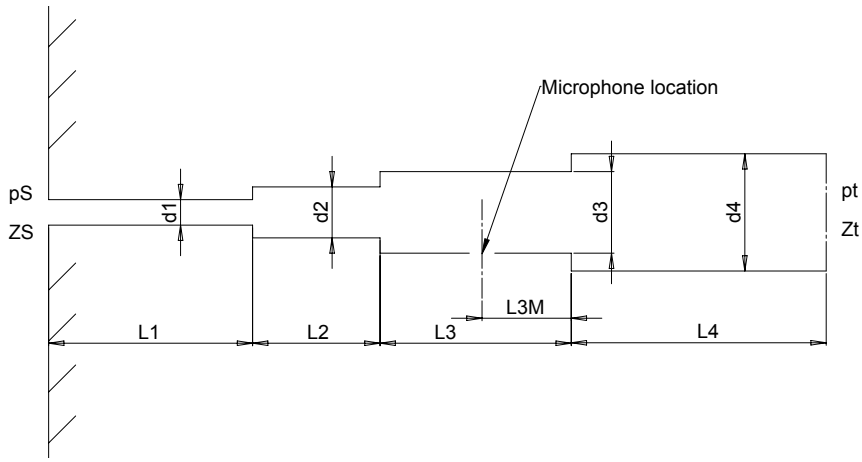

Figure 3.16: Schematic of the second generation of the microphone adapter with tubing system

microphone is not modeled! (It was actually tried, but this model gave the best results compared to measurements)
First, the transmission matrix for the whole tube system from entrance to termination as well as the transmission matrix from the position of the microphone to the termination of the tube system has to be evaluated. The one for the whole system is given by

$$\begin{aligned} \mathbf{T} &= \begin{pmatrix} A & B \\ C & D \end{pmatrix} \\ &= \prod_{n=1}^{4} \begin{pmatrix} \frac{1}{2}\left(e^{-ik_n L_n} + e^{ik_n L_n}\right) & \frac{\rho_0 c_0}{2S_n}\frac{k_n}{k_0}\left(e^{-ik_n L_n} - e^{ik_n L_n}\right) \\ \frac{S_n}{2\rho_0 c_0}\frac{k_n}{k_0}\left(e^{-ik_n L_n} - e^{ik_n L_n}\right) & \frac{1}{2}\left(e^{-ik_n L_n} + e^{ik_n L_n}\right) \end{pmatrix} \end{aligned} \tag{3.24}$$

and the transmission matrix from microphone position to tube termination by

$$\begin{aligned}
\mathbf{T}_{MT} &= \begin{pmatrix} A_{MT} & B_{MT} \\ C_{MT} & D_{MT} \end{pmatrix} \qquad (3.25)\\
&= \begin{pmatrix} \frac{1}{2}\left(e^{-ik_3L_{3M}} + e^{ik_3L_{3M}}\right) & \frac{\rho_0 c_0}{2S_3}\frac{k_3}{k_0}\left(e^{-ik_3L_{3M}} - e^{ik_3L_{3M}}\right) \\ \frac{S_3}{2\rho_0 c_0}\frac{k_3}{k_0}\left(e^{-ik_3L_{3M}} - e^{ik_3L_{3M}}\right) & \frac{1}{2}\left(e^{-ik_3L_{3M}} + e^{ik_3L_{3M}}\right) \end{pmatrix} \\
&\cdot \begin{pmatrix} \frac{1}{2}\left(e^{-ik_4L_4} + e^{ik_4L_4}\right) & \frac{\rho_0 c_0}{2S_4}\frac{k_4}{k_0}\left(e^{-ik_4L_4} - e^{ik_4L_4}\right) \\ \frac{S_4}{2\rho_0 c_0}\frac{k_4}{k_0}\left(e^{-ik_4L_4} - e^{ik_4L_4}\right) & \frac{1}{2}\left(e^{-ik_4L_4} + e^{ik_4L_4}\right) \end{pmatrix}.
\end{aligned}$$

Knowing the transmission matrices the ratio between the pressure at the position of the microphone and the source pressure can be given as [47]

$$\frac{\hat{p}_M}{\hat{p}_S} = \frac{A_{MT}Z_t + B_{MT}}{AZ_t + B + Z_S\left(CZ_t + D\right)}. \qquad (3.26)$$

Z_t is the termination impedance (ratio of sound pressure and volume velocity). For a closed tube with the reflexion factor R_a at the end it becomes [47]

$$Z_t = \frac{\rho_0 c_0}{S_4}\frac{1 + R_a}{1 - R_a} \qquad (3.27)$$

The reflexion factor R_a is unknown and has to be determined experimentally. Z_S is the source impedance. It is modeled by the formula of the radiation impedance of a circular piston in an infinite baffle from [47]

$$Z_S = \frac{\rho_0 c_0}{S_1}\left(1 - \frac{J_1(2k_0r_1)}{k_0r_1} + i\frac{H_1(2k_0r_1)}{k_0r_1}\right) \qquad (3.28)$$

where J_1 is the Bessel function of first kind and H_1 is the Struve function of first kind. This simplified analytical solution describes the actual setup very closely, even though the pinholes were placed close to the trailing edge. Note that this expression for the source impedance gives very similar results as the expression proposed by [45].

The tube adapter of the first generation is depicted in figure 3.17. Due to the geometry of the Sennheiser microphone a very shallow cavity appears in front of it when mounted in the adapter. It is very important to include this cavity in the analytical model of the transfer function between microphone and source pressure. The transmission matrix for the system depicted in figure 3.17 is

$$\begin{aligned}
\mathbf{T}_{g1} &= \begin{pmatrix} A_{g1} & B_{g1} \\ C_{g1} & D_{g1} \end{pmatrix} \qquad (3.29)\\
&= \begin{pmatrix} \frac{1}{2}\left(e^{-ik_tL_t} + e^{ik_tL_t}\right) & \frac{\rho_0 c_0}{2S_t}\frac{k_t}{k_0}\left(e^{-ik_tL_t} - e^{ik_tL_t}\right) \\ \frac{S_t}{2\rho_0 c_0}\frac{k_t}{k_0}\left(e^{-ik_tL_t} - e^{ik_tL_t}\right) & \frac{1}{2}\left(e^{-ik_tL_t} + e^{ik_tL_t}\right) \end{pmatrix} \\
&\cdot \begin{pmatrix} \frac{1}{2}\left(e^{-ik_cL_c} + e^{ik_cL_c}\right) & \frac{\rho_0 c_0}{2S_c}\frac{k_c}{k_0}\left(e^{-ik_cL_c} - e^{ik_cL_c}\right) \\ \frac{S_c}{2\rho_0 c_0}\frac{k_c}{k_0}\left(e^{-ik_cL_c} - e^{ik_cL_c}\right) & \frac{1}{2}\left(e^{-ik_cL_c} + e^{ik_cL_c}\right) \end{pmatrix}
\end{aligned}$$

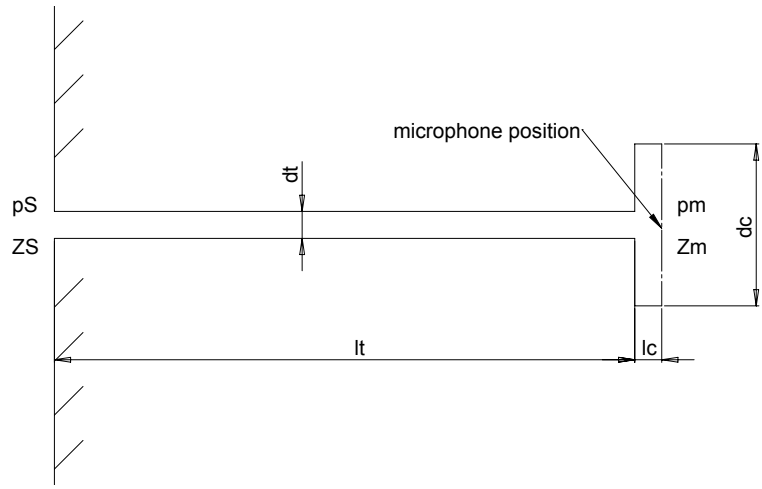

Figure 3.17: Schematic of the microphone adapter with tubing system of the first generation

and the transfer function between microphone and source pressure becomes

$$\frac{\hat{p}_M}{\hat{p}_S} = \frac{Z_m}{A_{g1}Z_m + B_{g1} + Z_S\left(C_{g1}Z_m + D_{g1}\right)}. \tag{3.30}$$

The source impedance Z_S is again given by eq. 3.28 and for the impedance at the microphone capsule Z_m eq. 3.27 is used.

3.4.3 Calibration of the surface Pressure Microphones

The calibration method for the NACA0015 is described in [36]. The calibration function we found by this method was contradictory to the one found by [44]. The calibration setup of [44] is considered more accurate, because the signal to noise ratio is improved by several orders of magnitude compared to the old one. Hence, it was decided not to use the calibration functions found by [36] for the reduction of the surface pressure PSD on the NACA0015 airfoil presented in this work. Instead we used the analytical transfer function, eq. 3.12 with the resonance frequency $f_0 = 12.4$kHz and the damping coefficient $\xi = 0.345$. Experience from previous experiments ([25], [36] and [44]) showed that a certain spread of the calibration function for each microphone has to be expected, especially in the high frequency range. Therefore, we have to keep in mind that the surface pressure PSD presented on the NACA0015 presented in this work have a higher uncertainty in the high frequency range.

Consequently, the calibration method of [44] was developed for the Virginia Tech Wind Tunnel experiment. The Brüel & Kjær Probe Microphone Type 4182 with a 50mm probe was used a reference. It was placed as close as possible to the pinhole, figure 3.18(a). A Sennheiser headphone HD650 was used as source for the

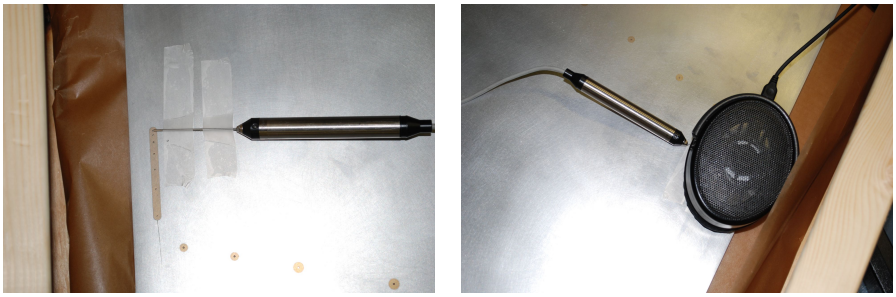

(a) reference microphone and pinhole (b) Sennheiser headphone HD650 source

Figure 3.18: Calibration Setup of the Surface Pressure Microphones in the VT Experiment

calibration, figure 3.18(b). A B&K PULSE Data Acquisition Hardware Type 3560-B-130 together with the PULSE LabShop v. 15.1.0.15 Software was used for data acquisition and source feeding. The high frequency compensation for the B&K Probe Microphone Type 4182 with a 50mm probe was implemented in the PulseLab software. The calibration signal was a sweep in 1/48th octave bands with center frequencies from 16kHz to 50Hz. An individual calibration function for microphone 10 to 24 as well as microphone 28 and 29 was obtained. The calibration was performed in a laboratory at Virginia Tech University. The ambient temperature, pressure and humidity were recorded.

3.4.4 Discussion of measured and analytic transfer functions

Figure 3.19 shows the transfer function of microphone no. 10, 12, 14 and 15 on the NACA64-618 airfoil. Those microphones were mounted directly on the airfoil. To compute the transfer function in dB the Sennheiser microphone electric signals were multiplied with a fictive sensitivity of 10mV/Pa (manufacturer value). A considerable scatter in the transfer function of the different microphones is observed. This points out the importance of individually calibrating the microphones after mounting. The transfer functions have the typical shape of the Helmholtz transfer function (eq. 3.12), but the Eigen frequency and the damping coefficient are very different compared to the ones of the configuration

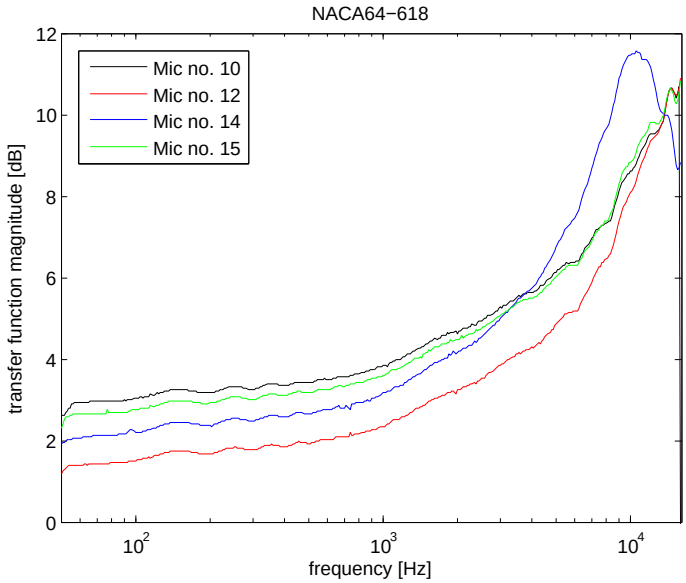

Figure 3.19: transfer function between microphone and source pressure as function of the frequency

microphone and housing, figure 3.14.
Figure 3.20 shows the transfer function of microphone no. 17, 19, 24 and 28 on the NACA64-618 airfoil. All of them are placed in a tube adapter. The scatter is less than for the directly mounted microphones, expect for frequencies above 7kHz. It exhibits a strong interference pattern in the frequency range below 1kHz. This is due to reflexions at the end of the plastic tube. In further applications, a longer and thinner (to increase the damping coefficient) plastic tube should be used.

3.4.5 Temperature Correction of the Measured Calibration Function

The influence of the temperature on the calibration of the microphones with tubing adapter was measured by Brüel & Kjær in the company owned laboratory, because it was known that the temperature in the wind tunnel would differ significantly from the temperature during calibration. The microphone adapter was mounted in a flange. Small differences in the setup compared to the installation in the airfoil are possible. Figure 3.21 shows the transfer func-

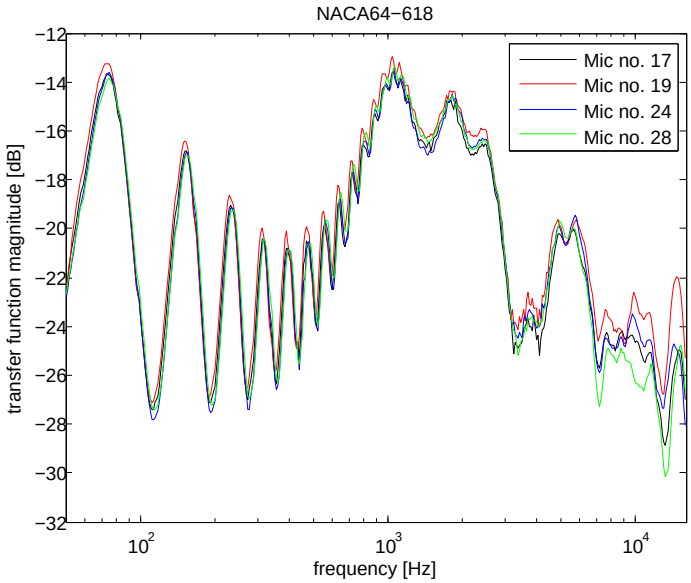

Figure 3.20: transfer function between microphone and source pressure as function of the frequency

tion between microphone and source pressure at temperature 5^oC, 25^oC and 50^oC and ambient pressure of $1.003 \cdot 10^5$Pa as function of the wave number. By plotting the transfer function over the wave number instead of the frequency, the change in speed of sound is accounted for. The measured data shows a difference of less than 1dB over all wave numbers. The differences are due to viscosity effects in the tubing. The analytical model gives qualitatively the right results and the right tendencies with changing temperature. However, the offset between measured and computed levels is up to 10dB. The analytical function can therefore not be used for data reduction. It can be used for the adapter design.
Note that a change in the ambient pressure causes a change in the damping coefficient α. The transfer function will hence also change with a changing ambient pressure. This change is not accounted for when using the measured transfer function as function of the wave number and gives additional uncertainty when reducing the data from the wind tunnel.

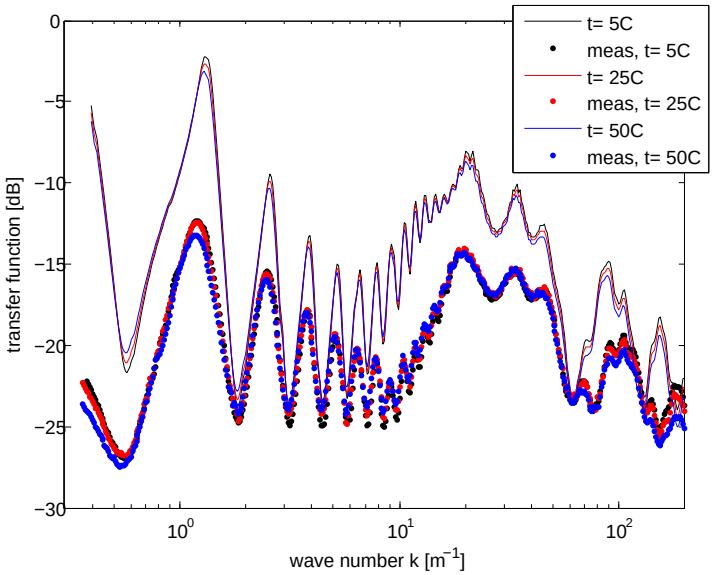

Figure 3.21: transfer function between microphone and source pressure as function of the wave number, dots:measurement, lines: analytical expression

Chapter 4

CFD

In chapter 4 the in-house flow solver EllipSys2D for the Reynolds-averaged Navier-Stokes equations (RANS) is presented. The focus is on the transition and turbulence model used in EllipSys2D. The turbulence model provides the most important input parameter for the TNO and the SPKM model. The correct prediction of the location of transition from laminar to turbulent flow is paramount to obtain useful boundary layer estimations at the TE of the airfoil. The computational domain and grid are also described. The whole setup of the LSWT including wind tunnel walls and airfoil is simulated. The setup of the VTST is very difficult to model in CFD, because the walls are flexible and allow transpiration of air through them. A large domain to obtain free flow conditions was used for the computation of the flow over the two airfoils tested in the VTST and the data was compared to the corrected wind tunnel measurements. In the second section a large eddy simulation (LES) on a NACA0015 airfoil performed at DTU is presented. The whole setup of the LSWT is simulated and the airfoil is turned to a geometric AoA of 8°. The velocity time series at several positions on a line perpendicular to the surface at the chordwise position x/c=0.91 were extracted. It provides data for the two-point quadratic correlation of the fluctuating velocity component perpendicular to the surface which could not be obtained by measurements, but is of great importance for TE noise modeling.

4.1 RANS computations

4.1.1 Flow Solver

The in-house flow solver EllipSys2D [49, 50, 51] is used for the flow computations in the present work. The code solves the incompressible RANS equations on a structured multiblock mesh in general curvilinear coordinates. No equation of state for the pressure exists as the code solves the incompressible flow equations. To enforce the pressure/velocity coupling for steady-state computations the classical SIMPLE algorithm is used.
The code can perform steady-state and unsteady computations. The flow around an airfoil which is not stalled is steady. Therefore all computations performed in the present work are steady-state computations. For steady-state computations the global time step is set to infinity which corresponds to the use of a local time step. A multilevel grid sequence is used to accelerate the computation. The convective terms are discretized using a third-order QUICK upwind scheme, the viscous terms are discretized with a central difference scheme.
Turbulence is modeled with the k-ω Shear Stress Transport (SST) eddy viscosity model [52]. The transition from laminar to turbulent flow is modeled either with the semi-empirical e^N model [53] or the γ-$\tilde{Re}_\theta$ correlation based model [54]. The equations for the turbulence and the transition model are solved after the momentum and pressure correction equations. The k-ω equations and the two transition model equations are solved decoupled with a red/black Gauss-Seidel point solver.

4.1.2 Simulation of the NACA0015 airfoil in the LSWT

A simplified setup of the whole test section of the LSWT with the NACA0015 airfoil model was simulated. In this case no wind tunnel corrections are necessary. The computational domain is three chord lengths high corresponding to the physical dimensions of the test section of the LSWT, figure 4.1. The boundary condition on the top and bottom of the domain is a slip wall condition. The boundary layer on the wind tunnel walls are neglected. The inlet is located 14 chord lengths upstream of the leading edge of the airfoil and the outlet is located 26 chord length downstream of the TE.
A fine mesh with 512 cells distributed on the airfoil surface was used, figure 4.2. 128 cells were distributed in the direction normal to the airfoil surface. The height of the cells on the surface of the airfoil was 10^{-6} chord lengths. The cells size was stretched towards the boundaries of a central block with the dimensions 3 times 3 chord length. The central block is divided in 4 subblocks. Attached

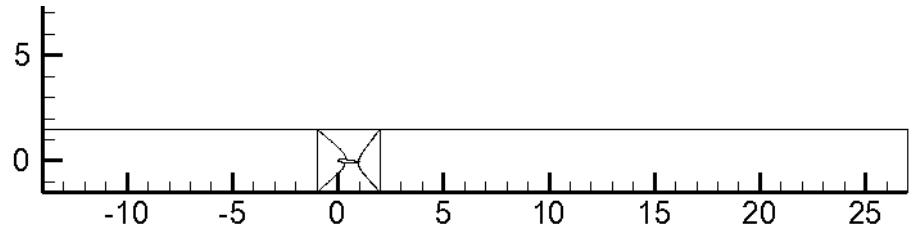

Figure 4.1: Computational domain for the NACA0015 airfoil in the LSWT (dimensions in chord length)

to the central block is an inlet block with a length of 13 chord lengths and an outlet block with a length of 25 chord lengths. Inlet block and outlet block contain both 128 times 128 cells. The cells were small at the boundary to the central block and increased size towards the inlet or outlet.
We used the e^N model for transition. The N-factor was set 9, corresponding to natural transition. It fits well with the low turbulence intensity in the flow of the LSWT.

4.1.3 Simulation of the airfoils in the VTST

The flow in the test section of the VTST cannot be simulated easily in CFD, because the boundary conditions along the Kevlar walls are hard to define. There is transpiration of air through the Kevlar walls and the walls deflect under aerodynamic load. Hence, we chose to use established wind tunnel correction methods [38] to obtain results as in free flight conditions and make simulations according to that.
An O mesh grid with a diameter of 40 chord lengths was created, figure 4.3. The cells were concentrated close to the airfoil and in the wake. 512 cells were distributed along the surface of the airfoil, figure 4.4. The cell height on the surface of the airfoil was 10^{-6} chord lengths and increases with a $sinh$ streching function towards the edge of the domain.
The γ-$\tilde{Re}_\theta$ correlation based transition model was used in the computations for the airfoils in the VTST. The turbulence intensity of the simulated flow was tuned that the transition location in the measurement was in good agreement with the results of the measurement. The result was a inflow turbulence intensity of 0.1%.

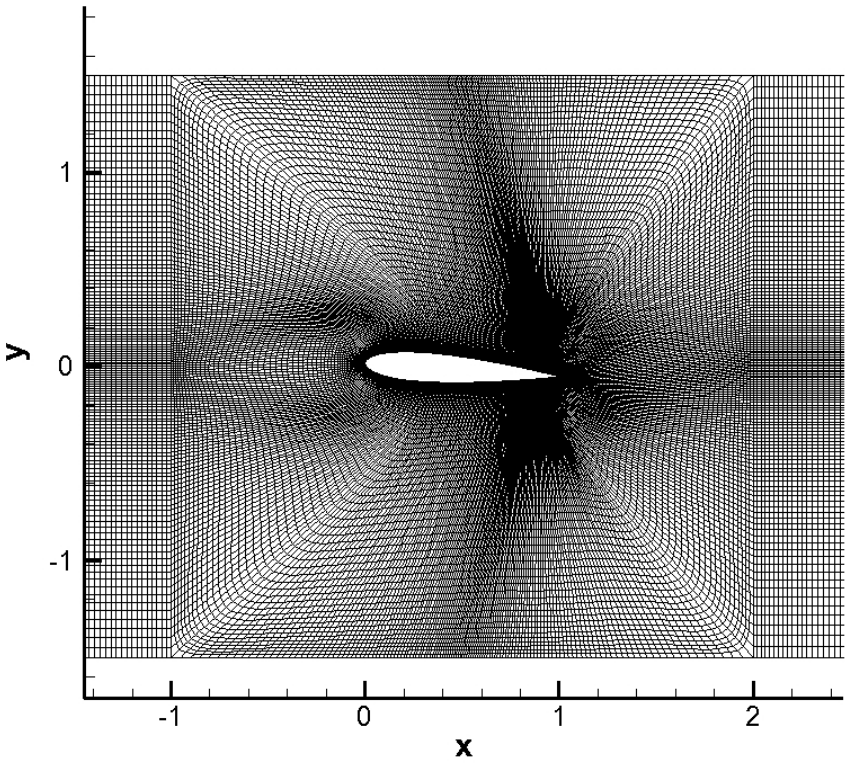

Figure 4.2: Computational mesh for the NACA0015 airfoil in the LSWT (dimensions in chord length)

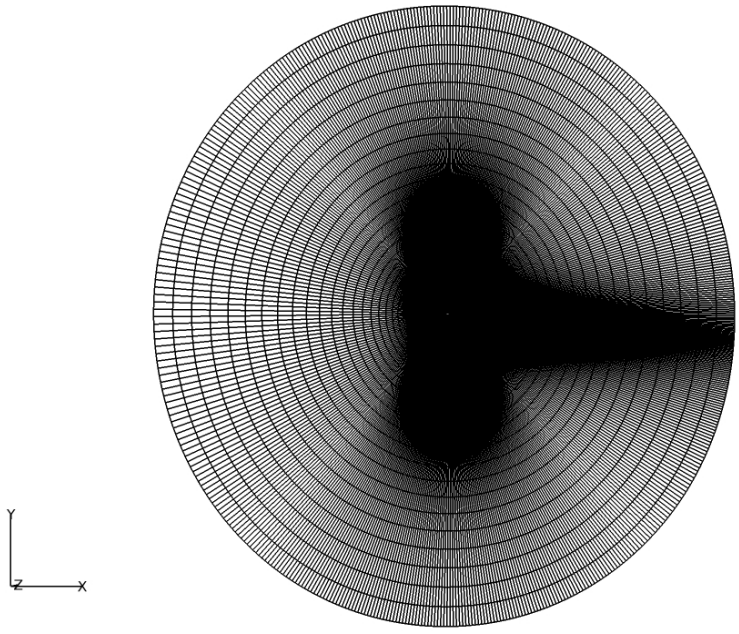

Figure 4.3: O mesh used for computation of the airfoils in the VTST

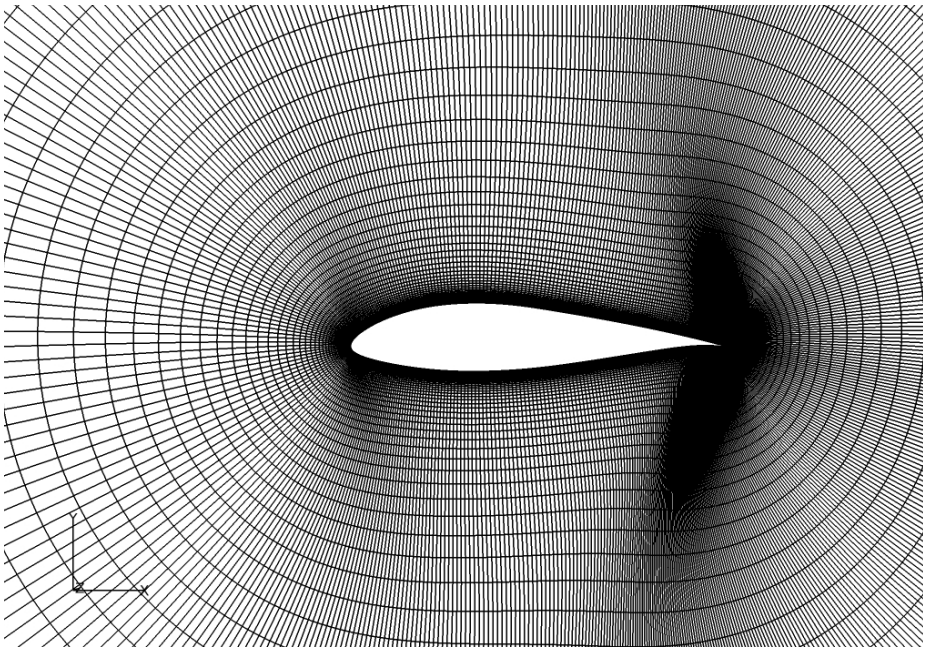

Figure 4.4: Computational mesh for the airfoils in the VTST

4.2 Computations of Airfoil Flows using LES

At flow-acoustic splitting technique for aeroacoustic computations on airfoils was developed at DTU-MEK [55]. It uses a decomposition of the compressible Navier-Stokes equations into an incompressible part that governs the flow motion and a perturbed compressible part dominating the acoustics. The flow equations are solved by using LES in which the large eddy scales are simulated and the small scales are modeled. Hence, a filter due to the finest mesh size has to be employed. The acoustic perturbation equations were obtained by subtracting the viscous incompressible solution from the compressible Navier-Stokes equations and neglecting the turbulent quantities contained in the acoustic variables. Details about the aero-acoustic code are found in [56] and [57].
The LES computations were performed at DTU-MEK by Wei Jun Zhu and the LES data used in the present work as well as the material presented below was provided by him.

4.2.1 Computational Domain

The LES domain reproduces the physical domain of the experiment in the LSWT in a simplified way, figure 4.5. All quantities are dimensional and the extend of

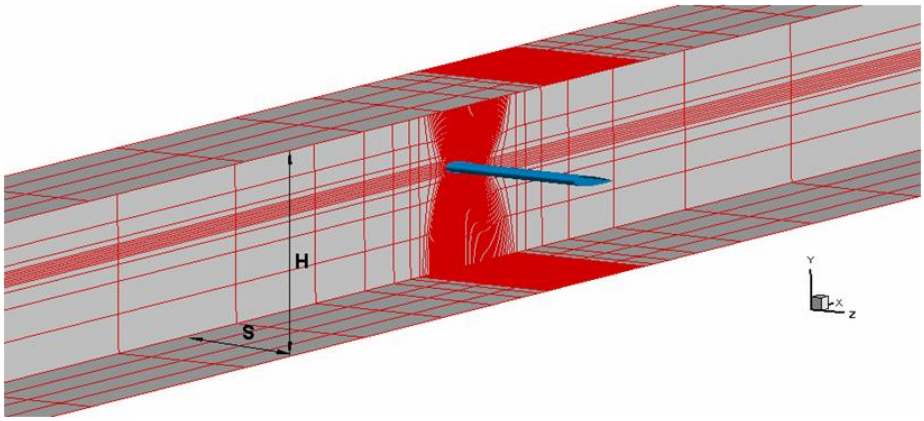

Figure 4.5: Computational Domain for LES Computations

the 'LES wind tunnel' are $0.9 \cdot 2\%$ m = 0.018m in width, 2.7m in height and 30m in length. The height corresponds to the actual height of the LSWT, but the width had to be reduced due to computational expenses. The consequences of this narrow domain will be discussed. The NACA0015 airfoil has a chord

length of 0.9m and is rotated at a geometric AoA of $\alpha = 8^o$. The grid consists of a total of $32^3 \cdot 140 \approx 4.6 \cdot 10^6$ cells. The grid spacing in the vicinity of the airfoil satisfies $\Delta x^+ \approx 30$, $\Delta y^+ \approx 2$ and $\Delta z^+ \approx 20$. The flow speed at the inlet was $U_\infty = 30m/s$, corresponding to a chord based Reynolds number of $Re = 1.71 \cdot 10^6$.

4.2.2 Velocity and Pressure Time Series

A time series of velocity and pressure of duration $T = 0.5725s$ and time step $\Delta t = 10^{-5}s$ was recorded. The time series were extracted on the suction side of the airfoil at the chordwise position $x/c = 0.91$ normal to the airfoil surface, figure 4.6. The velocity components were rotated in a way that the u-component

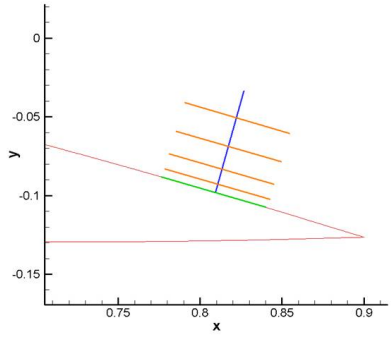

Figure 4.6: Velocity and Pressure Location in LES computations

was perpendicular to the airfoil surface and the v-component normal to the surface.
The mean and variance of the velocity components is compared to measurements to preliminary evaluate the LES computation, figure 4.7. The u-component (perpendicular to the airfoil surface) is better estimated by RANS than by LES. However, the agreement between v-component from measurement and LES is very good. The variance predicted by LES is lower than the measured one because of the filter function applied in the LES computation. The energy contained in the high frequency part of the spectrum is excluded. The LES computation is in error very close to the surface where the variance is significantly over predicted. A damping function should by applied to get rid of the peak close to the surface.

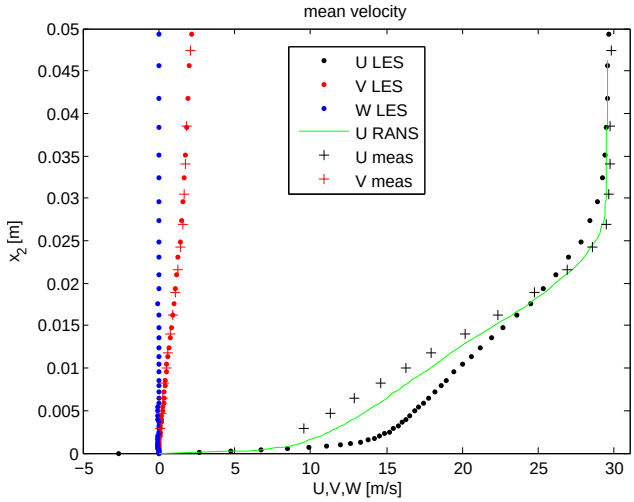

(a) mean velocity

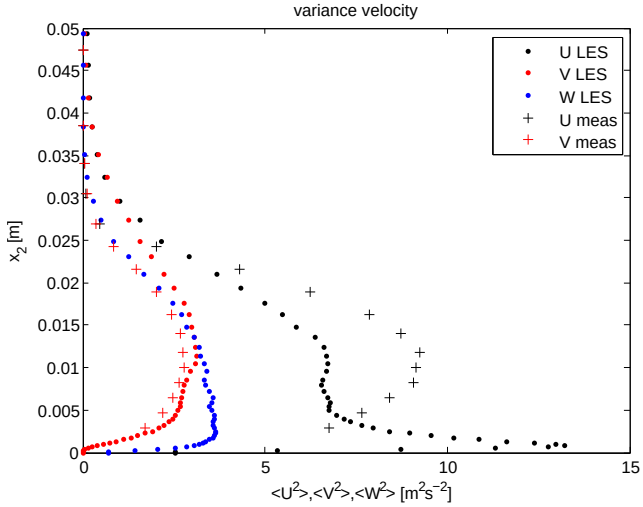

(b) variance of the velocity

Figure 4.7: Mean Value and Variance of the Velocity from Measurement and LES

Chapter 5

Results

The first section deals with wind tunnel correction applied to the data obtained in the VTST to convert the data from the conditions in the VTST to free space. Two different correction methods proposed by William Devenport were investigated. The resulting C_l-α polar of the NACA64-618 airfoil was compared to the measurements of [58]. The pressure distribution of the corrected wind tunnel data was compared to the one obtained from Ellipsys2D RANS computations. In the next section the focus is on the flow in the boundary layer. Measured velocity profiles are compared to the ones computed with EllipSys2D for validation. Then a method to relate the input parameter of the new TE noise model to the output of the $k-\omega$ turbulence model of EllipSys2D is developed by comparison with the measured one point velocity spectra for the data from the NACA0015 airfoil. Results from the LES computation for the NACA0015 airfoil are used for comparison of the cross correlation of the velocity fluctuations. The new model is then applied to model the one point velocity spectra for the airfoils tested in the VTST. In the following section surface pressure prediction are compared to the original TNO model and to measurements.
The next section of chapter 5 deals with surface pressure statistics. The one point surface pressure spectra from the experiment in the LSWT and the experiment in the VTST are analyzed for scaling laws. The streamwise and spanwise surface pressure statistics from the experiment in the VTST are investigated, because those give the input for the noise prediction in the last section. In the final section we compare far field sound predictions with input from measured

surface pressure statistics to measurements with the microphone array in the far field.

5.1 Wind Tunnel Corrections and Aerodynamic Performance of the Airfoils tested in the VTST

5.1.1 Wind Tunnel Corrections

The flow field around the airfoil in the wind tunnel is changed compared to unbounded flow conditions due to the presence of the Kevlar walls. Additionally the effects of transpiration of air through the Kevlar walls and the deflection of the walls under aerodynamic load have to be taken into account. A correction for the angle of attack (AoA) and solid blockage was derived with the help of a panel method code by [38]. It was found that the correction for solid blockage is only 0.42 times the value of the correction for a hard wall test section of equal dimensions. The correction for solid blockage in the hard wall test section for a thin airfoil with 0.6m chord length is small, because the dimensions of the cross section area of the test section of the VTST are very large compared to the airfoil dimensions. In the acoustic test section the effect of solid blockage is even smaller and can be ignored.
The angle of attack correction of ref. [38] (IFC1) models the effect of transpiration of air through the Kevlar wall, but not the deflection. Additionally, the model suggests a constant flow out of the section and into the anechoic chamber on the pressure side and the opposite on the suction side. No evidence of larger air streams in the anechoic chambers could be found experimentally. Therefore a new angle of attack correction (IFC3) was developed by William Devenport and provided to the author. The new correction accounts for the deflection of the walls and models the transpiration of air in a more appropriate way.
The boundary condition for the transpiration correction is no net flow over the length of the Kevlar window. Again with a panel method, he found that the velocity component due to transpiration for the new correction method was 0.35 times the value of the velocity component of the old one. To get the deflection of the walls the tension in the Kevlar sheet is computed. An empirical relation relates the deflection to the change in angle of attack.
The major difference between IFC1 and IFC3 is that IFC3 changes with flow speed while IFC1 only depends on C_l. The aerodynamic forces become larger with increasing flow speed and therefore the deflection becomes also larger. The effective angle of attack is then reduced with increasing flow speed.

5.1.2 Validation of the Wind Tunnel Correction

The C_l-α polar of the NACA64-618 for different Reynolds numbers and wind tunnel corrections in comparison with the measurement of [58] and measurements provided by LM Wind Power A/S at a Reynolds number of 3 million is shown in figure 5.1. The measurements in different facilities show a considerable

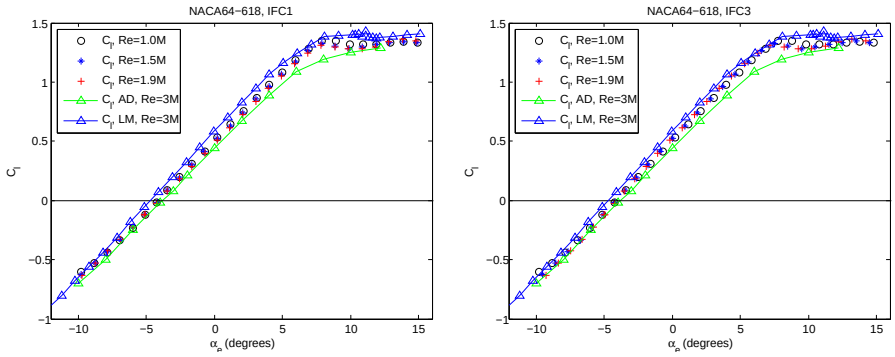

(a) old angle of attack correction (IFC1) (b) new angle of attack correction (IFC3)

Figure 5.1: The C_l-α polar of the NACA64-618 at different Reynolds numbers (green: measurements of [58] at Re=$3 \cdot 10^6$, blue: measurements of LM Wind Power A/S at Re=$3 \cdot 10^6$)

scatter. The measurements of [58] and LM Wind Power A/S were performed at the same Reynolds number. Hence, the difference must be an effect of the facility or the model used. The wind tunnel facility owned by LM Wind Power A/S is more modern and the standards for fabrication of the airfoil model are the same as for the models used in the VTST. We prefer the comparison of the present measurements with the ones from LM for benchmarking the wind tunnel corrections.
The slope of the C_l-α polar decreases with increasing Reynolds number when IFC1 is applied. The measurements of ref. [58] in a Reynolds number range from 3 to 9 million showed that the linear part of the polar was independent of the Reynolds number. The slope of the linear part of the polar measured in the VTST is less dependent on the Reynolds number when applying IFC3. Additionally the results are closer to the ones from the measurements of LM Wind Power A/S. Therefore we chose to use IFC3 in the following.

5.1.3 Influence of the angle of attack correction

The effective (corrected) AoA vs. the geometric AoA for both airfoils measured in the VTST at different Reynolds numbers is displayed in figure 5.2. The

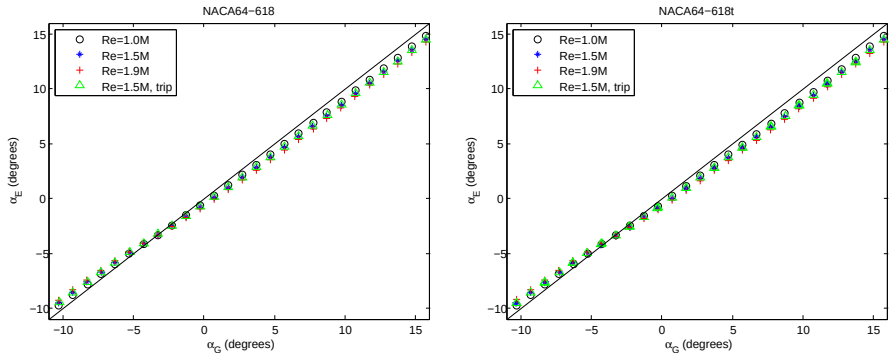

(a) NACA64-618 (b) NACA64-618t

Figure 5.2: The effective angle of attack α_E vs the geometric angle of attack α_G

correction is very similar for both airfoils. At the same geometric AoA the difference in effective AoA is maximum 0.1°. The difference between geometric and effective AoA is up to 1.5° for the highest lift coefficients and flow speeds. The effective AoA is decreased with increasing flow speed as explained above. The difference of effective AoA at a fixed geometric AoA for the highest and the lowest flow speed is up to 0.6° in the linear part of the polar. This has to be considered when scaling laws with the flow speed are sought.

5.1.4 Aerodynamic performance of the NACA64-618 and NACA64-618t airfoil

The C_l-α polar of the NACA64-618 for all tested configurations is depicted in figure 5.3. The linear part of the polar is independent of the Reynolds number as discussed above. The maximum lift coefficient is about 1.35 and decreases slightly with increasing Reynolds number. The stall behavior of the airfoil is very smooth. When tripped the performance of the airfoil decreases significantly, because it was designed to have laminar boundary layer flow over large parts of its chordwise extend.
The NACA64-618t airfoil has a higher maximum lift coefficient, figure 5.4. The drop in lift beyond stall is much bigger compared to the NACA64-618. The lift coefficient in the linear part of the polar shows a small increase with increasing

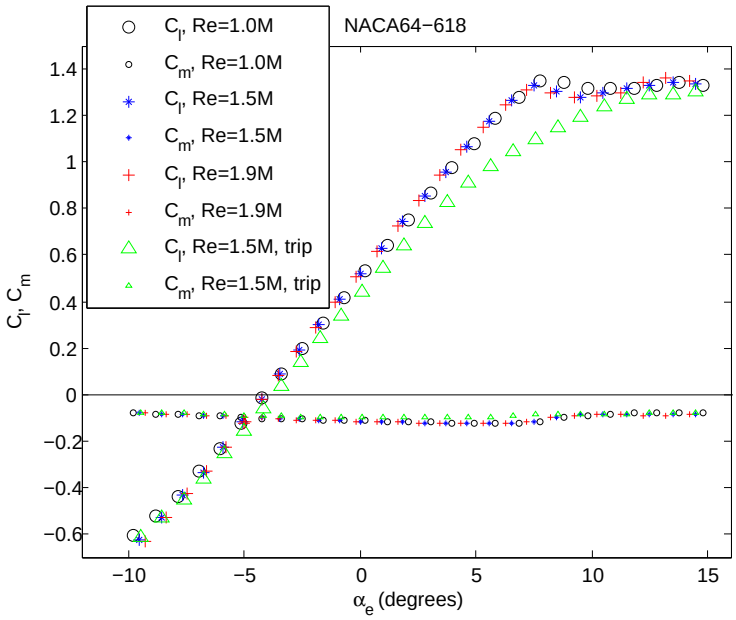

Figure 5.3: The C_l,C_m-α polar of the NACA64-618

Reynolds number. There is a loss of aerodynamic performance in the tripped case, but it is not as severe as in the case of the NACA64-618.
To compare the aerodynamic performance, the polar of the two airfoils for each configuration is plotted in figure 5.5. The slope of the lift curve of both airfoils is identical in the linear part, only the zero lift angle is shifted. The linear part of the lift curve of the NACA64-618t extends a larger range of AoAs than the one of the NACA64-618. In the AoA range encountered normally in wind turbine drift, both airfoils perform equally well, except in the tripped case. There the NACA64-618t performs better.

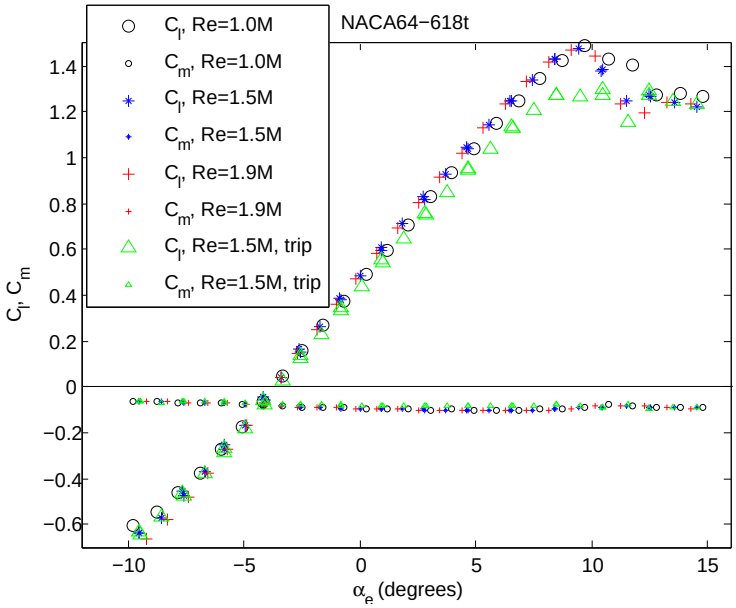

Figure 5.4: The C_l,C_m-α polar of the NACA64-618t

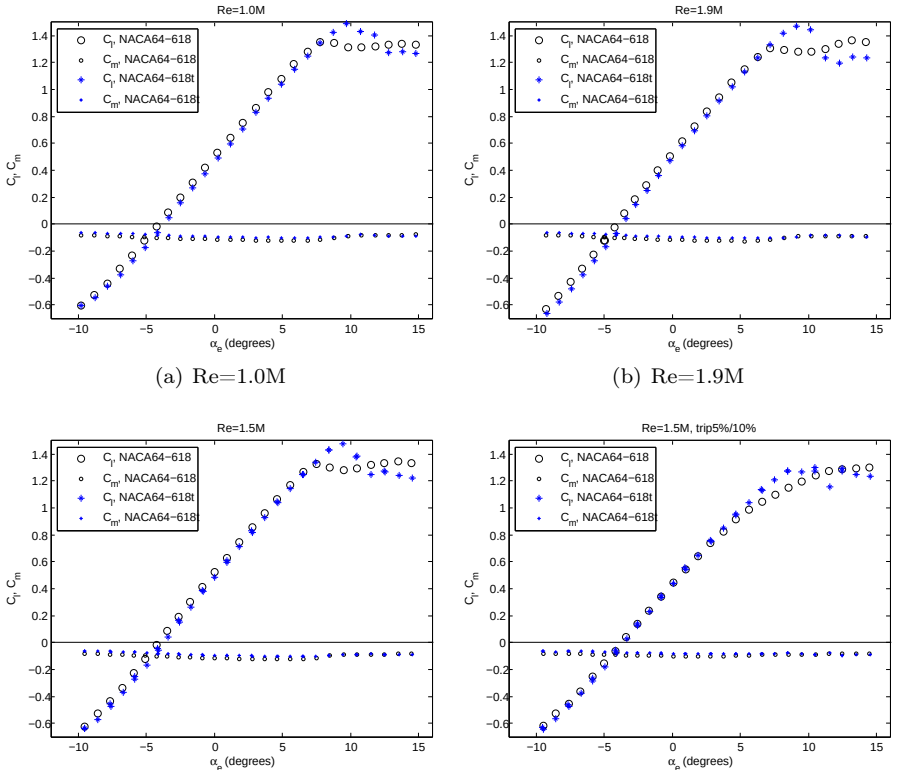

(a) Re=1.0M (b) Re=1.9M

(c) Re=1.5M (d) Re=1.5M, trip tape 5%/10%

Figure 5.5: Comparison of the C_l,C_m-α polar of the NACA64-618 and the NACA64-618t

The transition of the boundary layer from laminar to turbulent flow can be evaluated from the signal of the surface pressure microphones. The value of the auto spectral density integrated over a frequency range of 2000-6000Hz is used as indicator. It is shown as a function of the chordwise position for both airfoils on the suction side at a Reynolds number of 1.5 million and several effective AoAs in figure 5.6. In the linear part of the C_l-α polar ($\alpha_E = -3.3^o$

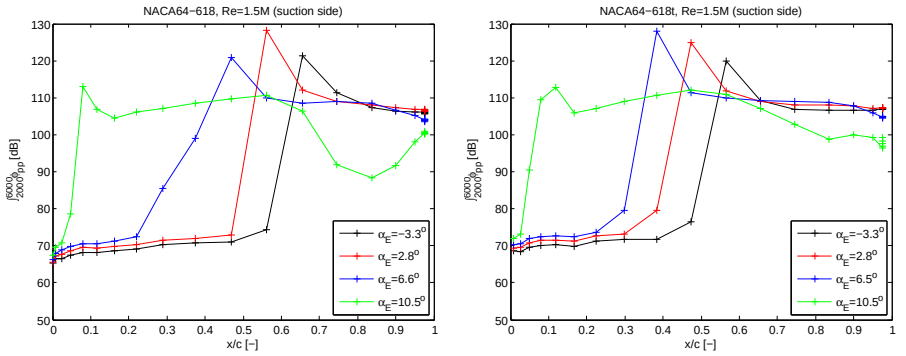

(a) NACA64-618 (b) NACA64-618t

Figure 5.6: The integrated PSD of the surface pressure on the suction side vs. chordwise position (Integration range: 2kHz - 6kHz)

and $\alpha_E = 2.8^o$) transition occurs further to the trailing edge for the NACA64-618 than for the NACA64-618t. The extend of laminar boundary layer flow is large for both airfoils. At the effective AoA $\alpha_E = 6.6^o$ the transition point moves fast towards the leading edge for the NACA64-618. The transition point of the NACA64-618t is now further downstream. At $\alpha_E = 10.5^o$ both airfoils are stalled and transition occurs almost directly at the leading edge.

5.1.5 Comparison with CFD

The comparison of the measured quantities in the Virginia Tech experiment with results from CFD is very important, because the correction of the measured data described above are of a high magnitude compared to the correction of the data measured in the LSWT. First, we compare the pressure distribution on the airfoil. The measured and computed pressure coefficient distribution for the NACA64-618 airfoil for AoAs in the linear range of the polar is shown in figure 5.7. The agreement between measurement and computation is excellent. There is only a small offset on the pressure side. The bump seen in the C_p distribution marks the transition location. The location of this bump is very

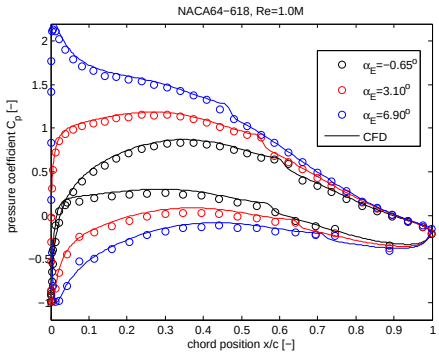

(a) Re=1.0M

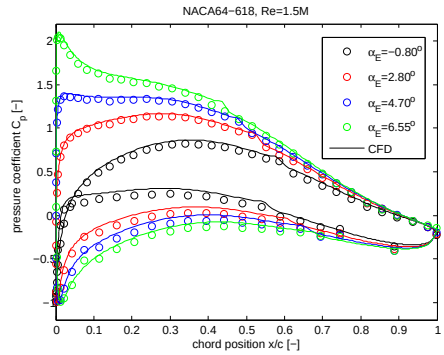

(b) Re=1.5M

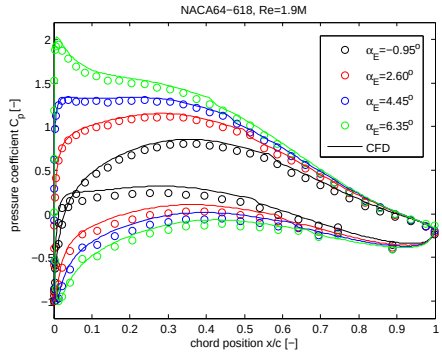

(c) Re=1.9M

Figure 5.7: Comparison of the measured and computed pressure coefficient C_p distribution of the NACA64-618 airfoil

similar in measurement and computation.
The C_p distribution of the NACA64-618t airfoil shows a less good agreement between computation and measurement, figure 5.8. The pressure coefficient C_p on the suction side of the airfoil is in fairly good agreement, but the suction peak at high AoAs is not predicted correctly by CFD. On the pressure side there is a considerable offset between measurement and computation. A possible explanation for this difference might be an error in the adjustment of the geometric zero AoA when inserting the airfoil into the wind tunnel. Typically the uncertainty of the geometric zero AoA is $\pm 0.5°$. But due to the various corrections of the measurement data also other error sources are possible and there might also be some uncertainty in the CFD computation. The measurements were therefore not corrected by adding an offset to the geometric AoA to match the CFD results.

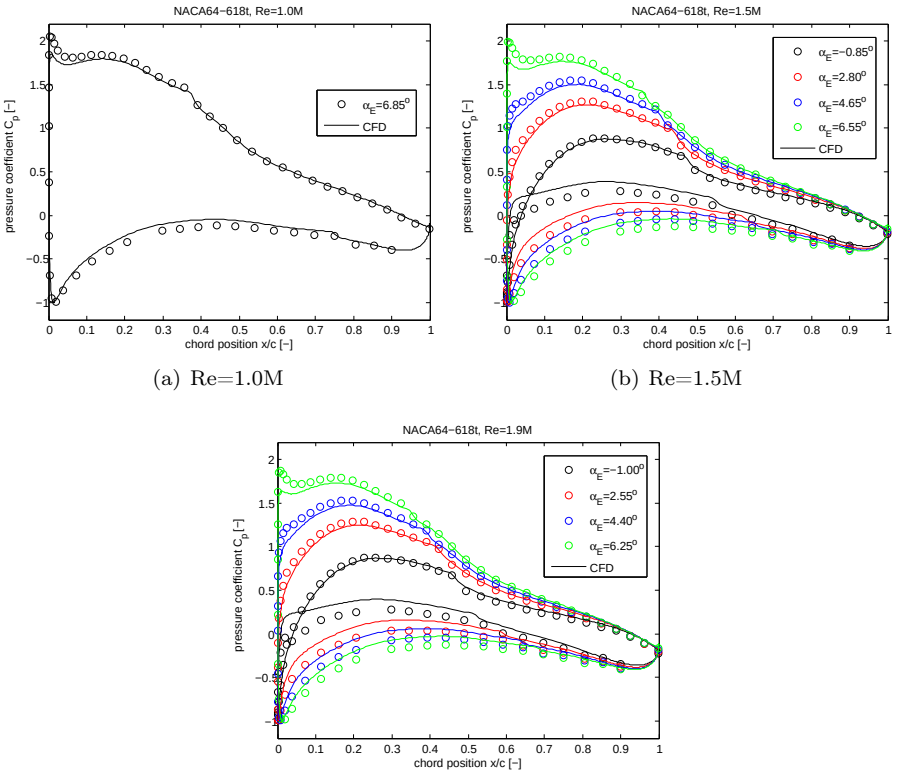

(a) Re=1.0M (b) Re=1.5M

(c) Re=1.9M

Figure 5.8: Comparison of the measured and computed pressure coefficient C_p distribution of the NACA64-618t airfoil

5.2 Airfoil boundary layer flow and turbulence

5.2.1 Evaluation of input parameters for the Mann Model

The spectral tensor of the Mann US+B model is determined by the three input parameters $\alpha\bar{\epsilon}^{2/3}$ (the mean dissipation times a constant), the length scale L and Γ (the eddy life time parameter). As a start we consider these parameters as free and adjust them by fitting the one point spectra with measurements. This was achieved by numerical optimization with the open source optimization code 'Iffco' [59]. The optimization was performed for the NACA0015 airfoil in the LSWT in five different flow situations at the chordwise position x/c=0.91.

The cost function of the optimization was

$$C_o = \sum_{i=1}^{3} \left(\frac{F_{1,m}^{ii} - F_{1,USB}^{ii}}{F_{1,m}^{ii}} \right)^2 + \left(\frac{F_{1,m}^{12} - F_{1,USB}^{12}}{F_{1,m}^{12}} \right)^2 \tag{5.1}$$

The optimization was bounded in wave number space. The lower bound was given by the wavenumber where the premultiplied measured one point spectral density $k_1 F_1^{11}$ peaked. The upper bound was the wavenumber k_1 corresponding to a frequency of 8000Hz. The hot wire data was low pass filtered with a cut-off frequency off 10000Hz, but the influence of the filter was felt already at 8000Hz. The parameters found by the numerical optimization as function of the distance normal to the airfoil surface at the position x/c=0.91 are displayed in figure 5.9. The results show that the parameters $\alpha\bar{\epsilon}^{2/3}$ and Γ are a function of the distance

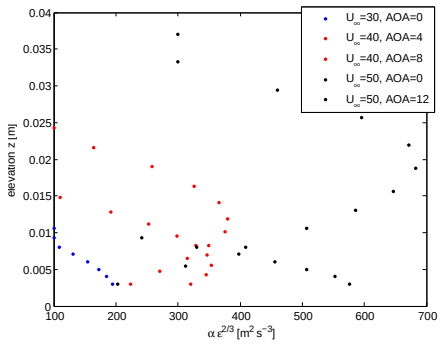

(a) mean dissipation $\alpha\bar{\epsilon}^{2/3}$

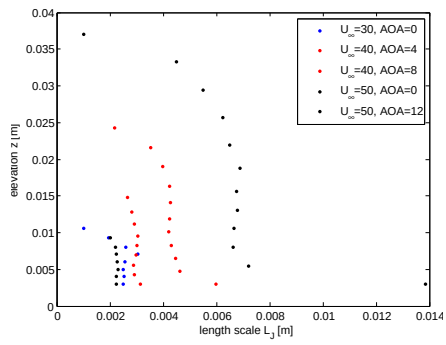

(b) length scale L

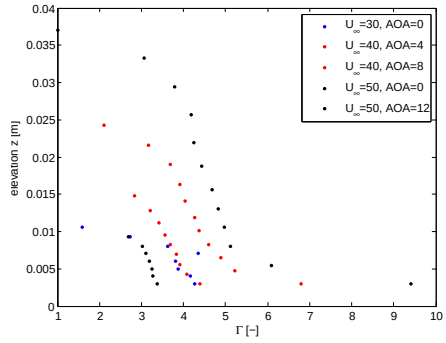

(c) eddy life time parameter Γ

Figure 5.9: Input parameters to Mann US+B Model obtained by fit to measurements

from the surface. The length scale L is rather independent of the distance from the wall, except for high AoAs very close to the wall and at the edge of the boundary layer. It is not possible to describe the turbulence in the whole boundary layer with one set of input parameters.
In the following we will compare the one point spectra obtained by measurement and computation with the Mann Model to see how well the optimization worked and how much the Mann Model is capable of describing the turbulence in the boundary layer. We use the case with flow speed $U_\infty = 40m/s$ and AoA $\alpha = 8°$ as example, figure 5.10, because the measurements cover the whole peak of the turbulent kinetic energy which roughly corresponds to the peak of the parameter $\alpha\bar{\epsilon}^{2/3}$. At the position closest to the wall ($x_2 = 3.0mm$), figure 5.10(a), the

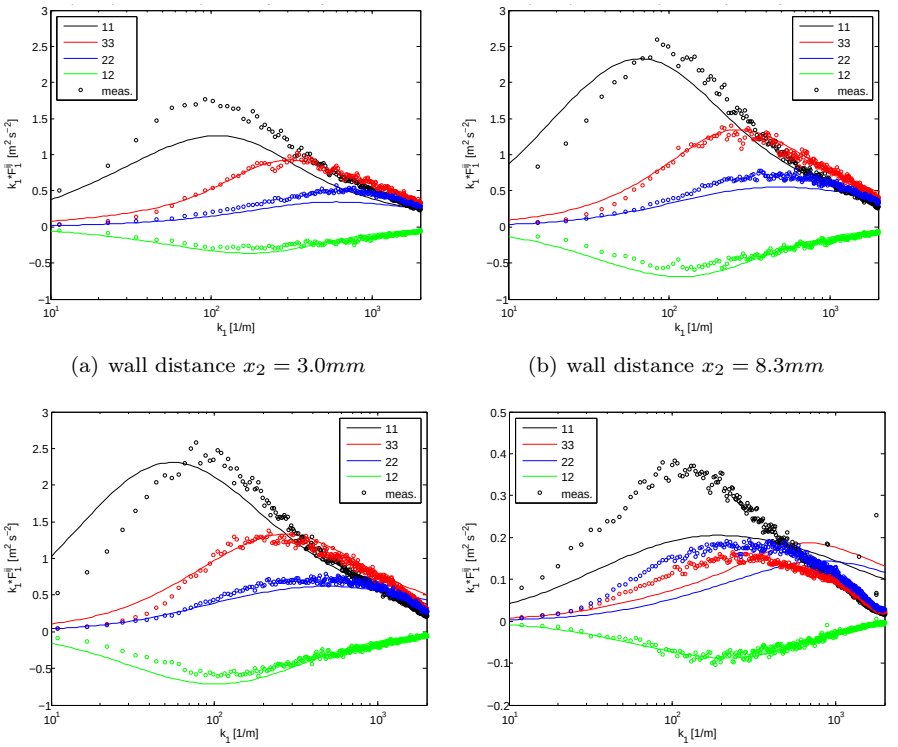

(a) wall distance $x_2 = 3.0mm$

(b) wall distance $x_2 = 8.3mm$

(c) wall distance $x_2 = 14.1mm$

(d) wall distance $x_2 = 24.3mm$, different y scale!

Figure 5.10: Computed One Point Spectra with Input Parameters from Optimization compared to Measurements for the case $U_\infty = 40m/s$ and AoA $\alpha = 8^o$

one point spectral densities of the longitudinal 11 and vertical 22 component are underestimated. The model is not capable of modeling all auto and cross

spectral densities correctly at the same time. For surface pressure estimation this position has minor importance, because the energy contained in the velocity spectrum is low. At the position $x_2 = 8.3mm$ and $x_2 = 14.1mm$, figure 5.10(b) and 5.10(c), all components of the spectral tensor are described excellently by the Mann Model. However, the model overestimates the 11-component at very low wave numbers. These positions are very important for the surface pressure calculation because of the relatively high energy content of the spectra. At the position $x_2 = 24.3mm$, figure 5.10(d), the optimization failed. The measurement is taken at the edge of the boundary layer and the energy content is very low. It exhibits more energy in the vertical component than in the lateral which is contradictory to the Mann Model. The measurement at this position has no relevance for turbulence modeling and can be ignored in the following.
A so-called 'badness' parameter was defined to give an overview of the success of the modeling the one point spectral densities. The 'badness' parameter is the ratio between the area of the difference between the measured and computed one point spectral density and the area of the measured one point spectral density, illustrated in figure 5.11. A 'badness' parameter of B=0 stands for a perfect

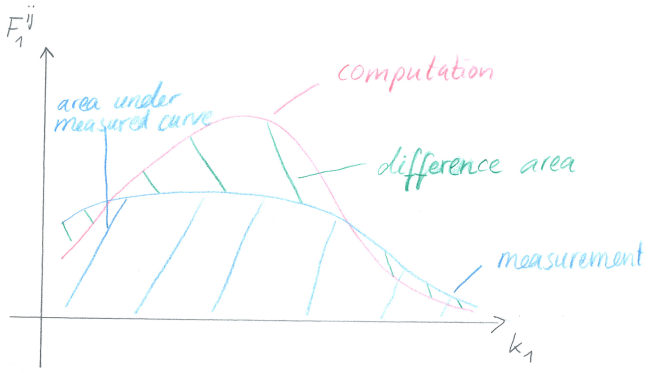

Figure 5.11: Definition of the 'badness' parameter

agreement between measurement and computation. The higher the 'badness' parameter the larger is the difference between model and measurement. The total 'badness' parameter is defined as mean value of the 'badness' parameter of one point auto and cross spectral density of each component.
The 'badness' parameter as function of distance from the wall for all cases is shown in figure 5.12.

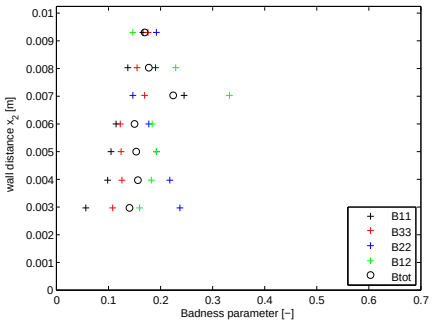

(a) $U_\infty = 30m/s$ and $\alpha = 0^o$

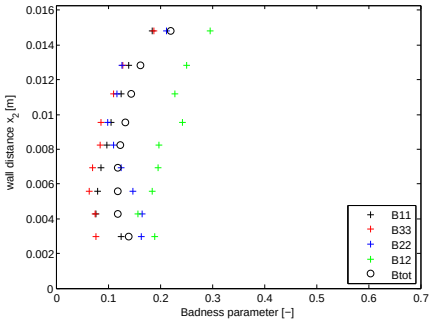

(b) $U_\infty = 40m/s$ and $\alpha = 4^o$

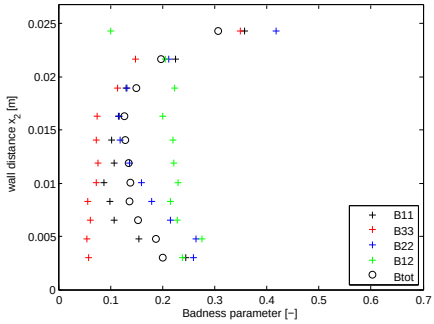

(c) $U_\infty = 40m/s$ and $\alpha = 8^o$

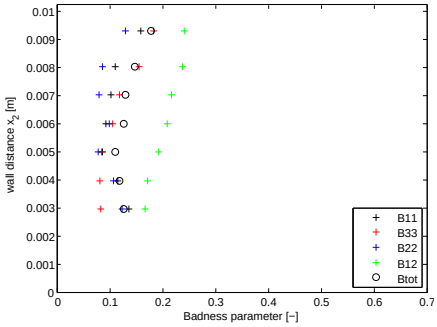

(d) $U_\infty = 50m/s$ and $\alpha = 0^o$

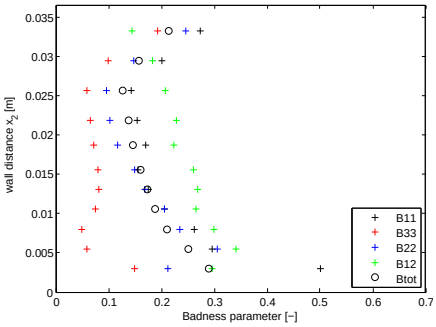

(e) $U_\infty = 50m/s$ and $\alpha = 12^o$

Figure 5.12: 'Badness' parameter for all cases used in the optimization

In most cases the 'badness' parameter is smaller than 0.3 which means a very good agreement between measurement and computation. The lowest values of the 'badness' parameter coincide with the peak of the energy of the spectrum. The Mann model captures excellently the physics of the boundary layer turbulence in the region which is important for surface pressure modeling.
The 'badness' parameter increases when approaching the wall, especially for the 22-component which is most important for surface pressure modeling. A different choice of input parameters might improve the agreement between measurement and computation.

5.2.2 Relating the Input Parameters of the Mann Model to RANS computation

As the Mann Turbulence model is based on the isotropic von Karman energy spectrum it is sought to relate the input parameters to the output of the isotropic $k-\omega$ turbulence model used in EllipSys2D RANS computations. In a first step, we compare the boundary layer velocity profile of the RANS computation with measurements to ensure that the turbulence model gives meaningful results, figure 5.13. The measured velocity profile exhibits a larger velocity gradient (shear) for AoAs up to $\alpha = 8°$. The boundary layer thickness is in very good agreement. It gives some confidence that the distance of the first measurement point to the airfoil was measured accurately. The the highest AoA ($\alpha = 12°$) there is an offset between measured and computed velocity profile and the boundary layer thickness is not in good agreement. The non-linear part of the $C_l - \alpha$ polar is reached. Hence, the results of the RANS computation might be more uncertain at AoA $\alpha = 12°$.
Overall, the RANS computations give good results and we are confident in the measurement accuracy. The present data set is a good basis to establish the relation between the input parameter of the Mann model and the output of the $k-\omega$ turbulence model.

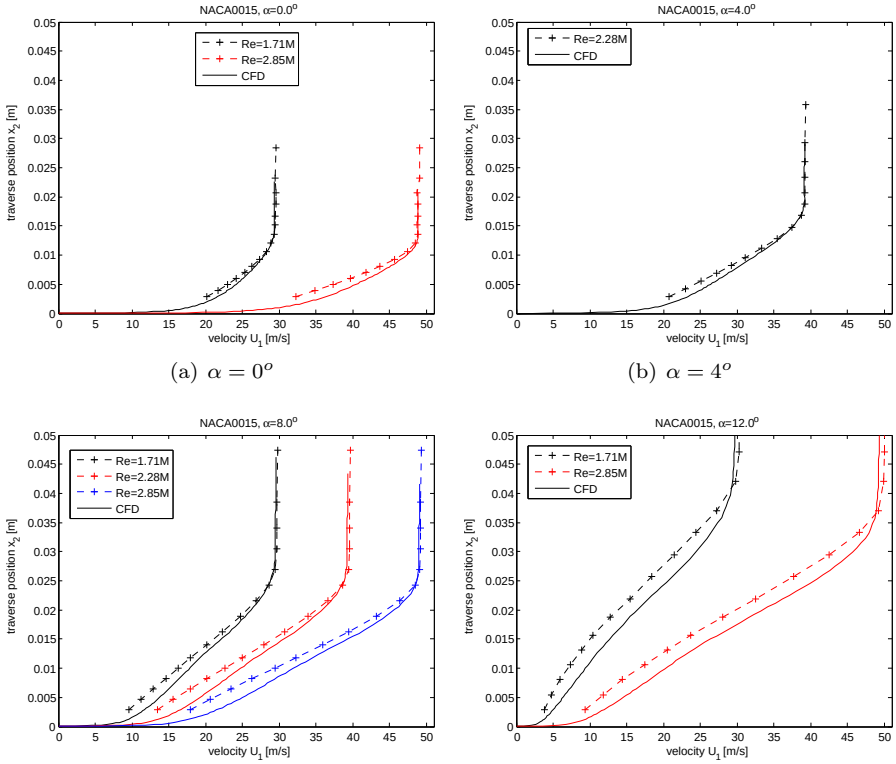

(a) $\alpha = 0^o$ (b) $\alpha = 4^o$

(c) $\alpha = 8^o$ (d) $\alpha = 12^o$

Figure 5.13: Comparison of the measured and computed boundary layer velocity profile of the NACA0015 airfoil at chordwise position x/c=0.91

It is obvious that the mean dissipation should be related to the dissipation obtained from the $k-\omega$ model. By comparing the asymptotic behavior of the von Karman spectrum with the Kolmogorov spectrum one finds that the length scale of the von Karman spectrum should be proportional to the quotient $\frac{(e_t)^{3/2}}{\bar{\epsilon}}$. The mean dissipation $\alpha\bar{\epsilon}^{2/3}$ and the length scale L normalized by the corresponding parameters from the $k-\omega$ turbulence model are shown in figure 5.14. Ignoring

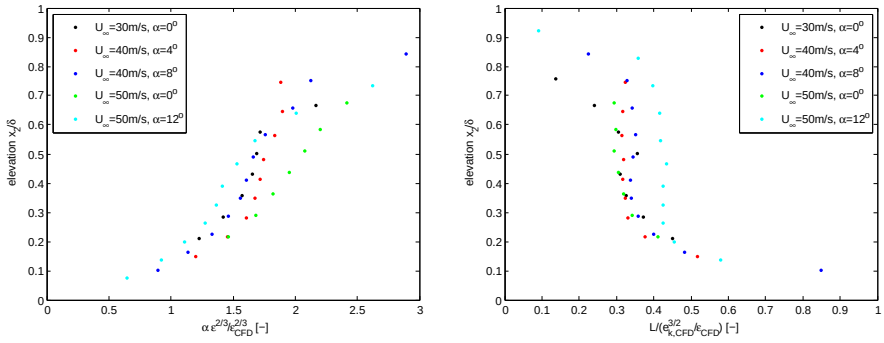

(a) mean dissipation $\alpha\bar{\epsilon}^{2/3}$ (b) length scale L

Figure 5.14: Mean dissipation $\alpha\bar{\epsilon}^{2/3}$ and the length scale L from optimization normalized by the corresponding parameters from the $k-\omega$ turbulence model

the outliers at the edge of the boundary layer and very close to the surface, the factor α is in between 1 and 2. To ensure the equality 2.106 of the von Karman energy spectrum α should take the value of 1.4528 [60]. The suggested empirical value from atmospheric boundary layer measurements is $\alpha \approx 1.7$. The present data shows at least an agreement in the order of magnitude. However, it suggests a variation with the position in the boundary layer. But this variation could be due to uncertainties of the output of the $k-\omega$ turbulence model and the absolute position of hot wire anemometer, because the dissipation changes strongly with the wall distance.

The proportionality factor between the length scale L and $\frac{(e_t)^{3/2}}{\bar{\epsilon}}$ from the turbulence model is in the range of 0.3 to 0.45 if outliers are discarded, figure 5.14(b). A very good collapse is achieved for four out of five cases. The proportionality factor is much higher in the case with flow speed $U_\infty = 50m/s$ and AoA $\alpha = 12°$ than for all other cases. At this high AoA the airfoil is close to stall and the RANS computation is more uncertain. The proportionality factor is rather independent of the position in the boundary layer.

It is not possible to relate the eddy life time parameter Γ to the output of the $k-\omega$ turbulence model. An empirical relation is sought instead. The first candidate to establish such a relation is the local shear, because the eddy life

time parameter is normalized by the shear in the model. The local shear of the RANS computation as function of the distance from the wall, figure 5.15, has a complete different characteristic than the eddy life time coefficient Γ as function of the wall distance, figure 5.9(c). All efforts to normalize the eddy life time

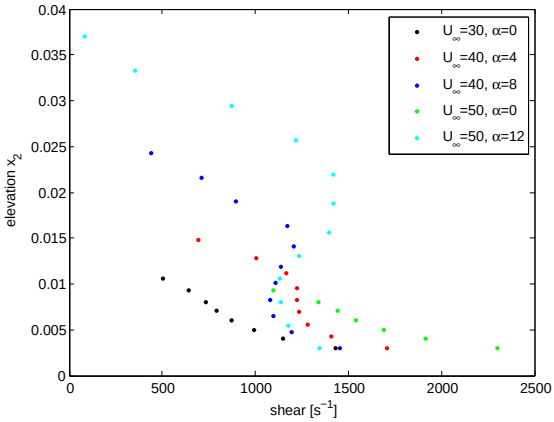

Figure 5.15: The shear of the mean velocity from RANS computation

parameter with any combination of flow quantities containing the local shear lead only to a bigger scatter of the data.
The Mann model does not account for the presence of an adverse pressure gradient in the flow. Bertagnolio [24] makes the hypothesis that the degree of anisotropy can be empirically related to the strength of the pressure gradient. The degree of anisotropy in the Mann Model is only steered by one parameter: the eddy life time parameter Γ. Following the approach of [24], we also define the non-dimensional pressure gradient as

$$\gamma = \left(\frac{\delta^*}{U_e}\right)\left(\frac{(\partial P/\partial s)^2}{\rho\mu}\right)^{1/3} \tag{5.2}$$

where U_e is the flow speed at the edge of the boundary layer and s is the coordinate running along the airfoil surface. By testing we found that scaling the life time parameter Γ with the power of $1/5$th of the pressure gradient parameter $\gamma^{1/5}$ collapsed the data well, figure 5.16. Outliers to the general trend can be observed at the edge of the boundary layer and close to the surface. The data for the case flow speed $U_\infty = 30m/s$ and AoA $\alpha = 0^o$ does not go with the general trend of the other cases. It is not clear if this is a real physical effect or only a consequence of the optimization procedure. There is the possibility of the existence of two local minima of the cost function C_o with very similar minimum values.

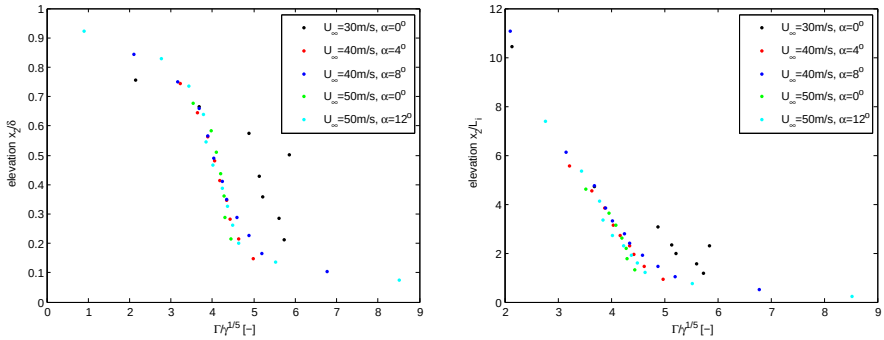

(a) elevation x_2 normalized by the boundary layer thickness δ

(b) elevation x_2 normalized by the length scale L

Figure 5.16: The eddy life time parameter Γ scaled by the power of 1/5th of pressure gradient parameter $\gamma^{1/5}$

5.2.3 Modeling Boundary Layer turbulence with the Mann Model and the $k-\omega$ model

In the following a simplified relation between the input parameters of the Mann Model and the output of the $k-\omega$ model is established which will be used for surface pressure modeling. The length scale L is approximated by the relation

$$L = 0.4\frac{(e_{t,k-\omega})^{3/2}}{\overline{\epsilon}_{k-\omega}} \tag{5.3}$$

and the mean dissipation times constant $\alpha\bar{\epsilon}^{2/3}$ by

$$\alpha\bar{\epsilon}^{2/3} = 1.5\bar{\epsilon}_{k-\omega}^{2/3} \tag{5.4}$$

where the subscript $k-\omega$ indicates the output from the $k-\omega$ model.
Even though the presented data suggests that the relation between $\alpha\bar{\epsilon}^{2/3}$ and ${\overline{\epsilon}_{k-\omega}}^{2/3}$ is dependent on the wall distance, we chose simply to relate them by a constant. The parameter $\alpha\bar{\epsilon}^{2/3}$ influences the level of the spectrum linearly. Hence, an error of this parameter by a factor of less than 1.5 has no big influence on the surface pressure. Moreover, it is very sensitive to uncertainties of the determination of the position.
The eddy life time parameter is modeled by an empirical relation with the pressure gradient parameter γ and a dependence on the wall distance. The data presented above, figure 5.16, suggests that anisotropy decreases with increasing distance from the surface. If the wall distance is normalized with the length

scale L of the Mann Model, figure 5.16(b), the decrease of Γ towards the edge of the boundary layer is linear. Hence, we chose the relation

$$\frac{\Gamma}{\gamma^{1/5}} = max(5 - 0.3\frac{x_2}{L}, 0) \tag{5.5}$$

for our model. The minimum value of Γ is 0. This corresponds to the fully isotropic case. The Mann Model does not support negative values of Γ.
The 'badness' parameter is used as measure to evaluate how well the model describes the turbulence, figure 5.17.
The one point cross spectral density F_1^{12} was adulterated the most, especially for high AoAs, figure 5.17(c) and 5.17(e). 'Badness' increased also for the F_1^{33} component. Fortunately those components are not important for surface pressure modeling. The computation of the one point spectral density F_1^{22} improved compared to using the parameters obtained by optimization. The increase of the 'badness' parameter towards the edge of the boundary layer at high AoAs is mainly due to the weakness of the RANS computation. It underestimates the boundary layer thickness.
The one point spectral densities of the 11 and 22-component are also compared to the one computed from the original von Karman spectrum. The one point cross spectral density F_1^{12} is zero in the case of the von Karman spectrum and the one point spectral density F_1^{33} is the same as F_1^{22}. They were excluded from the comparison. The one point spectral densities for the 11 and 22-component of the von Karman energy spectrum can be derived analytically and read

$$F_1^{11}(k_1) = \frac{\Gamma(5/6)}{\sqrt{\pi}\Gamma(1/3)}\sigma_{11}^2\frac{\Lambda}{(1+(k_1\Lambda)^2)^{5/6}} \tag{5.6}$$

$$F_1^{22}(k_1) = \frac{\Gamma(5/6)}{6\sqrt{\pi}\Gamma(1/3)}\sigma_{22}^2\Lambda\frac{3+8(\Lambda k_1)^2}{(1+(k_1\Lambda)^2)^{11/6}} \tag{5.7}$$

where $\Gamma(x)$ denotes the Gamma function. σ_{22}^2 is given by the empirical relation $\sigma_{22}^2 = 0.45\,e_t$. To conserve the total turbulent kinetic energy we set $\sigma_{11}^2 = 0.8833\,e_t$. The 'badness' parameter is shown in figure 5.18. The one point spectral density F_1^{22} is modeled well by both models with more or less the same value of the 'badness' parameter. At some positions the von Karman Model gives slightly better results. Only in one case, figure 5.18(e), the Mann model gives a significantly better results close to the wall. The Mann Model significantly improves the prediction of the one point spectral density F_1^{11}.

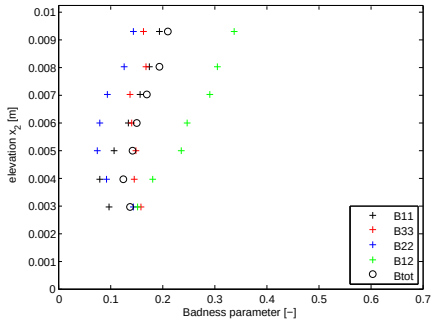

(a) $U_\infty = 30m/s$ and $\alpha = 0^o$

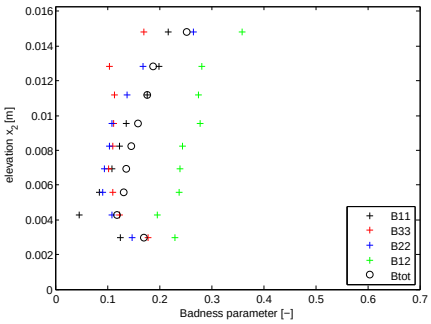

(b) $U_\infty = 40m/s$ and $\alpha = 4^o$

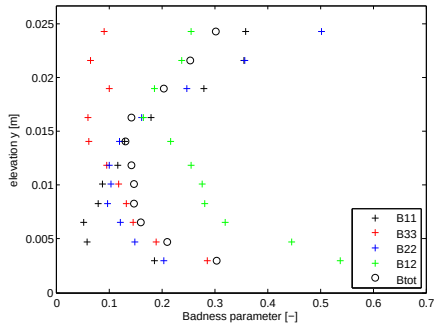

(c) $U_\infty = 40m/s$ and $\alpha = 8^o$

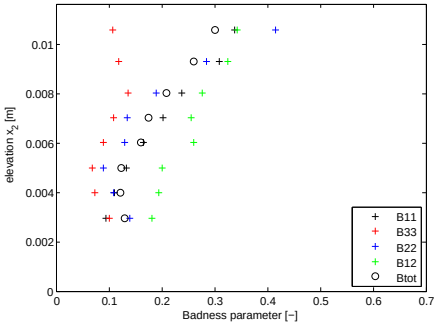

(d) $U_\infty = 50m/s$ and $\alpha = 0^o$

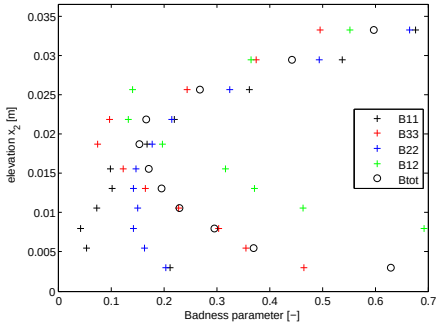

(e) $U_\infty = 50m/s$ and $\alpha = 12^o$

Figure 5.17: 'Badness' parameter for one point spectral densities with Mann Model Input from RANS

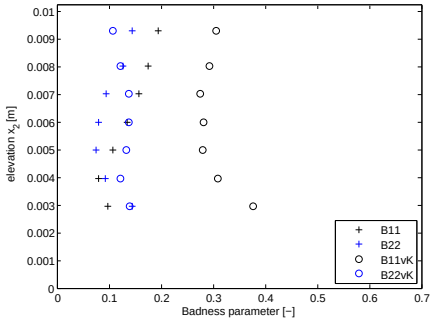

(a) $U_\infty = 30m/s$ and $\alpha = 0^o$

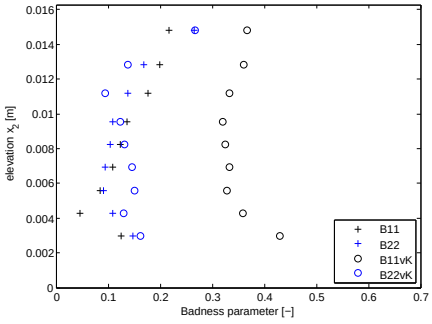

(b) $U_\infty = 40m/s$ and $\alpha = 4^o$

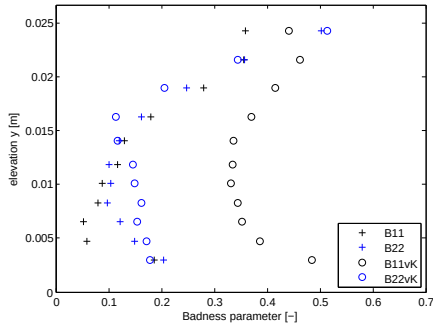

(c) $U_\infty = 40m/s$ and $\alpha = 8^o$

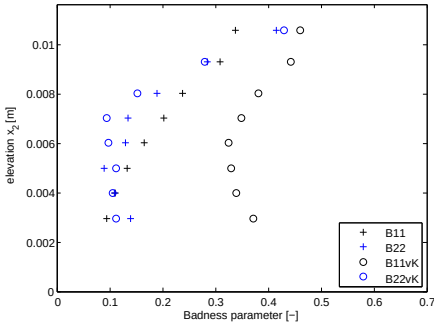

(d) $U_\infty = 50m/s$ and $\alpha = 0^o$

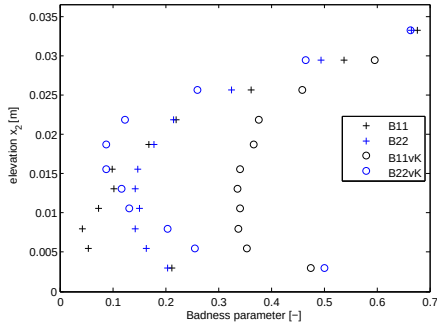

(e) $U_\infty = 50m/s$ and $\alpha = 12^o$

Figure 5.18: Comparison of the 'Badness' parameter for one point spectral densities with Mann Model and von Karman energy Spectrum (Input from RANS)

5.2.4 Evaluation of the cross correlation by Comparison with LES

The present measurements give only access to the one point auto spectral density. However, modeling the cross correlation of the vertical velocity fluctuations as function of two wall distances x_2 and y_2 is of utmost importance. In chapter 2 we discussed several possibilities to model this cross correlation function. The SPKMa and SPKMi model do not fulfill the cross correlation inequality, eq. 2.158. In some cases, this can lead to severe mistakes, figure 5.19. In the

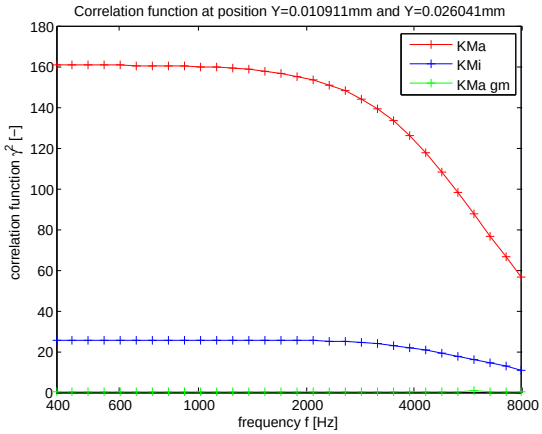

Figure 5.19: The correlation function γ^2 for the case $U_\infty = 50m/s$ and $\alpha = 0°$

selected case of $U_\infty = 50m/s$ and $\alpha = 0°$ the boundary layer is relatively thin and the cross correlation was evaluated very close to the airfoil surface. A cross correlation coefficient γ^2 of 160 as predicted by the SPKMa model is highly unphysical. In a thin boundary layer the input parameter $\alpha\bar{\epsilon}^{2/3}$, L and Γ of the Mann model change rapidly and it is not sufficient to use arithmetic mean values. Using integral mean values decreases the value of the correlation function largely, but it's value is still too high. The only realistic estimation of the correlation function is given by the SPKMagm model.
For the case of $U_\infty = 30m/s$ and $\alpha = 8°$, the correlation function γ^2 of the SPKM model can be compared to the LES calculation described in chapter 4. The correlation function computed with LES is much higher than the correlation function predicted by the model in all displayed cases, figure 5.20. The cross correlation function was evaluated at positions where the energy content of the spectral density was significant. The different SPKM models give very similar results in this case. The correlation function computed from LES data is not only higher, but it decreases also slower. It can be observed by its relative

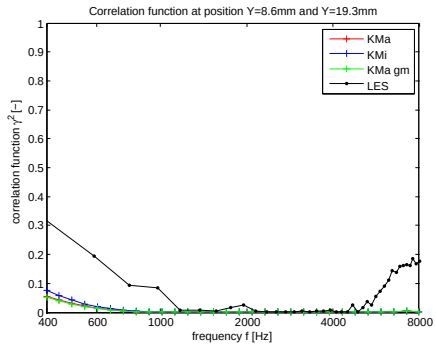

(a) wall normal position y=8.6mm and y=19.3mm

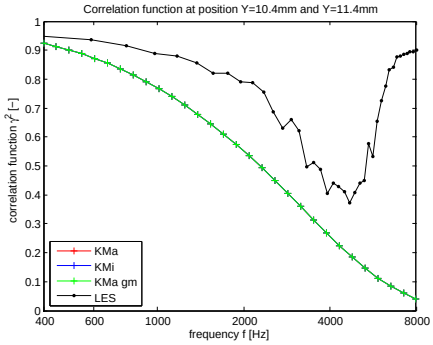

(b) wall normal position y=10.4mm and y=11.4mm

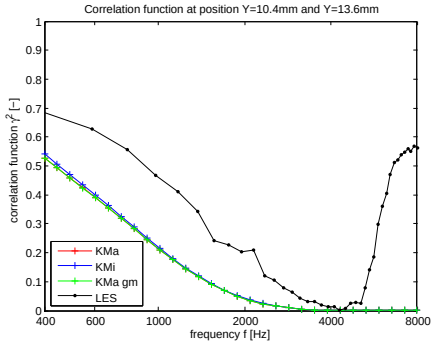

(c) wall normal position y=10.4mm and y=13.6mm

Figure 5.20: The correlation function γ^2 for the case $U_\infty = 30m/s$ and $\alpha = 8^o$ in comparison with LES data

difference for the case of a small separation distance, figure 5.20(b) and a larger separation distance, figure 5.20(c). The correlation function from LES might be biased high on the other hand, because the computational domain was very narrow in spanwise direction. This leads to an accumulation of energy. It can be proven by comparing the one point velocity spectral density to measurements, figure 5.21. The auto spectral density predicted by LES is larger than the measured ones while the SPKM model predicts the PSD very good. Considering this, LES can only be used for a qualitative judgment of the SPKM model. For quantitative improvement measurements are needed.
The correlation length l_c provides a good overview of how well the correlation

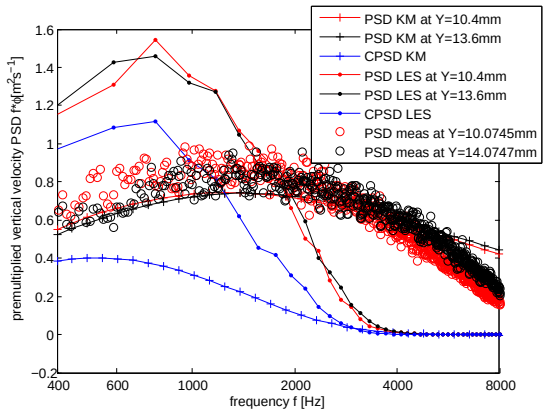

Figure 5.21: PSD and CPSD for the case $U_\infty = 30m/s$ and $\alpha = 8^o$ from SPKM model, LES and measurement

function γ^2 is modeled. It is defined as

$$l_c(x_2, \omega) = \int_0^\infty \gamma(x_2, y_2, \omega) dy_2 \tag{5.8}$$

and shown in figure 5.22 for LES and the SPKMagm model. Note that the

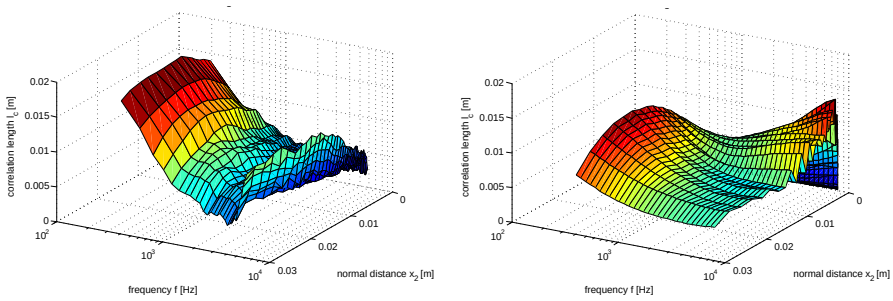

(a) LES (b) SPKMagm

Figure 5.22: The correlation length l_c (eq. 5.8) from LES and SPKMagm

upper integration limit was reduced to the boundary layer thickness. In the low frequency range the characteristics of the length scale from LES and SPKMagm are similar. The LES data is only valid up to a frequency of about 4000Hz, because of the filter. The SPKMagm model gives too high length scales in the high frequency range close to the airfoil surface. The high frequency range is linked to the high wave number range, especially in the present case where the

convection velocity in the boundary layer is small. At high wave numbers and small values of the normal distance to the wall x_2 the e-function terms in eq. 2.141 $e^{-ik_2x_2}$ and $e^{ik_2y_2}$ oscillate very fast. This might explain the wavy shape of the correlation length at high frequencies with increasing normal distance. The undesired increase of the correlation length with frequency close to the wall has a sinusoidal shape and might therefore be linked to these terms as well. The rapid change of the model input parameter $\alpha\bar{\epsilon}^{2/3}$, L and Γ can not lead to an overestimation, because of the definition of the cross spectral density in the SPKMagm model. The defect of the model close to the airfoil surface influences the surface pressure prediction in the lower frequency range only if the boundary layer is thin and the velocity spectrum there contains a significant amount of energy. In the high frequency range almost the whole boundary layer is affected and surface pressure prediction are supposed to be biased high.
For a quantitative comparison between LES and SPKMagm the correlation length l_c at a fixed similar frequency and function of the wall distance or fixed wall distance and function of frequency is plotted in figure 5.23. The correla-

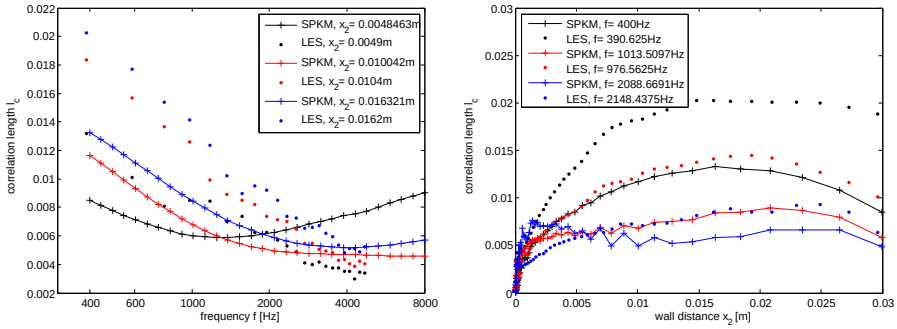

(a) fixed wall distance x_2 (b) fixed frequency f

Figure 5.23: The correlation length l_c from LES and SPKMagm at fixed frequency or wall distance

tion length computed with the SPKMagm model is about a factor 2 smaller than the result from LES. The fact that the correlation length does not decrease monotonously with increasing frequency are a clear defect of the model, figure 5.23(a). The over prediction of the correlation length close to the wall and the oscillations can be observed for the two highest frequencies shown in figure 5.23(b). The oscillation problem arises from a change of the wall distance, because the plots with varying frequency are smooth.
The correlation length from the SPKMagm model is shown in figure 5.24 for several other flow conditions at a chordwise position x/c=0.894. The defects of the SPKMagm model are less severe for low AoAs, figure 5.24(a) and 5.24(c)

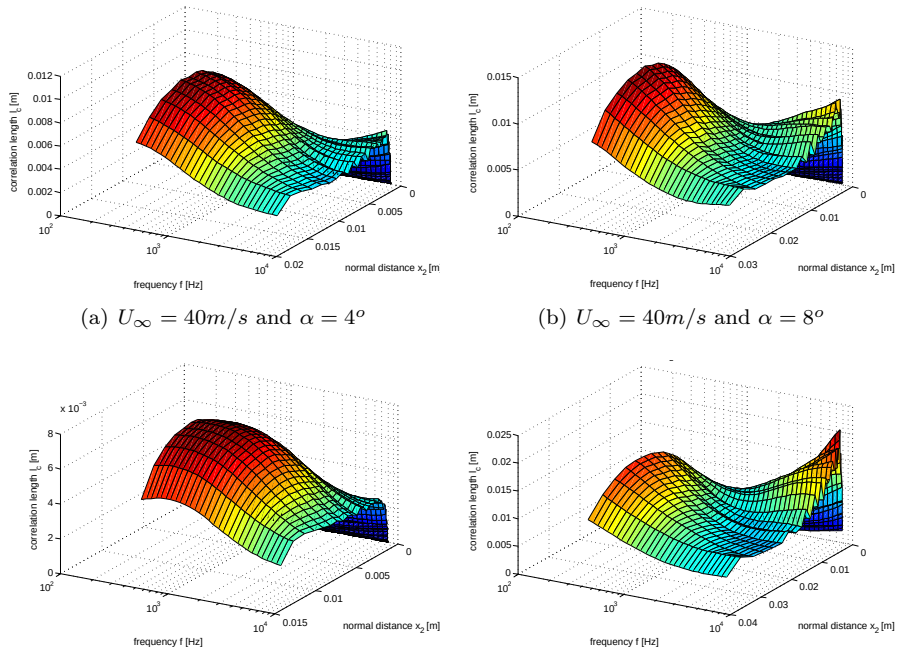

(a) $U_\infty = 40m/s$ and $\alpha = 4^o$

(b) $U_\infty = 40m/s$ and $\alpha = 8^o$

(c) $U_\infty = 50m/s$ and $\alpha = 0^o$

(d) $U_\infty = 50m/s$ and $\alpha = 12^o$

Figure 5.24: The correlation length l_c from SPKMagm at chordwise position x/c=0.894

than for high AoAs, figure 5.24(b) and 5.24(d), because the local velocity close to the wall is higher in the case of low AoAs and thin boundary layers. In this case the wave number associated with a certain frequency is lower and the model is consequently valid in a larger frequency range.

5.2.5 Velocity Profiles measured in the VTST

The SPKM model shall also be applied to the two airfoils tested in the VTST. The RANS flow solver is the basis of the SPKM model and the boundary layer velocity profile obtained from the computation was first compared to the hot wire measurements for validation, before we compared the velocity PSD.
The comparison between the measured and computed boundary layer profiles for the NACA064-618 airfoil show significant differences, figure 5.25. At high AoAs ($\alpha_E > 4.4°$) the measured boundary layer profile is much thicker than the one predicted by RANS and the velocity gradient is much smaller. This

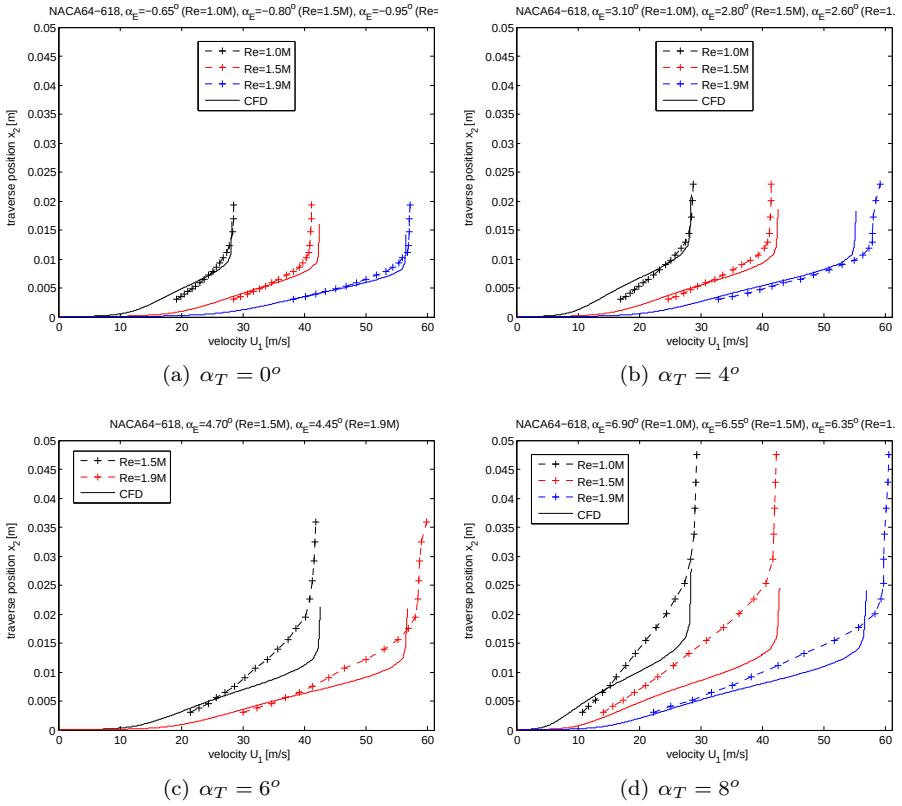

(a) $\alpha_T = 0^o$ (b) $\alpha_T = 4^o$

(c) $\alpha_T = 6^o$ (d) $\alpha_T = 8^o$

Figure 5.25: Comparison of the measured and computed boundary layer velocity profile of the NACA064-618 airfoil at chordwise position x/c=0.975

is in contrast to the good agreement of the measured and predicted surface pressure distributions. A good agreement is achieved only at low AoAs and the highest Reynolds number. Possible explanations for the differences are the higher uncertainty of the probe positioning compared to the experiment in the LSWT, the influence of the TE on the flow at position x/c=0.975 and the far downstream transition from laminar to turbulent flow which makes it difficult for RANS to give good predictions.

For the NACA64-618t airfoil a very good agreement between measurement and computation is achieved for Reynolds number $Re = 1.9M$, figure 5.26. For the lower Reynolds number, the agreement is not so good, but better than for the NACA64-618 airfoil. Transition occurs earlier on the NACA64-618t than on the NACA64-618 which might be the reason why the RANS computation works better.

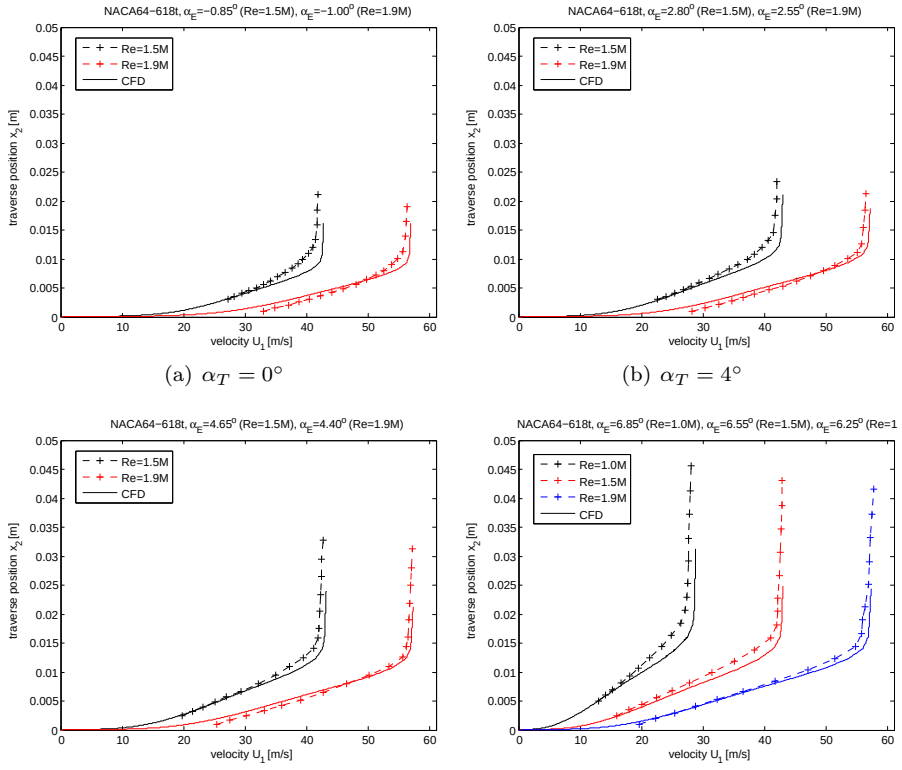

(a) $\alpha_T = 0°$ (b) $\alpha_T = 4°$

(c) $\alpha_T = 6°$ (d) $\alpha_T = 8°$

Figure 5.26: Comparison of the measured and computed boundary layer velocity profile of the NACA064-618t airfoil at chordwise position x/c=0.975

5.2.6 Application of the SPKM model to the Data measured in the VTST

The way of computing the input parameter for the Mann Model in the SPKM model was optimized for the NACA0015. To check if this model is general we compare the premultiplied measured one point spectra on the NACA64-618 and NACA64-618t airfoil with the SPKM model. We chose only cases where the measured and RANS computed boundary layer velocity profile was in good agreement to minimize the uncertainty of the SPKM model introduced by the RANS computation. The comparison at a Reynolds number of $Re = 1.5M$ is shown in figure 5.27. The maximum of the premultiplied spectral density is predicted very well for all components (expect slight shortcomings for the 11-component) at the wall distance of $x_2 \approx 4mm$. It confirms that the length

scale L is modeled correctly. The length scale is insensitive to positioning errors of the probe, because it changes little with the wall distance. At the position closer to the edge of the boundary layer, the length scale is still in fairly good agreement with the measurement, but not as good as at the position closer to the wall. This is probably due to uncertainties of the RANS computation at the edge of the boundary layer.
The levels of the measured and computed spectral density are in fairly good agreement indicating a good prediction of the dissipation $\alpha\bar{\epsilon}^{2/3}$ by RANS. However, the spectral density of the streamwise component F_1^{11} and the cross spectral density F_1^{12} are overpredicted while the one of the vertical component F_1^{22} is well predicted. A better overall agreement would be achieved with a lower value of the eddy life time parameter Γ, because F_1^{11} and F_1^{12} grow relative to F_1^{22} with increasing Γ, see figure 2.5. Length scale and spectral level grow linearly with Γ, except the streamwise component which grows exponentially. A change of Γ mainly effects the streamwise component. A lower value of Γ would decrease the length scale of the 11-component considerably and should improve the agreement between measurement and computation. A change in the length scale is not so obvious as a change of spectral level in figure 5.27, because the wave number axis is logarithmic.
At a Reynolds number of $Re = 1.9M$, computation and measurement do not match, figure 5.28. It is very unlikely that the SPKM model becomes non-valid because of a change of the Reynolds number or flow speed. During the development a range of velocities and Reynolds numbers were considered. The boundary layer is very thin in this case and the measured one point spectral densities are very sensitive to positioning errors of the hot wire probe. At high velocities the traversing mechanism might not have worked properly. It is therefore highly recommend to repeat the experiment with a more accurate traversing system to detect Reynolds number effects.
The badness parameter is shown in figure 5.29 for various flow situations and the two airfoils. It is higher as the badness parameter for the comparison of measurement and prediction on the NACA0015 airfoil. This means that the SPKM model is not general with its previous parametrization. A data base with different airfoil models has to be considered for improvement of the SPKM model. The increase of the badness parameter at the boundary layer edge (which is found in every case) is due to an underestimation of the boundary layer thickness by the RANS computation. The increase of the badness parameter has to be investigated with a more accurate traversing system as discussed above.

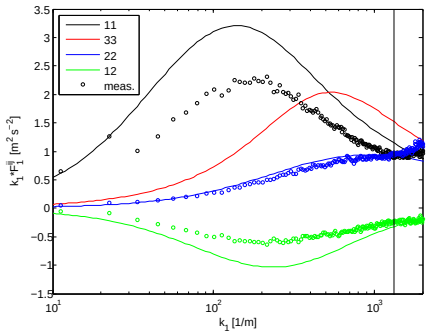

(a) NACA64-618, $\alpha_E = 2.80°$, wall distance $x_2 = 4.1mm$

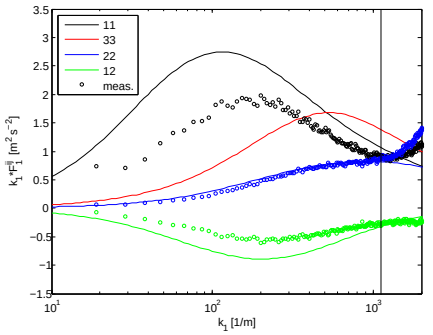

(b) NACA64-618, $\alpha_E = 2.80°$, wall distance $x_2 = 6.5mm$

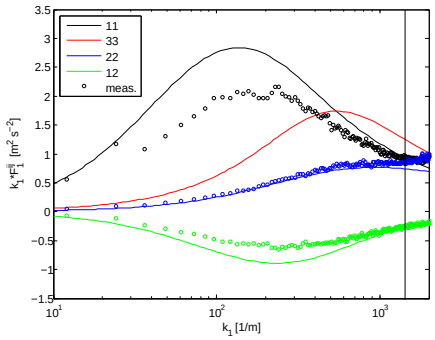

(c) NACA64-618t, $\alpha_E = 2.80°$, wall distance $x_2 = 4.2mm$

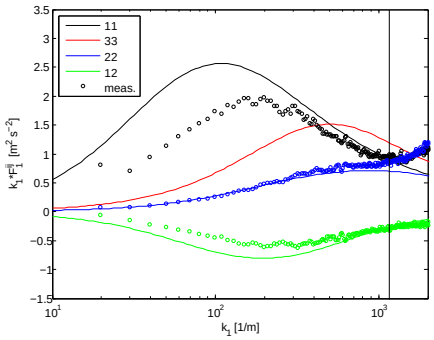

(d) NACA64-618t, $\alpha_E = 2.80°$, wall distance $x_2 = 6.6mm$

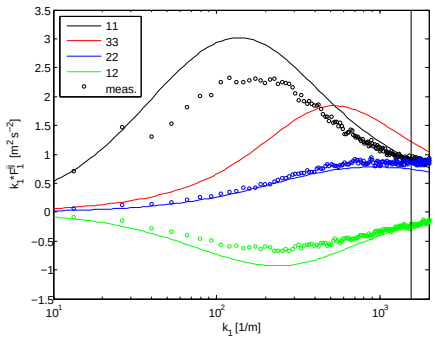

(e) NACA64-618t, $\alpha_E = 4.65°$, wall distance $x_2 = 4.0mm$

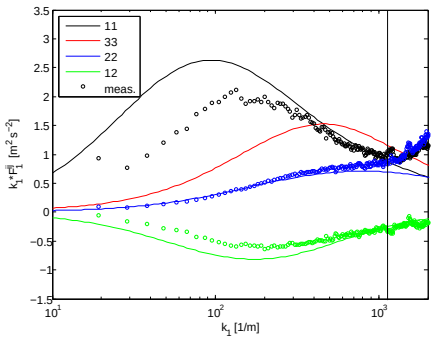

(f) NACA64-618t, $\alpha_E = 4.65°$, wall distance $x_2 = 8.0mm$

Figure 5.27: Computed One Point Spectra with Input Parameters from the SPKM model compared to Measurements for the NACA64-618 and NACA64-618t airfoil at chordwise position x/c=0.975 and Reynolds number $Re = 1.5M$ (black line: wave number k_1 corresponding to a frequency of 5800Hz)

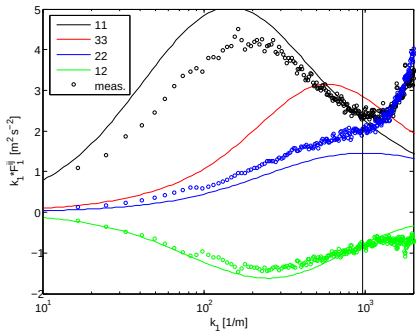

(a) NACA64-618, $\alpha_E = 2.60°$, wall distance $x_2 = 4.1mm$

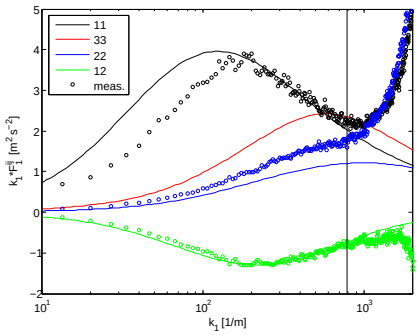

(b) NACA64-618, $\alpha_E = 2.60°$, wall distance $x_2 = 6.5mm$

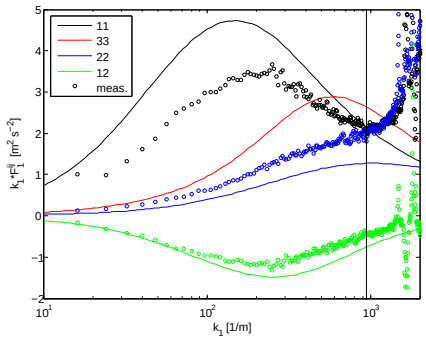

(c) NACA64-618t, $\alpha_E = 2.55°$, wall distance $x_2 = 3.9mm$

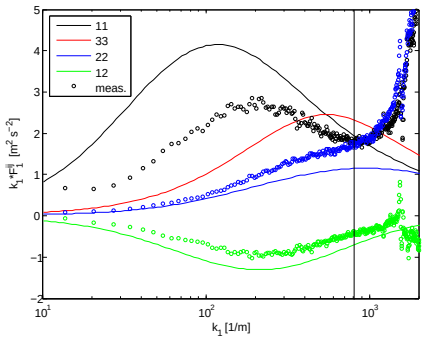

(d) NACA64-618t, $\alpha_E = 2.55°$, wall distance $x_2 = 6.3mm$

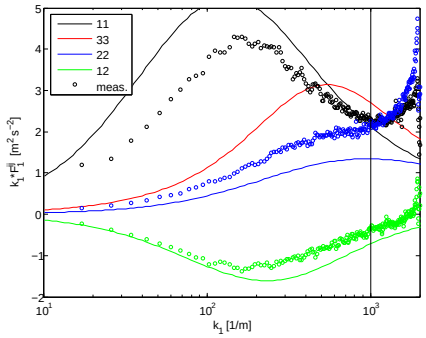

(e) NACA64-618t, $\alpha_E = 4.40°$, wall distance $x_2 = 4.2mm$

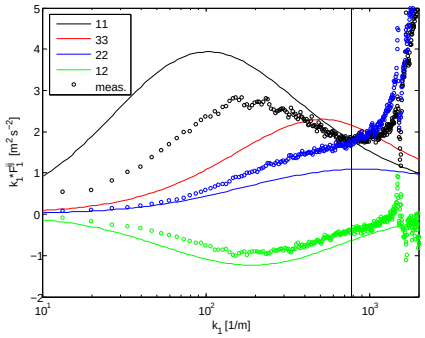

(f) NACA64-618t, $\alpha_E = 4.40°$, wall distance $x_2 = 8.0mm$

Figure 5.28: Computed One Point Spectra with Input Parameters from the SPKM model compared to Measurements for the NACA64-618 and NACA64-618t airfoil at chordwise position x/c=0.975 and Reynolds number $Re = 1.9M$ (black line: wave number k_1 corresponding to a frequency of 5800Hz)

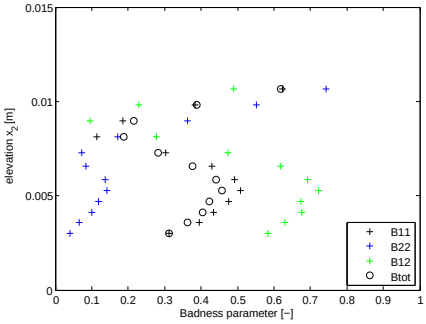

(a) 64-618, $Re = 1.5M$ and $\alpha_E = 2.80°$

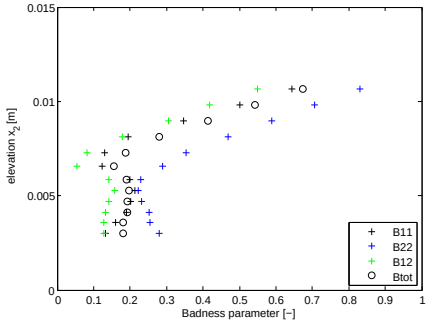

(b) 64-618, $Re = 1.9M$ and $\alpha_E = 2.60°$

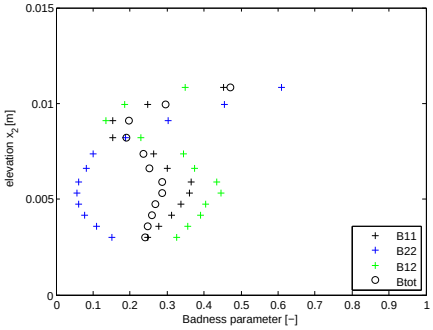

(c) 64-618t, $Re = 1.5M$ and $\alpha_E = 2.80°$

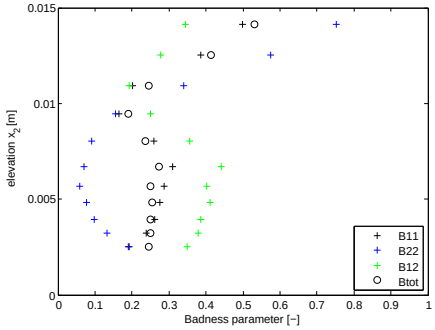

(d) 64-618t, $Re = 1.5M$ and $\alpha_E = 4.65°$

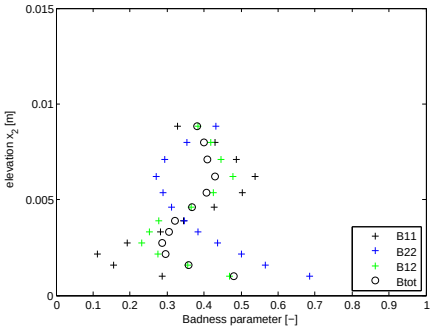

(e) 64-618t, $Re = 1.9M$ and $\alpha_E = 2.55°$

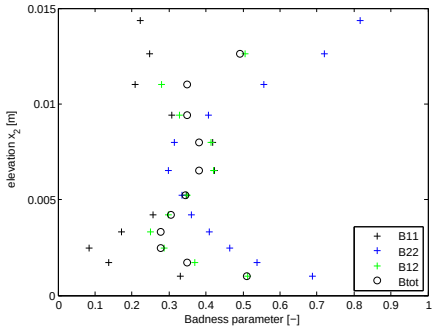

(f) 64-618t, $Re = 1.9M$ and $\alpha_E = 4.40°$

Figure 5.29: Comparison of the 'Badness' parameter for one point velocity spectral densities with SPKM Model

5.3 Prediction of the Surface Pressure

5.3.1 Model Comparison

The different models will be compared by source integral computations of the surface pressure. The source integral is defined by eq. 2.160 integrated over the wave number space and one time in normal direction y_2. The source integral $I_p = I_p(\omega, x_2)$ is a function of the angular frequency ω and the distance normal to the wall x_2. It shows where in the boundary layer the surface pressure fluctuations are created.
The case of $U_\infty = 50m/s$ and $\alpha = 0°$ is a difficult test case for the SPKM model, because the boundary layer is thin and the surface pressure integrand has its maximum close to the surface, figure 5.30. The SPKMa and the SPKMi model

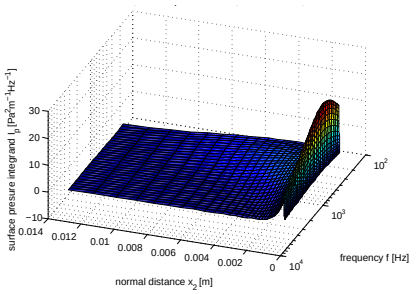

(a) SPKMa

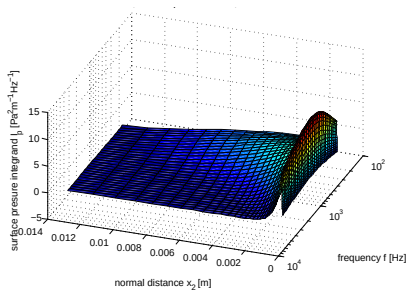

(b) SPKMi

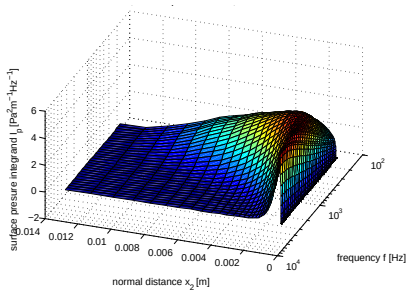

(c) SPKMa gm

Figure 5.30: Surface pressure integrand I_p at $U_\infty = 50m/s$ and $\alpha = 0°$ and chordwise position x/c=0.894

overestimate the surface pressure integrand close to the wall. Even though the overestimation occurs only in a very narrow wall distance band, it is so

severe that the value of the integral is influenced. The SPKMagm model works much better in the vicinity of the surface, but in the higher frequency range it overestimates the surface pressure integrand as well. It is only valid in a limited frequency range.
In the case of $U_\infty = 50m/s$ and $\alpha = 12°$ the boundary layer is much thicker and the SPKM model shows very good results in the low frequency where the levels are dominant in this case, figure 5.31. The SPKMa and SPKMi model still

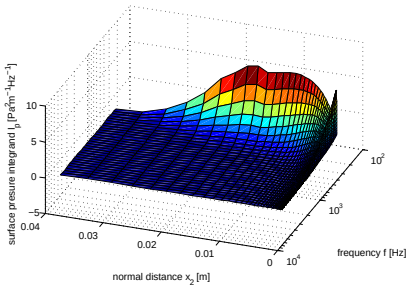

(a) SPKMa

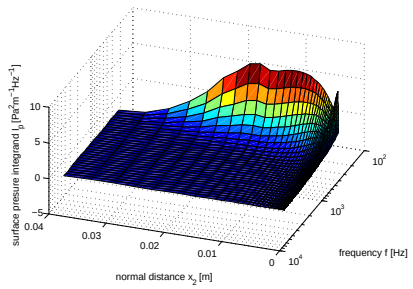

(b) SPKMi

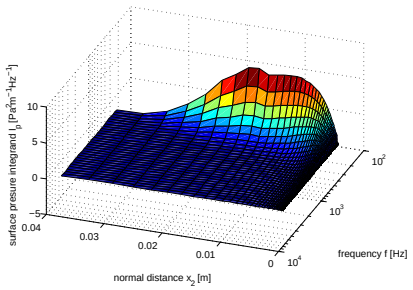

(c) SPKMa gm

Figure 5.31: Surface pressure integrand I_p at $U_\infty = 50m/s$ and $\alpha = 12°$ and chordwise position x/c=0.894

overestimate the surface pressure integrand close to the airfoil surface, but the effect on the value of the integral is negligible. Further away from the surface the models produce almost identical values. Therefore the SPKMagm model should be preferred, because it doesn't suffer so much from shortcomings close to the airfoil surface.

5.3.2 Comparison of the Surface Pressure

We compare model predictions of the surface pressure with measurements. Due to reasons mentioned above we concentrate on the SPKMagm model. Besides of the comparison with measurements it is also compared to prediction with the TNO model of section 2.4.1, figure 5.32. The SPKMagm model gives very

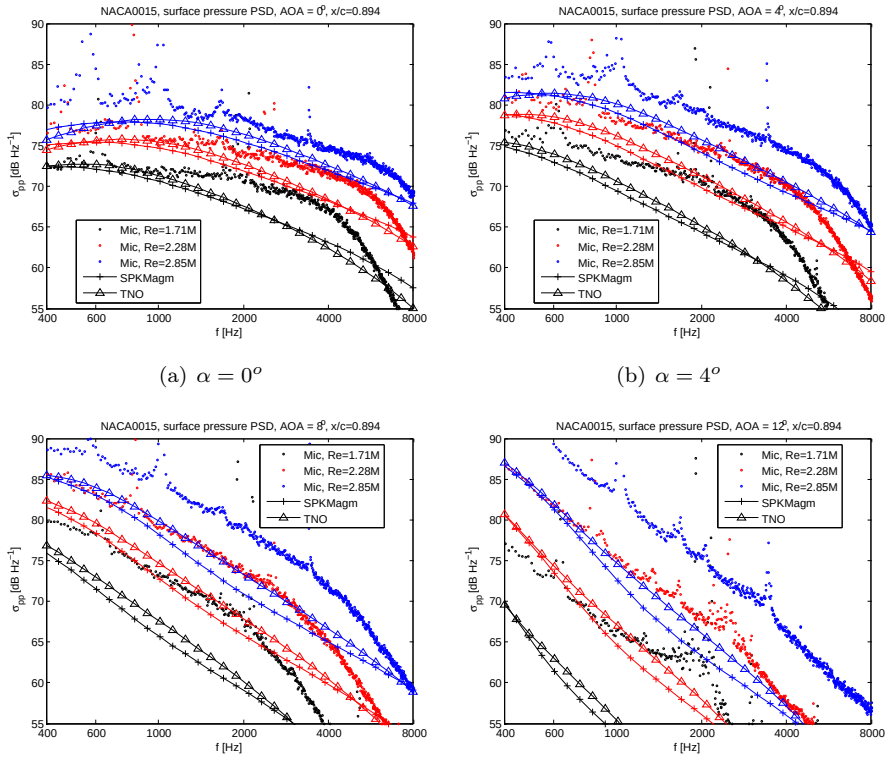

(a) $\alpha = 0^o$ (b) $\alpha = 4^o$

(c) $\alpha = 8^o$ (d) $\alpha = 12^o$

Figure 5.32: Comparison of the surface pressure PSD from measurement, SPKMagm and TNO model

similar results as the TNO model. The measured surface pressure PSD is underestimated. The difference between measurement and prediction increases with increasing AoA. The local mean pressure gradient increases with increasing AoA and during the development of the models the assumption of a zero pressure gradient boundary layer was made. The one point velocity auto spectral density was empirically tuned to take pressure gradient effects into account. The cross spectral function is not corrected for the presence of a pressure gradient.

The comparison with LES computations revealed that the SPKMagm model underestimates the velocity cross spectral density and the vertical length scale. Unfortunately the LES computation was only available for one particular flow situation. A study investigating a possible link between the underestimation of the cross spectral density and the local pressure gradient could not be performed. Even though the absolute values of the LES computation are questionable, it is very likely that the too low levels of the surface pressure PSD predicted by the SPKM model are caused by the smaller value of the correlation function compared to LES. The output of the $k-\omega$ turbulence model and the velocity profile of the RANS computation is another possible source of error, because the $k-\omega$ turbulence model is tuned to fit zero pressure gradient boundary layer data.

The overestimation of the surface pressure integrand I_p is orders of magnitude lower than the errors leading to the underestimation of the surface pressure PSD. The error occurring in the surface pressure gradient becomes more severe with increasing frequency. The surface pressure PSD of the SPKMagm model reflects this with the inflection point which is a clearly unphysical behavior. The SPKMagm model is only valid up to the frequency of the inflection point. But when comparing the slope of the surface pressure PSD at high frequencies, it has to be noted that the microphones were not individually calibrated. There is a higher uncertainty of the measured PSD in the high frequency range because of the unknown Helmholtz eigen frequency. This might partly explain why both models show a steeper decline of the surface pressure PSD than the measurement.

The similarity of the result of the SPKMagm and the TNO model is remarkable, because both models are very different. The vertical correlation length scale L_2^{22} in eq. 2.154 is independent of the frequency. LES and the SPKMagm model show that the correlation length scale is a function of the frequency and therefore one would expect a difference in the slope of the predicted surface pressure PSD. In the TNO model the convection velocity is less than the local flow speed. It seems to compensate for the unrealistic correlation length scale modeling. Finally, the length scale correction of a factor 2 proposed by [24] ensures a good agreement of the level of the surface pressure PSD of the TNO and SPKMagm model.

For some selected cases, computations with the SPKMagm model assuming the ratio of 0.7 between the convection velocity and the local flow speed (as in the TNO model) were compared to computations assuming a ratio of 1, figure 5.33. The computations assuming a ratio $c_v = 1.0$ give a better agreement with the measurement in all cases. Only in the case of $U_\infty = 50m/s$ and $\alpha = 0°$ the computations with a ratio of $c_v = 0.7$ are quantitatively closer to the measurement, but the slope of the measured surface pressure PSD is better predicted by assuming a ratio of $c_v = 1.0$.

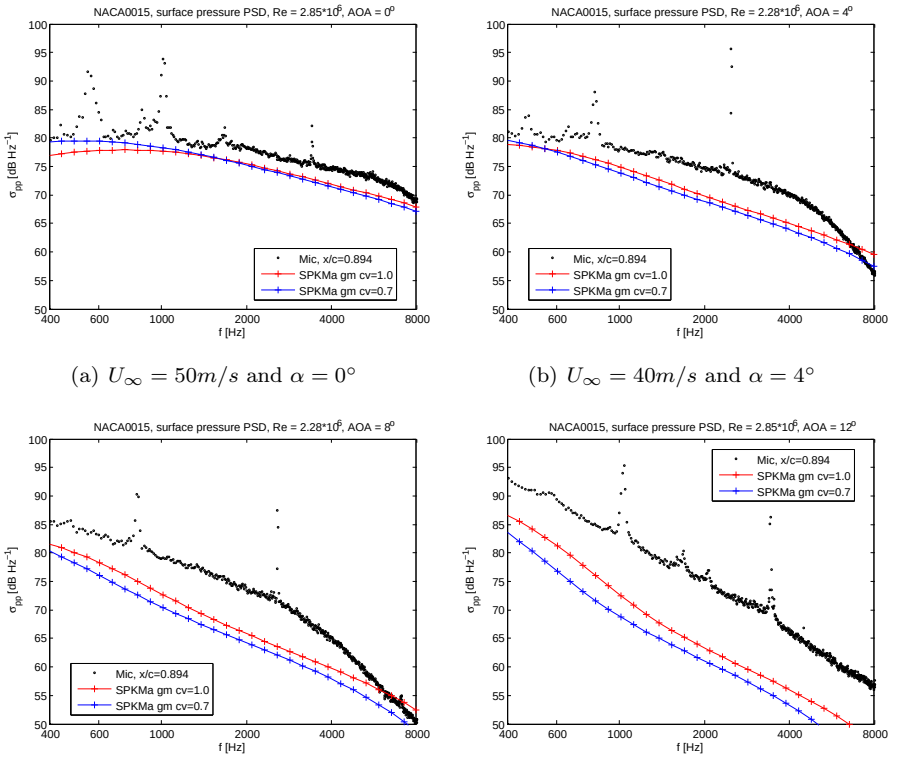

(a) $U_\infty = 50m/s$ and $\alpha = 0°$

(b) $U_\infty = 40m/s$ and $\alpha = 4°$

(c) $U_\infty = 40m/s$ and $\alpha = 8°$

(d) $U_\infty = 50m/s$ and $\alpha = 12°$

Figure 5.33: Comparison of the surface pressure PSD from measurement, SPKMagm model with convection speed to local flow speed ratio $c_v = 1.0$ and $c_v = 0.7$

5.3.3 Application of the SPKM model to the Surface Pressure PSD measured in the VTST

In the case of the NACA0015 airfoil, the measured velocity spectral densities matched the computed ones, but the surface pressure PSD was not predicted correctly. For the NACA64-618 and NACA64-618t airfoil there is already a mismatch in the velocity spectral density, hence the surface pressure PSD predictions are not expected to be good. On the other hand it is interesting to investigate how much uncertainty the mismatch of the velocity spectral density introduces.

For the NACA64-618t airfoil at the Reynolds number of $Re = 1.5M$, the one point vertical velocity spectral density was predicted well. The surface pressure

PSD for various AoAs in this case is predicted badly, figure 5.34. The predicted

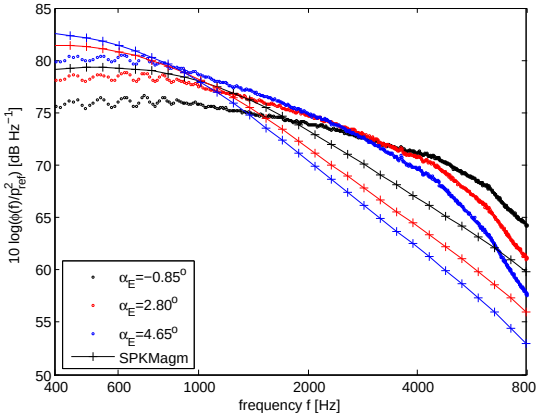

Figure 5.34: Comparison of the surface pressure PSD from measurement and SPKMagm at chordwise position x/c=0.975 on the NACA64-618t airfoil and Reynolds number $Re = 1.5M$

surface pressure PSD have more energy in the low frequency range and less in the high frequency range than the measurement. It typically corresponds to a thicker boundary layer. But the measured and computed boundary layer velocity profiles showed that the computation underestimates the boundary layer thickness and we would expect the reversed trend in the surface pressure PSD. The boundary layer is thinner than one of the NACA0015 airfoil, because the chord length in the VT experiment was only 0.6m compared to 0.9m in the LM experiment. Hence, we have to check if the problems of the SPKMagm model close to the airfoil surface lead to this error. The surface pressure Integrand I_p for the NACA64-618t airfoil at a Reynolds number of $Re = 1.5M$ and the effective AoA $\alpha_E = 2.8°$ is shown in figure 5.35. The maximum of the surface pressure integrand I_p is located away from the surface of the airfoil. An overestimation by the model occurs only at high frequencies if at all.
Another possible explanation is that the surface pressure PSD is influenced by edge effects, because the the location x/c=0.975 is very close to the TE. The basis of the surface pressure modeling, eq. 2.91, assumes that the flow is bounded by a surface of infinite extension. This is clearly a simplification of the physical setup. Moreover, the turbulent flow in the boundary layer might not be fully developed, because transition occurs far downstream of the LE on this airfoil. In this case the surface pressure model would not be valid.
The same qualitative difference between measurement and computation can be observed for NACA64-618 and NACA64-618t airfoil at Reynolds numbers $Re = 1.5M$ and $Re = 1.9M$ at similar effective AoAs, figure 5.36. The un-

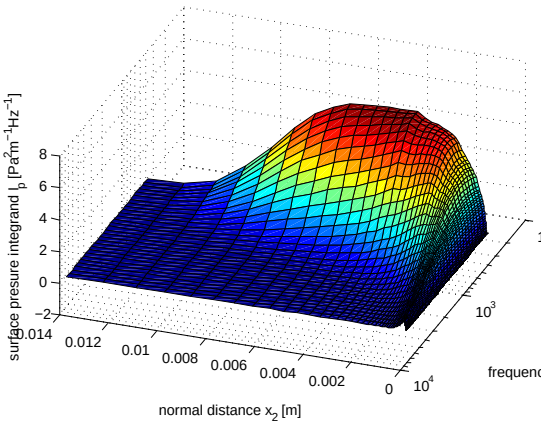

Figure 5.35: The surface pressure integrand I_p from the SPKMagm model at chordwise position x/c=0.975 on the NACA64-618t airfoil at Reynolds number $Re = 1.5M$ and effective AoA $\alpha_E = 2.8°$

derestimation of the one point velocity spectral density at Reynolds number $Re = 1.9M$ for both airfoils does not lead to an underestimation of the surface pressure PSD. The dominating error is the same as for the cases with Reynolds number $Re = 1.5M$. A further investigation of the error source is beyond the scope of the present work.

5.4 Surface Pressure Statistics

The surface pressure statistics are analyzed via its spectral data. We used the method of [61] to compute the cross and power spectral density ((C)PSD). The time series of measured surface pressures were sampled with a frequency of f_s=50kHz. The sampling time was 30s in the VT experiment and 19s in the LM experiment. The time segments to compute the periodogram were 2048 samples in the LM experiment, yielding a frequency resolution of ∼24.41Hz and 4096 samples in the VT experiment, yielding a frequency resolution of ∼12.21Hz. This was chosen to get a well averaged PSD. If the PSD is presented in dB the reference pressure is $p_{ref} = 2 \cdot 10^{-5}$Pa.

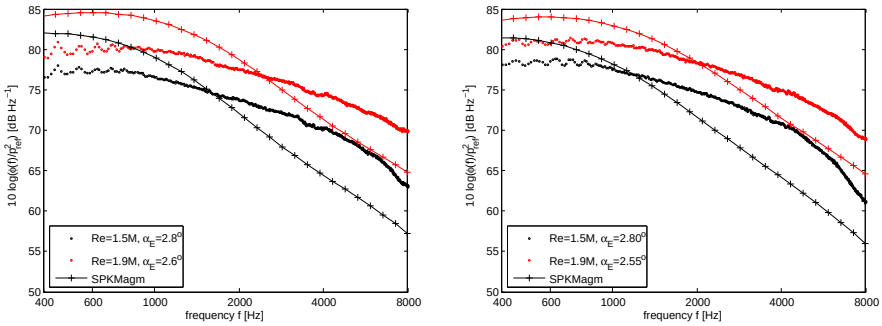

(a) NACA64-618 (b) NACA64-618t

Figure 5.36: Comparison of the surface pressure PSD from measurement and SPKMagm at chordwise position x/c=0.975 on the NACA64-618 and NACA64-618t airfoil

5.4.1 Power Spectral Density (PSD) close to the Trailing edge

The PSD close to the TE is the most important input to the noise models of chapter 2. First we analyze the variation of the PSD at several streamwise distances from the TE for the NACA64-618t airfoil, figure 5.37. The PSD varies significantly within the last 10% of the chord. The slope of the PSD gets steeper when reaching the TE, because the boundary layer becomes thicker and more energy is transfered from high to low frequencies. The model to predict the far field sound pressure using surface pressure statistics as input of Howe [11] and Amiet with Roger's extension [14] assume homogenity in the streamwise direction close to the TE. This assumption is clearly violated in the case presented in figure 5.37. The consequences for the noise prediction will be discussed later. On the other hand, no sign of TE backscattering is found in the PSD even at x/c=0.975. Backscattering is supposed to cause an interference pattern in the surface pressure PSD. But the measured PSD are very smooth.
The PSD is expected to scale in proportion with the boundary layer thickness. Therefore it is appropriate to evaluate the PSD as function of the Strouhal number instead of the frequency. The reference length for the Strouhal number is the displacement thickness δ^*. As reference velocity one can either use the free stream velocity or the friction velocity. Hence, we define the Strouhal number as $S_t = 2\pi f \delta^* / U_{ref}$. The PSD has to be rescaled according to $PSD(S_t) = PSD(f)\ U_{ref}/(2\pi\delta^*)$. The PSD as function of the Strouhal number for the same situation as in figure 5.37 is displayed in figure 5.38. The displacement thickness and friction velocity are taken from the CFD calculation, because no

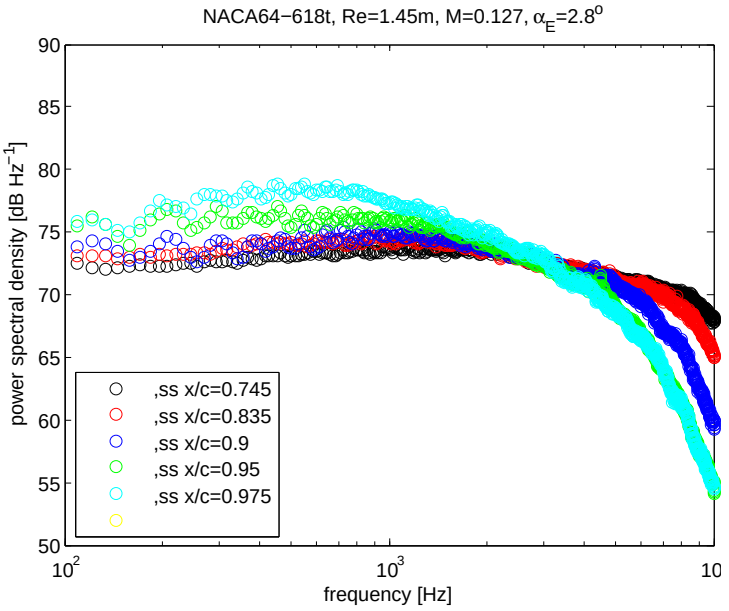

Figure 5.37: Streamwise variation of the PSD for the NACA64-618t airfoil

measurement data was available. The scaling with the free stream velocity as reference velocity works better than the scaling with the friction velocity and will be used in the following. The PSD collapse within an allowance for variation of 3dB. The scaling with the friction velocity has reversed the order of the PSD compared to the unscaled data. It overestimates the effect of the boundary layer. This could be due to the uncertainty when using scaling parameters from CFD.

The scaled PSD at varying chordwise position for the NACA64-618 and the NACA0015 measured in the LSWT are also displayed, figure 5.39. For the NACA64-618, the scaled PSD collapse except the one furthest away from the TE at x/c=0.746. The peak which is not found in the other PSD might be due to vortex shedding from a laminar separation bubble. The transition from laminar to turbulent occurs about x/c=0.5 at this flow speed and AoA. Hence, the boundary layer might not be fully turbulent at x/c=0.746.

The sharp peaks seen in the PSD of the NACA0015 are due to the background noise in the LSWT and should be ignored. Apart from that, the scaled PSD collapse. The scaling law works well for a range of different airfoils, Reynolds numbers and AoAs. Note that it was only evaluated in the linear part of the C_l-α polar.

The effect of a changing AoA for the 3 different airfoils is studied in figure 5.40. In all cases the scaled PSD do not collapse. The transfer of the energy

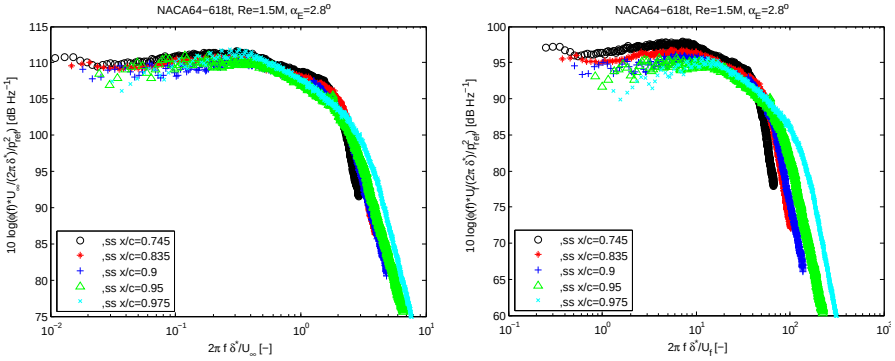

(a) reference velocity: flow speed U_∞ (b) reference velocity: friction velocity U_f

Figure 5.38: Streamwise variation of the normalized PSD for the NACA64-618t airfoil (scaling parameters from CFD)

from high to low frequencies with increasing AoA goes faster than the growth of the boundary layer thickness. An explanation might be that the loading of the boundary changes, because the adverse pressure gradient on the suction side of the airfoil changes with the AoA. Hence, the pressure gradient has to be taken into account when describing the development of the boundary layer. Another explanation could be that the boundary layer grows faster with the AoA than the CFD results suggest. This explanation can be discarded, because the normalized PSD scaled with the displacement thickness obtained from hot wire measurements at x/c=0.975 show qualitatively the same picture as when using the scaling parameters from CFD, figure 5.41. The effect of changing flow speed on the normalized PSD can be balanced by using the free stream dynamic pressure $q_0 = 0.5\rho_0 U_\infty^2$ to normalize the PSD. The result for various airfoils and AoAs is shown in figure 5.42. For the NACA0015 at geometric AoA $\alpha_G = 8°$ the PSD coalesce. In the other cases the PSD do not coalesce. Another systematic pattern is found. The PSD at the higher flow speed is shifted to lower frequencies compared to the PSD at the lower flow speed. To get a better match the frequency should be scaled with a velocity that is less different for the three cases. But in this case the level of the PSD with the highest flow speed would become lower and be lower than the PSD measured at the lowest flow speed. The change of effective AoA with the flow speed in the VTST can not explain this difference, because the same is observed for the NACA0015 in the LSWT at geometric AoA $\alpha_G = 0°$ and the effective AoA is independent of the flow speed in the LSWT.

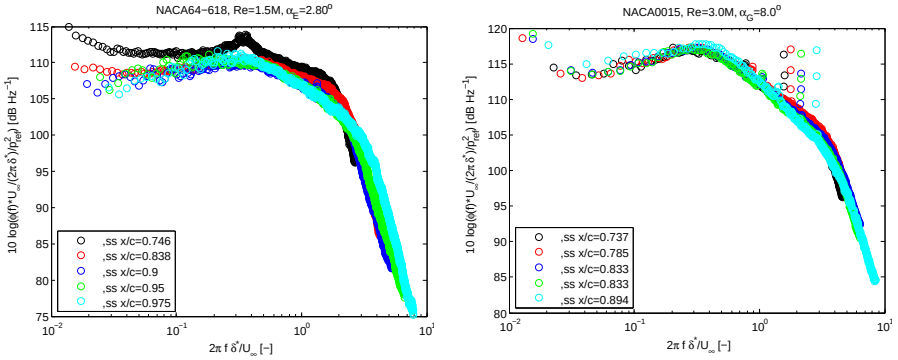

(a) NACA64-618, Re=1.5M, VTST (b) NACA0015, Re=3.0M, LSWT

Figure 5.39: Streamwise variation of the normalized PSD for the NACA64-618 and NACA0015 airfoil (scaling parameters from CFD)

5.4.2 Streamwise Statistics of the Pressure Field

The streamwise pressure field is mainly defined by the convection of the eddies in the boundary layer. As the surface of the pressure sensors is small, the eddy field can be approximated as frozen while convecting past the sensor. The moving axis spectrum (defined in chapter 2) becomes a delta function and the streamwise wave number $k_1 = \omega/U_c$ is selected in the integration over k_1. Both acoustic formulations of chapter 2 make the assumption of a frozen turbulence field convected past the trailing edge. Hence, the only but very important quantity of the streamwise pressure field is the convection velocity U_c.
The convection velocity can be evaluated from the phase of the CPSD between two sensors located at different streamwise positions. Following [12], the convection velocity can be calculated by

$$U_c = 2\pi f \Delta s/\varphi \tag{5.9}$$

with Δs the streamwise separation distance of the two sensors on the airfoil surface. The spanwise separation of two sensors is not considered in eq. 5.9, because a mean flow exists only in the streamwise direction. It was checked that the phase of the CPSD of only spanwise separated sensors was zero in all cases. However, the larger the separation in spanwise direction is the smaller is the frequency range in which significant coherence exists, because the lifespan of the eddy is proportional to its scale. Only the large scales (correponding to low frequencies) will remain coherent for large separation distances. Hence, the microphone setup in Virginia Tech experiment allows only a evaluation of the convection velocity for low frequencies. The microphones on the NACA0015 in

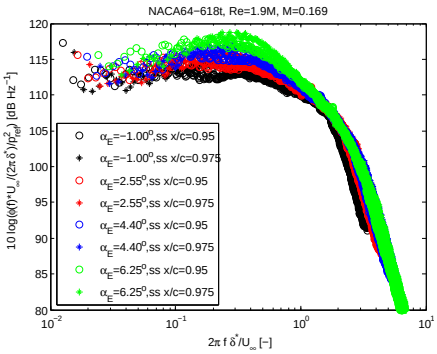

(a) NACA64-618t, Re=1.9M, VTST

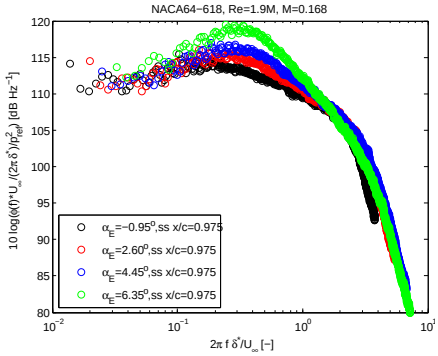

(b) NACA64-618, Re=1.9M, VTST

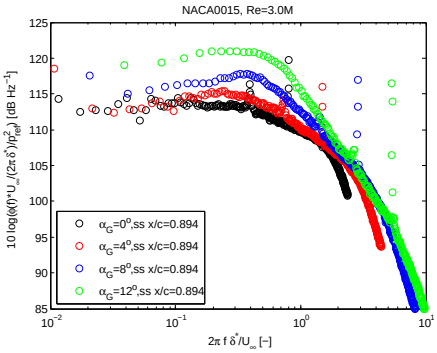

(c) NACA0015, Re=3.0M, LSWT

Figure 5.40: Variation of the normalized PSD with changing angle of attack (scaling parameters from CFD)

the LM experiment are too far separated to allow an investigation of the convection velocity. For the higher frequencies we have to rely on the analysis of [12]. However, these results have only limited validity for the present experiment, because Brooks [12] found that the normalized convection velocity depends on the flow speed. It is very probable that it also changes with different airfoil shape and AoA. Anyways, we will compare our results to the empirical relation Brooks [12] gives for the NACA0015 airfoil at AoA $\alpha = 0°$ and flow speed U_∞=69.5m/s in the low frequency range

$$\frac{U_c}{U_\infty} = -9 \cdot 10^6 f + 0.5(1 + \Delta s/\delta^*)^{0.16}. \tag{5.10}$$

The normalized convection velocity as function of the Strouhal number at different chordwise positions and separation for the NACA64-618 at two different

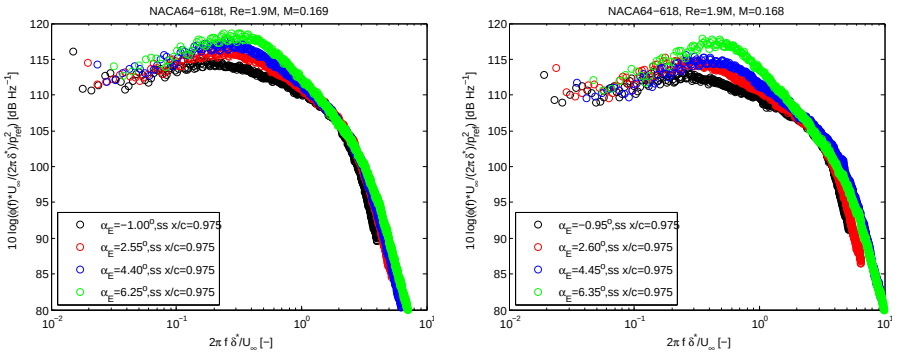

(a) NACA64-618t, Re=1.9M (b) NACA64-618, Re=1.9M

Figure 5.41: Variation of the normalized PSD with changing angle of attack for the NACA64-618t and NACA64-618 airfoil (scaling parameters from measurement)

AoAs and flow speeds is plotted in figure 5.43. The displayed chordwise position is the one of the upstream microphone and the displacement thickness is calculated at this position. The plots show only data with significant coherence. The lowest frequency considered is 200Hz. The three positions furthest away from the TE show the same characteristic trend for all flow conditions. We find in agreement with Brooks [12] that the higher the separation $\Delta s/\delta^*$, the higher is the convection velocity. The curves increase monotonously in the low Strouhal number range and tend towards the empirical value by eq. 5.10. This is quite remarkable, because the empirical relation was obtained for completely different flow conditions. However, there is no data for the high frequencies to show that the convection velocity follows Brooks' [12] relation in the high Strouhal number range.
Following Brooks' [12] relation means also that the convection velocity increases the smaller the displacement thickness is. In other words, the thinner the boundary layer is the higher the convection velocity. Hence, at high AoAs the convection velocity decreases. Therefore the far field sound pressure is expected to grow slower with increasing AoA than the surface pressure fluctuations.
At the position closest to the TE the convection velocity behaves completely different. The vortices in the boundary layer seem to be accelerated when approaching the TE. The measured value of the convection velocity is the highest compared to the other positions even though the separation of the sensors $\Delta s/\delta^*$ is the smallest. When comparing the convection velocity at this position for different AoAs, one can see that the convection velocity decreases with increasing boundary layer thickness. This observation is in agreement with the results of the measurements further upstream.

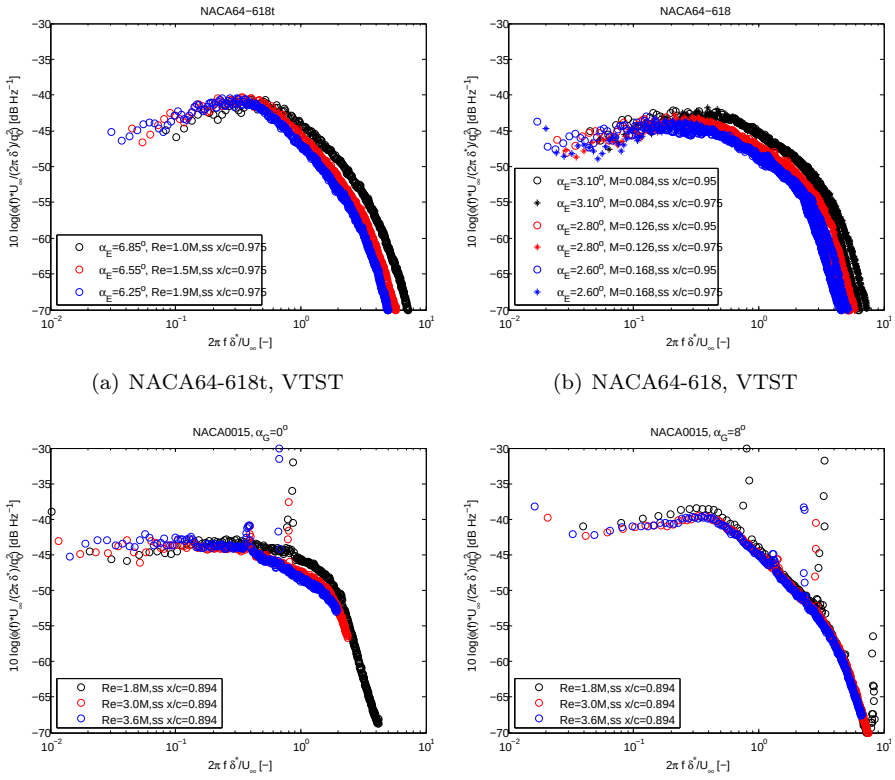

(a) NACA64-618t, VTST

(b) NACA64-618, VTST

(c) NACA0015, $\alpha_G = 0°$, LSWT

(d) NACA0015, $\alpha_G = 8°$, LSWT

Figure 5.42: Variation of the normalized PSD with changing flow speed (scaling parameters from CFD). Note: the PSD is normalized by the free stream dynamic pressure

This acceleration effect would have significant influence on the radiation of sound in the low frequency range. To verify whether this is a 'real' effect or just an artifact of the measurement technique an uncertainty estimation is carried out. The main error sources in the evaluation of the convection velocity is a possible phase mismatch between two sensors and the uncertainty in the positioning of the pin holes on the airfoil model. A phase mismatch between two sensors can occur due to differences between individual microphones because of machining tolerances and differences in the sound transmission in the individual adapter (geometric differences and differences in medium temperature or pressure). All surface pressure microphones are calibrated with the B&K Probe Microphone Type 4182 and difference in the placement of the probe relative to the pinhole gives a phase difference. This phase difference increases linearly with the

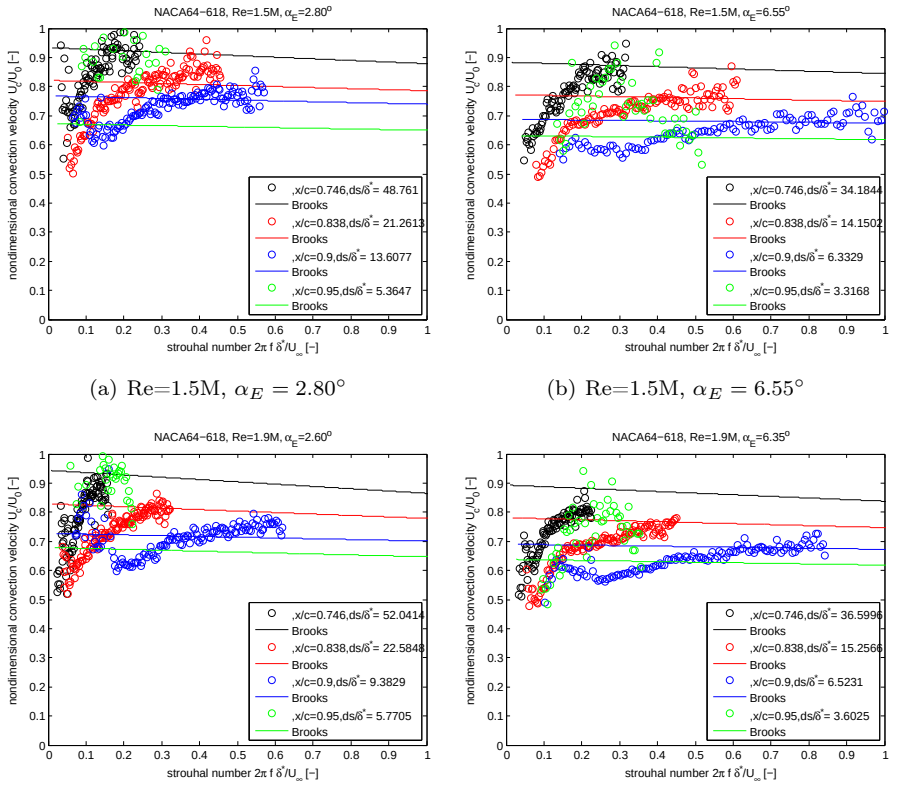

(a) Re=1.5M, $\alpha_E = 2.80°$

(b) Re=1.5M, $\alpha_E = 6.55°$

(c) Re=1.9M, $\alpha_E = 2.60°$

(d) Re=1.9M, $\alpha_E = 6.35°$

Figure 5.43: Convection velocity for the NACA64-618 airfoil (displacement thickness from CFD)

frequency and is about $\pm 2.1^o$ at 2000Hz, if the reference microphone tip is positioned with an accuracy of $\pm$1mm relative to the pinhole. The frequency limit up to which we found significant coherence between two microphones was 1800Hz in the best case. The phase difference due to fabrication tolerances of the microphone are not stated by the manufacturer and the phase difference due to transmission in the individual adapter can not be calculated. Therefore we assumed that the phase error is $\pm 5^o$ in the whole frequency range of interest. The error due to misplacement of the tip of the reference microphone is small compared to this and neglected in the error calculation. The uncertainty of the position of the pinhole is about $\pm$0.2mm (manufacturer tolerances). There is an additional uncertainty due the calculation of the distance between two microphones, because we assumed the airfoil surface to be linear between two sensors. The overall positioning accuracy is then estimated as $\pm$0.5mm.

The relative uncertainty of the convection velocity is given by the relation

$$\frac{u(U_c)}{U_c} = \sqrt{\left(\frac{u(\Delta s)}{\Delta s}\right)^2 + \left(\frac{u(\varphi)}{\varphi}\right)^2} \tag{5.11}$$

It is plotted as function of the Strouhal number for the NACA64-618 airfoil at Reynolds number Re=1.9M and effective AoA $\alpha_E = 6.35°$ in figure 5.44(a). The smaller the separation of the two sensors the larger is the uncertainty in

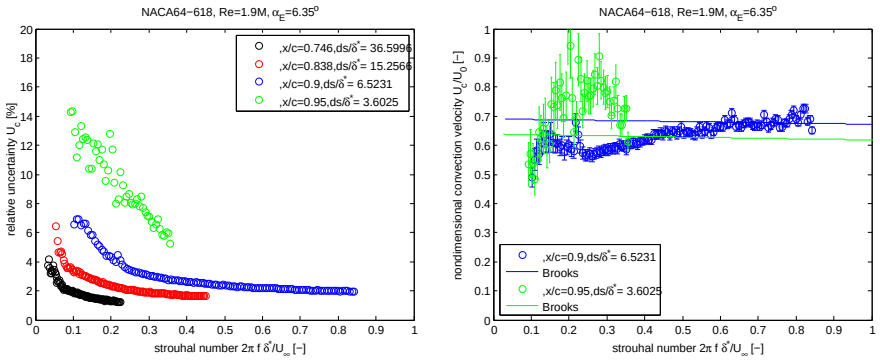

(a) relative uncertainty (b) error bar plot

Figure 5.44: Convection velocity for the NACA64-618 airfoil at Re=1.9M and $\alpha_E = 6.35°$ with uncertainty estimation(displacement thickness from CFD)

the measurement of the convection velocity. The uncertainty due to the positioning of the pinhole is constant over the frequency and small compared to the uncertainty due to phase mismatch between two sensors. The uncertainty due to phase mismatch is high at low frequencies and decreases monotonously, because the phase increases with frequency and the phase mismatch was considered constant over the frequency. The smaller the separation distance between two sensors, the smaller is also the phase. Hence, the relative uncertainty increases with reduced sensor separation.

The impact of the relative uncertainty on the measurement of the convection velocity is visualized with error bars, figure 5.44(b). The error bars represent the interval $\frac{U_c \pm 2u(U_c)}{U_\infty}$, the 95% confidence interval. The uncertainty estimation clearly confirms the acceleration of the boundary layer vortices when approaching the TE. However the peak value can be anywhere between 0.8 and 1. The impact on the noise predictions will be discussed below.

The normalized convection velocity as function of the Strouhal number at different chordwise positions and separation for the NACA64-618t at two different AoAs and flow speeds is plotted in figure 5.45. The basic features are the same as for the NACA64-618. Again we find a good agreement with Brooks' [12] em-

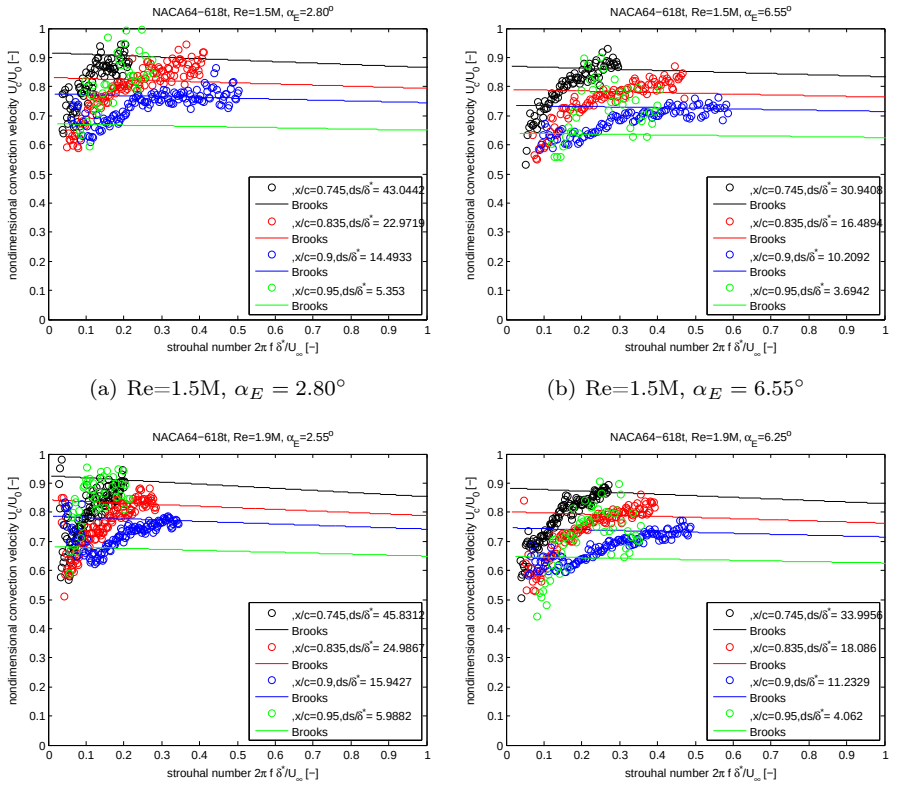

(a) Re=1.5M, $\alpha_E = 2.80°$

(b) Re=1.5M, $\alpha_E = 6.55°$

(c) Re=1.9M, $\alpha_E = 2.55°$

(d) Re=1.9M, $\alpha_E = 6.25°$

Figure 5.45: Convection velocity for the NACA64-618t airfoil (displacement thickness from CFD)

pirical relation for high Strouhal numbers. The biggest difference compared to the NACA64-618 airfoil is that the acceleration of the boundary layer vortices approaching the TE is less strong.
In the case of a tripped boundary layer the acceleration effect disappears, figure 5.46. In the tripped case transition from laminar to turbulent occurs much further upstream and the turbulent boundary layer is more developed when reaching the TE. The acceleration effect might be an effect of a non equilibrium boundary layer.

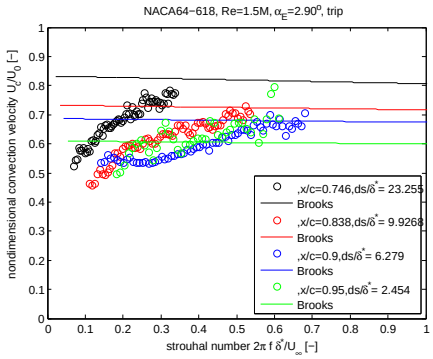

(a) NACA64-618, Re=1.5M, $\alpha_E = 2.90°$

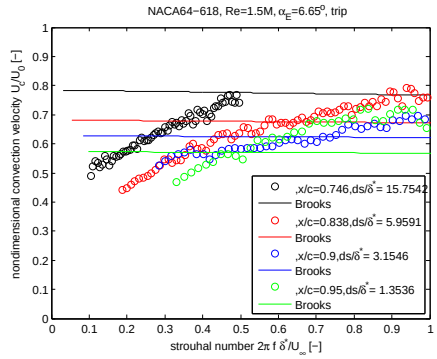

(b) NACA64-618, Re=1.5M, $\alpha_E = 6.65°$

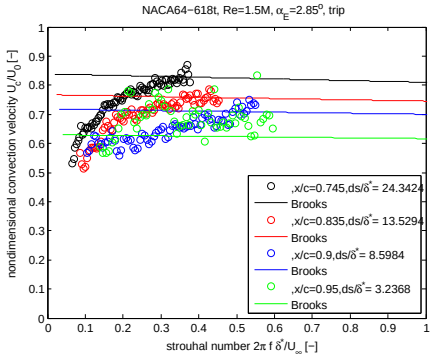

(c) NACA64-618t, Re=1.5M, $\alpha_E = 2.85°$

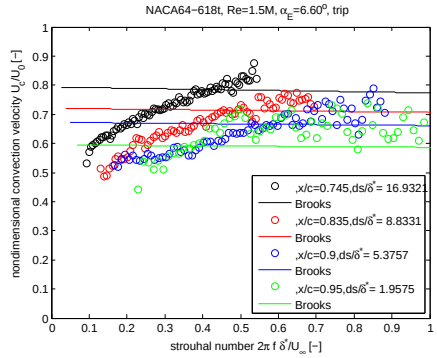

(d) NACA64-618t, Re=1.5M, $\alpha_E = 6.60°$

Figure 5.46: Convection velocity for the tripped airfoils (displacement thickness from CFD)

5.4.3 Spanwise Statistics of the Pressure Field

The correlation function γ as function of the frequency f and the spanwise separation η is measured with the microphone array located at chordwise position x/c=0.975 on the NACA64-618 and NACA64-618t airfoil. The spanwise distributed microphone array on both airfoils consists of 7 microphones, but when making use of homogeneity of the pressure field in spanwise direction the correlation function can be evaluated for 19 separations. Figure 5.47 shows some sample results of the measured correlation function. The sharp peaks observed in figure 5.47(a) and 5.47(c) in the low frequency range are due to the not perfect temperature and pressure correction of the calibration function and have to be ignored. The spanwise extend for which significant correlation exists becomes

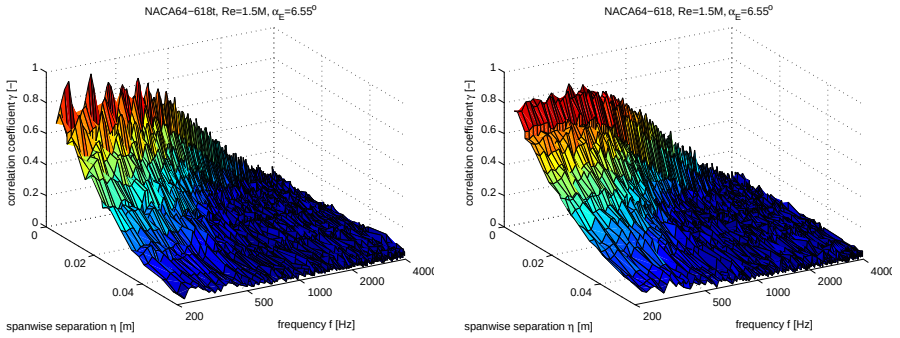

(a) NACA64-618t, Re=1.5M, $\alpha_E = 6.55°$ (b) NACA64-618, Re=1.5M, $\alpha_E = 6.55°$

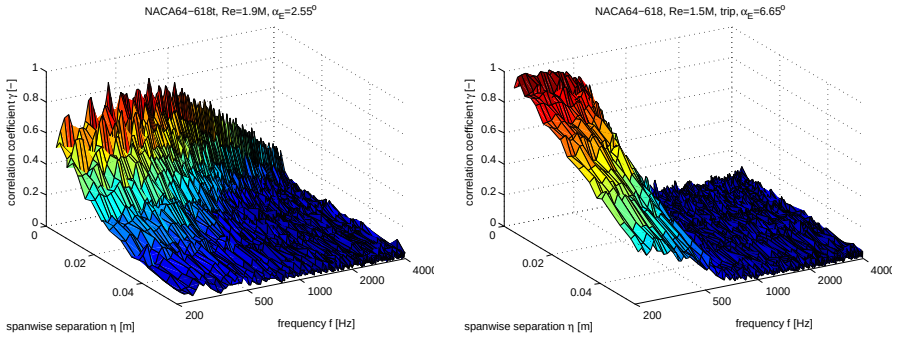

(c) NACA64-618t, Re=1.9M, $\alpha_E = 2.55°$ (d) NACA64-618, Re=1.5M, $\alpha_E = 6.65°$, trip

Figure 5.47: Correlation function measured with microphone array at x/c=0.975

smaller with increasing frequency. It is a direct measure of the physical size of the boundary layer vortices. It means that the eddy size is inversely proportional with the frequency, an expected result. However, the absolute value of the correlation function decreases in the low frequency range. It has the maximum at a characteristic frequency inversely proportional to the boundary layer thickness. For example, the correlation function for the NACA64-618t peaks at higher frequencies for a Reynolds number Re=1.9M and AoA $\alpha_E = 2.55°$ (thin boundary layer, figure 5.47(c)) than for a Reynolds number Re=1.5M and AoA $\alpha_E = 6.55°$ (thick boundary layer, figure 5.47(a)). In the tripped case (figure 5.47(d)), the correlation function changes significantly. Its value remains non zero for much larger spanwise separations in the low frequency range than for all other cases, indicating much larger eddies. But the correlation function tends also more rapidly to zero with increasing frequency.
The spanwise length scale is the integral of the correlation function over the spanwise separation. It can be evaluated directly from the measurements in a

frequency range from 500Hz to 4000Hz for most cases. Only in the tripped case a larger spacing of the sensors would have been necessary.
To have a better overview over this huge amount of data, the correlation function can be presented as function of a pseudo phase, the product of the spanwise wave number and separation. Note that the measured phase of the cross correlation between two sensors at the same chordwise position was zero in all cases, because there was no mean flow in spanwise direction. The spanwise wave number is not well defined and was quite arbitrarily selected as

$$k_3 = \frac{2\pi f}{0.7U_\infty} \tag{5.12}$$

where $0.7U_\infty$ is a very rough estimate of the streamwise convection velocity. Note that Brooks [12] used the measured streamwise convection velocity to define the spanwise wave number.
The effect on the correlation of changing the Reynolds number is illustrated in figure 5.48 for the NACA64-618 airfoil at effective AoA $\alpha_E = -3.3°$ (the zero lift angle). At the zero lift angle the effective AoA is not a function of the flow

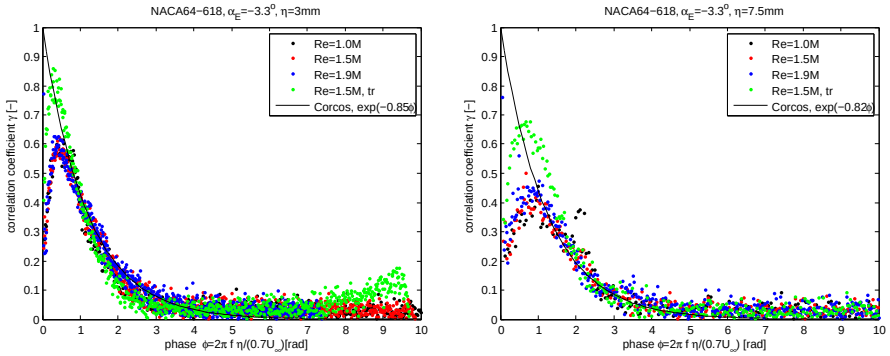

(a) spanwise separation η=3mm (b) spanwise separation η=7.5mm

Figure 5.48: Correlation function vs pseudo phase for the NACA64-618 at effective AoA $\alpha_E = -3.3°$ and varying Reynolds number (green: tripped case)

speed. The data collapses for both separation distances. For phases above a characteristic value the agreement with Corcos' exponential model is good. Below this characteristic phase the measured correlation function is much reduced compared to the exponential model. Note that the empirical constant used to fit the exponential model with the measured data is slightly different for the two different separation distances. In the case of the tripped boundary layer the measured data does not collapse with the data of the other cases. The structure of the boundary layer turbulence is significantly altered by the trip tape.
The effect of a changing AoA on the correlation function is studied for the

NACA64-618 airfoil at Reynolds number Re=1.5M, figure 5.49. The data col-

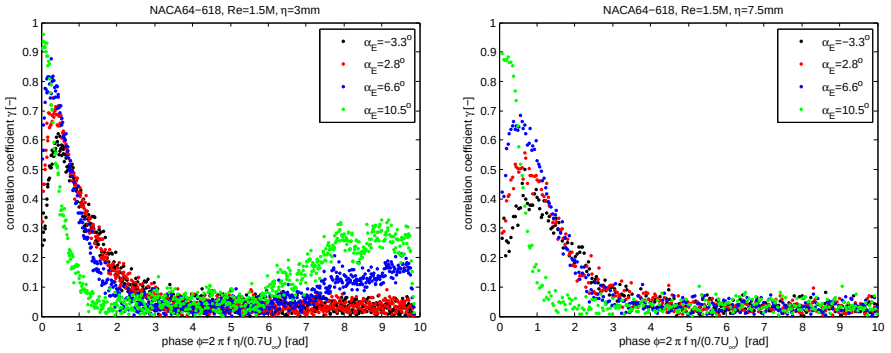

(a) spanwise separation η=3mm (b) spanwise separation η=7.5mm

Figure 5.49: Correlation function vs pseudo phase for the NACA64-618 at varying AoA and Reynolds number Re=1.5M

lapse for both AoA in the linear range of the polar, $\alpha_E = -3.3°$ and $\alpha_E = 2.8°$. At AoA $\alpha_E = 6.6°$ the boundary layer flow on NACA64-618 airfoil begins to separate at the TE. The correlation function begins to deviated from the one of the AoAs in the linear part of the polar. When stalled ($\alpha_E = 10.5°$), the correlation data is significantly different.
A comparison of the NACA64-618 and the NACA64-618t airfoil at an AoA in the linear range of the polar for two different Reynolds numbers is depicted in figure 5.50. The data coalesce. The spanwise surface pressure statistics are

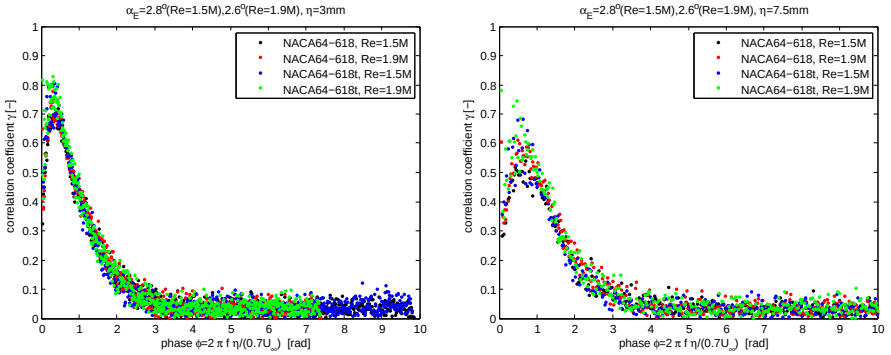

(a) spanwise separation η=3mm (b) spanwise separation η=7.5mm

Figure 5.50: Correlation function vs pseudo phase for the NACA64-618 and NACA64-618t airfoil at varying Reynolds number

almost identical for both airfoils. But the airfoils are very similar, so one has to be careful when generalizing this result.
The noise models of chapter 2 use the spanwise correlation length as input which can be directly derived from the above measurements by integration over the separation distance. The correlation length for both airfoils for several Reynolds numbers and an AoA in the linear range of the polar is plotted in figure 5.51. The correlation length is almost identical for both airfoils. In the untripped

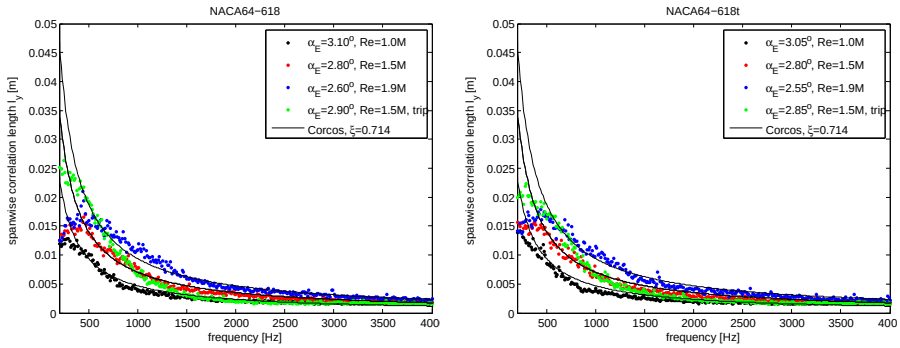

(a) NACA64-618 (b) NACA64-618t

Figure 5.51: Spanwise correlation length vs frequency for the NACA64-618 and NACA64-618t airfoil at varying Reynolds number (green: tripped case)

cases the correlation length can be described by the Corcos model

$$l_c = \frac{U_c}{\xi\omega} \tag{5.13}$$

for frequencies higher than a characteristic frequency. The best fit is achieved with an empirical constant $\xi = 0.714$ when the convection velocity is chosen as $U_c = 0.7U_\infty$. This corresponds to the empirical constant found for a turbulent boundary layer above a flat plate. As the correlation length is an integral parameter the experimental variation is expected to be smaller than for the correlation function and the difference in the empirical constant found for the correlation function might be due to experimental variation of the latter.
The influence of a changing AoA on the correlation length for the NACA64-618 airfoil is presented in figure 5.52. For AoAs in the linear range of the polar the correlation length is independent of the AoA for high frequencies. The characteristic frequency, however, changes with the AoA. It is probably linked to the boundary layer thickness. A good fit with Corcos model is found using the same empirical constant as above. In stall ($\alpha_E = 10.5°$), the function describing the correlation length is much different.

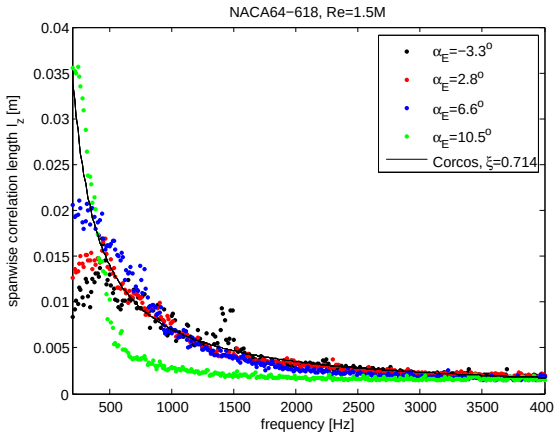

Figure 5.52: Spanwise correlation length vs frequency for the NACA64-618 at Reynolds number Re=1.5M

5.5 Far Field Noise Predictions with measured Surface Pressure PSD

This section aims on validating the acoustic formulation of Howe [11] and Amiet with Roger's extensions [14] by comparison of the far field sound pressure spectrum predicted by using measured surface pressure statistics with the far field sound pressure spectrum measured with the microphone array in the VT experiment.

5.5.1 Assessment of the Prediction Method

The far field sound prediction models of Howe, eq. 2.36, and Amiet/Roger, eq. 2.63, need the surface pressure PSD close to the trailing edge, the spanwise correlation length and the convection velocity on pressure and suction side of the airfoil as input. For the suction side, the first two quantities can be taken directly taken from the measurements at chord position x/c=0.975 presented in section 5.4. The convection velocity could only be measured with high uncertainty in the low frequency range. Additionally, it varied significantly when measured at different chordwise locations, because the turbulent field is highly inhomogeneous in flow direction and it varied also when measured with different separation of the sensors [12]. In the frequency range up to 800Hz we used the convection velocity measured between chordwise position x/c=0.95

and x/c=0.975. This implies assuming the convection field remains unchanged between x/c=0.95 and x/c=1 (TE). In the high frequency range we used the empiric expression by Brooks [12]

$$\frac{U_c}{U_\infty} = 0.39(1 + 2\Delta s/\delta^*)^{0.19} \tag{5.14}$$

valid in the high frequency range for a NACA0012 airfoil at AoA $\alpha = 0°$. In the frequency range between 800Hz and 2000Hz we interpolated linearly between the measured value and the value given by eq. 5.14.
On the pressure side, only the measured surface pressure PSD at x/c=0.95 is available as input for the acoustic model. The focus of the comparison is therefore on cases where the surface pressure PSD on the pressure side was at least 5dB lower than the one on the suction side in the frequency range of interest. It comprises basically all cases for effective AoAs of $\alpha_E = 2.6^o$ and higher. Those are also the relevant cases for wind turbine operation. The contribution of the pressure side to the far field sound pressure is then roughly estimated by assuming that the spanwise correlation length is the same as measured on the suction side and the ratio of the convection velocity to flow speed is 0.7 for frequencies up to 1000Hz, decreasing linearly to 0.4 between frequencies of 1000Hz and 2000Hz and then staying constant at 0.4.
Another important issue is where to take the wall pressure statistics as input for each model. In Amiet's model the measurement should represent the surface pressure on the airfoil at the TE without the effect of edge scattering. As we have seen in section 5.4 the surface pressure PSD measured at x/c=0.975 was free of scattering effects. It is our best estimate of the surface pressure PSD directly at the TE and is used directly as input to the model.
In Howe's model the surface pressure PSD has to be taken directly at the TE. But as outlined in chapter 2 one can take it further upstream where the contribution of the error function in eq. 2.34 tends to one and divide it by four. Hence we take the measured PSD at x/c=0.975 divided by four as input.

5.5.2 Comparison of the Acoustic Models with Microphone Array Response

To compare Howe's and Amiet's model with each other and the measurements we first only evaluated the sound radiated from the suction side. To be able to roughly compare with far field sound measurements we chose a test case in which the surface pressure PSD was about 7dB higher than the one on the pressure side, the NACA64-618 airfoil at Reynolds number Re=1.5M and effective AoA $\alpha_E = 6.55°$, figure 5.53. The observer is assumed to be situated in the center of the microphone array in the computation with both acoustic models. The full solution of Amiet's model with Roger's extensions (eq. 2.63, green

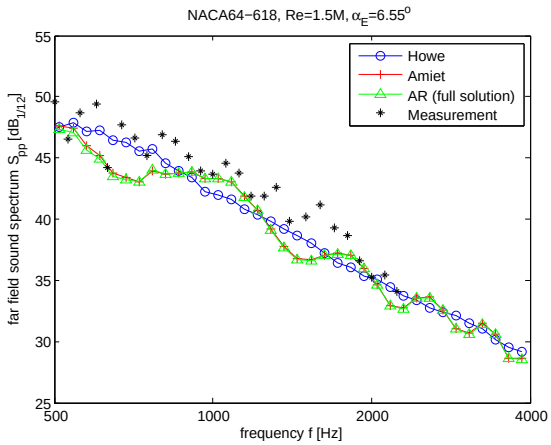

Figure 5.53: Comparison of the Far Field Sound Pressure Spectrum for the NACA64-618 airfoil at Re=1.5M and $\alpha_E = 6.55^o$ (observer position for model: center of mic. array; model: suction side contribution to far field sound only)

triangle) produces almost the same solution as the simplified version (eq. 2.65, red cross). There are only small differences in the low frequency range up to 700Hz. This is a quite unexpected result, because the simplification was based on the assumption of a large aspect ratio. But in the computation a span of 0.6m was used (to get a result equivalent to the array measurement). It yields an aspect ratio of 1, far from being large. An explanation might be that the observer position is very close to mid span and the $sinc^2$ function of eq. 2.63 is centered about low values of the spanwise wave number and it is narrow enough that the radiation integral is constant in the range of significant spanwise wave numbers.

The main difference between Howe's and Amiet's model is the more elaborated directivity of Amiet's model which is a function of the frequency. In Howe's model the directivity for an infinite high frequency is assumed for all frequencies. The far field sound pressure spectrum predicted with Amiet's model oscillates about the one predicted with Howe's model as 'mean value'. However, those oscillations are not observed in the microphone array measurement. On the other hand, the microphone array is placed quite close to the airfoil compared to its geometric extend. There is a aperture angle of about 36° from the TE of the airfoil model. The far field sound pressure spectrum measured by the microphone array is an average over its area. This setup can be approximately simulated using a line of 10 observer positions and averaging. The line of observer is placed in the center of the microphone array in the spanwise direction and equally spaced along its chordwise extension. The result is shown in figure 5.54. The Amiet's model yields a nearly identical far field sound pressure spec-

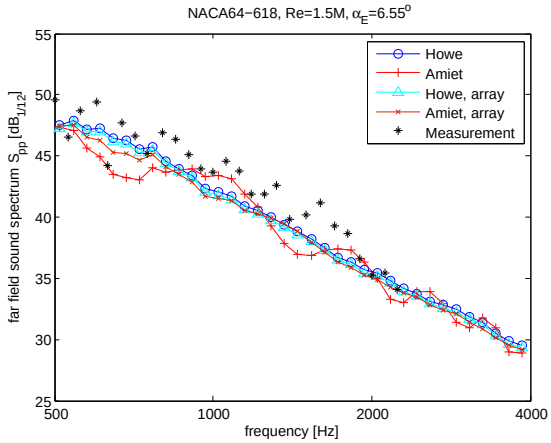

Figure 5.54: Comparison of the Far Field Sound Pressure Spectrum for the NACA64-618 airfoil at Re=1.5M and $\alpha_E = 6.55^o$ (observer position for model: center of mic. array; observer position for model simulating array: spanwise center of mic. array, 10 positions equally spaced over chordwise extend; model: suction side contribution to far field sound only)

trum as Howe's model when averaging over 10 observer positions. The difference is less than 0.4dB, expect in the frequency range lower than 800Hz. There it can be up to 0.9dB. The difference compared to the far field sound pressure spectrum measured with the microphone array is up to 2dB. The difference between the models can be neglected compared to this. The setup with the microphone array positioned close to the airfoil is not suitable to detect directivity effects.

5.5.3 Influence of Convection Velocity on Far Field Sound Prediction

The main source of uncertainty in the far field sound pressure prediction using input from the measurement is the unknown convection velocity in the high frequency range. Simulations with different convection velocities assumed constant over the frequency for simplicity were performed for the test case, figure 5.55. Only the suction side contribution to the far field sound pressure is taken into account. A doubling of the convection velocity corresponds approximately also to a doubling of the far field sound pressure (it can be directly inferred from eq. 2.36), confirmed by the 3dB difference of the prediction with $U_c/U_\infty = 0.4$ and $U_c/U_\infty = 0.8$ in figure 5.55.
In the high frequency range at about 2500Hz the measured sound pressure drops

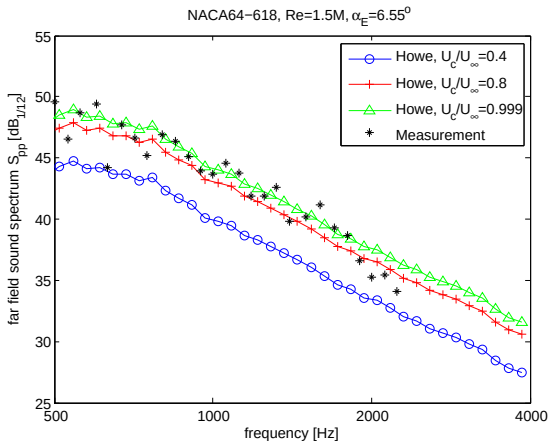

Figure 5.55: Comparison of the Far Field Sound Pressure Spectrum for the NACA64-618 airfoil at Re=1.5M and $\alpha_E = 6.55^o$ (observer position: spanwise center of mic. array, 10 positions equally spaced over chordwise extend; model: suction side contribution to far field sound only)

suddenly very strong. This would correspond to sudden drop of the convection velocity in the prediction model. With the present measurements it can not be proven.

5.5.4 Contribution of the Suction and Pressure Side to the Far Field Sound

An estimate of the contribution of the pressure side surface pressure fluctuations to the far field sound pressure for the NACA64-618 at Reynolds number Re=1.5M is displayed in figure 5.56 for two different AoAs. The slope of the predicted far field sound pressure spectrum is less steep when taking the contribution from both sides into account. The surface pressure PSD on the pressure side is flatter than the one on the suction side for these AoAs. Compared to the measured far field sound pressure the agreement is improved for frequencies up to 3000Hz, but for higher frequencies the overestimation becomes more severe. In the frequency range below 700Hz for the effective AoA $\alpha_E = 6.55°$, the model underpredicts the real sound pressure, even when taking into account the contribution from the pressure side. But an overestimation of the real sound pressure level by the microphone array in the low frequency range is also possible, because the mainlobe and sidelobe of the beamforming array are broad at low frequencies and it is more difficult to eject extraneous noise sources than at

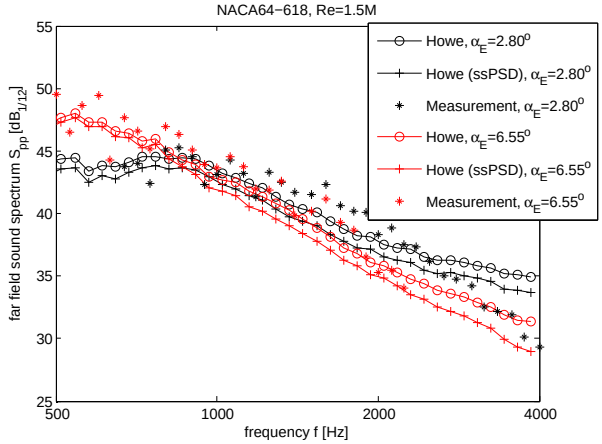

Figure 5.56: Comparison of the Far Field Sound Pressure Spectrum for the NACA64-618 airfoil at Re=1.5M (observer position: spanwise center of mic. array, 10 positions equally spaced over chordwise extend)

high frequencies.

5.5.5 Comparison of Measurement and Prediction for Several Relevant Cases

The model used in the comparison of the predicted and measured far field sound pressure takes the contribution from both sides into account and is assessed as described in subsection 5.5.1. The test cases are chosen in a way that the AoA is in the linear range of the polar and the suction side PSD is at least 5dB higher than the pressure side PSD. The comparison is displayed in figure 5.57. In all cases, the slope of the predicted far field sound pressure spectrum is flatter than the measured one. It is higher in the high frequency range and lower in the low frequency range. The difference for high frequencies can be due to a bad estimate of the convection velocity. Improving the setup to measure the convection velocity at higher frequencies can improve the prediction. In the low frequency range, say up to 2000Hz, the predictions are excellent.
Another point of controversy in the model is the fulfillment of the Kutta condition at the TE in the high frequency range. If the Kutta condition is fulfilled suction and pressure side can be treated separately. If the Kutta condition is not fulfilled the flow around the TE has to be treated as a whole and a model dealing with different pressure distributions on both sides is necessary. The results above showed that the prediction of the far field sound pressure in the

high frequency range is better if only the suction side contribution is taken into account. This leads to the speculation that the flow at the TE is more complex in reality and a simple summation of the contribution of both sides to the far field sound is not appropriate.
Another reason for the difference could be the inhomogeneity of the surface pressure PSD close to the TE. The model assumption is clearly violated.

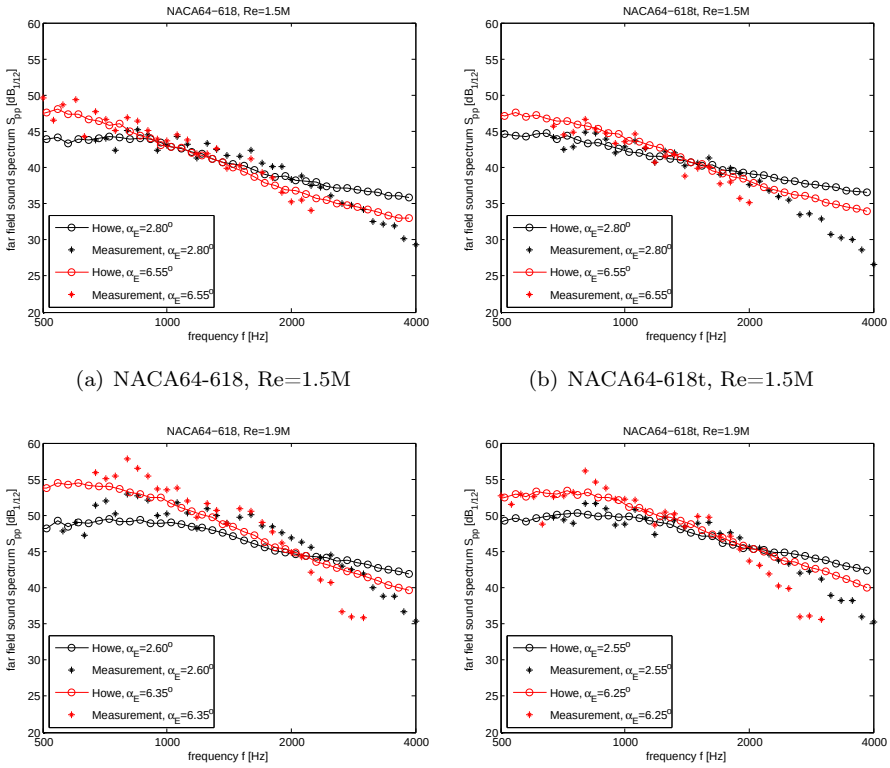

(a) NACA64-618, Re=1.5M

(b) NACA64-618t, Re=1.5M

(c) NACA64-618, Re=1.9M

(d) NACA64-618t, Re=1.9M

Figure 5.57: Comparison of Measured and Predicted Far Field Sound Pressure Spectrum (observer position: spanwise center of mic. array, 10 positions equally spaced over chordwise extend; model: suction and pressure side contribution to far field sound)

Chapter 6

Discussion

6.1 Conclusions

This work aims at the development and refinement of measurement techniques to characterize airfoil trailing edge noise and to improve existing theoretical trailing edge noise models by means of those measurements. To characterize trailing edge noise one needs to measure the velocity fluctuations in the boundary layer and the surface pressure fluctuations close to the trailing edge as well as the far field sound pressure.
The first measurements were conducted in the aerodynamic wind tunnel of LM Wind Power A/S. Due to the high background noise level a direct measurement of the far field trailing edge noise was not possible. We developed a traversing system for a hot wire probe to measure the velocity in the boundary layer of a NACA0015 airfoil with high positioning accuracy. Surface pressure fluctuations were measured with microphones mounted inside the airfoil and connected to the surface with a pinhole. To reach the position close to the trailing edge of the airfoil, a tubing system was needed to connect the microphone to the surface pinhole because of the limited mounting space. The transmission of sound in this duct system was modeled analytically and also an experimental calibration method was attempted. The calibration failed and it was not possible to recover to signal with the analytical transmission function, because some constants in the formula have to be determined empirically. The surface pressure

measurements were hence restricted to positions considerably far upstream of the trailing edge.
The next experiment was conducted in the acoustic wind tunnel of the Virginia Tech University. In this tunnel a measurement technique for the far field sound with a microphone array existed. The surface pressure had to be measured close to the trailing edge. A new tubing system was adapted from the design of [45]. Brüel & Kjær Sound and Vibration A/S developed a setup for the calibration of the surface pressure microphones which gave excellent results. The measured transfer function was less dependent on the ambient temperature when formulated as function of the wave number and could be applied to the measurements in the wind tunnel. The ambient temperature during the wind tunnel measurement was very different from the temperature during calibration. The analytical model for the sound propagation in the duct system was applied to the new adapter design and gave good qualitative results. However, there was a large offset in level. Therefore, it was not possible to use the analytical function for data reduction, but it can be used for future adapter design.
The so-called TNO model for trailing edge noise was investigated and the results were compared to measured data. In previous work the computations with the TNO model were directly compared to far field sound measurements and an underestimation of the measured level was observed. The TNO model describes the far field sound in two steps. First, the turbulent velocity field close to the TE of an airfoil is related to the fluctuating surface pressure field. Then, by assuming a half plane configuration, an analytical solution by [11] for the scattering of the surface pressure fluctuations gives the far field sound pressure. Unlike in publications before, we compared the model to relate the velocity fluctuation to the surface pressure and the acoustic formulation to compute far field sound by means of the surface pressure fluctuations separately.
The acoustic formulation of [11] gave excellent results for the far field sound pressure, if we used measurements to determine the fluctuating surface pressure field. At high frequencies (above 2000Hz) the prediction gave higher levels than the measurements. However, the streamwise surface pressure statistics could only be measured in the low frequency range and the difference might be explained by a wrong assumption of the high frequency part of the streamwise surface pressure statistics. It was also shown that the pressure side contribution to the far field sound was not negligible. With the microphone setup we could only measure the one point spectral density of the surface pressure close to the trailing edge. The streamwise and spanwise statistics could not be measured. Hence, only an estimate of the pressure side contribution could be made.
An alternative to Howe's [11] model for the far field trailing edge noise is the formulation of Amiet [13], recently refined by Roger [14]. This formulation is very similar to Howe's. The main difference is that the directivity pattern of trailing edge noise is described in more detail. We showed that both formulations produced almost identical results when we accounted for the microphone array extend by evaluating the far field noise at several observer positions dis-

tributed over the array disc and averaged the result. For our application Howe's formulation was more suitable, because the computational time was much lower and the far field microphone array could not detect a fine directivity pattern due to its relative large size compared to the distance from the trailing edge of the airfoil. On the other hand, for far field sound computations for a single observer position we recommend to use Amiet's model with Roger's extensions.
It was already known from previous measurements ([36],[24]) that the one point spectra of the fluctuating surface pressure were underestimated by the formulation used in the original TNO model. An improvement of the TNO model has to be sought in this part. The main shortcoming of the TNO model was that the velocity spectrum of the vertical velocity component was assumed to have the form of the well-known isotropic von Karman spectrum and the vertical correlation length was also derived from the von Karman spectrum. The vertical velocity component is influenced by the surface of the airfoil and the velocity spectrum is anisotropic in reality. The turbulence model by [26] describes anisotropy by the influence of uniform shear on a initially isotropic von Karman spectrum with rapid distortion theory. It also attempts to describe the influence of a blocking surface. Hence, the model seemed to be ideal for the surface pressure formulation, except that the shear of the mean velocity is not uniform in an airfoil boundary layer. It was attempted to integrate the Mann turbulence model into the surface pressure formulation.
First, we compared the one point velocity spectral density of all three velocity components plus the one point cross spectral density of the streamwise and vertical component of the Mann model with measurements in the boundary layer of a NACA0015 airfoil in the wind tunnel of LM Wind Power A/S at several distances from the surface. A function for the input parameters of the Mann model in dependence of the distance from the wall was found giving excellent results compared to the measurements for most positions in the boundary layer and a large range of different flow situations. The two input parameters of the Mann model related the initial von Karman spectrum could be related to the output of the $k-\omega$ turbulence model of the RANS solver. The third input parameter describing the degree of the anisotropy was related to the local pressure gradient. A new formulation for the surface pressure with the anisotropic turbulence model was developed. The surface pressure prediction gave however very similar results as the original TNO model.
The problem encountered during the development of the new model was that there was no measurement data for the cross correlation of the vertical velocity fluctuations at two different wall distances, because this would require the simultaneous measurement of the velocity time series at two positions in the boundary layer. The only data available for this cross correlation is from a large eddy simulation of the NACA0015 airfoil at one single flow angle and Reynolds number. The LES data for the surface pressure and velocity one point spectral densities showed differences compared to measurements. To compensate for this difference we compared the normalized correlation coefficient computed from the

LES with the one computed with the developed surface pressure model. It was found that the correlation coefficient from the new model was significantly lower than the one found by the LES data. This might explain the underestimation of the surface pressure. But a more sound investigation of the cross correlation preferably based on measurements instead of LES is needed and possibly the formulation of the cross correlation between two positions used in the Mann model has to be recast.
The model was also applied to the two airfoils tested in the Virginia Tech wind tunnel. The velocity spectra in the boundary layer were not as well predicted as for the NACA0015 airfoil. The surface pressure predictions showed the typical underestimation in the high frequency range. We conclude that the model in its present parametrization is not generally applicable. It was probably wrong to relate the parameter of anisotropy of the Mann model to the local pressure gradient.
Another important aspect of this work was to find a method for the evaluation of trailing edge noise radiated by airfoils in an aerodynamically optimized wind tunnel with high background noise like the one of LM Wind Power A/S. Surface pressure fluctuations are of high amplitude and can be measured in a wind tunnel with high background noise. The good results of the far field sound predictions on the basis of measured surface pressure statistics (confirmed also by similar measurements for a different set of airfoils conducted by [12] and [15]) encourage the approach to evaluate trailing edge noise by means of the surface pressure fluctuations in presence of high background noise in the measurement setup. A dedicated microphone setup close to the trailing edge as for example the one implemented on the two airfoils tested in the wind tunnel of Virginia Tech University is needed for this task. The setup used in the Virginia Tech wind tunnel allows the correct prediction of trailing edge noise up to a frequency of 2000Hz. The spanwise separation of the microphones aligned in streamwise direction should be reduced to extend the frequency range of the trailing edge noise prediction. The surface pressure statistics on the pressure side should also be measured to account correctly for the contribution of the pressure side to the far field sound.

6.2 Future Work

A possible alternative to the analytical relation between the surface pressure fluctuations and boundary layer velocity field used in the TNO model was developed. The model includes a more elaborated approach for the boundary layer turbulence based on the turbulence model by [26], but in its present implementation the results are not improved compared to the TNO model. The problem seems to be the right modeling of the cross correlation of the vertical velocity

component at two different positions in the boundary layer. We recommend to conduct measurements of the fluctuating velocity in the boundary layer at two positions simultaneously. Based on those measurements the analytical model for the cross correlation should be revised. Such a revision should improve the predictions of the fluctuating surface pressure. The model has to be tested for far field sound predictions as well. Even if an improvement of the modeling of the one point surface pressure fluctuations is achieved, it is not certain that the far field sound pressure is predicted correctly, because it depends on the convecting pressure field. The one point spectrum of the surface pressure contains only a small amount of the pressure field.

The relation between the input parameter of the Mann model and the output of the RANS computation should be revised to make it work for various different airfoil shapes. Hot wire measurements similar to the ones conducted in the present work for other well known airfoil shapes are recommended to fulfill this task. The hot wire measurements performed in the Virginia Tech wind tunnel are of limited use for this task, because the tested airfoil are very difficult to model with RANS and introduce a high uncertainty in the validity of the output of the $k-\omega$ turbulence model, the positioning accuracy was not as good as in the experiment in the LM wind tunnel and the frequency range was more limited.

The far field noise prediction technique should be tested in a wind tunnel with background noise like LMs. Therefore a setup of surface pressure microphones needs to be implemented on several airfoil shapes. There should be far field noise data available for those airfoils to compare with the predictions from measured surface pressures.

Bibliography

[1] Wagner S, Bareiss R, Guidati G. *Wind Turbine Noise*. Springer, 1996.

[2] Schepers JG, Curvers A, Oerlemans S, Braun K, Lutz T, Herrig A, Würz W, Lopez BM. SIROCCO: Silent Rotors by Acoustic Optimization. *Wind Turbine Noise: Perspectives for Control (Proc.)*, Berlin, Germany, 2005.

[3] Schepers JG, Curvers A, Oerlemans S, Braun K, Lutz T, Herrig A, Würz W, Mantesanz A, Garcillán L, Fischer M, *et al.*. SIROCCO: Silent Rotors by Acoustic Optimization. 2^{nd} *International Meeting on Wind Turbine Noise (Proc.)*, Lyon, France, 2007.

[4] Oerlemans S, Lopez BM. Localization and Quantification of Noise Sources on a Wind Turbine. *Proc. of the First International Meeting on Wind Turbine Noise: Perspectives for Control*, Berlin, DE, 2005.

[5] Oerlemans S, Fisher M, Maeder T, Kögler K. Reduction of Wind Turbine Noise Using Optimized Airfoils and Trailing-Edge Serrations. *AIAA JOURNAL* 2009; **47**(6):1470–1481.

[6] Lighthill MJ. On Sound Generated Aerodynamically; I. General Theory. *Proc. of the Royal Society of London*, *Series A*, vol. 211, 1952; 564–587.

[7] Lighthill MJ. On Sound Generated Aerodynamically; II. Turbulence as a Source of Sound. *Proc. of the Royal Society of London*, *Series A*, vol. 222, 1954; 1–32.

[8] Ffowcs Williams JE, Hall LH. Aerodynamic Sound Generation by Turbulent Flow in the Vicinity of a Scattering Half Plane. *J. Fluid Mech.* 1970; **40**(4):657–670.

[9] Chase D. Sound Radiated by Turbulent Flow off a Rigid Half-Plane as Obtained from a Wavevector Spectrum of Hydrodynamic Pressure. *J. Acoust. Soc. Am.* 1972; **52**:1011–1023.

[10] Chandiramani K. Diffraction of Evanescent Waves with Applications to Aerodynamically Scattered Sound and Radiation from Unbaffled Plates. *J. Acoust. Soc. Am.* 1974; **55**(1):19–29.

[11] Howe MS. A Review of the Theory of Trailing Edge Noise. *J. Sound Vib.* 1978; **61**(3):437–465.

[12] Brooks TF, Hodgson TH. Trailing Edge Noise Prediction from Measured Surface Pressures. *J. Sound Vib.* 1981; **78**(1):69–117.

[13] Amiet RK. Noise due to Turbulent Flow Past a Trailing Edge. *J. Sound Vib.* 1976; **47**(3):387–393.

[14] Roger M, Moreau S. Back-scattering correction and further extensions of Amiet's trailing-edge noise model. Part 1: theory. *J. Sound Vib.* 2005; **286**:477–506.

[15] Moreau S, Roger M. Back-scattering correction and further extensions of Amiet's trailing-edge noise model. Part II: Application. *J. Sound Vib.* 2009; **323**:397–425.

[16] Brooks TF, Pope SD, Marcolini MA. Airfoil Self-Noise and Prediction. *NASA Reference Publication 1218*, Langley Research Center 1989.

[17] Kraichnan R. Pressure Fluctuations in Turbulent Flow over a Flat Plate. *J. Acoust. Soc. Am.* 1956; **28**(3):378–390.

[18] Blake WK. *Mechanics of Flow-Induced Sound and Vibration, Vol.I and II*, vol. in Applied Mathematics and Mechanics. Frenkiel, F.N. and Temple, G. (eds.), Academic Press, 1986.

[19] Parchen R. Progress report DRAW: A Prediction Scheme for Trailing-Edge Noise Based on Detailed Boundary-Layer Characteristics. *TNO Rept. HAG-RPT-980023*, TNO Institute of Applied Physics, The Netherlands 1998.

[20] Lutz T, Herrig A, Würz W, Kamruzzaman M, Krämer E. Design and Wind-Tunnel Verification of Low-Noise Airfoils for Wind Turbines. *AIAA Journal* 2007; **45**(4):779–785.

[21] Kamruzzaman M, Lutz T, Herrig A, Krämer E. RANS Based Prediction of Airfoil Trailing Edge Far-Field Noise: Impact of Isotropic & Anisotropic Turbulence. *Proc. of the* 14^{th} *AIAA/CEAS Aeroacoustics Conf.*, AIAA Paper 2008-2867, Vancouver, 2008.

[22] Bertagnolio F. Trailing Edge Noise Model Applied to Wind Turbine Airfoils. *Tech. Rep. Risø-R-1633(EN)*, Risø-DTU, Roskilde, Denmark January 2008.

[23] Kamruzzaman M, Lutz T, Herrig A, Krämer E. Semi-empirical Modeling of Turbulent Anisotropy for Airfoil Self Noise Predictions. *AIAA Journal* 2011; under review.

[24] Bertagnolio F. Surface Pressure Measurements on a NACA0015 airfoil compared to Computations with the TNO Trailing Edge Noise Model. *Proc. of the Inter-noise 2011 Conf.*, Osaka, JP, 2011.

[25] Madsen H, Bak C, Paulsen U, Gaunaa M, Fuglsang P, Romblad J, Olesen N, Enevoldsen P, Laursen J, Jensen L. The DAN-AERO MW Experiments: Final report. *Tech. Rep. Risø-R-1726(EN)*, Risø-DTU, Roskilde, Denmark September 2010.

[26] Mann J. The spatial structure of neutral atmospheric surface-layer turbulence. *J. of Fluid Mech.* 1994; **273**:141–168.

[27] Chase D. Noise Radiated from an Edge in Turbulent Flow. *AIAA J.* 1975; **13**(8):1041–1047.

[28] Abramowitz M, Stegun IA. *Handbook of Mathematical Functions,*. Dover Publications Inc., New York, 1970.

[29] Wagner S. Vorlesung Strömungslehre. Universität Stuttgart 1998.

[30] Mathieu J, Scott J. *Introduction to Turbulent Flow*. Cambridge University Press, Cambridge (UK), 2000.

[31] Sumer BM. Lecture notes on turbulence. Technical University of Denmark 2007.

[32] Bertagnolio F. Boundary Layer Measurements of the NACA0015 and Implications for Noise Modeling. *Tech. Rep. Risø-R-1761(EN)*, Risø-DTU, Roskilde, Denmark January 2011.

[33] Townsend AA. *The Structure of Turbulent Shear Flow*. 2nd edn., Cambridge University Press, Cambridge (UK), 1976.

[34] Pope SB. *Turbulent Flows*. Cambridge University Press, 2000.

[35] Bæk P. Experimental Detection of Laminar to Turbulent Boundary Layer Transition on Airfoils in an Industrial Wind Tunnel Facility. Master's Thesis, The Technical University of Denmark DTU September 2008.

[36] Fischer A, Bertagnolio F, Bak C, Madsen HA. Surface Pressure Measurements on a NACA0015 airfoil compared to Computations with the TNO Trailing Edge Noise Model. *Proc. of the Torque 2010 'The science of making torque from wind' Conf. (EWEA)*, Heraklion, GR, 2010; 81–92.

[37] Devenport WJ, Burdisso RA, Camargo H, Crede E, Remillieux M, Rasnick M, VanSeeters P. Aeroacoustic Testing of Wind Turbine Airfoils. *Tech. Rep. Prj.No. 208-11-110F-101-408-1*, NREL 2008.

[38] Devenport WJ, Burdisso RA, Borgoltz A, Ravetta P, Barone MF. Aerodynamic and Acoustic Corrections for a Kevlar-Walled Anechoic Wind Tunnel. *Proc. of the 16th AIAA/CEAS Aeracoustics Conference*, 2010.

[39] (Ed) TJM. *Aeroacoustic Measurements*. Springer, 2002.

[40] STREAMWARE MANUAL 2009. Dantec Dynamics A/S.

[41] Bruun HH. *Hot-Wire Anemometry: Principles and Signal Analysis*. Oxford University Press, 1995.

[42] Jørgensen FE. How to Measure Turbulence with Hot-Wire Anemometer - A Practical Guide 2004. Dantec Dynamics A/S.

[43] Corcos GM. Resolution of pressure in turbulence. *J. Acoust. Soc. Am.* 1963; **35**(2):192–199.

[44] Gustavino R. Sennheiser KE 4-211-2 Report 2010. Brüel & Kjær Sound and Vibration A/S.

[45] Perénnès S. Caractérisation des sources de bruit aérodynamique à basses fréquences de dispositifs hypersustentateurs. PhD Thesis, Ecole Centrale de Lyon 1999.

[46] Meirovich L. *Elements of Vibration Analysis*. McGraw Hill, 1975.

[47] Jacobsen F. Propagation of sound waves in ducts. Technical University of Denmark 2008.

[48] Pierce AD. *Acoustic: An Introduction to Its Physical Principle and Application*. McGraw Hill, 1991.

[49] Sørensen NN. General Purpose Flow Solver Applied to Flow over Hills. *Risø-R-827-(EN)*, Risø National Laboratory, Roskilde, Denmark June 1995.

[50] Michelsen JA. Basis3D - A Platform for Development of Multiblock PDE Solvers. *Tech. Rep. AFM 92-05*, Technical University of Denmark 1992.

[51] Michelsen JA. Block Structured Multigrid Solution of 2D and 3D Elliptic PDE's. *Tech. Rep. AFM 94-06*, Technical University of Denmark 1994.

[52] Menter FR. Zonal Two-Equations k–ω Turbulence Models for Aerodynamic Flows. *Proceedings*, AIAA Paper 93-2906, 1993.

[53] Drela M, Giles MB. Viscous-Inviscid Analysis of Transonic and Low Reynolds Number Airfoils. *AIAA Journal* 1987; **25**(10):1347–1355.

[54] Menter FR, Langtry RB, Likki SR, Suzen YB, Huang PG, Völker S. A Correlation-Based Transition Model Using Local Variables, Part I - Model Formulation. *Proceedings of ASME Turbo Expo 2004, Power for Land, Sea, and Air*, GT2004-53452, Vienna, Austria, 2004.

[55] Shen WZ, Sørensen JN. Aero-Acoustic Modeling of Turbulent Airfoil Flows. *AIAA Journal* 2001; **39**(6):1057–1064.

[56] Shen WZ, Zhu WJ, Sørensen JN. Aero-acoustic Computations for Turbulent Airfoil Flows. *AIAA Journal* June 2009; **47**(6):1518–1527.

[57] Zhu WJ, Shen WZ, Sørensen JN. High-order numerical simulations of flow induced noise. *Int. J. f. Numerical Methods in Fluids* 2011; **66**(1):17–37.

[58] Abbott IH, von Doenhoff AE. *Theory of Wing Sections*. Dover Publications Inc., New York, 1959.

[59] Choi TD, Eslinger OJ, Gilmore PA, Kelley CT, Patrick HA. User's guide to iffco. http://www4.ncsu.edu/ ctk/SOFTWARE/iffco.pdf 2001.

[60] Batchelor GK. *The Theory of Homogeneous Turbulence*, vol. in Applied Mathematics and Mechanics. Cambridge University Press, Cambridge (UK), 1953.

[61] Welch PD. The Use of Fast Fourier Transform for the Estimation of Power Spectra: A Method Based on Time Averaging Over Short, Modified Periodograms. *IEEE Trans. Audio Electroacoustics* 1967; **15**:70–73.

Appendix A

Definitions and Basic Functions

A.1 Fourier Transform

The Fourier transformation of a random vector $\vec{u}$ is defined as

$$\mathbf{F}(\vec{u}(\vec{x},t)) \equiv \vec{U}(\vec{k},\omega) = \frac{1}{(2\pi)^4}\int_{-\infty}^{\infty} \vec{u}(\vec{x},t)e^{-i\vec{k}\cdot\vec{x}}e^{i\omega t}\, d^3\vec{x}dt. \tag{A.1}$$

A.2 Correlation Function

The correlation function of two signals u_i and u_j is defined as

$$R_{ij}(\vec{r},\tau) = \langle u_i^*(\vec{x},t)u_j(\vec{x}+\vec{r},t+\tau)\rangle \tag{A.2}$$

where the operator $\langle\ \rangle$ denotes ensemble averaging. The correlation coefficient function is the normalized correlation function given by

$$\gamma_{ij}(\vec{r},\tau) = \frac{\langle u_i^*(\vec{x},t)u_j(\vec{x}+\vec{r},t+\tau)\rangle}{\langle u_i^*(\vec{x},t)u_j(\vec{x},t)\rangle}. \tag{A.3}$$

The cross spectrum is the Fourier transform of the correlation function

$$\Phi_{ij}(\vec{k},\omega) = \frac{1}{(2\pi)^4}\int_{-\infty}^{\infty} R_{ij}(\vec{r},\tau)e^{-i\vec{k}\cdot\vec{r}}e^{i\omega\tau}\,d^3\vec{r}d\tau \tag{A.4}$$

in three dimensional space. The inverse Fourier transform is

$$R_{ij}(\vec{r},\tau) = \int_{-\infty}^{\infty} \Phi_{ij}(\vec{k},\omega)e^{i\vec{k}\cdot\vec{r}}e^{-i\omega\tau}\,d^3\vec{k}d\omega. \tag{A.5}$$

The Fourier-Stieltjes integral can be introduced for the velocity, if the velocity field is not square integrable over all physical space. For the velocity component u, as example, it reads:

$$u_i(\vec{x},t) = \int_{-\infty}^{\infty} e^{-i\vec{k}\cdot\vec{x}}e^{i\omega t}\,d^4Z_i(\vec{k},\omega) \tag{A.6}$$

and the following relation with the cross spectrum can be established:

$$\Phi_{ij}(\vec{k},\omega) = \frac{\left\langle dZ_i^*(\vec{k},\omega)dZ_j(\vec{k},\omega)\right\rangle}{dk_1dk_2dk_3d\omega} \tag{A.7}$$

The equations above hold for homogeneous flow. In inhomogeneous flow the correlation coefficient function as example has to be redefined as

$$\gamma_{ij}(\vec{x},\vec{y},\tau) = \frac{\langle u_i^*(\vec{x},t)u_j(\vec{y},t+\tau)\rangle}{\sqrt{\langle u_i^*(\vec{x},t)u_i(\vec{x},t)\rangle\left\langle u_j^*(\vec{y},t)u_j(\vec{y},t)\right\rangle}}. \tag{A.8}$$

A.3 Length and Time Scale

The length scale of two components u_i and u_j in the direction of the spatial separation vector r is defined as

$$L_{\vec{n}}^{ij} = \frac{1}{R_{ij}(\vec{0},0)}\int_0^{\infty} R_{ij}(\vec{r},0)d\vec{r} = \int_0^{\infty} \mathscr{R}_{ij}(\vec{r},0)d^3\vec{r} \tag{A.9}$$

where $\vec{n}$ is a unit vector in the direction of $\vec{r}$. The length scale in the direction of the cartesian axis x_k is abbreviated with L_k^{ij}. The integral time scale is defined as

$$T^{ij} = \frac{1}{R_{ij}(\vec{0},0)}\int_0^{\infty} R_{ij}(\vec{0},\tau)d\tau = \int_0^{\infty} \mathscr{R}_{ij}(\vec{0},\tau)d\tau \tag{A.10}$$

Appendix B

Microphone Array Position

The position of the microphone array relative to the airfoil is shown in figure B.1. The coordinate system is defined as follows: the x-direction is parallel with the flow direction (positive against flow direction), the y-direction is parallel with the rotation axis of the airfoil (positive pointing upwards) and the z-direction is normal to both (positive pointing away from the suction side). The origin of is located at the center of rotation of the airfoil in streamwise direction and centered in the cross section of the wind tunnel test section.
The integration area for beamforming is displayed in figure B.1(b). It is 2-dimensional with extend in the x- and y- direction and located in the plane z=0.

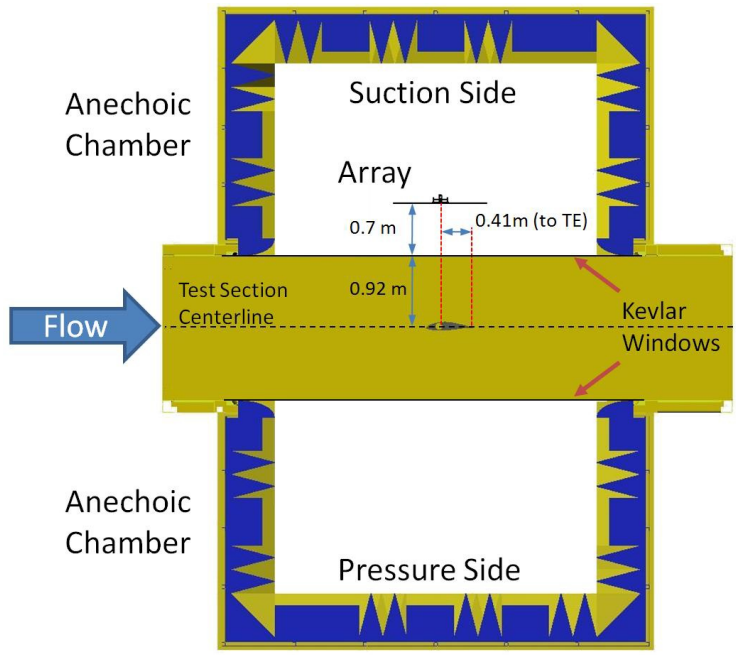

(a) view from top

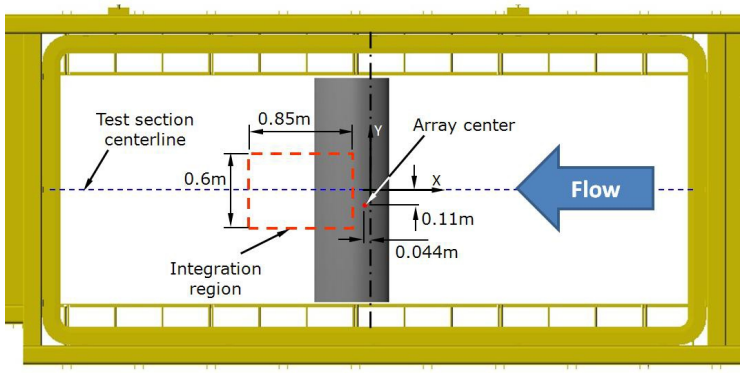

(b) view from starboard

Figure B.1: Position of the Microphone Array relative to the Airfoil

Appendix C

Hot wire Calibration Data

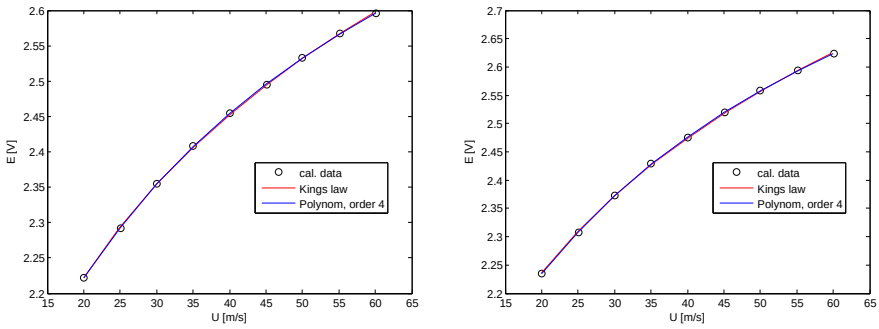

(a) wire 1 (b) wire 2

Figure C.1: Calibration associated with run 7

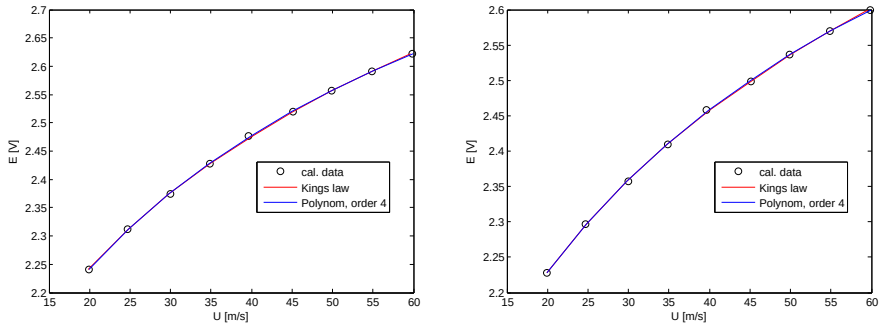

(a) wire 1 (b) wire 2

Figure C.2: Calibration associated with run 8

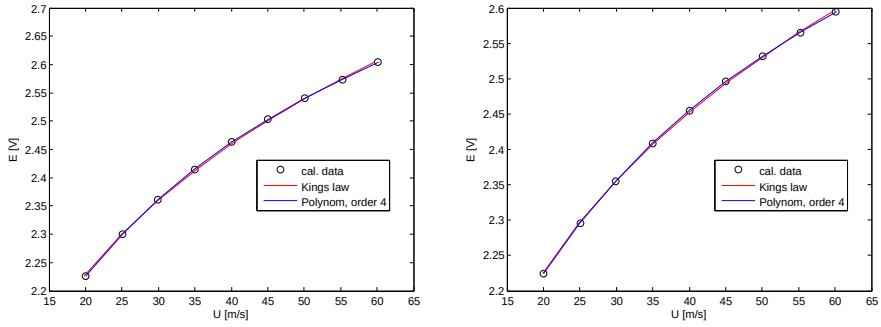

(a) wire 1 (b) wire 2

Figure C.3: Calibration associated with run 9

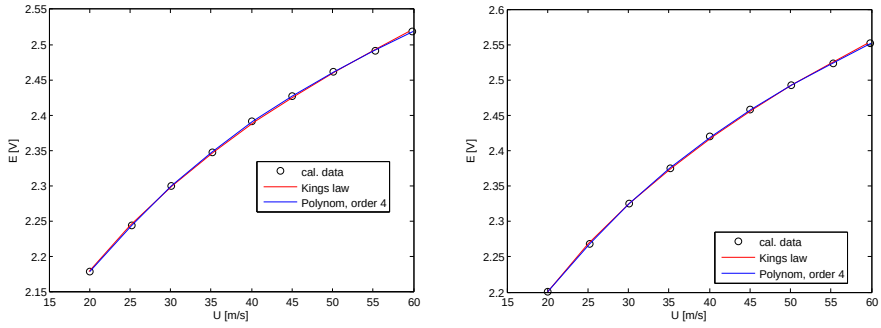

(a) wire 1 (b) wire 2

Figure C.4: Calibration associated with run 11 and 12

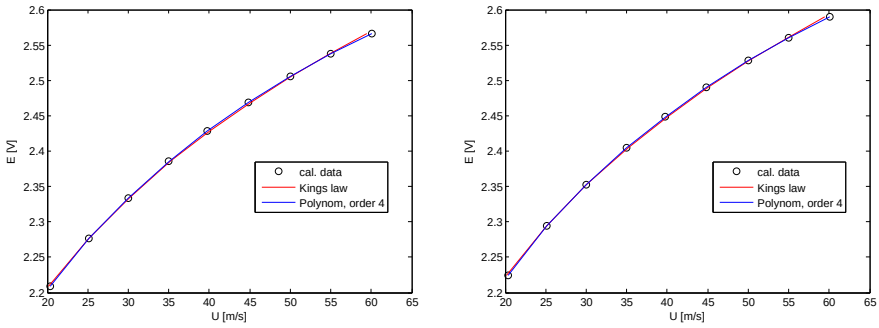

(a) wire 1 (b) wire 2

Figure C.5: Calibration associated with run 13

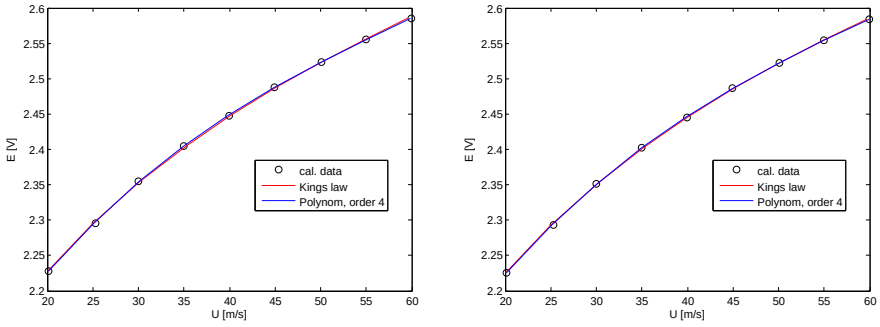

(a) wire 1 (b) wire 2

Figure C.6: Calibration associated with run 14, 15 and 16

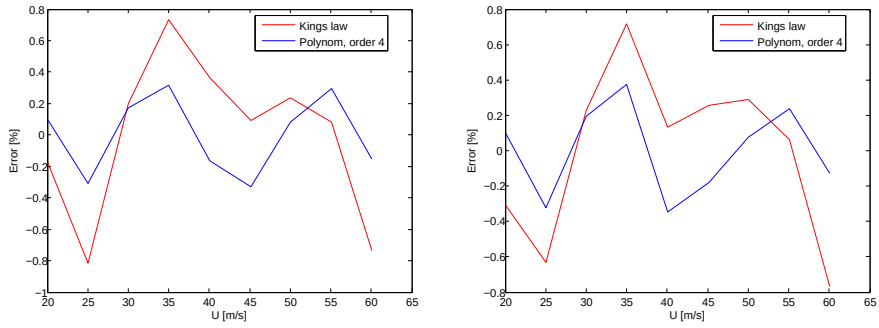

(a) wire 1 (b) wire 2

Figure C.7: Linearisation error calibration associated with run 7

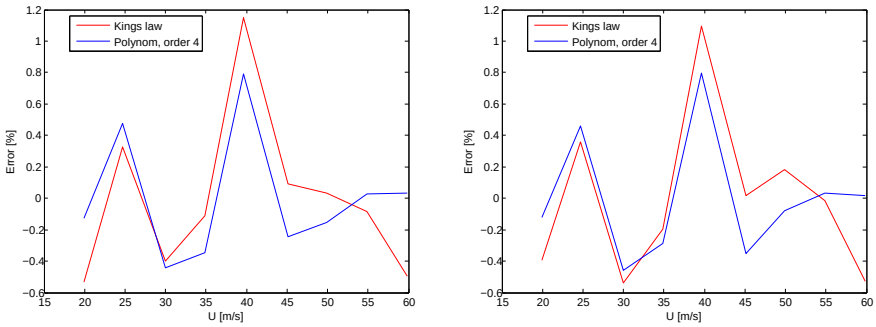

(a) wire 1 (b) wire 2

Figure C.8: Linearisation error calibration associated with run 8

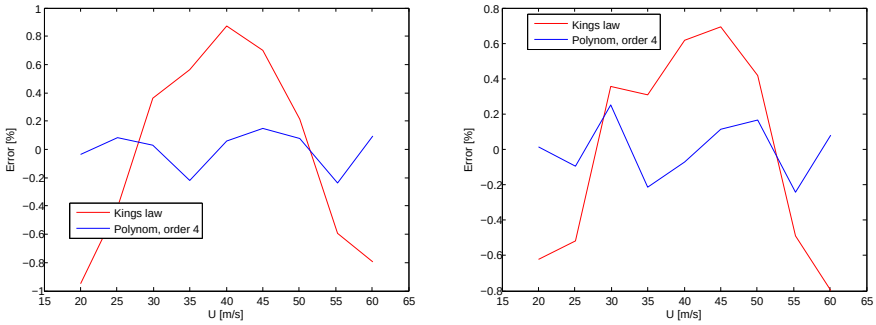

(a) wire 1 (b) wire 2

Figure C.9: Linearisation error calibration associated with run 9

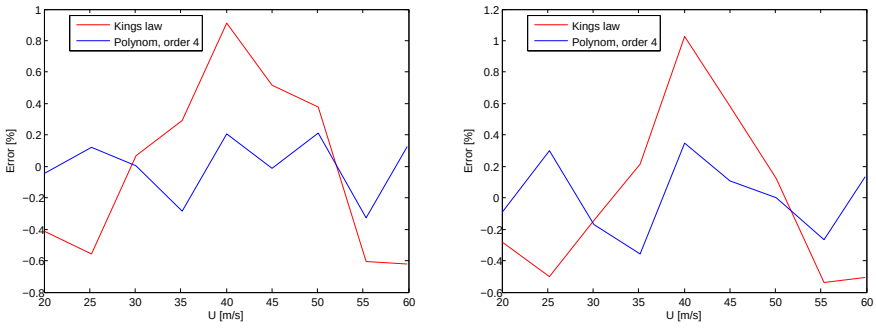

(a) wire 1 (b) wire 2

Figure C.10: Linearisation error calibration associated with run 11 and 12

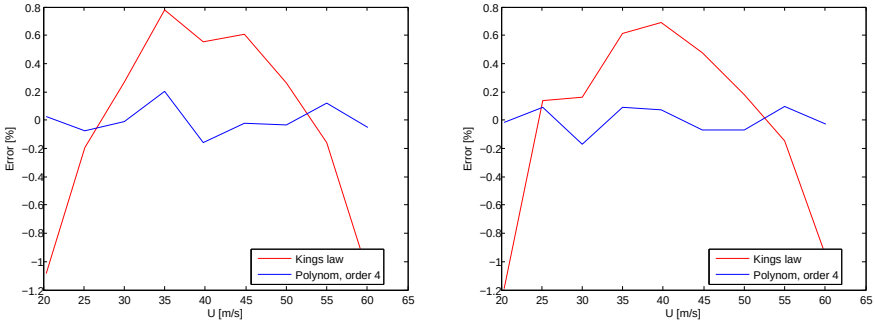

(a) wire 1 (b) wire 2

Figure C.11: Linearisation error calibration associated with run 13

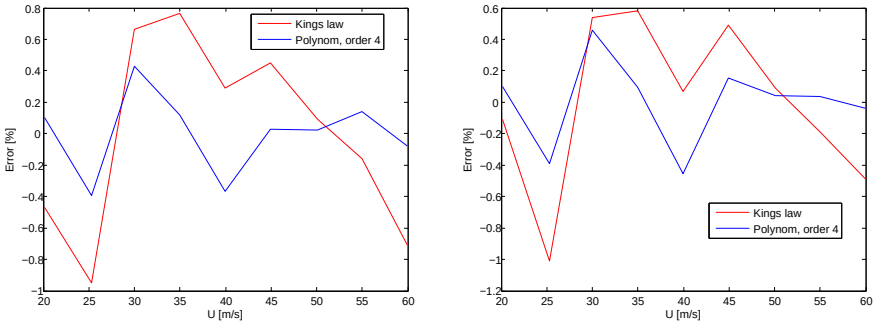

(a) wire 1 (b) wire 2

Figure C.12: Linearisation error calibration associated with run 14, 15 and 16

Appendix D

Pressure Tap and Microphone Distribution

suction side				pressure side			
no.	x_1/c	x_2/c	x_3/c	no.	x_1/c	x_2/c	x_3/c
1	1.000000	0.000401	1.426160	37	0.000725	0.000493	1.285928
2	0.974872	0.008472	1.418728	38	0.002396	-0.003709	1.276390
3	0.935802	0.018224	1.411297	39	0.005611	-0.008211	1.266852
4	0.896306	0.028252	1.403865	40	0.011664	-0.013773	1.257313
5	0.856547	0.038651	1.396434	41	0.022095	-0.020074	1.247775
6	0.815948	0.049434	1.389002	42	0.041833	-0.027787	1.238237
7	0.775823	0.060035	1.381571	43	0.073748	-0.036125	1.228698
8	0.736687	0.070106	1.374139	44	0.114538	-0.043675	1.219160
9	0.698373	0.079516	1.366708	45	0.159444	-0.049794	1.209621
10	0.660767	0.088140	1.359276	46	0.205884	-0.054385	1.200083
11	0.623743	0.095894	1.351845	47	0.252843	-0.057430	1.190545
12	0.587194	0.102721	1.344413	48	0.299942	-0.058944	1.181006
13	0.551046	0.108561	1.336982	49	0.347139	-0.058900	1.171468
14	0.515246	0.113322	1.329550	50	0.394577	-0.057349	1.291339
15	0.479737	0.117017	1.322119	51	0.442337	-0.054333	1.281801
16	0.444487	0.119577	1.314687	52	0.490602	-0.049903	1.272262
17	0.409471	0.120975	1.307256	53	0.539574	-0.044179	1.262724
18	0.374649	0.121218	1.299824	54	0.589551	-0.037297	1.253186
19	0.340091	0.120233	1.421802	55	0.640895	-0.029456	1.243647
20	0.305811	0.118065	1.414371	56	0.693925	-0.020980	1.234109
21	0.271810	0.114620	1.406939	57	0.745864	-0.012830	1.224571
22	0.238110	0.109971	1.399508	58	0.795484	-0.005739	1.215032
23	0.204896	0.104047	1.392076	59	0.842737	-0.000181	1.205494
24	0.172343	0.096922	1.384645	60	0.887461	0.003428	1.195956
25	0.140763	0.088603	1.377213	61	0.929230	0.004732	1.186417
26	0.110662	0.079170	1.369782	62	0.966685	0.003453	1.176879
27	0.082797	0.068811	1.362350				
28	0.058140	0.057876	1.354919				
29	0.037934	0.046963	1.347487				
30	0.022870	0.036851	1.340056				
31	0.012675	0.028129	1.332624				
32	0.006478	0.021095	1.325193				
33	0.002887	0.015548	1.317761				
34	0.001065	0.011298	1.310330				
35	0.000196	0.007710	1.302898				
36	0.000000	0.004581	1.295467				

Table D.1: Pressure tab distribution of the NACA64-618 airfoil

suction side				pressure side			
no.	x_1/c	x_2/c	x_3/c	no.	x_1/c	x_2/c	x_3/c
1	1.000000	0.000404	1.426160	37	0.000462	-0.003600	1.289632
2	0.962953	0.011130	1.418838	38	0.001715	-0.007129	1.279951
3	0.925676	0.020412	1.411516	39	0.004310	-0.010943	1.270270
4	0.887778	0.029317	1.404195	40	0.009193	-0.015548	1.260589
5	0.849430	0.037846	1.396873	41	0.018982	-0.021616	1.250909
6	0.810710	0.046053	1.389551	42	0.039115	-0.029734	1.241228
7	0.771674	0.053955	1.382230	43	0.072785	-0.039168	1.231547
8	0.732394	0.061581	1.374908	44	0.114681	-0.047957	1.221866
9	0.692895	0.068949	1.367587	45	0.159446	-0.055150	1.212185
10	0.653220	0.076080	1.360265	46	0.205108	-0.060542	1.202505
11	0.613422	0.082980	1.352943	47	0.250979	-0.064075	1.192824
12	0.573558	0.089647	1.345622	48	0.297428	-0.065783	1.183143
13	0.533798	0.096056	1.338300	49	0.344788	-0.065799	1.173462
14	0.494927	0.102012	1.330979	50	0.393026	-0.064219	1.293191
15	0.458173	0.107099	1.323657	51	0.441442	-0.061196	1.283510
16	0.423656	0.110934	1.316335	52	0.490054	-0.056736	1.273829
17	0.390057	0.113507	1.309014	53	0.539626	-0.050866	1.264148
18	0.356587	0.114858	1.301692	54	0.590772	-0.043779	1.254468
19	0.323209	0.114984	1.423780	55	0.643270	-0.035857	1.244787
20	0.290217	0.113835	1.416458	56	0.696710	-0.027417	1.235106
21	0.258040	0.111443	1.409137	57	0.750849	-0.018693	1.225425
22	0.226855	0.107770	1.401815	58	0.804264	-0.010136	1.215744
23	0.196630	0.102681	1.394494	59	0.854208	-0.002726	1.206064
24	0.167319	0.096238	1.387172	60	0.898696	0.002402	1.196383
25	0.138996	0.088413	1.379850	61	0.936916	0.004515	1.186702
26	0.111838	0.079233	1.372529	62	0.969860	0.003385	1.177021
27	0.086160	0.068794	1.365207				
28	0.062465	0.057333	1.357885				
29	0.041655	0.045358	1.350564				
30	0.025183	0.033923	1.343242				
31	0.013882	0.024161	1.335921				
32	0.007009	0.016536	1.328599				
33	0.003224	0.010816	1.321277				
34	0.001185	0.006379	1.313956				
35	0.000288	0.002893	1.306634				
36	0.000000	0.000000	1.299313				

Table D.2: Pressure tab distribution of the NACA64-618t airfoil

suction side				pressure side			
no.	x_1/c	x_2/c	x_3/c	no.	x_1/c	x_2/c	x_3/c
1	1.000000			47	0.000567		
2	0.972822			48	0.001856		
3	0.945644			49	0.004022		
5	0.891144			50	0.007422		
6	0.863833			51	0.012544		
7	0.836478			52	0.019989		
8	0.809111			53	0.030211		
9	0.781711			54	0.043622		
10	0.754300			55	0.059833		
11	0.726922			56	0.078500		
12	0.699633			57	0.099089		
13	0.672344			58	0.121078		
14	0.644978			59	0.144067		
15	0.617589			60	0.167944		
16	0.590233			62	0.217378		
17	0.562922			63	0.242767		
18	0.535656			64	0.268467		
19	0.508444			65	0.294456		
20	0.481300			66	0.320689		
21	0.454244			67	0.347100		
22	0.427278			68	0.373678		
23	0.400422			69	0.400422		
24	0.373678			70	0.427278		
25	0.347100			71	0.454244		
26	0.320689			72	0.481300		
27	0.294456			73	0.508444		
28	0.268467			74	0.535656		
29	0.242767			75	0.562922		
30	0.217378			76	0.590233		
31	0.192411			77	0.617589		
32	0.167944			78	0.644978		
33	0.144067			79	0.672344		
34	0.121078			80	0.699633		
35	0.099089			81	0.726922		
36	0.078500			82	0.754300		
37	0.059833			83	0.781711		
38	0.043622			84	0.809111		
39	0.030211			85	0.836478		
40	0.019989			86	0.863833		
41	0.012544			87	0.891144		
42	0.007422			90	0.972822		
43	0.004022						
44	0.001856						
45	0.000567						
46	0.000000						

Table D.3: Pressure tab distribution of the NACA0015 airfoil

suction side				pressure side			
no.	x_1/c	x_2/c	x_3/c	no.	x_1/c	x_2/c	x_3/c
1	0.000000	0.004583	1.517717	25	0.166667	-0.050617	1.766667
2	0.007333	0.022250	1.532400	26	0.500000	-0.048900	1.686667
3	0.024500	0.038083	1.538017	27	0.800000	-0.005133	1.614667
4	0.048367	0.052867	1.544767	28	0.950000	0.004367	1.578667
5	0.078883	0.067217	1.552867	29	0.950000	0.004367	1.545333
6	0.116850	0.081233	1.562583				
7	0.163483	0.094750	1.574233				
8	0.220450	0.106983	1.588217				
9	0.289717	0.116600	1.605017				
10	0.373500	0.121217	1.625150				
11	0.467883	0.118017	1.647833				
12	0.561667	0.106933	1.670500				
13	0.654500	0.089500	1.693167				
14	0.746400	0.067633	1.715850				
15	0.837783	0.043633	1.738517				
16	0.900000	0.027300	1.753950				
17	0.950000	0.014683	1.766333				
18	0.975000	0.008433	1.891333				
19	0.975000	0.008433	1.886333				
20	0.975000	0.008433	1.878833				
21	0.975000	0.008433	1.866333				
22	0.975000	0.008433	1.849667				
23	0.975000	0.008433	1.828833				
24	0.975000	0.008433	1.800500				

Table D.4: Microphone distribution of the NACA64-618 airfoil

suction side				pressure side			
no.	x_1/c	x_2/c	x_3/c	no.	x_1/c	x_2/c	x_3/c
1	0.000000	0.000000	1.518000	25	0.166667	-0.056117	1.766667
2	0.008133	0.017933	1.532817	26	0.500000	-0.055650	1.686667
3	0.025700	0.034333	1.538600	27	0.800000	-0.010800	1.614667
4	0.049767	0.050300	1.545533	28	0.950000	0.004467	1.578667
5	0.080533	0.066267	1.553850	29	0.950000	0.004467	1.545333
6	0.119083	0.081867	1.563850				
7	0.166917	0.096150	1.575833				
8	0.225717	0.107600	1.590217				
9	0.297283	0.114200	1.607467				
10	0.383533	0.113900	1.628183				
11	0.474600	0.104933	1.650150				
12	0.565050	0.091033	1.672100				
13	0.655283	0.075717	1.694067				
14	0.745283	0.059117	1.716033				
15	0.834983	0.040950	1.738000				
16	0.900000	0.026500	1.753983				
17	0.950000	0.014417	1.766333				
18	0.975000	0.008000	1.891333				
19	0.975000	0.008000	1.886333				
20	0.975000	0.008000	1.878833				
21	0.975000	0.008000	1.866333				
22	0.975000	0.008000	1.849667				
23	0.975000	0.008000	1.828833				
24	0.975000	0.008000	1.800500				

Table D.5: Microphone distribution of the NACA64-618t airfoil

suction side				pressure side			
no.	x_1/c	x_2/c	x_3/c	no.	x_1/c	x_2/c	x_3/c
1	0.000000		0.750000	34	0.001300		0.760000
2	0.001300		0.740000	35	0.006500		0.770000
3	0.006500		0.730000	36	0.019000		0.780000
4	0.019000		0.720000	37	0.029300		0.784900
5	0.029300		0.715100	38	0.042200		0.789900
6	0.042200		0.710100	39	0.057400		0.794900
7	0.057400		0.705100	40	0.074200		0.799900
8	0.074200		0.700100	41	0.092000		0.804900
9	0.092000		0.695100	42	0.110600		0.809900
10	0.110600		0.690100	43	0.129700		0.814900
11	0.129700		0.685100	44	0.148900		0.819900
12	0.148900		0.680100	45	0.188000		0.829900
13	0.188000		0.670100	46	0.227700		0.839900
14	0.227700		0.660100	47	0.268300		0.849800
15	0.268300		0.650200	48	0.310300		0.859800
16	0.310300		0.640200	49	0.354200		0.869800
17	0.354200		0.630200	50	0.400000		0.875956
18	0.400000		0.624044	51	0.447100		0.918178
19	0.447100		0.587378	52	0.495000		0.928078
20	0.495000		0.577478	53	0.543200		0.938078
21	0.543200		0.567478	54	0.591600		0.948078
22	0.591600		0.557478	55	0.640000		0.958078
23	0.640000		0.547478	56	0.688400		0.968078
24	0.688400		0.537478	57	0.736500		0.978078
25	0.736500		0.527478	58	0.784800		0.987978
26	0.784800		0.517578	59	0.833000		0.997978
27	0.833000		0.507578	60	0.833000		0.816667
28	0.833000		0.683333	61	0.894444		0.800889
29	0.894444		0.699111	62	0.950000		0.783333
30	0.950000		0.716667	63	0.977778		0.772222
31	0.977778		0.727778	64	0.994444		0.761111
32	0.994444		0.738889				
33	1.000000		0.750000				

Table D.6: Microphone distribution of the NACA0015 airfoil

Appendix E

Microphone Adapter Design

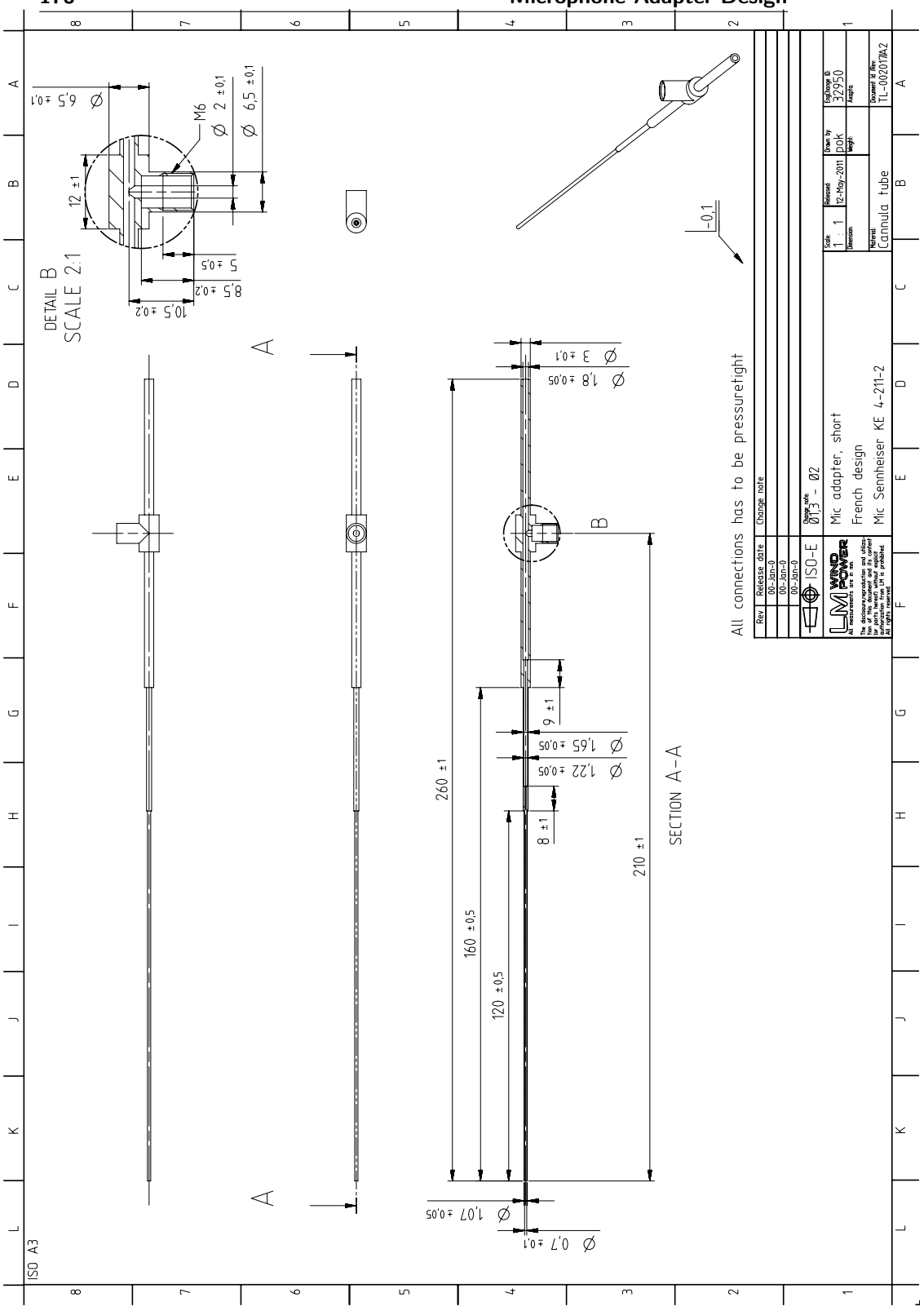
DETAIL B
SCALE 2.1
M6
Ø 2 ±0,1
Ø 6,5 ±0,1
Ø 6,5 ±0,1
12 ±1
5 ±0,5
8,5 ±0,2
10,5 ±0,2
A
A
B
SECTION A-A
Ø 3 ±0,1
Ø 1,8 ±0,05
Ø
9 ±1
Ø 1,65 ±0,05
Ø 1,22 ±0,05
8 ±1
260 ±1
160 ±0,5
120 ±0,5
210 ±1
Ø 1,07 ±0,05
Ø 0,7 ±0,1
-0,1
All connections has to be pressuretight
Rev
Release date
Change note
00-Jan-0
00-Jan-0
00-Jan-0
ISO-E
Change code
013_ 02
LM WIND POWER
A GE Power Conversion Business
The disclosure, reproduction and utilization of this document and its content is forbidden, unless given written authorization from LM is prohibited.
All rights reserved
Mic adapter, short
French design
Mic Sennheiser KE 4-211-2
Scale
1 : 1
Released
12-May-2011
Drawn by
pak
Weight
Material
Cannula tube
Logforce ID
32950
Assets
Document id. Rev.
TL-002017WA2
ISO A3

Nomenclature

roman

$a_v = \frac{U_\infty}{U_c}$	ratio of free stream to convection vel.	-
b	half airfoil chord	m
b	derivative of stagnation enthalpy in normal direction	ms^{-2}
b	beamforming output	Pa
B	stagnation enthalpy	m^2s^{-2}
c	Airfoil chord	m
$c_v = \frac{U_c}{U_\infty}$	ratio of convection to free stream vel.	-
c_0	speed of sound	m/s
C_d	drag coefficient	-
C_l	lift coefficient	-
C_m	moment coefficient	-
C_o	cost function	-
C_p	pressure coefficient	-
dZ	Fourier-Stieltjes differential of velocity	-
D	magnitude factor	-
e_t	turbulent kinetic energy	m^2s^{-2}
E	energy spectrum	m^2s^{-2}
E	voltage	V
f	frequency	Hz
F	vel. spectral density integrated over k_2, k_3	m^3s^{-2}
i	imaginary unit	-
l	correlation length scale	m
L	wetted spanwise extent	m
L	length scale	m
$M_0 = \frac{U_0}{c}$	free flow Mach number	-

p	pressure	Pa
p_o	point spread function	-
P	pressure	Pa
Pr	Prandtl number	-
q	volume velocity	$m^3 s^{-1}$
r	radius	m
R_a	reflexion coefficient	-
R_t	modified coordinate	m
R_S	modified coordinate	m
Re	Reynolds number	-
s	Surface curvilinear coordinate	m
S	cross sectional area	m^2
S_0	modified coordinate	m
S_f	far field sound pressure frequency spectral density	$Pa^2 Hz^{-1}$
t	time	s
T	integral time scale	s
U_∞	free stream velocity	ms^{-1}
U_c	convection velocity	ms^{-1}
U_e	velocity at edge of boundary layer	ms^{-1}
U_f	friction velocity	ms^{-1}
V	volume	m^3
z	surface normal coordinate	m
Z	acoustic impedance	$Pam^{-3}s^1$
$\vec{C}$	array propagation vector	-
$\vec{k} \equiv (k_1, k_2, k_3)$	wave number	m^{-1}
$\vec{K} \equiv (K_1, K_2, K_3)$	convective wave number	m^{-1}
$\vec{M}_V = \frac{\vec{V}}{c}$	boundary layer Mach number	-
$\vec{M}_W = \frac{\vec{W}}{c}$	wake Mach number	-
$\vec{N}$	modified wave number	m^{-1}
$\vec{q}$	wake dipole source	ms^{-2}
$\vec{Q}$	incident dipole source	ms^{-2}
$\vec{R}$	polar coordinate of observer position	m, rad
$\mathbf{T}$	transmission matrix	-
$\vec{x} \equiv (x_1, x_2, x_3)$	cartesian coordinate	m
$\vec{X}$	cartesian coordinate normalized by half chord	m
$\vec{y} \equiv (y_1, y_2, y_3)$	cartesian coordinate of observer position	m
$\vec{v}$	velocity	ms^{-1}
$\vec{V}$	mean boundary layer velocity	ms^{-1}
$\vec{W}$	near wake mean velocity	ms^{-1}

greek

α	Angle of attack	$^\circ$
α	scaling parameter in energy spectrum	-
α	damping parameter	-
δ^*	displacement thickness	m
$\overline{\epsilon}$	mean dissipation	$m^2 s^{-3}$
γ	normalized pressure gradient	-
Γ	proportionality constant for eddy life time	-
Γ	Gamma function	-
ν	kinematic viscosity	$m^2 s^{-1}$
μ	dynamic viscosity	Pas
ω	angular frequency	rad
ω_z	convective angular frequency	rad
ϕ	phase	rad
Φ	velocity spectral density	$m^5 s^{-1}$
Φ	angle to observer position	$^\circ$
Φ_m	moving axis spectrum	-
ρ_0	Mass density	kgm^{-3}
Π	pressure frequency wave number spectral density	$Pa^2 m^3 s$
Π_0	Π integrated over K_1	$Pa^2 m^2 s$
Θ	angle to observer position	$^\circ$
τ_e	eddy life time	s
ξ	normalization parameter in beamforming algorithm	Pa
ξ	empirical constant in Corcos' model	-
$\vec{\kappa} = (K_1, K_3)$	two dimensional wave number	m
$\vec{\eta}$	separation distance	m
$\vec{\omega} = \nabla \times \vec{v}$	vorticity	s^{-1}

subscripts

1	streamwise direction
2	surface normal direction
3	lateral direction
c	corrected
cal	calibration
E	effective
i	inlet
G	geometric

max	maximum
M	microphone position
o	outlet
p	probe coordinate system
R	component in observer direction
s	surface
sub	sub-system
S	source
T	turn table
w	wire

abbrevations

AoA	angle of attack
CFD	Computational fluid dynamics
DTU	Technical University of Denmark
IFC	interference correction
LES	large eddy simulation
LSWT	Low Speed Wind Tunnel
RANS	Reynolds-Averaged Navier-Stokes
RDT	rapid distortion theory
SPKM	surface pressure Kraichnan Mann
US	uniform shear
US+B	uniform shear and blocking
TE	trailing edge
VT	Virginia Tech
VTST	Virginia Tech Stability Tunnel